Theoretical and experimental investigation on surface segregation of Cu-Ni(S) bulk and thin film alloys

By

Xin Liang Yan

(M.Sc)

A thesis submitted in accordance with the requirements for the degree

PHILOSOPHIAE DOCTOR

in the

Department of Physics

Faculty of Natural and Agricultural Sciences

at the

University of the Free State

Republic of South Africa

Supervisor:
Prof. J.J. Terblans

Co-supervisor:
Prof. H.C. Swart

July 2017

Acknowledgements

The author wishes to express his thanks to the following individuals and institutions:

- **Prof. J.J.(Koos) Terblans**, my supervisor for his advice, friendship and positive attitude. You truly were and remain to be a mentor to me.
- **Prof. Hendrik C. Swart,** my co-supervisor for his advice, time and in particular for his fruitful discussions and guidance in all the papers published from this study. You are a really good friend and mentor.
- **Prof. JiangYong Wang,** Shantou University, China, for introducing me into the diffusion and segregation project, and for his continued support.
- **Prof. Wiets D. Roos,** for interesting this project and useful discussions.
- **Dr. Liza Hugo-Coetzee,** for assisting with the PHI 700 depth profile with sample rotation measurement, **Dr. Mart-Mari Biggs,** for assisting with the ToF-SIMS depth profile measurement, **Dr. Shaun Cronjé,** for assisting with maintenance on the e-beam evaporation system, and **Dr. Pieter E. Barnard** and **Dr. Moshawe Jack Madito** for assisting with the PHI 590 SAM and PHI 600 SAM system.
- All the staff at the Instrumentation Unit at the University of the Free State. In particular **Mr. Kobus Kruger** and **Mr. Johan Erasmus** for assisting in cutting the sample and making the equipment unit in PHI 590 system.
- All the staff at the Electronics Unit at the University of the Free State. In particular **Mr. Innes Basson** and **Mr. Adriaan B. Hugo** for assisting in solving equipment (PHI 600 SAM and e-beam evaporation system) problems.
- The staff and students at the Department of Physics, University of the Free State. **Mrs. Karen Cronje** and **Mrs. Yolandie Fick** for the support of the administrative.
- The funding from Cluster program of the University of the Free State and South African Research Chairs Initiative of the Department of Science and Technology (Grant No. 84415) for financial support.
- My family and friends for their inspiration and encouragement. In particular **my wife Mrs. LinYing Li** for her unwavering love!
- *God* for giving me strength and courage (Philippians 4:13) to complete this study.

Abstract

In this study, the surface segregation in a Ni-Cu alloy was investigated by modeling the segregation process theoretically and also measuring it experimentally. This was performed for a bulk crystal and thin films. In addition to the segregation measurements, the Ni/Cu multilayer thin films were also used to study the interdiffusion of Cu and Ni with AES depth profiling. The MRI model was used to quantitatively evaluate the sputtering-induced surface roughness and depth resolution for AES and SIMS depth profiling.

Depth profiles of the Ni/Cu polycrystalline multilayer thin films were performed by AES and SIMS in combination with ion sputtering. The measured depth profiles data were quantitative analyzed with the MRI model. The sputtering-induced surface roughness and depth resolution were evaluate for sputtering with (i) a stationary sample, (ii) a rotating sample and (iii) a stationary sample with two ion beams simultaneously. The results show that the depth resolution is smaller when profiling with dual-ion beam vs. a single-ion beam. It was also found that profiling with a lower ion energy result in a better (smaller) depth resolution. Rotation of the sample during ion sputtering had the better (smaller) depth resolution. Depth profiling with Cs^+ ion sputtering had the best depth resolution compared to Xe^+ and O_2^+ ion sputtering.

The MRI model was also used for extracting the interdiffusion coefficients for the AES depth profiles of a Ni/Cu multilayer. The interdiffusion parameter for Cu/Ni multilayer thin films was characterized for the first interface $D_o = 6.2 \times 10^{-13}$ m^2/s and $Q = 101.4$ kJ/mol, and the last Cu/Ni interface $D_o = 6.3 \times 10^{-14}$ m^2/s and $Q = 79.0$ kJ/mol. It was clearly showing that the depth-dependent interdiffusion coefficients are depth-dependent.

The segregation of Cu and S from a ternary Ni-Cu(S) bulk alloy was measured with AES using linear temperature programmed heating and constant temperature heating. The segregation data were fitted with the modified Darken model and the segregation parameters were $D_{o\text{Cu in Ni}} = 8.6\times10^{-14}$ m^2/s, $Q_{\text{Cu in Ni}} = 145.2$ kJ/mol, $D_{o\text{S in Ni}} = 9.2\times10^{-2}$ m^2/s, $Q_{\text{S in Ni}} = 224.0$ kJ/mol, $\Delta G_{Cu} = -36.0$ kJ/mol, $\Delta Gs = -136.0$ kJ/mol, $\Omega_{Cu\text{-}Ni} = 7.6$ kJ/mol, $\Omega_{S\text{-}Ni} = 28.1$ kJ/mol and $\Omega_{Cu\text{-}S} = -10.3$ kJ/mol.

The segregations of Cu from a Ni-Cu thin film alloy were measured using AES with linear temperature programmed heating. The segregation measured profile data were fitted with a modified Fick's model and the segregation parameters obtained $D_o = 2.8\times10^{-13}$ m^2/s and $Q = 135.3$ kJ/mol for the 26 nm thin film and for thicker film (52 nm) $D_o = 2.9\times10^{-13}$ m^2/s and $Q = 140.5$ kJ/mol. The modified Darken model is there adapted to simulate segregation from thin films and also showed that the thickness of the thin film significantly affects the segregation.

Key words

Surface segregation
Ni-Cu alloy thin films
Interdiffusion
Ni/Cu multilayer thin films
Modified Darken model
MRI model
Ni-Cu(S)
AES depth profile
ToF-SIMS depth profile
Depth resolution
Sputtering induced roughness
Segregation energy
Interaction energy
Diffusion coefficient
Ternary alloy system

Contents

Chapter 1

Introduction

1.1 Overview

Surface segregation is a well-known interface segregation phenomenon which has many academic and practical interests. Interface segregation (*i.e.* surface or grain boundary) is regarded as the redistribution of solute atoms between the interface and the bulk of a material resulting in a solute interface concentration, which is generally higher than the solute bulk concentration [1]. Interface segregation is not a new phenomenon, it was treated formally by Gibbs a century ago [2]. Today, interface segregation investigations have been applied in many aspects, for example, surface segregation influencing adsorption and catalytic properties of the material [3-4]; grain boundary segregation is directly responsible for the processes of inter-crystalline corrosion, hydrogen and liquid metal embrittlement, and high and low-temperature fracture [5-10]. Especially, S impurity segregation is a common phenomenon in many metals and alloys. Grain boundary segregation of S can cause embrittlement of a metal or alloy due to the S-induced changes in the electronic structure that can lead to the weakening of atomic bonds between grain boundaries [8-10].

Nowadays, nanoscale metallic alloy systems (thin films and particles) have become increasingly important in a wide range of technologically important applications. For example, nanoscale particles are used in catalysis because of their high reactivity and reaction specificity [11]. The catalytic properties of a material are largely determined by the composition and structure of its surface which in turn depend on the average

composition. The composition, structure and property of a surface in alloy thin films are affected by surface segregation. Although there has been a great deal of experimental and theoretical work devoted to understanding the thermodynamics of bulk systems [12, 13], there have been relatively few studies of the thermodynamics of nanoscale systems [14-22]. In nanoscale systems, unlike in bulk materials, the surface properties also depend on the size of the system and can vary significantly from those of surfaces bounding a semi-infinite bulk.

The Ni-Cu alloy system has been extensity investigated because of its application in catalysis and metallurgy [23]. It has a simple phase diagram and forms a solid solution in the entire range of composition. Therefore, surface segregation in Ni-Cu alloy system has been a subject of many investigations over more than thirty years [24-30]. In theory, numerous models (methods) have been/can be used for simulation of segregation profile in Ni-Cu alloy system, for example, the Monte Carlo method [24], the electronic-structure based methods [25] and the Langmuir-Mclean model [18, 21] to name a few. All these models predict that Cu atoms must segregate to the surface for the all composition of Ni-Cu alloys. This prediction has been verified experimentally by X-ray photoelectron spectroscopy (XPS) [27], atom probe field ion microscopy (AP-FIM) [28], ion-scattering-spectroscopy (ISS) [29], low-energy ion scattering (LEIS) [30] and Auger electron spectroscopy (AES) [17]. These models and experimental observation of surface segregation are all for bulk system. For a thin film system, the number of segregated atoms on the surface is a significant fraction of the total number of atoms in the system and therefore the bulk concentration of the thin film is modified significantly during segregation. The lack of a reservoir of segregating atoms in thin films may cause significant differences in surface segregation as compared to bulk materials. Therefore, the surface segregation from a Ni-Cu alloy will be studied theoretically and experimentally for both bulk and thin film systems.

1.2 Research aims

(a) To quantitatively study the depth resolution and sputtering-induced surface roughness of AES depth profiles with MRI model and how it is affected by

different experiment setups;

(b) To further study the influence of the different ion source (O_2^+, Cs^+ and Xe^+) and different sputter ion energies on ToF-SIMS depth profiling of polycrystalline Ni/Cu multilayer thin films with MRI model;

(c) To demonstrate how to determine the interdiffusion coefficients in Ni/Cu multilayer thin films by fitting the AES depth profiles by using the MRI model;

(d) To study the surface segregations in a Ni-18.7at.%Cu alloys bulk material by using AES measurement in combination with both the linear temperature programmed heating and the constant temperature heating methods. The segregation measured data will be used to extract for the segregation parameters, namely, segregation energy, interaction energy and diffusion coefficient (pre-exponential and activation energy) with a modified Darken model;

(e) To study the size effects on surface segregations in Ni-Cu alloy thin films.

1.3 Outline of the thesis

Chapter 2 provides the fundamental concepts of surface segregation and diffusion and in crystalline bulk materials and thin films. In this chapter, the surface segregation theories for the modified Darken model (that describe equilibrium and kinetics segregation) are introduced and the constraining condition t for simulating segregation in a thin film system will be derived. These models are used to extract the segregation parameters from the experimental segregation data in Chapters 8 and 9.

Chapter 3 describes the preparation methods, techniques and equipment used of growing Ni/Cu multilayer systems and Cu-Ni thin film alloys that was used in this study.

Chapter 4 provides a brief description of surface analysis techniques (Auger electron spectroscopy (AES), time-of-flight secondary ion mass spectrometry (ToF-SIMS), X-Ray diffraction (XRD) and atom force microscope (AFM)) used in this study.

Chapter 5 is a quantitatively investigates the depth resolution and sputtering-induced surface roughness in AES depth profiles are studied utilising the MRI model. Different experiment setups which include sample rotation with single ion beam sputtering, no sample rotation with single ion beam sputtering, no sample rotation with dual ion beam sputtering and no sample rotation with single ion beam sputtering at different ion energies are invalidated.

Chapter 6 is investigates the influence of the different ion source (O_2^+, Cs^+ and Xe^+) and different sputter ion energies on the depth resolution and sputtering-induced surface roughness for ToF-SIMS depth profiling of polycrystalline Ni/Cu multilayer thin films.

Chapter 7 demonstrate how to determine the interdiffusion coefficients in Ni/Cu multilayer thin film by fitting the AES depth profiles with the MRI model

Chapter 8 is to study the surface segregations in a Ni-18.7at.%Cu alloys bulk material using AES measurement in combination with the linear temperature programmed heating and the constant temperature heating methods. The segregation measured data was used to extract for the segregation parameters (segregation energy, interaction energy, pre-exponential and activation energy) with the modified Darken model.

Chapter 9 is to study the surface segregations in Ni-Cu alloy thin films (two samples with different thickness) using AES measurement in combination with the linear temperature programmed heating method. The measured segregation data was used to extract the segregation parameters using thin film constrained condition in the modified Darken model to simulate the segregation.

Chapter 10 concludes outlining the results obtained in this thesis.

References

[1] J. Du Plessis, Solid State Phenomena-Part B, surface segregation, Sci-Tech Publications, Brookfield USA, 1990.

[2] J.W. Gibbs, The scientific papers of J.W. Gibbs, 1, Dover, NewYork, 1961.

[3] V. Stamenković, T.J. Schmidt, P.N. Ross, N.M. Marković, Surface segregation effects in electrocatalysis:kinetics of oxygen reduction reaction on polycrystalline Pt_3Ni alloy surfaces, J. Electroanal. Chem. **554** (2003) 191-199.

[4] H.B. Liao, F. Adrian, Z.J. Xu, Surface segregation in bimetallic nanoparticles: a critical issue in electrocatalyst engineering, Small **11** (2015) 3221-3246.

[5] L.S. Chang, E. Rabkin, B.B. Straumal, B. Baretzky, W. Gust, Thermodynamic aspects of the grain boundary segregation in Cu (Bi) alloys, Acta Mater. **47**(1999) 4041-4046.

[6] J. Kang, G.C. Glatzmaier, S.H. Wei, Origin of the Bismuth-induced decohesion of nickel and copper grain boundaries, Phys. Rev. Lett. **111** (2013) 055502.

[7] M.R. Chellali, L. Zheng, R. Schlesiger, B. Bakhti, A. Hamou, J. Janovec, G. Schmitz, Grain boundary segregation in binary nickel-bismuth alloy, Acta Mater. **103** (2016) 754-760.

[8] M. Allart, F. Christien, R. Le Gall, Ultra-fast sulphur grain boundary segregation during hot deformation of nickel, Acta Mater. **61** (2013) 7938-7946.

[9] E. Pellicer, A. Varea, K.M. Sivaraman, S. Pane, S. Surinach, M.D. Baro, J. Nogues, B.J. Nelson, J. Sort, Grain boundary segregation and interdiffusion effects in nickel-copper alloys: an effective means to improve the thermal stability of nanocrystalline nickel, ACS Appl. Mater. Interfaces **3** (2011) 2265-2274.

[10] M. Yamaguchi, S. Motoyuki, K. Hideo, Grain boundary decohesion by impurity segregation in a nickel-sulfur system, Science **307** (2005) 393-397.

[11] R. Ferrando, J. Jellinek, R.L. Johnston, Nanoalloys: from theory to applications of alloy clusters and nanoparticles, Chem. Rev. **108** (2008) 845-910.

[12] S. Swaminarayan, R. Najafabadi, D.J. Srolovitz, Polycrystalline surface properties from spherical crystallites: Ag, Au, Cu and Pt, Surf. Sci. **306** (1994) 367-380.

[13] F.R. de Boer, R. Boom, W.C.M. Mattens, A.R. Miedema, A.K. Niessen, Cohesion in metals: Transition metals alloys, North Holland, Amsterdam, 1988.

[14] C. Cserháti, I.A. Szabó, D.L. Beke, Size effects in surface segregation, J. Appl. Phys. **83** (1997) 3021-3027.

[15] A.M. Llois, C.R. Mirasso, Segregation in thin films of binary alloys A_xB_{1-x} Phys. Rev. B **41**(1990) 8112.

[16] M. Schmid, W. Hofer, P. Varga, P. Stoltze, K.W. Jacobsen, J.K. Norskov, Surface stress, surface elasticity, and the size effect in surface segregation, Phys. Rev. B **51** (1995) 10937.

[17] J. Nyeki, C. Girardeaux, G. Erdelyi, A. Rolland, J. Bernardini, Equilibrium surface segregation enthalpy of Ge in concentrated amorphous SiGe alloys. Appl. Surf. Sci. **212** (2003) 244-248.

[18] S. Swaminarayan, D.J. Srolovitz, surface segregation in thin films, Acta Mater. **44 (**1996) 2067-2072.

[19] J.A. Brown, Y. Mishin, Effect of surface stress on Ni segregation in (110) NiAl thin films, Phys. Rev. B **69** (2004) 195407.

[20] S. Swaminarayan, R. Najafabadi, D.J. Srolovitz, Finite size effects on the thermodynamics of Cu-Ni alloys:{100} and {110} thin films, Acta Mater. **45 (**1997) 1715-1724.

[21] X.L. Yan, J.Y. Wang, Size effects on surface segregation in Ni-Cu alloy thin films, Thin Solid Films **529** (2013) 483-487

[22] X.L. Yan, M. Lin, J.Y. Wang, Equilibrium and kinetic surface segregations in Cu-Sn thin films, Appl. Phys. A **113**(2013) 423-430

[23] T. Sakurai, T. Hashizume, A. Kobayashi, A. Sakai, S. Hyodo, Y. Kuk, H.W. Pickering, Surface segregation of Ni-Cu binary alloys studied by an atom-probe, Phys. Rev. B **34** (1986) 8379.

[24] S. Ouannasser, L.T. Wille, H. Dreysse, Cluster expansions at alloy surfaces: Formalism and application to segregation in Ni-Cu, Phys. Rev. B **55** (1997) 14245.

[25] A.V. Ruban, I.A. Abrikosov, D.Y. Kats, D. Gorelikov, K.W. Jacobsen, H.L. Skriver, Self-consistent electronic structure and segregation profiles of the Cu-Ni (001) random-alloy surface, Phys. Rev. B **49** (1994) 11383.

[26] M.J. Madito, H.C. Swart, J.J. Terblans, Surface segregation measurements of In and S impurities from a dilute Cu (In, S) ternary alloy, Surf. Interface Anal. **45** (2013) 1020-1025.

[27] W.F. Egelhoff Jr, Thermochemical Values for Cu-Ni Surface and Interface Segregation Deduced from Core-Level Binding-Energy Shifts, Phys. Rev. Lett. **50** (1983) 587.

[28] T.Sakurai, T. Hashizume, A. Jimbo, A. Sakai, S. Hyodo, New result in surface segregation of Ni-Cu binary alloys, Phys. Rev. Lett. **55** (1985) 514.

[29] Y.S. Ng, T.T. Tsong, S.B. McLane, Jr., Absolute composition depth profile of a NiCu alloy in a surface segregation study, Phys. Rev. Lett. **42** (1979) 588.

[30] H.H. Brongersma, M.J. Sparnaay, T.M. Buck, Surface segregation in Cu-Ni and Cu-Pt alloys: A comparison of low-energy ion-scattering results with theory, Surf. Sci.**71** (1978) 657.

Chapter 2

Segregation theory

2.1 Introduction

Surface segregation is regarded as the redistribution of solute atoms between the surface and bulk of a material resulting in a solute surface concentration which is generally higher than the solute bulk concentration. The driving force in the segregating system is the minimization of the total Gibbs energy of the crystal. [1] Surface segregation is not a new phenomenon, it was treated formally by Gibbs a century ago [2]. Today, surface segregation investigations have been applied in many aspects [3-7] and the theories have developed rapidly in response to the growing experimental measurements requiring interpretation. The equilibrium state of surface segregation for non-interacting segregating species is described by the well-known Langmuir-McLean expression that was derived by McLean [8]. Fowlers adsorption theory that considered the interaction energy between adjacent adsorbed atoms was further extended to allow for interaction between two co-segregation species in ternary or higher multi-component systems by Guttmann [9-10]. For kinetic segregation, most models follow McLean's approach in which the solute atoms are assumed to segregate to the surface from a semi-infinite crystal of a uniform solute content and diffusion in the crystal is described by Fick's laws [11-15].

The Modified Darken model proposed by du Plessis and van Wyk based on the Darken approach, which is a unified model giving the full description of surface segregation from kinetics to equilibrium in combination with the regular solution

approximation and sub-regular solution approximation. This model has been successfully used in the equilibrium and kinetic surface segregation and linear heating measurements [4-7, 11-15]. In this chapter, we will derive the surface segregation theory for the modified Darken model to describe equilibrium and kinetics segregation, and to introduce a constrained condition that followed for a thin film system.

2.2 Equilibrium surface segregation

In this section the equilibrium condition for surface and bulk is derived from the thermodynamic framework. The equilibrium equation for binary and ternary system was obtained, are the popular Langmuir-McLean expression with no interaction and the Bragg-Willians expression (Fowler adsorption theory) with interaction for the binary alloy system, and the Guttmann expression for the multi-components segregation.

2.2.1 Equilibrium condition for surface and bulk

The basic hypotheses for the surface segregation model (layer-by-layer model) proposed by du Plessis *et al*. [16] are as follows:

(a) The crystal is regards as a closed system consisting of two phases: surface and bulk, which are both open systems;
(b) The surface region is finite and the bulk is infinite in size;
(c) Atoms may be exchange between the two phases until the energy of the system is minimized.

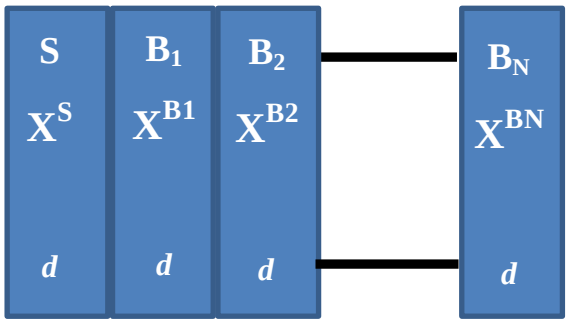

Figure 2.1: Division of the crystal in *N*+ 1 layer (one surface and *N* bulk layers).

Based on the above hypotheses, the crystal is divided into *N*+1 open subsystem which is identical in size as shown in Fig. 2.1. These subsystems may be identified as the atomic layers parallel to the surface plane but may also extend over several atomic layers. The limiting factor is the requirement that after equilibrium has been reach, each subsystem should have a constant composition.

The first subsystem is identified as the surface layer and all parameters are indicated by ***S***. The remaining ***N*** bulk subsystems are all indicated by ***B*** (see Fig. 2.1). The total Gibbs free energy of the crystal (closed system) before any segregation takes place is given by:

$$G^0 = \sum_{i=1}^{m} n_i^{0S} \mu_i^{0S} + \sum_{j=1}^{N} \sum_{i=1}^{m} n_i^{0B_j} \mu_i^{0B_j} \tag{2.1}$$

where n_i^{0S} is the number of mole of the *i*-th specie in the surface layer, μ_i^{0S} is the surface chemical potential of the *i*-th specie, $n_i^{0B_j}$ is the number of mole of the *i*-th specie in the *j*-th bulk subsystem and $\mu_i^{0B_j}$ is the chemical potential of the *i*-th specie in the *j*-th bulk subsystem. The number of species is given by *m*. The atoms of the different species are now allowed to redistribute between the various subsystems and after the redistribution has taken place the Gibbs free energy is given by:

$$G = \sum_{i=1}^{m} n_i^{S} \mu_i^{S} + \sum_{j=1}^{N} \sum_{i=1}^{m} n_i^{B_j} \mu_i^{B_j} \tag{2.2}$$

Assumption A: If the system is very large (N → ∞) the segregation will not change the bulk concentration and the number of mole of specie *i* will therefore remain unchanged:

$$n_i^{B_j} \approx n_i^{0B_j}$$

Assumption B: It is assumed that the chemical potential terms of the species *i* in bulk will remain constant:

$$\mu_i^{B_j} = \mu_i^{0B_j} = \mu_i^{B}$$

Based on the above **Assumption A** and **B**, the change in Gibbs free energy is now defined as:

$$\Delta G = G - G^0 = \sum_{i=1}^{m} n_i^S \mu_i^S + \sum_{i=1}^{m} \left[\sum_{j=1}^{N} \left(n_i^{B_j} - n_i^{0B_j} \right) \right] \mu_i^B - \sum_{i=1}^{m} n_i^{0S} \mu_i^{0S} \qquad (2.3)$$

The conservation of solute atom of species *i* may be described by:

$$n_i^S + \sum_{j=1}^{N} n_i^{B_j} = n_i^{0S} + \sum_{j=1}^{N} n_i^{0B_j}$$

Eq. 2.3 thus becomes:

$$\Delta G = \sum_{i=1}^{m} n_i^S \mu_i^S + \sum_{i=1}^{m} n_i^{0S} (\mu_i^B - \mu_i^{0S}) - \sum_{i=1}^{m} n_i^S \mu_i^B \qquad (2.4)$$

The change in Gibbs free energy ΔG is now independent of the number of cell *N* as *N* was eliminated using the conservation of atoms in crystal (shown in Fig. 2.1). In combination with Eq. 2.4, the Gibbs free energy after redistribution is given by:

$$G = G^0 + \Delta G = \left[\sum_{i=1}^{m} n_i^{0B} \mu_i^{0B} + \sum_{j=1}^{N} \sum_{i=1}^{m} n_i^{0B_j} \mu_i^B \right] + \sum_{i=1}^{m} n_i^S \left(\mu_i^S - \mu_i^B \right)$$

The expression in square brackets is a function of the initial bulk parameters only and sums over the full *N*+1 subsystems. It therefore gives the Gibbs free energy of the crystal as if no interface existed and may be denoted by G^{0B}. The summation term containing the surface parameters n_i^S and μ_i^S may be viewed as the energy required creating an interface of a surface. This energy may be noted by σ_s where σ is the surface tension and *s* is the surface area. Therefore:

$$G = G^{0B} + \sigma s$$

The molar Gibbs free energy is given by:

$$G_{mol} = G_{mol}^{0B} + \sigma \xi \qquad (2.5)$$

where ξ is the molar surface area (*s/n*) and *n* is the total number of moles in the surface layer. It therefore follows that

$$\sigma\xi = \sum_{i=1}^{m} X_i^S \left(\mu_i^S - \mu_i^B\right) \tag{2.6}$$

where X_i^S is the mole fraction or fractional concentration of species *i* in the surface.

The equilibrium state will be reached when the Gibbs free energy is a minimum at constant temperature and pressure. The equilibrium condition from Eq. 2.5 is therefore:

$$\frac{\partial G_{mol}}{\partial X_i^S} = \frac{\partial(\sigma\xi)}{\partial X_i^S} = 0$$

This condition for a constant ξ becomes:

$$\frac{\partial \sigma}{\partial X_i^S} = 0 \tag{2.7}$$

i.e. the interface or surface will be in equilibrium with the bulk when the surface tension σ is a minimum. The driving force behind the surface segregation of solute atoms is thus the change in the surface tension σ [17].

If the number of moles in the surface layer is fixed,

$$\sum_{i=1}^{m} n_i^S = n^S$$

then

$$\delta n_1^S + \delta n_2^S + \cdots \delta n_m^S = 0$$

or

$$\frac{\partial n_m^S}{\partial n_i^S} = -1 \tag{2.8}$$

This expression is different from that of two bulk phase in equilibrium since the δn_i^{υ} are independent in that case. Substituting Eq. 2.6 and Eq. 2.8 in Eq. 2.7:

$$\mu_i^S - \mu_i^B - \mu_m^S + \mu_m^B + \sum_{i=1}^{m} n_i^S \frac{\partial \mu_i^S}{\partial n_i^S} = 0 \tag{2.9}$$

The last term is equal to zero because of the Gibbs-Duhem equation [18], therefore,

$$\mu_i^S - \mu_i^B - \mu_m^S + \mu_m^B = 0 \tag{2.10}$$

2.2.2 Equilibrium equation for binary system

For a binary system (*m*= 2), the equilibrium condition in Eq. 2.10 becomes:

$$\mu_1^S - \mu_1^B - \mu_2^S + \mu_2^B = 0 \tag{2.11}$$

According to the regular solution model, the chemical potential μ_i^{υ} of species *i* in phase *v* can be expanded in terms of the surface concentration X_i^S and bulk concentration X_i^B:

$$\begin{aligned} \mu_1^{\upsilon} &= \mu_1^{0\upsilon} + \Omega_{12}\left(X_2^{\upsilon}\right)^2 + RTInX_1^{\upsilon} \\ \mu_2^{\upsilon} &= \mu_2^{0\upsilon} + \Omega_{12}\left(X_1^{\upsilon}\right)^2 + RTInX_2^{\upsilon} \end{aligned} \tag{2.12}$$

where *v* indicates the relevant phase *S* and *B*, the term of $\mu_i^{0\upsilon}$ is the standard chemical potential and Ω_{12} is the interaction parameters of system. Substituting Eq. 2.12 in Eq. 2.11, the equilibrium segregation equation for the binary system can be obtained:

$$\frac{X_1^S}{1-X_1^S} = \frac{X_1^B}{1-X_1^B} \exp\left[\frac{\Delta G + 2\Omega_{12}\left(X_1^S - X_1^B\right)}{RT}\right] \tag{2.13}$$

where $\Delta G = \mu_1^{0B} - \mu_1^{0S} - \mu_2^{0B} + \mu_2^{0S}$ is called the segregation energy. The contribution to ΔG be normal regards as the sum of the different of the pure element's surface energy and the elastic strain energy which depends on the pure solute and solvent atomic size [18]. The system with bigger different in surface energy or bigger different in atomic size will have the stronger surface segregation. The segregation energy ΔG is one of the important parameters in any segregation model.

The expression of Eq. 2.13 is in accordance with the Bragg-Willians equation deduced from the statistical thermodynamics, which has been widely used to describe the equilibrium surface segregation in bulk materials. When the interaction parameter Ω_{12} is zero, the Bragg-Williams expression of Eq. 2.13 reduces to the Langmuir-Mclean expression:

$$\frac{X_1^S}{1-X_1^S} = \frac{X_1^B}{1-X_1^B} \exp\left[\frac{\Delta G}{RT}\right] \tag{2.14}$$

Ni-Cu alloy system is a model system for the study of surface segregation since it has a simple phase diagram and forms a solid solution in the entire range of composition. Therefore, with negligible interaction parameter Ω, the Langmuir-Mclean expression of Eq. 2.14 can be applied for describing the equilibrium surface segregation for Ni-Cu. Fig. 2.2 is a plot of the equilibrium surface segregation with Langmuir-McLean expression (Eq. 2.14) for a Ni-4.6at.%Cu system with different segregation energy for different orientation. The segregation energy parameters obtained from Refs. [19, 20].

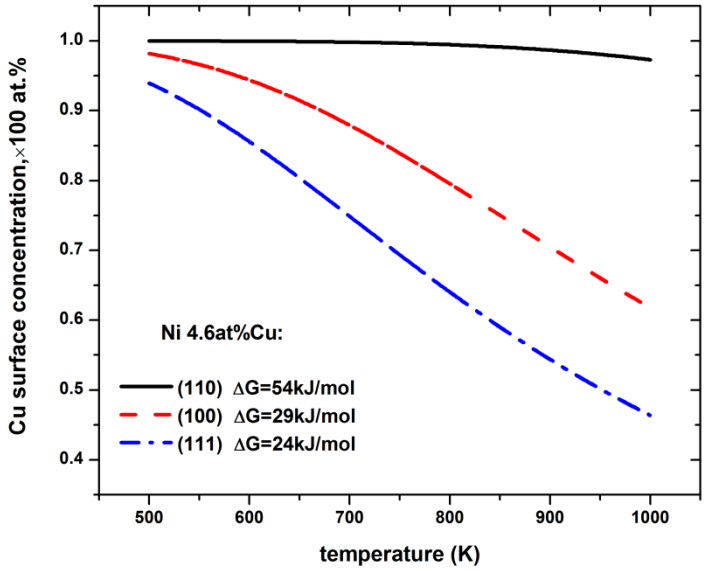

Figure 2.2: Equilibrium surface segregation with Langmuir-McLean expression (Eq. 2.14) for a Ni-4.6at.%Cu system with different segregation energy for different orientation. The segregation energy parameters obtained from Refs. [19, 20].

2.2.3 Equilibrium equation for ternary system

For a ternary system (m= 3), the equilibrium condition from Eq. 2.10 are given by

$$\begin{aligned} \mu_1^S - \mu_1^B - \mu_3^S + \mu_3^B = 0 \\ \mu_2^S - \mu_2^B - \mu_3^S + \mu_3^B = 0 \end{aligned} \tag{2.15}$$

Expanding each of the chemical potential terms using the regular solution equations [18], the following surface concentration segregation energy equations are obtained at equilibrium:

$$X_1^S = \frac{X_1^B \exp(\Delta G_1/RT)}{1 - X_1^B + X_1^B \exp(\Delta G_1/RT) - X_2^B + X_2^B \exp(\Delta G_2/RT)} \tag{2.16}$$

$$X_2^S = \frac{X_2^B \exp(\Delta G_2/RT)}{1 - X_2^B + X_2^B \exp(\Delta G_2/RT) - X_1^B + X_1^B \exp(\Delta G_1/RT)} \tag{2.17}$$

where

$$\Delta G_1 = \Delta G_1^0 + 2\Omega_{13}(X_1^s - X_1^B) + \Omega'(X_2^B - X_2^S) \quad (2.18)$$

$$\Delta G_2 = \Delta G_2^0 + 2\Omega_{23}(X_2^s - X_2^B) + \Omega'(X_1^B - X_1^S) \quad (2.19)$$

where $\Omega' = \Omega_{12} - \Omega_{13} - \Omega_{23}$, ΔG_i is the segregation energy of species *i* and Ω_{ij} is the interaction energy between species *i* and *j*.

It is noted from Eq. 2.16 and Eq. 2.17 that element *i* will segregate to the surface if $\Delta G_i > 0$. There are three driving forces in the segregation energy ΔG_i. The first term is the difference in standard chemical potentials between the surface and the bulk ΔG_i, the second is the term in Ω_{i3} which could be called the self-interaction term and the last term Ω' which takes into account the interactions between the solute atoms. The segregation energy ΔG_i will thus be positive for $\Omega_{i3} < 0$ and $\Omega' > 0$.

2.3 Kinetic surface segregation

In this section the two best known formulas to describe the kinetics of surface segregation namely the semi-infinite solution of Fick's equation and modified Darken model rate equations will be discussed. The surface segregation is rate limited by the bulk diffusion and it is therefore appropriate to apply the semi-infinite solution of Fick's equation to describe the kinetics of the segregation. The modified Darken model assumes that the driving force in a segregating system is the minimization of the chemical potential instead of the concentration gradient as is assumed in the Fick description.

2.3.1 Semi-infinite solution of Fick's equation

The Semi-infinite solution of the diffusion of Fick's is based on the following two assumptions:

(a) The initial condition is a uniform concentration distribution;
(b) The surface concentration is kept at zero for all time $t > 0$.

In order to keep mathematical relations in a familiar form, the concentration is denoted as *C*. According to the above assumption the boundary condition is

$$C = 0, \qquad x = 0, \text{ and } \qquad t > 0$$

and the initial condition is

$$C = C_B, \qquad x \geq 0, \text{ and } \qquad t = 0$$

The diffusion of atoms is controlled by Fick's equation as:

$$\frac{\partial C}{\partial t} = D\frac{\partial^2 C}{\partial x^2} \tag{2.20}$$

The solution of Eq. 2.20 subject for the above boundary and initial conditions can be obtained through Laplace transform [17] as:

$$C_S = C_B\left[1+\frac{2}{d}\left(\frac{Dt}{\pi}\right)^{1/2}\right] \tag{2.21}$$

where C_S and C_B are the surface concentration and bulk concentration, respectively, D is the diffusion coefficient and d is the thickness of a segregated layer. This expression Eq. 2.21, called $t^{1/2}$ law, is widely used to describe the time dependence of the segregated surface concentration at a constant temperature.

Linear heating

It is noted that Eq. 2.21 is applicable only for constant temperature experiments. For a linear heating experiment, the crystal is pre-heated at T_0 and the crystal temperature (T) is then increased linearly with time at a constant heating rate (α). The temperature time relation is therefore given by [12]

$$T = \mathrm{T_o} + \alpha t \tag{2.22}$$

By defining a surface enrichment factor $\beta = (C_S - C_B)/C_B$ in the surface segregation and the well-known Arrhenius relation $D = D_o \exp(-Q/RT)$, where D_o is the pre-exponential factor, Q is the activation energy and R is the universal gas constant with a value of 8.314 *kJ/mol*, Eq. 2.21 can be solved for linear heat as [12]

$$\frac{1}{2}\beta^2 = \frac{2D_o}{\pi\alpha d^2}\int_{T_0}^{T_E} \exp(-Q/RT)dT \qquad (2.23)$$

Integration of Eq. 2.23 over the temperature range of the linear programmed heating, from T_o to T_E, and one have

$$\beta^2 = \frac{4D_o}{\pi\alpha d^2}\left[\frac{RT}{E_a}\exp(-Q/RT)\right] \qquad (2.24)$$

Eq. 2.23 and 2.24 is widely used to describe the kinetics of surface segregation with pre-exponential factor D_o and activation energy Q. Fig. 2.3 illustrates the Eq. 2.23 used to describe the kinetics of S segregation in the Cu-Ni(S) alloy surface and obtain the diffusion parameters D_o and Q.

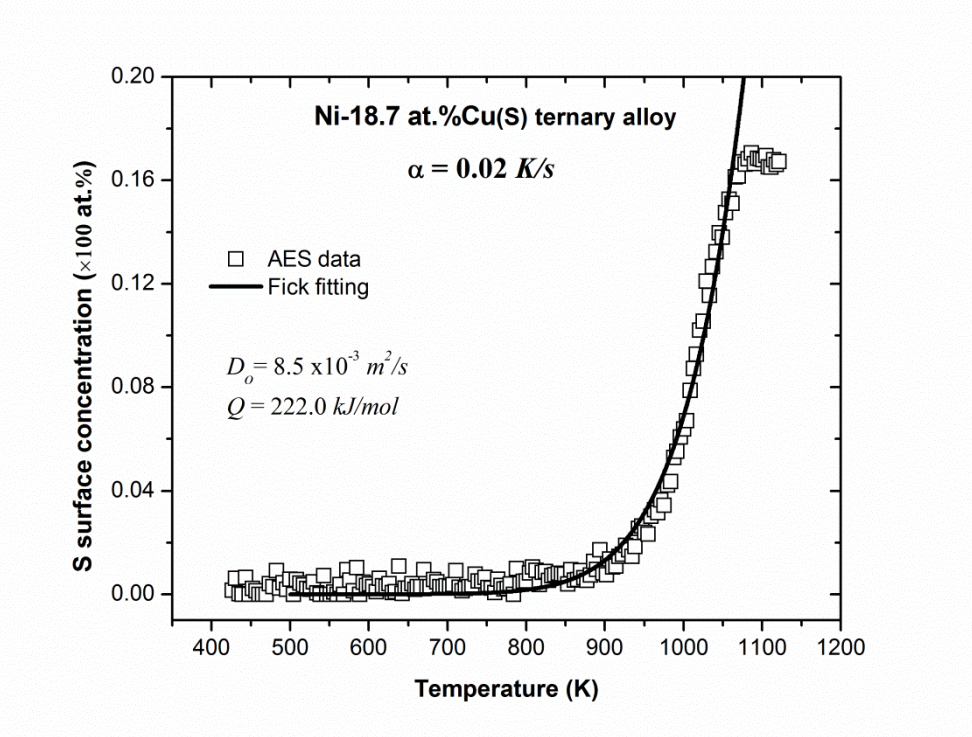

Figure 2.3: Fick's equation (Eq. 2.23) used for linear heating fitted to the surface segregation data of S to the surface of the Cu-Ni(S) alloy.

2.3.2 Modified Darken model

In the modified Darken model, it is assumed that the driving force in the segregating system is the minimization of the chemical potential instead of the concentration gradient as is assumed in the Fick description. Surface segregation is the redistribution process of solute atoms in order to minimize the total energy.

Basic assumptions

The Darken model proposes that the net flux of species *i* through a plane at $x=b$ is given by:

$$J_i = -M_i C_i^{(b)} \frac{\partial \mu_i}{\partial x} \tag{2.25}$$

where $C_i^{(b)}$ is the concentration of the species *i* in this plane and μ_i is the chemical potential of the species *i*, M_i is the mobility of the species *i*. It is clear that the spatial derivative of μ_i serves as the driving force for the movement of atoms of the species *i*.

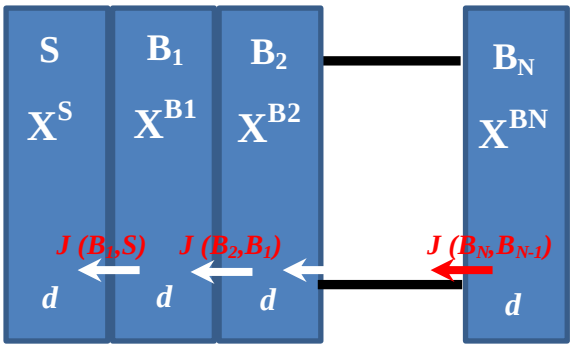

Figure 2.4: Discrete concentration distribution and the various flux terms.

Space derivative of the chemical μ_i

The crystal is divided into N+1 layers of the thickness *d* as is shown in Fig. 2.4. The Gibbs free energy of the two adjacent layers *j* and *j*+1 consisting of *m* components is given by

$$G = \sum_{i=1}^{m} n_i^{(j)} \mu_i^{(j)} + \sum_{i=1}^{m} n_i^{(j+1)} \mu_i^{(j+1)} \tag{2.26}$$

where $n_i^{(j)}$ is the number of mole of species *i* in the *j*-th layer and $\mu_i^{(j)}$ is the surface chemical potential of species *i* in the *j*-th layer. Due to the Gibbs-Duhem equation [18], the variation in the Gibbs free energy can be expressed as:

$$\begin{aligned} \delta G &= \sum_{i=1}^{m} \left(\delta n_i^{(j)} \mu_i^{(j)} + n_i^{(j)} \delta \mu_i^{(j)} \right) + \sum_{i=1}^{m} \left(\delta n_i^{(j+1)} \mu_i^{(j+1)} + n_i^{(j+1)} \delta \mu_i^{(j+1)} \right) \\ &= \sum_{i=1}^{m} \left(\delta n_i^{(j)} \mu_i^{(j)} + \delta n_i^{(j+1)} \mu_i^{(j+1)} \right) \end{aligned} \tag{2.27}$$

Considering that atoms move from layer *j*+1 to layer *j*, one has $\delta n_i^{(j)} = -\delta n_i^{(j+1)}$ and then Eq. 2.27 becomes

$$\delta G = \sum_{i=1}^{m} \delta n_i^{(j)} \left(\mu_i^{(j)} - \mu_i^{(j+1)} \right) \tag{2.28}$$

If $\delta n_i^{(j)}$ is independent, one would have

$$\frac{\partial G}{\partial n_i^{(j)}} = \left(\mu_i^{(j)} - \mu_i^{(j+1)} \right) \tag{2.29}$$

However, if the alloy is substitutional, the total number of moles in the layer is fixed, say as *n*, and one obtains the following relations:

$$\sum_{i=1}^{m} n_i^{(j)} = n$$

$$\sum_{i=1}^{m} \delta n_i^{(j)} = 0$$

i.e.:

$$\delta n_m^{(j)} = -\sum_{i=1}^{m-1} \delta n_i^{(j)} \tag{2.30}$$

Then the Eq. 2.28 may be rewritten as:

$$\begin{aligned} \delta G &= \sum_{i=1}^{m-1} \delta n_i^{(j)} \left(\mu_i^{(j)} - \mu_i^{(j+1)} \right) + \delta n_m^{(j)} \left(\mu_m^{(j)} - \mu_m^{(j+1)} \right) \\ &= \sum_{i=1}^{m-1} \delta n_i^{(j)} \left(\mu_i^{(j)} - \mu_i^{(j+1)} - \mu_m^{(j)} + \mu_m^{(j+1)} \right) \end{aligned} \tag{2.31}$$

from which it follows that:

$$\frac{\partial G}{\partial n_i^{(j)}} = \left(\mu_i^{(j)} - \mu_i^{(j+1)} - \mu_m^{(j)} + \mu_m^{(j+1)} \right) \tag{2.32}$$

Since all the m-1 $\delta n_i^{(j)}$'s are independent. There are now two results: for an unrestricted layer and restricted (or substitutional) layer, given by Eq. 2.29 and Eq. 2.32 respectively. Comparing Eq. 2.29 with the discrete form of the space derivative in Eq. 2.25, one obtains:

$$\frac{\mu_i^{(j)} - \mu_i^{(j+1)}}{d} = \frac{-\partial G / \partial n_i^{(j)}}{d}$$

One can identify the expression $\left(\mu_i^{(j+1)} - \mu_i^{(j)} \right)$ as decrease in G with $n_i^{(j)}$. The driving force as proposed by Darken is therefore the decrease in the Gibbs free energy as atoms are interchanged (or move) between two layers as opposed to the Fick's description where the driving force is taken as the difference in concentration. The spatial derivative implies that the driving force is the decrease in energy which is given by $\left(\mu_i^{(j+1)} - \mu_i^{(j)} \right)$ for an unrestricted layer but by $\left(\mu_i^{(j)} - \mu_i^{(j+1)} - \mu_m^{(j)} + \mu_m^{(j+1)} \right)$ for a substitutional layer. Therefore the Darken flux equation can be modified using:

$$-\frac{\partial \mu_i}{\partial d} \to \frac{\Delta \mu_i^{(j+1,j)}}{d}$$

where $\Delta \mu_i^{(j+1,j)} = \left(\mu_i^{(j)} - \mu_i^{(j+1)} - \mu_m^{(j)} + \mu_m^{(j+1)}\right)$ for substitutional alloy.

Supply concentration $C_i^{(b)}$

The secondary modification to the flux equation is for the term of $C_i^{(b)}$, which is defined by Darken to be at a plane between the two layer *j* and *j*+1. This has no physical meaning in a layer-by-layer description. The $C_i^{(b)}$ term may be regarded as the supply of atoms diffusing through the plane at *b*. If one consider the flow of atoms to be in the direction of lower values of *j*, *i.e.* in the direction of the surface at *j* =0, and defines the flux term $J_i^{(j+1,j)}$ describing flow from the *j*+1-st layer to the *j*-th layer, one obtains:

$$J_i^{(j+1,j)} = M_i C_i^{(j+1)} \frac{\Delta \mu_i^{(j+1,j)}}{d} \tag{2.33}$$

It is clear that if atoms flow from the *j*+1-st layer to the *j*-th layer the concentration of the *j*+1-st layer $C_i^{(j+1)}$serves as the supply. If the flux is in the opposite direction, i.e. away from the surface, the flux equation should change to

$$J_i^{(j,j+1)} = M_i C_i^{(j)} \frac{\Delta \mu_i^{(j+1,j)}}{d} \tag{2.34}$$

But only one is relevant at a specific time. If $\Delta \mu_i^{(j+1,j)} > 0$, the Gibbs free energy would decrease as atoms of species *i* move from the *j*+1-st layer to the *j*-th layer; the flux is therefore from *j*+1 to *j* and $C_i^{(j+1)}$ serves as supply. If $\Delta \mu_i^{(j+1,j)} < 0$, the Gibbs free energy would increase if atoms of species *i* move from the *j*+1-st layer to the *j*-th layer; the flux is therefore in the opposite direction (from *j* to *j*+1) and C_i^j serves as supply. Explicitly

$$J_i^{(j+1,j)} = M_i C_i^{(j+1)} \frac{\Delta\mu_i^{(j+1,j)}}{d} \qquad \text{if} \quad \Delta\mu_i^{(j+1,j)} > 0$$

$$J_i^{(j,j+1)} = M_i C_i^{(j)} \frac{\Delta\mu_i^{(j+1,j)}}{d} \qquad \text{if} \quad \Delta\mu_i^{(j+1,j)} < 0$$

Mobility M_i

The mobility given by M_i and defined by Eq. 2.30 and Eq. 2.31 may be used in the same way as the diffusion coefficient D to define the movement of atoms in crystal lattice for a given temperature etc. However, in order to compare the Darken flux equation with Fick's flux equation, one has:

$$-M_i C_i^{(b)} \left(\frac{\partial \mu_i}{\partial x} \right)_{x=b} = J_i = -D_i \left(\frac{\partial C_i}{\partial x} \right)_{x=b}$$

and therefore

$$D_i = M_i C_i^{(b)} \frac{\partial \mu_i}{\partial C_i}$$

or

$$D_i = M_i \frac{\partial \mu_i}{\partial InX_i}$$

where $X_i = C_i d^3$ is the fractional concentration and $\partial\mu_i/\partial C_i = \partial\mu_i/\partial X_i$ recalling $\mu_i = \mu_i^0 + RTInf_i + RTInX_i$, one has:

$$\frac{\partial \mu_i}{\partial InX_i} = RT\left(1 + \frac{\partial f_i}{\partial InX_i}\right)$$

For an ideal solution (f_i=*1*) or dilute solution (f_i = constant), $\partial f_i/\partial InX_i = 0$, yielding:

$$D_i = M_i RT \tag{2.35}$$

It should be stated that Eq. 2.32 is valid for the diffusion process in the bulk only.

Rate equations

In this section the rate equations for the surface segregation in a multicomponent alloy of *m* components will be derived. The rate at which it the fractional concentration ($C_i^{(j)}$) of species *i* in the *j*-th layer changes is given by:

$$\frac{\partial C_i^{(j)}}{\partial t} = \frac{\left(J_i^{(j+1,j)} - J_i^{(j,j-1)}\right)}{d} \tag{2.36}$$

If one considers the flux in the direction of the surface only, then Eq. 2.33 and Eq. 2.34 can be rewritten as:

$$J_i^{(j+1,j)} = M_i C_i^{(j+1)} \frac{\Delta\mu_i^{(j+1,j)}}{d} \tag{2.37}$$

and

$$J_i^{(j,j-1)} = M_i C_i^{(j)} \frac{\Delta\mu_i^{(j,j-1)}}{d} \tag{2.38}$$

Substituting the Eq. 2.37 and Eq. 2.38 in Eq. 2.36, one obtains:

$$\frac{\partial C_i^{(j)}}{\partial t} = \left[\frac{M_i C_i^{(j+1)}}{d^2} \Delta\mu_i^{(j+1,j)} - \frac{M_i C_i^{(j)}}{d^2} \Delta\mu_i^{(j,j-1)} \right] \tag{2.39}$$

Writing the $C_i^{(j)} = X_i^{(j)} / d^3$ where $X_i^{(j)}$ is the fraction concentration and substituting in Eq. 2.39,

$$\frac{\partial X_i^{(j)}}{\partial t} = \left[\frac{M_i X_i^{(j+1)}}{d^2} \Delta\mu_i^{(j+1,j)} - \frac{M_i X_i^{(j)}}{d^2} \Delta\mu_i^{(j,j-1)} \right] \tag{2.40}$$

Now there are (*m*-1) (*N*+1) rate equations for the *N*+1 layers. The segregation system of surface *S* and bulk *B* is therefore described by

$$
\begin{aligned}
&\frac{\partial X_i^S}{\partial t} = \frac{D_i X_i^{B_1}}{RTd^2}\Delta\mu_i^{B_1,S} \\
&\frac{\partial X_i^{B_1}}{\partial t} = \frac{D_i X_i^{B_2}}{RTd^2}\Delta\mu_i^{B_2,B_1} - \frac{DX_i^{B_1}}{RTd^2}\Delta\mu_i^{B_1,S} \\
&\vdots \\
&\frac{\partial X_i^{(j)}}{\partial t} = \frac{D_i X_i^{(j+1)}}{RTd^2}\Delta\mu_i^{(j+1,j)} - \frac{D_i X_i^{(j)}}{RTd^2}\Delta\mu_i^{(j,j-1)} \\
&\vdots
\end{aligned}
\tag{2.41}
$$

for i=1, 2,..., m-1 and j=1, 2,…, N+1. X_i^S is the surface concentration of species i, and X_i^{B1} is the first bulk concentration of species i, and D is the diffusion coefficient. Furthermore, $\Delta\mu^{(j+1,j)} = \mu_1^{(j+1)} - \mu_1^{(j)} - \mu_2^{(j+1)} + \mu_2^{(j)}$, where $\mu_i^{(j)}$ is the chemical potential of species i in layer j. The above equations Eq. 2.41 is a system of coupled rate equation, was solved simultaneously to describe the kinetic surface segregation in Cu-Ni(S) alloy and Cu-Ni alloy thin films in Chapter 8 and Chapter 9.

It is instructive to write down the first rate equation in Eq. 2.41 in terms of ΔG and Ω to observe the roles played by the different parameters [12]:

$$
\frac{\partial X^S}{\partial t} = \frac{DX^{B_1}}{RTd^2}\left[\Delta G + RT\ln\frac{X^{B_1}\left(1-X^S\right)}{X^S\left(1-X^{B_1}\right)} - 2\Omega\left(X^{B_1} - X^S\right)\right] \tag{2.42}
$$

The system of N+1 differential equations can be integrated for a given set of parameters (ΔG, Ω, D and X^S). In order to minimize boundary effects, the choice of a suitable value of N for the model calculation depends on the values of equilibrium surface concentration or depletion in the bulk layers. Normally the values of N is choice to be more than 10 times the values of $X^S_{equ.}/X^B$, in which $X^S_{equ.}$ is the equilibrium surface concentration value and X^B is the bulk concentration.

2.3.3 Modified Darken model in thin film

In the nanoscale thin films, surface segregation often plays an important role in determining material properties because of the changes of composition and structure. For a finite sized system, surface segregation can be very different as compared with bulk solids (i.e. effectively semi-infinite solids) (See Fig. 2.5). In nanoscale thin films, the number of segregated atoms on the surface is a significant fraction of the total number of atoms in the system so that the bulk concentration of the system is modified significantly. The lack of a reservoir of the segregating atoms in thin films may cause significant differences in surface segregation as compared with that in bulk materials.

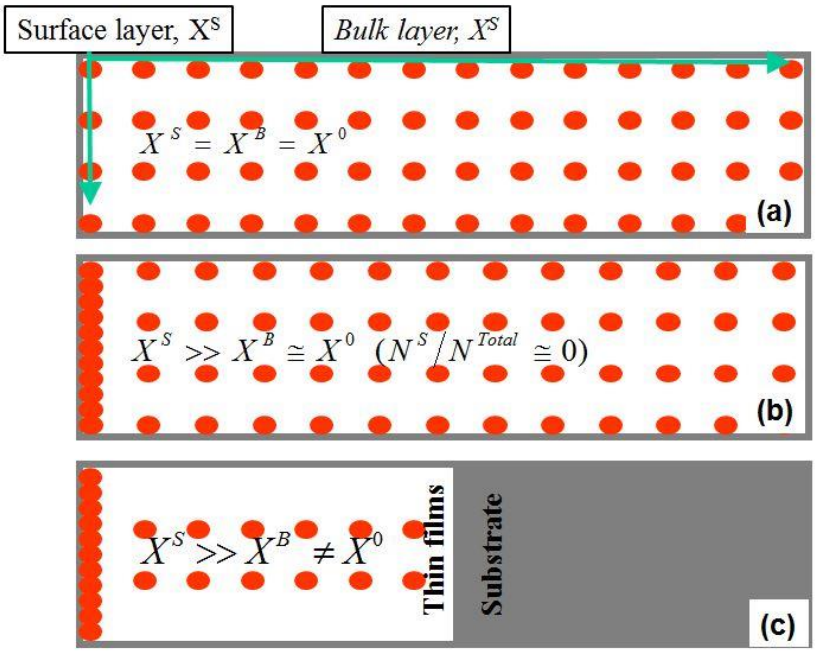

Figure 2.5: The sketch of the surface segregation (a) no segregation, (b) segregation in bulk and (c) segregation in thin films.

For a thin film system, because of limited number of segregated atoms, the final equilibrium bulk concentration value X^B is modified from the initial bulk concentration value X^0 as [19]:

$$X^B = \frac{X^0 - X^S K}{1 - K} \tag{2.43}$$

where K is the ratio of the number of segregated atoms in the surface layer (N^S) to the total number of segregated atoms in the system (N^{total}), i.e. $K= N^S/ N^{total}$. The value of K is inversely proportional to the film thickness, i.e. $K=2/l$, where l is the film thickness in the unit of ML, $K=1$ represents a two-layer thin film system and $K=0$ represents a bulk system. Eq. 2.43 is a constrained condition for the surface segregation in thin films. Swaminarayan e*t al* [19] studied surface segregation in thin films with the Langmuir-Mclean approximation, e.g. no interaction and no kinetics have been considered in the analysis. In this study, equilibrium and kinetic surface segregation in Cu-Ni thin films will be investigated with Modified Darken Model considered interaction between the segregated atoms (in Chapter 9).

2.4 Diffusion

Diffusion is the transport of matter from one point to another by thermal motion of atoms or molecules. It is relatively fast in gases, slow in liquids, and very slow in solids. Diffusion in solids is fundamental in the science of materials and thus an important topic of solid-state physics, physical chemistry, physical metallurgy, and materials science. [21] A deeper knowledge about diffusion requires information on the position of atoms and how they move in solids. The atomic mechanisms of diffusion in crystalline solids are closely connected with defects. Point defects such as vacancies or interstitials are the simplest defects and often mediate diffusion in crystals. Dislocations, grain-boundaries, phase boundaries, and free surfaces are other types of defects. They can act as high-diffusivity paths (diffusion short circuits), because the mobility of atoms along such defects is usually much higher than in the lattice.

2.4.1 Diffusion mechanism

In the crystalline, it is possible to describe diffusion mechanisms in simple terms. The crystal lattice restricts the positions and the migration paths of atoms and allows a simple description of each specific atom displacements. [21] As we known, substitutional (vacancy) and interstitial diffusion are the dominating diffusion mechanisms in the metals material. These two types of diffusion mechanisms are briefly discussed in this section.

Substitutional (vacancy) diffusion:

As knowledge about solids expanded, vacancies have been accepted as the most important form of thermally induced atomic defects in metals crystals [21]. It has also been recognized that the dominant mechanism for the diffusion of matrix atoms and of substitutional solutes in metals is the vacancy mechanism. An atom is said to diffuse by this mechanism, when it jumps into a neighbouring vacancy (Fig. 2.6). In order for this to occur, the creation of a lattice vacancy is required. The probability, P, for each of these processes, the creation of a vacancy and the migration of a solute atom into a vacancy can be obtained from [22]:

$$P_v = \exp(-\frac{E_v}{RT}) \tag{2.44}$$

$$P_m = \exp(-\frac{E_m}{RT}) \tag{2.45}$$

where E_v is vacancy formation energy and E_m migration energy, R is the universal gas constant and T is the temperature. Thus, the diffusion probability (P_D) is expressed as

$$P_D = P_v \times P_m \tag{2.46}$$

the diffusion coefficient can be written as

$$D = kP_D \tag{2.47}$$

where k is a constant. Taking k as pre-exponential factor and inserting Eqs. 2.44-2.46 into Eq. 2.47, the following expression is obtained.

$$D = D_o \exp(-\frac{E_v}{RT}) \times \exp(-\frac{E_m}{RT}) = D_o \exp(-\frac{E_v + E_m}{RT}) = D_o \exp(-\frac{Q}{RT}) \tag{2.48}$$

where $Q = E_v + E_m$.

In Eq. 2.48 it can be seen that the diffusion coefficient of atoms depends on the atomic vacancy formation and atom migration energy. Hence, substitutional diffusion in a solid requires the presence of vacancies next to the diffusing (moving) atom. In Eq. 2.48, the diffusion coefficient varies with temperature.

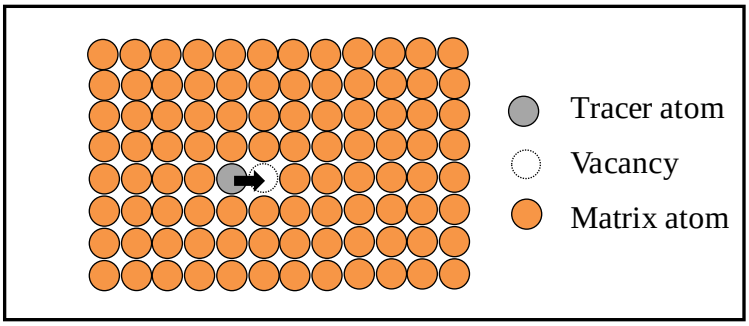

Figure 2.6: A schematic representation of the substitutional (vacancy) diffusion mechanism.

Interstitial diffusion

Solute atoms which are considerably smaller than the solvent atoms are incorporated on interstitial sites of the host lattice thus forming an interstitial solid solution. Interstitial sites are defined by the geometry of the host lattice. In fcc and bcc lattices, for example, interstitial solutes occupy octahedral and/or tetrahedral interstitial sites (Fig. 2.7). An interstitial solute can diffuse by jumping from one interstitial site to one of its neighbouring sites as shown in Fig. 2.7. Then the solute is said to diffuse by an interstitial mechanism. This mechanism is relevant for diffusion of small foreign atoms such as H, C, N, and O in metals and other materials. Small atoms fit in interstitial sites and in jumping do not greatly displace the solvent atoms from their normal lattice sites.

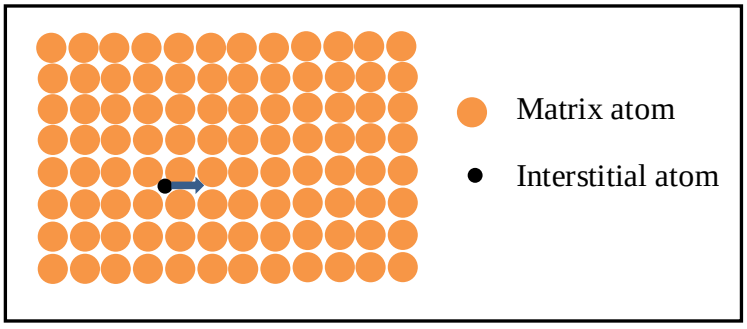

Figure 2.7: A schematic representation of the interstitial diffusion mechanism.

2.4.2 Interdiffusion coefficient

Interdiffusion is defined as the mutual diffusion of two or more different materials into one-another as shown in Fig. 2.8. This process is also described by Fick's second law and can be solved either analytically or numerically, depending on the type of calculation involved. The analytical solution is a very fast solution, but it is limited to constant diffusion coefficients while the numerical solution is more involved but it allows varying diffusion coefficients and temperatures.

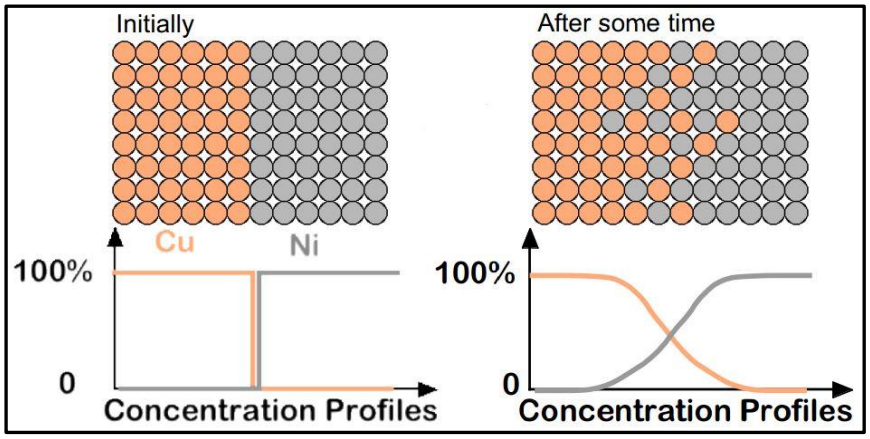

Figure 2.8: A schematic representation of the Interdiffusion mechanism. (Adapted from [23])

The importance of the diffusion coefficient becomes apparent when observing diffusion in binary and higher order alloys. In such a situation, diffusion coefficient composed of the intrinsic diffusion coefficients of the constituent parts A and B [24, 25], given by

$$D = D_A X_B + D_B X_A \tag{2.49}$$

where X_A and X_B is the fractional concentration of component A and B, respectively; and D_A and D_B is the intrinsic diffusion coefficients of component A and B, respectively. Eq. 2.49 is also known as Darken's second equation [25]. These intrinsic diffusion coefficients can be related to with the corresponding self-diffusion coefficients D_A^* and D_B^*, in which case Eq. 2.49 becomes

$$D = (D_A^* X_B + D_B^* X_A)\alpha_{AB} \tag{2.50}$$

where α_{AB} is a thermodynamic factor which characterises how the solution deviate from an ideal solution and α_{AB} is given by [25]

$$\alpha_{AB} = 1 + \frac{\partial f_A}{\partial In X_B} = 1 + \frac{\partial f_B}{\partial In X_A} \tag{2.51}$$

where f_A and f_B is the activity coefficient of component A and B, respectively. Eq. 2.51 is sometimes referred to as the Darken-Hartley-Crank equation [25]. A detailed discussion can be found in reference [26] and Chapter 7 where the experiment result of the interdiffusion of Cu/Ni multilayer will be discussed.

References

[1] S. Hofmann, Scanning Electron Microsc. III, 1071, 1985.

[2] J.W. Gibbs, The Scientific Papers of J.W. Gibbs, 1, Dover, New York 1961.

[3] L.S. Chang, E. Rabkin, B.B. Straumal, B. Baretzky, W. Gust, Thermodynamic aspects of the grain boundary segregation in Cu (Bi) alloys, Acta Mater. **47** (1999) 4041-4046.

[4] M.J. Madito, H.C. Swart, J.J. Terblans, Surface segregation measurements of In and S impurities from a dilute Cu (In, S) ternary alloy, Surf. Interface Anal. **45** (2013) 1020-1025.

[5] H.C. Swart, W.D. Roos, J.J. Terblans, Surface segregating kinetics in a ternary system, Surf. Interface Anal. **36** (2004) 285-289.

[6] J.J. Terblans, H.C. Swart, The segregation of Bi and S from a Cu (Bi, S) ternary system, e-J. Surf. Sci. Nanotech. **7** (2009) 480-485.

[7] P.E. Barnard, J.J. Terblans, H.C. Swart, Surface orientation dependence of the activation energy of S diffusion in bcc Fe, Appl. Surf. Sci. **356** (2015) 213-220.

[8] D. McLean, Grain boundaries in Metals, Oxford University Press, Oxford 1957.

[9] R.H. Fowler, E.A. Guggenheim, Statistical Thermodynamics, Cambridege University Press 1939.

[10] M. Guttmann, Equilibrium segregation in a ternary solution: A model for temper embrittlement, Surf. Sci. **53**(1975) 213-227.

[11] J. du Plessis, P.E. Viljoen, G.N. van Wyk, The effect of high temperature sputtering on the $t^{1/2}$ dependence of segregation kinetics in an Al alloy, Surf. Sci. **244** (1991) 277-284.

[12] J. du Plessis, P.E. Viljoen, Linear programmed heating in surface segregation measurements, Appl. Surf. Sci. **59** (1992) 171-175.

[13] E.C. Viljoen, J. Du Plessis, Auger/LEED linear heating study of Sn and S bulk-to-surface diffusion in a Cu (111)(Sn, S) single crystal, Surf. Interface Anal.**23** (1995) 110-114.

[14] J.J. Terblans, W.J. Erasmus, E.C. Viljoen, J. Du Plessis, Orientation dependence of the surface segregation kinetics in single crystals, Surf. Interface Anal.**28** (1999) 70-72.

[15] J.K.O. Asante, W.D. Roos, J.J. Terblans, Sequential segregation of Sn and Sb in a Cu (111) single crystal, Surf. Interface Anal. **35** (2003) 441-444.

[16] J. Du Plessis, Solid State Phenomena- Part B, surface segregation, Sci-Tech Publications, Brookfield USA 1990.

[17] Jiang Yong Wang, Surface segregation of Cu(Ag) alloys, Ph. D. Thesis, University of the Free State, South Africa 1997.

[18] C.H.P. Lupis, Chemical Thermodynamics of Materials, Amsterdam North-Holland 1983.

[19] S. Swaminarayan, D.J. Srolovitz, surface segregation in thin films, Acta Mater. **44 (**1996) 2067-2072.

[20] T. Sakurai, T. Hashizume, A. Kobayashi, A. Sakai, S. Hyodo, Y. Kuk, H.W. Pickering, Surface segregation of Ni-Cu binary alloys studied by an atom-probe, Phys. Rev. B **34** (1986) 8379.

[21] H. Mehrer, Diffusion in Solids: Fundamentals, Methods, Materials, Diffusion-Controlled Processes, Springer-Verlag, Heidelberg Berlin, 2007.

[22] M.E. Glicksman, Diffusion in Solids: Fields theory solid state principles and applications, John Wiley & Sons Inc., New York 2000.

[23] W.D. Callister Jr., Materials Science and Engineering: An Introduction, 6^{th} Edition, John Wiley & Sons Inc., New York 2002.

[24] A. Vignes, Industrial and Engineering Chemistry Fundamentals, **189**(1966) 5.

[25] L.S. Darken, Diffusion, mobility and their interrelation through free energy in binary metallic systems, Transactions of the American Institute of Mining and Metallurgical Engineers **175** (1948)184-201.

[26] H.D. Joubert, A theoretical and experimental investigation on the effect that slow heating and cooling has on the inter-diffusion parameters of Cu/Ni thin films, Ph.D. thesis, University of the Free State 2010.

Chapter 3

Sample preparation

3.1 Introduction

In this chapter, we will describe in detail the methods and equipment used to prepare the Cu/Ni multilayer thin film and Ni/Cu/Ni sandwich layer thin film. The Ni/Cu multilayer thin film deposited with electron beam physical vapour deposition was used to study the sputter depth profile with both Auger Electron Spectroscopy (AES) and Time-of-Flight Secondary Ion Mass Spectrometry (ToF-SIMS) technique in combination with the Atom Force Microscope (AFM), and the results will be discussed in the Chapters 5 and 6. The Ni/Cu multilayer thin film is also used to study the interdiffusion of Cu and Ni with AES depth profiling in combination with the MRI model, the results will be discussed in the Chapter 7. The Ni/Cu/Ni sandwich layer was grown into a Cu-Ni alloy thin film by following a heat treatment. The Cu-Ni alloy thin film was used to study surface segregation under a constrained condition for thin film system. The segregation results will be discussed in the Chapter 9. A part of this chapter is also described the methods and equipment system of heating treatment.

3.2 Sample prepared by EBPVD

3.2.1 Electron beam physical vapour deposition

E-beam evaporation is a physical vapour deposition (PVD) technique and the process is similar to thermal evaporation. A photo of the electron beam evaporation system (at the Department of Physics at the University of the Free State) used in this study is shown in Fig. 3.1. During the e-beam evaporation, a high energy e-beam is formed using a tungsten filament to generate the electrons, high voltages of 4 kV to accelerate the electrons, and a magnetic field to focus and deflect the electron beam onto the surface of the material (Cu and Ni) to be evaporated as shown in the Fig. 3.1(b) and Fig. 3.1(c).

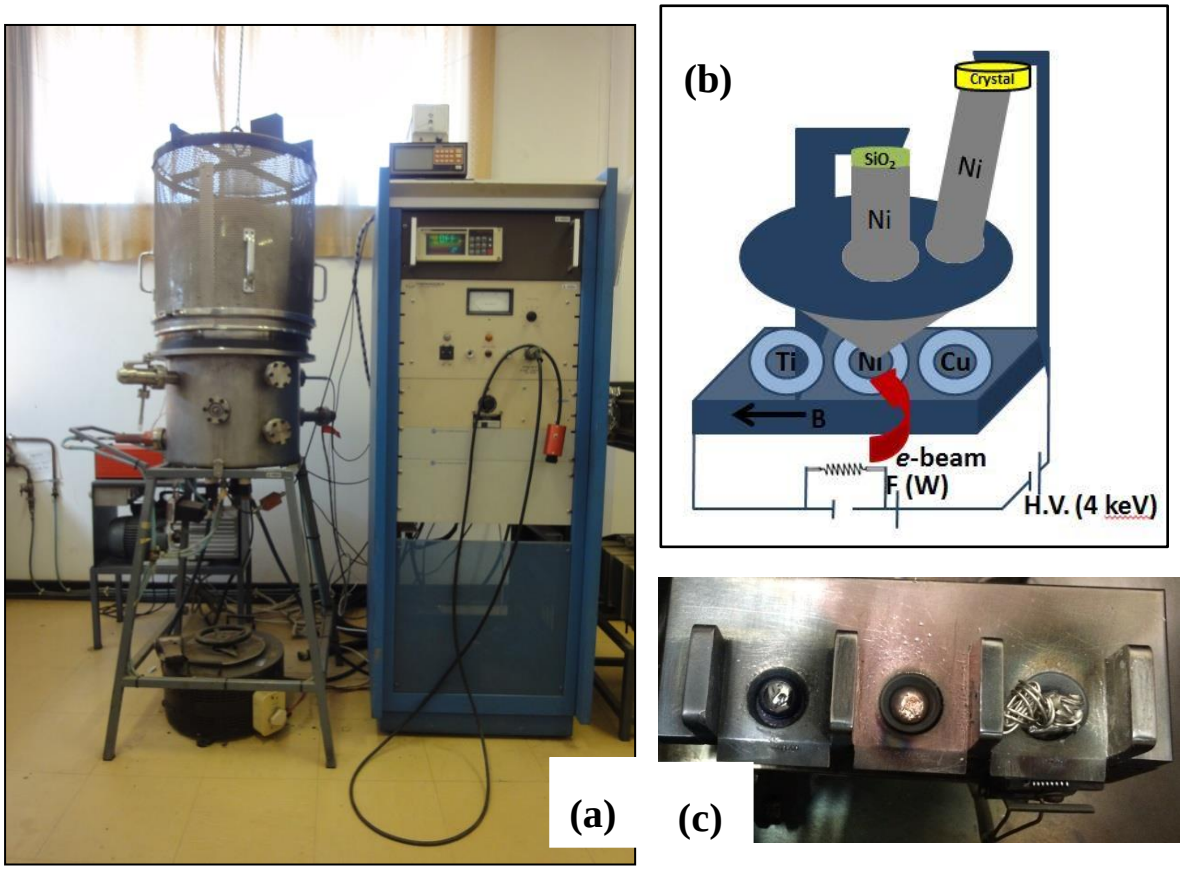

Figure 3.1: (a) A photo of the electron beam evaporation system, (b) schematic representation of the key parts and (c) the three crucible compartments with Ti, Cu and Ni material in the evaporation system.

The thickness of the evaporated Cu and Ni layers is measured with an Inficon Quartz Crystal deposition Monitor (QCM) which monitors the deposition rate and the thickness. There are some advantages for using e-beam evaporation to deposited thin films, such as, a lager range of deposition rate (1-1000 nm/min.), a good morphological surface finish and a uniform microstructure in films. [1-3]

3.2.2 Thickness monitor and QCM calibration

The layer thickness is measured with an Inficon Quartz Crystal deposition Monitor (QCM). The QCM utilize mass measure to determine the deposition rate and the final thickness. When mass is added to the resonating quartz crystal its resonance frequency is reduced. This change in frequency is very repeatable and is precisely understood for specific oscillating modes of quartz and can easily detect the addition of less than an atomic layer of foreign material added to the resonating quartz crystal [4].

There is difference between the crystal sensor (in the QCM) and the substrate (sample) thicknesses due to the different distances from the deposition source (material in crucible). A tooling factor parameter is used to correlate thicknesses between the crystal sensor and the substrate. The calculated tooling factor is given as [4]:

$$Tooling\ (\%) = TF_i \times \left(\frac{T_m}{T_x} \right) \tag{3.1}$$

where TF_i is the initial tooling factor, T_m is the actual thickness of the deposited layer at the substrate, and T_x is the thickness of the deposited layer on the sensor. To calibrate the tooling factor in the e-beam evaporation system, the pure Cu thin film was deposited on a SiO_2 substrate and the actual thickness was measured with SEM cross-section measurements as shown in the Fig. 3.2. An average tooling factor of 275% was determined using Eq. 3.1.

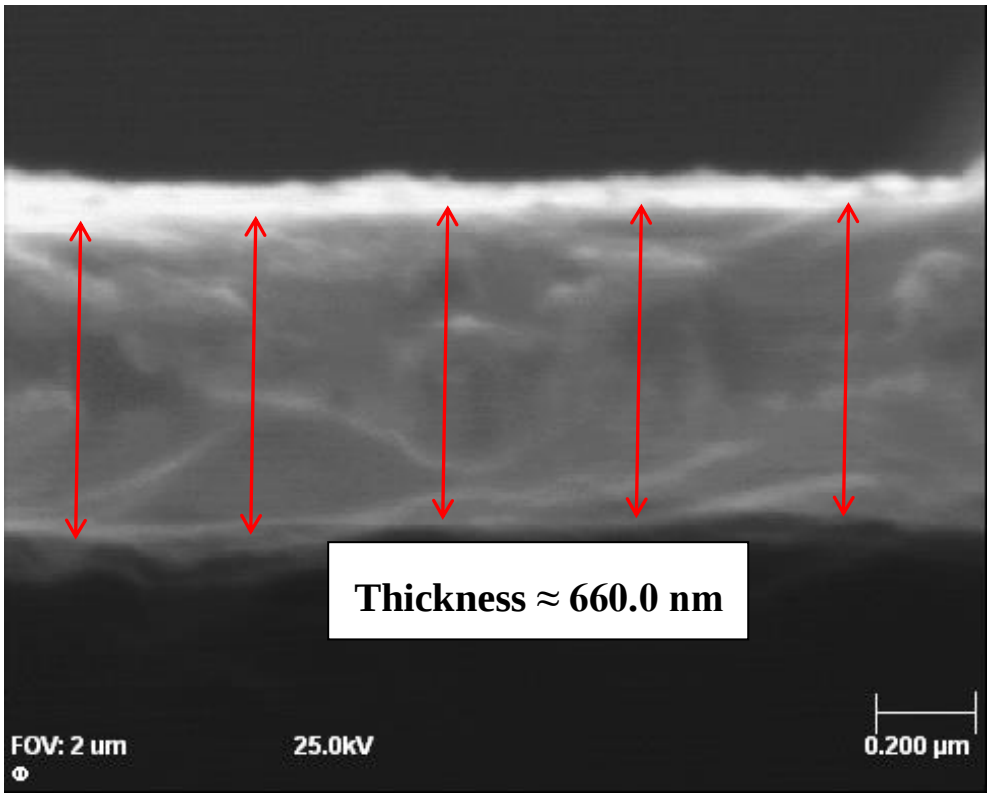

Figure 3.2: Cross-section SEM image of pure Cu film on the SiO_2 substrate with the thickness values bout 660.0 nm.

3.2.3 Ni/Cu multilayer prepared with EBPVD

The Ni/Cu multilayer thin films were prepared by evaporating Cu and Ni (purity 99.99+ %) onto passivated (SiO_2) silicon. SiO_2 substrates were prepared by wet oxidation of Si (100) at 1000 ℃ for 1 hour, resulting in a SiO_2 layer with a thickness about 1 µm. The SiO_2 act as a diffusion barrier and prevents the Ni and/or Cu from diffusing into Si. The SiO_2 substrates (cut to desired size) were cooled to room temperature and loaded inside the electron beam evaporation system (see in Fig. 3.3). The Ni/Cu multi-layered structures composed of four pairs of Ni and Cu sublayers that were grown by electron beam physical vapour deposition.

The evaporation system was pumped to a base pressure of 6×10^{-6} Torr by a rotary vane and turbo molecular pump. Before the depositing the Ni/Cu, Ti was vapored for 1 mins to clean the residual oxygen in the deposition chamber. After cleaning the system with Ti, the Cu film was deposited onto the SiO_2 substrates with the deposition

rates of about 0.4 nm/s. The Ni film was then deposited onto the Cu layer with the deposition rates of about 0.7 nm/s. This was done without breaking the vacuum. All four Cu/Ni layers were grown in the same manner.

The emission current during deposition of Ni was 120 mA and for Cu it was 50 mA and the high voltage was 4 kV. The thickness of the individual sublayers was controlled using the calibrated Inficom thickness monitor during vapour deposition. The Ni/Cu/Ni sandwich thin film structures were prepared in the same way on a SiO_2 substrates.

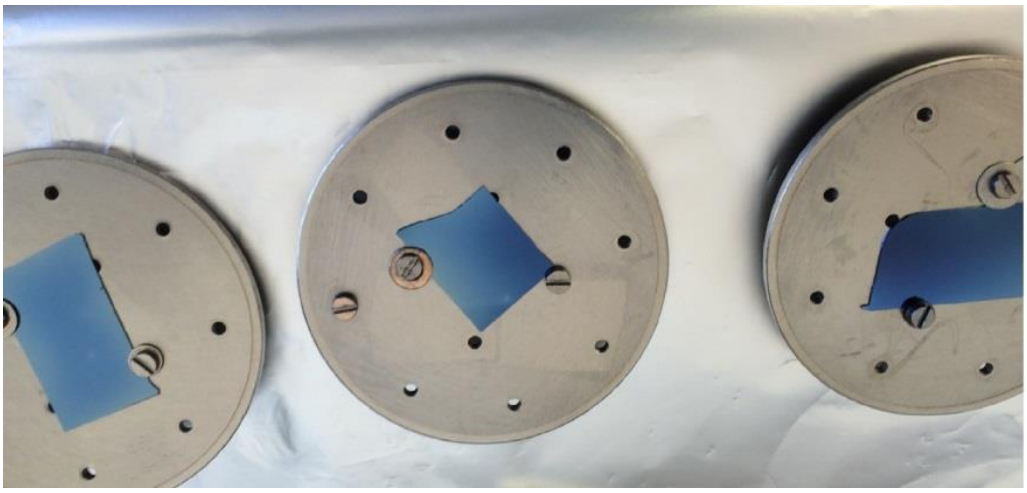

Figure 3.3: SiO_2 substrates mounted on a sample plate.

3.3 Sample annealing

3.3.1 For the interdiffusion

To investigate the interdiffusion in the Ni/Cu multilayer, the Ni/Cu multilayer structures composed of four pairs of Cu and Ni sublayers were annealed. This was done using a Lindberg vacuum furnace system with two vacuum pumps, a rotary vane and turbo molecular pump. The chamber in the annealing system is a custom built system with a carousel holder, allowing one to anneal multiple samples sequentially without breaking vacuum. The samples were placed on a ceramic boat and a magnetically coupled arm pushed the ceramic boat into and out of the furnace. A photo of the vacuum annealing furnace is shown in Fig. 3.4. Before loading the sample for anneal,

the quartz tube was cleaned by annealing it at 800 ℃ (higher than the desired annealing temperature) for 1 hour to make sure the contamination in the tube furnace evaporates and is pumped to a base pressure of 5×10^{-6} Torr, this was repeated 3 times to ensure a clean environment during the annealing. The Ni/Cu multilayer was cut into 5 piece of 1×1 mm^2 each. The samples were then annealed at the low temperature 325 ℃, 350 ℃ and 375 ℃ for 30 min, respectively, in a high vacuum tube furnace at the base pressure of $< 5\times10^{-6}$ Torr. After each annealing temperature, the sample was spontaneously cooled down to the room temperature in the same furnace under the same pressure. After annealing the annealed and an as-deposited (unannealed) sample were loaded into the AES system (PHI 600) to measure depth profile the results is shown in Chapter 7.

Figure 3.4: The Lindberg vacuum annealing furnace used in this study.

3.3.2 For the segregation

For the surface segregation experiments a Ni-Cu alloy thin films were required. Hence, different thicknesses of Ni/Cu/Ni sandwich samples were prepared and annealed in the above-discussion Lindberg vacuum furnace high to form Ni-Cu alloy thin films.

If the diffusion is one-dimensional and isotropic, the differential equation for diffusion is given by Fick's second law:

$$\frac{\partial C}{\partial t} = D\frac{\partial^2 C}{\partial x^2} \tag{3.2}$$

where C is the concentration of the diffusion substance and D is the diffusion coefficient. The general solution of Eq. 3.2 could be obtained for a variety of initial and boundary condition provided that the diffusion coefficient is constant. In our case Ni/Cu/Ni sandwich thin film, the thickness of two Ni layer approximately equal, a Ni layer thickness L, where the surface is at $x = 0$. Assume that initially no Cu atoms are present in the Ni deeper layer. The meddle Cu layer has a thickness $2h$. So, the frame of the half Cu layer thickness h and deeper Ni layer thickness L can be regards as a finite solid from a certain region sours and the initial and boundary conditions are as follows:

$$\begin{cases} 0 \le x \le L \\ C(x) = 0 \quad for \quad x > h, \qquad and \ t = 0 \\ C(x) = C_0 \quad for \ 0 \le x \le h, \ and \ t = 0 \\ \dfrac{\partial C}{\partial x} = 0 \ at \ \ x = L, \qquad\quad and \ t \ge 0 \end{cases} \tag{3.3}$$

The solution of Eq. 3.2 for a finite solid from a certain region sours (under the initial and boundary conditions in Eq. 3.3) could be obtained as following [5]:

$$C = C_0 \sum_{n=-\infty}^{\infty} \left[\operatorname{erf}\left(\frac{h + 2nL - x}{2\sqrt{Dt}} \right) + \operatorname{erf}\left(\frac{h - 2nL + x}{2\sqrt{Dt}} \right) \right] \tag{3.4}$$

This solution shows the concentration of Cu atoms which diffused into the Ni layer. The uniformity of a Cu layer in the Ni layer is calculated with Eq. 3.4 as a function of annealing time at different temperature (a) for sample 10 (b) for sample 20, as shown in Fig. 3.5(a) and Fig. 3.5(b), respectively. And the setting parameters are also

indicated in Fig. 3.5. The calculation results in Fig. 3.5 shows that annealing at 425 ℃ for 2 hours is necessary to obtain a uniformity of 99.9 % for a sample 10, and for sample 20 needs to anneal at 425 ℃ for 9 hours, which can be chose to get Ni-Cu alloy and the result will be presented in Chapter 9.

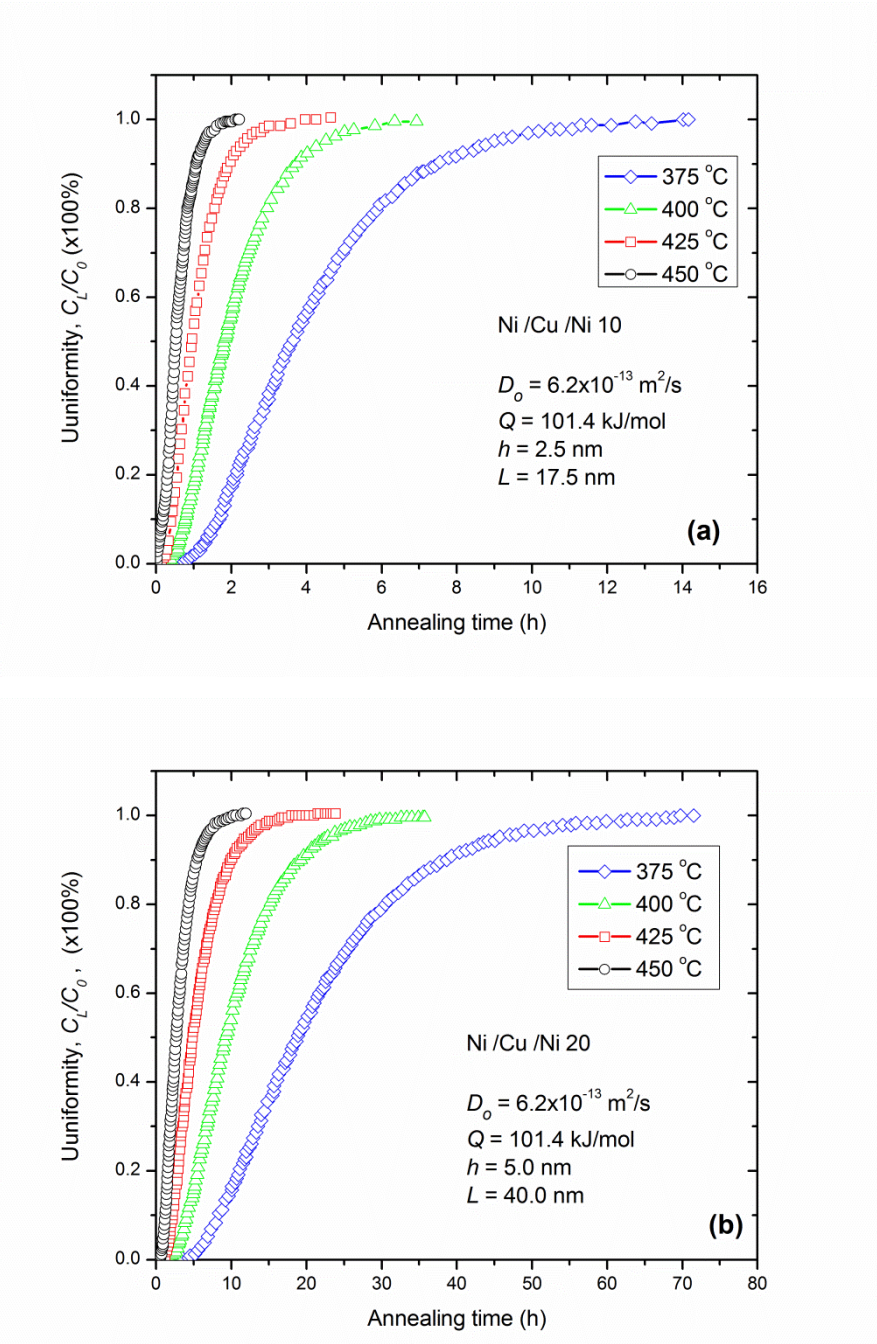

Figure 3.5: The uniformity of a Cu layer in the Ni layer as a function of annealing time at different temperature (a) for sample 10 (b) for sample 20. D_o and Q values are obtained from the Chapter 7 results.

References

[1] M. Ohring, Materials Science of Thin Films, 2nd Edition, Academic Press, New York, USA 2002.

[2] D.M. Mattox, Handbook of Physical Vapor Deposition (PVD) Processing, 2nd Edition, Elsevier, Amsterdam, Netherlands 2010.

[3] B. Amin-Ahmadi, H. Idrissi, M. Galceran, M.S. Colla, J.P. Raskin, T. Pardoen, S. Godet, D. Schryvers, Effect of deposition rate on the microstructure of electron beam evaporated nanocrystalline palladium thin films, Thin Solid Films **539** (2013)145-150.

[4] INFICON, Operating manual, XTC 3 thin film deposition controller, New York, USA 2006.

[5] J. Crank, The Mathematics of diffusion, 2nd edition, Elsevier, Amsterdam, Netherlands 1975.

Chapter 4

Experimental setup

4.1 Introduction

A wide variety of surface analysis techniques were used to study depth profiles, diffusion and surface segregation of bulk and thin film Ni-Cu systems (or Ni/Cu multilayer thin films). These include Auger Electron Spectroscopy (AES), Time-of-Flight Secondary Ion Mass Spectrometry (ToF-SIMS), X-ray Diffraction (XRD), and Atom Force Microscope (AFM). AES and ToF-SIMS were used to carry out the depth profiles measurement of the Ni/Cu multilayer thin films prepared by e-beam evaporation. In addition, AES in combination with a heating unit was also used to measure the surface segregation in bulk and thin films Ni-Cu alloy systems. XRD was used to identify the crystalline structure of the Ni/Cu thin films and bulk Ni-Cu alloy. AFM was used to measure the surface roughness caused by ion bombardment. In this chapter, we will introduce the overview of some of the techniques used in this study and a considerable part of this chapter is focused on the AES system and the data quantitative analysis methods.

4.2 XRD measurements

XRD is a powerful non-destructive technique used to investigate structural properties of crystalline materials. It was used to obtain the crystalline structure for the

polycrystalline Ni/Cu multilayer thin films and the lattice constants and composition of solid solution alloy ($Ni_{1-x}Cu_x$) used in this study.

As it is known, Bragg's law is the basis for determination the lattice constants by XRD analysis. This law relates the wavelength of electromagnetic radiation to the diffraction angle and the lattice spacing in a crystalline sample. When a monochromatic X-ray beam with wavelength λ is irradiated onto a crystal sample, constructive diffraction (or interference) from parallel planes of atoms with inter-planar spacing *d* occur if Bragg's law is satisfied [1] (Fig. 4.1):

$$n\lambda = 2d_{hkl} \sin \theta_{hkl} \tag{4.1}$$

Where *n* is an integer that indicates the order of the reflection, θ_{hkl} is the Bragg angle and d_{hkl} is the different space in polycrystalline materials. The lattice parameters are related with Miller indexes (*hkl*) of each reflection plane and inter-planar distance (d_{hkl}). The Cu and Ni (Ni_xCu_{1-x} alloy) is a cubic structures and the lattice parameter *a* can be calculated [1]:

$$a = 2d_{hkl}\sqrt{h^2 + k^2 + l^2} \tag{4.2}$$

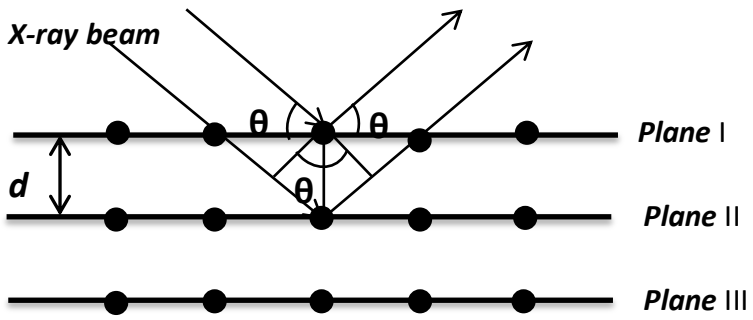

Figure 4.1: The schematic diagram of Bragg's law.

The X-ray diffractometer used in this study was a Bruker D8 Advance X-ray diffractometer, shown in Fig. 4.2. The crystalline nature of the as-deposited Ni/Cu multilayer was investigated using XRD, which uses a Cu anode and a Ni-filter to produce monochromatic X-rays with a wavelength of λ = 0.15406 nm. The diffraction

angle (2θ) was scanned from 30° to 80° with a step size of 0.01° and the diffracted X-ray photons counted for 0.5 s at each angle step. The XRD spectrum obtains from the Ni/Cu multilayer thin film is shown in Fig. 4.3. From the XRD spectrum it is clear that the Cu and Ni sublayers were polycrystalline with a (111), (200) and (220) orientation texture. The results of the crystalline structure of the thin films and bulk Ni-Cu (and Ni/Cu) samples will be presented in Chapter 5 and 8, respectively.

Figure 4.2: A photo of the Bruker D8 Advance x-ray diffractometer.

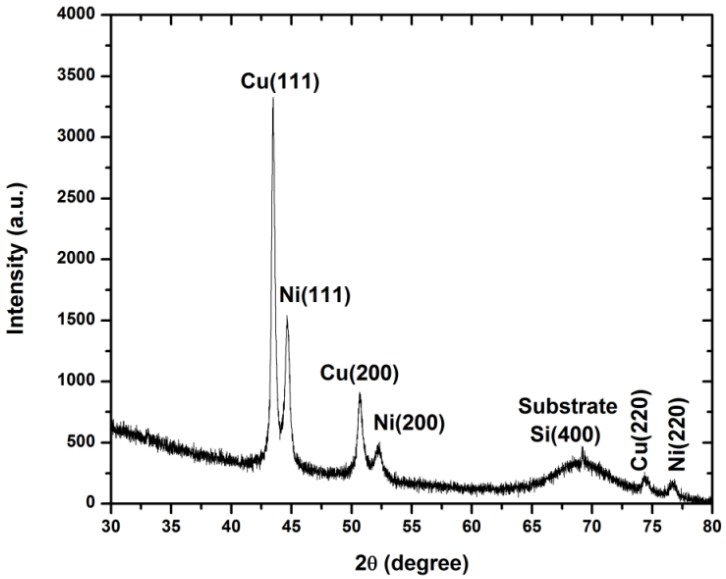

Figure 4.3: XRD pattern of the as-deposited Ni/Cu multilayer crystalline structure with 2θ range of 30-80 degree.

4.3 AFM measurements

AFM is a scanning probe microscopy (SPM) type of microscopy that uses a (very sharp) physical probe to image a surface by scanning the probe across the surface while measuring atomic force on the surface. The AFM provides a 3D profile (image) at a nanoscale of the forces between the sharp probe (radius less than 10 nm) and surface at very short distance (0.2-10 nm probe-sample separation) or a height map for a constant force on the probe. The probe is supported on a flexible cantilever and the AFM tip gently touches the surface and records the small force between the probe and the surface. Forces involved in the tip-sample interaction affect how the probe interacts with the sample. If the probe experiences repulsive forces the probe will be in contact mode otherwise as the probe moves further away from the surface, attractive forces dominate and the probe will be in non-contact mode. The advantages of in contact mode are: fast scanning, well for rough samples and it can be used in friction analysis [2, 3].

AFM in this study was performed using Shimadzu SPM-9600 Atom Force Microscope in contact model (shown in Fig. 4.4). The surface topography of the as-deposited Ni/Cu multilayer measurements and the centre of the crater bottoms after sputtering were performed with AFM in contact model. All the AFM images of surface topography measurement were collected using the same silicon tips with a scan area of 3×3 μm^2. The surface roughness was represented by the root mean square (RMS) value R_q of the as-deposited sample surface and after sputtering in the air ambient condition. In additional, AFM also is used to determine the thickness of the as-deposited Ni/Cu multilayer thin films with cross-section measurement and the scan area is 1×1 μm^2. The topographies measured by AFM are shown in Fig. 4.5 for the surface of the as-deposited sample and the corresponding root mean square (RMS) roughness value was determined as 1.6 nm.

The root mean square of roughness (R_q) is a function that takes the square of the measures. The RMS roughness of a surface is similar to the roughness average, with the only difference being the mean squared absolute values of surface roughness profile. The function R_q is defined as: [2]

$$R_q = \sqrt{\frac{1}{L}\int_0^L \left|Z^2(x)\right| dx} \tag{4.3}$$

where *Z(x)* is the height function that describes the surface profile in terms of position (*x*). *L* is the evaluation length over which the root mean square value of the roughness is calculated. The R_q is more sensitive to peaks and valleys than the average roughness (R_a) due to the squaring of the amplitude in the calculation.

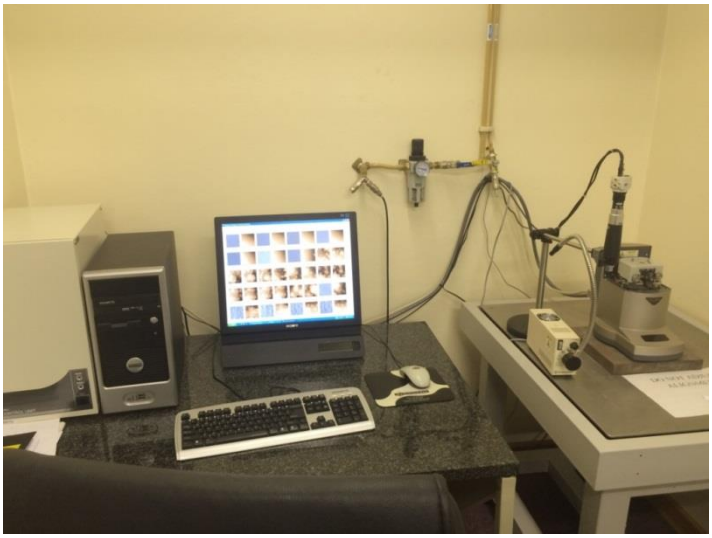

Figure 4.4: A photo of the Shimadzu SPM-9600 Atom Force Microscope.

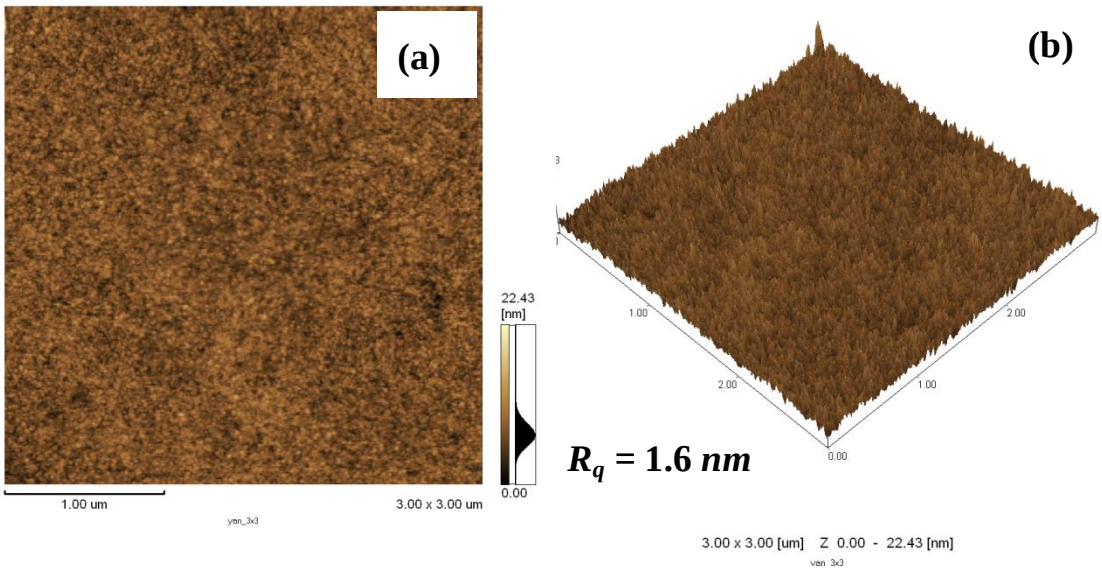

Figure 4.5: AFM images of the surface of the as-deposited Ni/Cu multilayer in 2D (a) and in 3D (b). The corresponding RMS value was determined as 1.6 nm.

4.4 AES measurements

AES is a surface-sensitive spectroscopic technique and is widely used for elemental analysis of surfaces of solid materials with high sensitivity (0.05% monolayer) for all elements except H and He. It should be noted that Li can be detected in solid material state but not in isolated atom. Quantitative compositional analysis of the surface region is relatively easy. In addition to surface analysis, it is also used for depth profiling with the advantage to obtain quantitative compositional information as a function of depth. AES was used in this study to obtain depth profile measurements of the Ni/Cu multilayer thin films and it was also used to measure surface segregation.

4.4.1 AES principle

Fig. 4.6 shows schematically the process of the emission of a $KL_{2,3}L_{2,3}$ Auger electron. When an atom is radiated by an external energy, such as a photon or a beam of electrons with energies in the range of several eV to 50 keV, a core state electron can be removed leaving behind a hole (in Fig. 4.6(a)). As this is an unstable state, the core hole can be filled by an outer shell electron, whereby the electron moving to the lower energy level loses an amount of energy equal to the difference in orbital energies (in Fig. 4.6(b)). The transition energy can be coupled to a second outer shell electron, which will be emitted from the atom as an Auger electron if the transferred energy is greater than the orbital binding energy (in Fig. 4.6(c)). Hence, the kinetic energy of a $KL_{2,3}L_{2,3}$ Auger electron is approximately equal to the difference between the energy of the core hole and the energy levels of the two outer shell electrons, $E_{L2,3}$ (the term $L_{2,3}$ is used in this case because, for light elements, L_2 and L_3 cannot be resolved):[4,5]

$$E_{KL_{2,3}L_{2,3}} \approx E_K - E_{L_{2,3}} - E_{L_{2,3}} \tag{4.4}$$

This Eq. 4.4 does not take into account the interaction energies between the core holes ($L_{2,3}$ and $L_{2,3}$) in the final atomic state nor the inter- and extra-relaxation energies which come about as a result of the additional core screening needed.

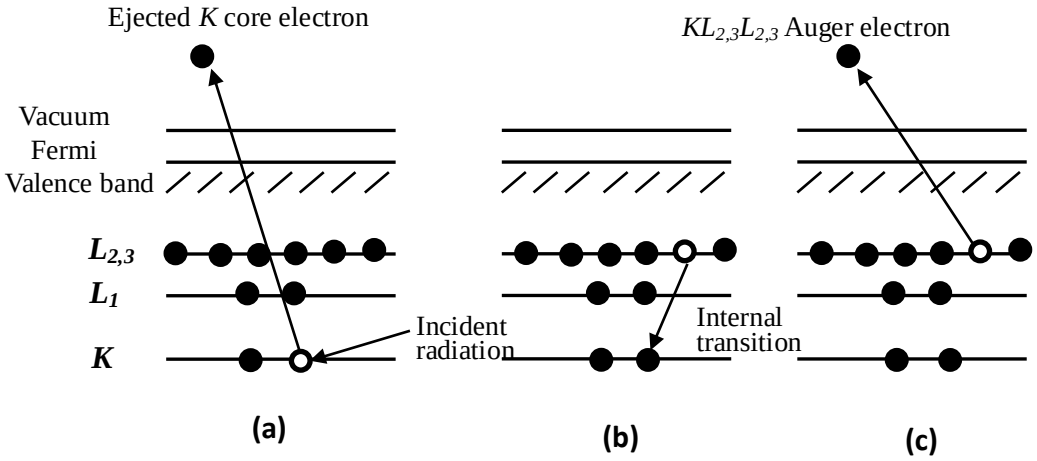

Figure 4.6: The schematic diagram of the process of the emission of $KL_{2,3}L_{2,3}$ Auger electron. (Adapted from Ref. [5])

4.4.2 AES Apparatus

Three different AES systems were used for the depth profiles and surface segregation measurements in this study. The PHI 600 SAM and PHI 700 Auger Nanoprobe were used for depth profile analysis, elemental mapping and SED imaging, while the PHI 590 and PHI 600 SAM system was used for the surface segregation study. All three of these AES systems were manufactured by the Physical Electronics Company and comprises of an ultra-high vacuum system (up to 10^{-10} torr), electron beam source, electron energy analysis system (CMA), sputtering ion gun, heating unit (only PHI 590 and PHI 600 SAM) and a control system. The PHI 590 and PHI 600 SAM system is equipped with a heat unit and a temperature control system for surface segregation studies. PHI 600 SAM is equipped with two ion guns that can be operated in dual beam mode and was used for the depth profiling measurement. The PHI 700 Auger Nanoprobe with a small electron beam diameter (beam size ~ 6 nm) provided by the field emission electron gun was used for the SEM imaging and in combination with Zalar rotation it was also used for depth profiles measurements with sample rotation. Pictures of the systems are shows in Fig. 4.7 (the PHI 590), Fig. 4.8 (the PHI 600 SAM) and Fig. 4.9 (the PHI 700 Nanoprobe).

Figure 4.7: A photo of the PHI 590 system.

The PHI 590 system comprised of the following components:

1. **PHI 18-085** electron gun with its control unit provides the electron beam from a LaB_6 crystal that is used to ionize the target atoms.
2. **PHI 25-110** single pass cylindrical mirror analyser (CMA) for the energy analysis of the Auger electrons.
3. **PHI 20-075** electron multiplier (high voltage supply) provides high voltage to the electron multiplier inside the CMA.
4. **PHI 20-805** analyser control for changing the electric field in the analyser and the Auger signal modulation.
5. **PHI 32-010** Lock in amplifier for differentiating the Auger signal.
6. **PHI 11-065** differential Ion gun for the sputtering during the depth profiling.
7. **PHI 20-070** scanning system and secondary electron detector (SED) to obtain a topographic image of the sample.
8. **Ultra-High vacuum system** with the Rotary, turbo molecular and ion pump with titanium sublimation provides the capable of pressures down to ~10^{-9} Torr.
9. **Heat unit and temperature control system** produced by UFS provides the temperature control of the sample up to 900℃.
10. **Software VisiScan** for controlling the system and recording of data.

Figure 4.8: A photo of the PHI 600 SAM system.

The PHI 600 S system comprised of the following components:

1. **PHI 20-620A** and **PHI 20-610** electron gun with its control unit that provides the electron beam from a LaB_6 crystal used to ionize the target atoms.
2. **PHI 25-120A** single pass cylindrical mirror analyser (CMA) for the energy analysis of the Auger electrons.
3. **PHI 32-150 digital AES control** and **PHI 20-250 signal processor** for Auger signal.
4. **Dual symmetry PHI 11-065** differential Ion gun for the sputtering during depth profiling.
5. **PHI 18-175** and **PHI 18-170** scanning system and secondary electron detector (SED) to obtain a topographic image of the sample.
6. **Ultra-High vacuum system** with the Rotary, turbo molecular and ion pump with a titanium sublimation provides the capable to work at pressures down to ~10^{-9} Torr.
7. **Heat unit and temperature control system** produced by UFS provides the temperature up to 900℃.
8. **Software VisiScan 4.0.1** for controlling the system and recording of data.

Figure 4.9: A photo of the PHI 700 Auger Nanoprobe system.

The PHI 700 Auger Nanoprobe system comprised of the following components:

1. **PHI 20-630 and PHI 18-197** electron guns with its control unit provides the electron beam from a field emission tip used to ionize the target atoms.
2. **PHI 25-140** single pass cylindrical mirror analyser (CMA) with multi-channel detector for the energy analysis of the Auger electrons with
3. **PHI 11-066** differential Ion gun for the sputtering during the depth profiling with sample Zalar rotation system
4. **Ultra-High vacuum system** with the Rotary, turbo molecular and ion pump with titanium sublimation provides the capable of pressures down to ~10^{-10} Torr.
5. **Smartsoft AES version 4.1.3.2 software** for controlling the system and recording of data.

4.4.3 AES depth profiles measurement

AES depth profiles measurement was performed by using the PHI 700 Auger NanoProbe and PHI 600 SAM instrument. The PHI 700 Auger NanoProbe was used to carry out the depth profiles measurement with sample Zalar rotation and the measurement parameters setting are listed in Table 4.1. The PHI 600 SAM was used to measure the depth profiles without sample rotation (stationary) with single and dual ion beam sputtering; and the measuring parameters setting are listed in Table 4.1 and Table 4.2.

Before the depth profile measurements was performed with PHI 600 system, the system was turned on and allowed to stabilise for one day (24 hours). The filament of electron gun and ion gun were de-gassed by slowly increasing the current flowing through the filaments. Once the system was fully degassed and the base pressure was allowed to stabilise. The distance between the sample and the CMA was adjusted until the correct position (using the elastic peak). The two ion beams and the electron beams were aligned to the same position in the centre of the analysis area using the Faraday cup. The energy scale of detector was also calibrated using a pure copper standard after which the system was ready for use. For sputtering the sample was tilted to 30°, the angle between the both ion guns was 60° as shown in Fig. 4.10. The current densities and scan areas used for during sputtering are also listed in Table 4.2.

The Auger peaks of Ni, Cu, Si, C and O were used for AES depth profile with and without rotation by recording the peak heights as a function of sputtering time. The low energy peaks of Ni, Cu and Si are overlapped and they were recoded as one region that ranging from 40-110 eV, the C peak was recoded from 240-275 eV, the O peak was recoded from 480-529 eV, the Si high energy peak was recorded from 1580-1649 eV and then the high energy peaks of Ni and Cu_ overlapped and both were recorded from 680-960 eV.

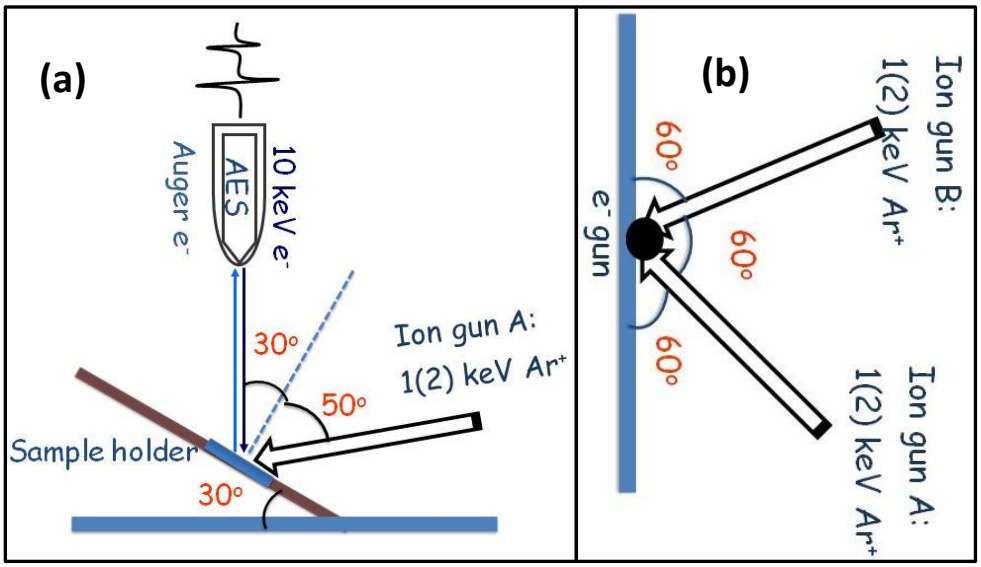

Figure 4.10: (a) The schematic diagram of the relation of angle between sample holder, e-beams and ion beams in the PHI 600 SAM system; (b) The relation of angle between both ion beams (side view).

Table 4.1: The values of the setting parameter were used for the depth profiles measurement with the PHI 600 and PHI 700 with single ion gun.

	Parameters	PHI 600 Single gun	PHI 700 Rotation
Electron gun:	Primary beam voltage	10 keV	25 keV
	Primary beam voltage (elastic peak)	2 keV	1 keV
	Emission current	29 µA	280 µA
	Beam current	2.83 µA	10 nA (AES) 1 nA (SEM)
	Beam size (diameter)	9.2 µm	12 nm (10 nA) 8-10 nm (1 nA)
Ion gun:	Argon beam voltage	2 keV	2 keV
	Beam current	44.1 nA	110.0 nA *
	Raster size	2x2 mm^2	1x1 mm^2
	Emission current	25mA	12.5 mA
	Incident angle	50 °	45 °
	Ar Pressure	5 mPa	15 mPa
	Zalar rotaion		4 r/min.
Measurement settings	eV/step	1 eV	1 eV
	Time/step	200 ms/ eV	50 ms/ eV
	Photomultiplier voltage (measurements)	1700 eV	2200 eV
	Photomultiplier voltage (elastic peak)	1400 eV	2200 eV

*Ion beam current measured for Zalar rotation in PHI 700 without raster scanning, and the others measured in PHI 600 with raster scanning area 2×2 mm^2.

Table 4.2: The values of the setting parameter were used for the depth profiles measurement with the PHI 600 with dual ions gun.

	Parameters	PHI 600 dual gun
Electron gun:	Primary beam voltage	10 keV
	Primary beam voltage (elastic peak)	2 keV
	Emission current	29 μA
	Beam current	2.83 μA
	Beam size (diameter)	9.2 μm
Ion gun A:	Argon beam voltage	1, 2 keV
	Beam current	15.4 nA (1 keV) 31.6 nA (2 keV)
	Raster size	2x2 mm^2
	Emission current	25mA
	Incident angle	50 °
	Ar Pressure	3.5 mPa
Ion gun B:	Argon beam voltage	1, 2 keV
	Beam current	15.4 nA (1 keV) 31.5 nA (2 keV)
	Raster size	2x2 mm^2
	Emission current	25mA
	Incident angle	50 °
	Ar Pressure	4.1 mPa
	Beam current (A+B)	30.8 nA (1 keV) 63.1 nA (2 keV)
Measurement settings	eV/step	1 eV
	Time/step	200 ms/ eV
	Photomultiplier voltage (measurements)	1700 eV
	Photomultiplier voltage (elastic peak)	1400 eV

4.4.4 AES surface segregation measurement

(1) Heater unit and temperature measurement

The *in-situ* sample heater unit used for the segregation measurement was first designed by Terblans [6] for PHI 590 and modified by Barnard and Terblans [7] for PHI 600 SAM. For the PHI 590 system, a cupped shape sample holder with a screw top machined out of non-magnetic 316 stainless steel, backed by a non-magnetic 316 stainless steel housing isolating the tungsten filament. The Type K chromel-alumel

thermocouple was placed on the ceramic and the back of the crystal was pressed onto the thermocouple junction with the stainless steel screw cap (see in Fig. 4.11(a)). The back temperature was calibrated in terms of the true surface temperature using a second thermocouple that was pressed into the surface of a dummy copper sample (see Ref. [6]). For the PHI 600 SAM system, the heating unit with sample holder is shown in Fig. 4.12(b). The heating filament with tungsten was embedded in the ceramic under the measured sample; the temperature was measured from the Type K chromel-alumel thermocouple placed on the surface of sample. The heating temperature settings and temperature measurement of the sample was controlled with a computer. The temperature can be calibrated as shown in Ref. [7]. To ensure accurate temperature readings from the thermocouple, a reference temperature is used. The reference temperature is obtained from a unit that contains a solid aluminium block, heated to 35 ℃. The connection of the thermocouple to the sample, reference temperature block and control unit, is shown in Fig. 4.12.

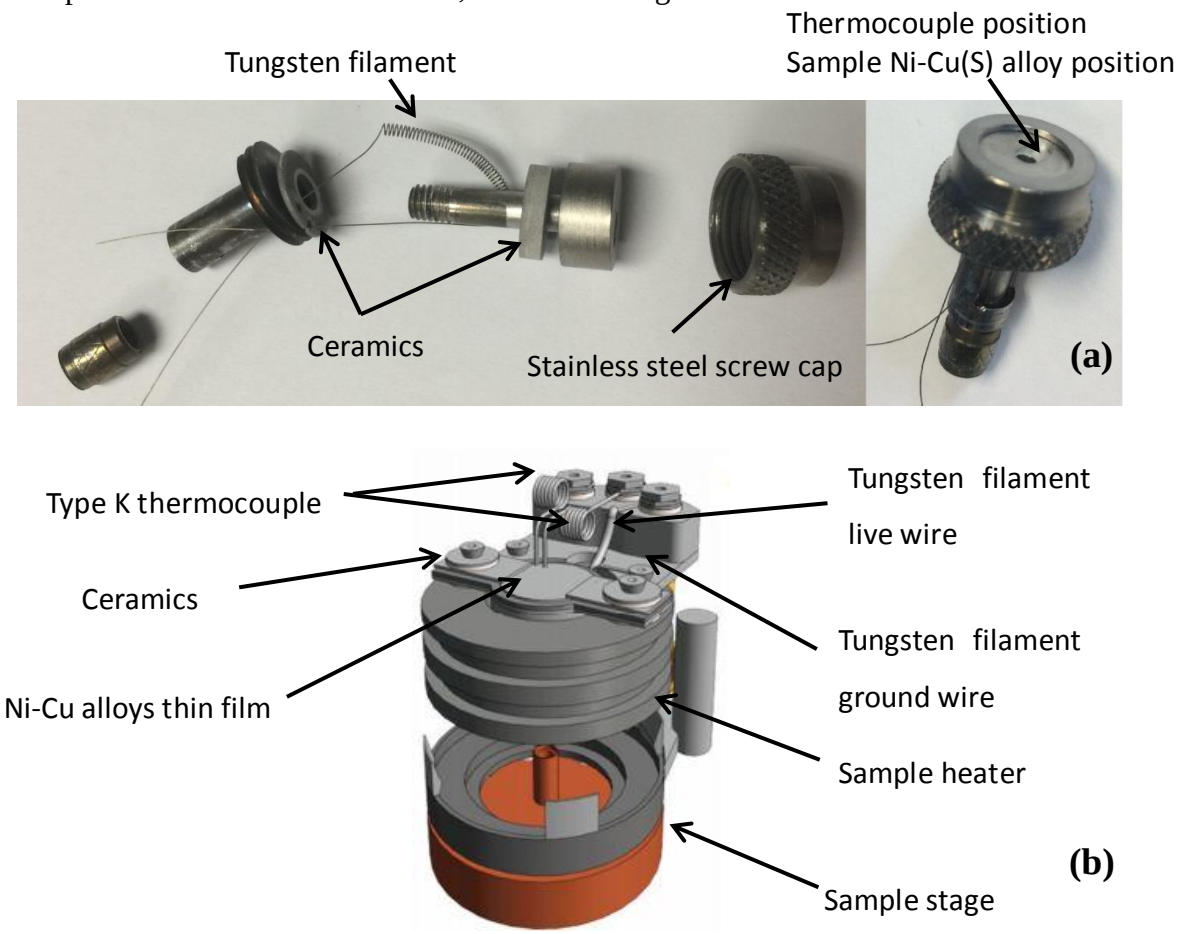

Figure 4.11: The arrangement of sample heater unit for (a) PHI 590 and (b) PHI 600 (adapted from Ref. [7]).

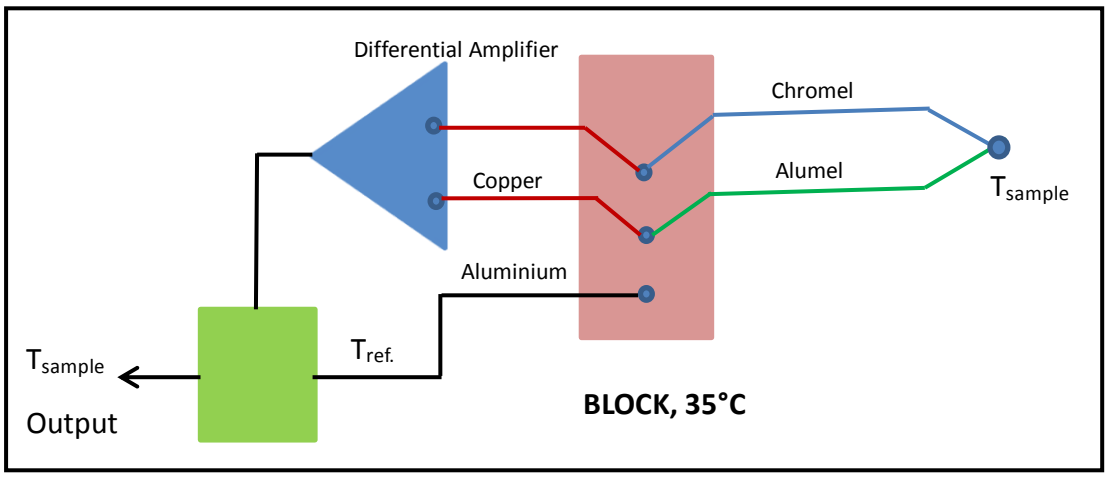

Figure 4.12: Schematic of the thermocouple connection used to measure a samples temperature.

(2) Measurement procedures

For the Ni-Cu alloys bulk material, surface segregation measurement was performed by Auger electron spectroscopy with a PHI 590 Scanning Auger Microprobe at a base pressure of 2×10^{-9} Torr. A static primary electron beam of 5 keV and beam current of 0.71 μA with beam size diameter of 13.4 μm was used for the AES measurements, and the modulation energy was 2.0 eV, the scan rate was 5.0 eV/s and the time constant was 0.1 s. The ion gun sputter (for cleaning) was performed with 2 keV Ar^+ ion, the argon pressure was 2.0×10^{-3} Pa and the ion beam was rastered over a 2×2 mm^2 area, which is much larger than the Auger primary electron beam diameter (13.4 μm) to avoid the influence from the lateral surface diffusion of impurities. The ion beams and the electron beams were aligned to the same position in the centre of the analysis area using a Faraday cup. The crystal was tilted with the normal of the crystal surface at a 30 °angle with respect to the direction of the incident electron beam. The others measurement setting parameters for surface segregation are listed in Table 4.3.

Surface segregations were measured with both linear and constant temperature heating methods. Before these segregation measurements, the Ni-Cu alloys crystal was first sputter cleaned at room temperature, then the temperature was increased to 727 K and sputter cleaned and then cold to room temperature, the cleaning procedure was repeated few times to clean the surface by removing the impurity (*i.e.* C, O, and N) on the surface. The alloy crystal was then annealed at 961 K for 24 h to restore the initial condition of the crystal (uniform bulk concentration) and cooled to 423 K at

rate of -0.05 K/s. After the reconditioning heat treatment the segregation measurements were performed by either linear or constant temperature heating.

For linear temperature heating measurements, the Ni-Cu alloys was pre-heated at the initial temperature of 423 K for 1 h and sputter cleaned for exactly 30 s. Then the linear temperature heating was immediately carried out in the temperature range 423-1121 K at a constant heating rate of 0.02 K/s. Auger spectrums were recorded as a function of temperature for the Auger peaks of Ni, Cu, S, C and O. The low energy peaks of Ni and Cu are overlapped and they were recorded as one region that ranging from 40-130 eV, the S peak was recorded from 131-239 eV, the C peak was recorded from 240-275 eV, the O peak was recorded from 480-529 eV and then the high energy peaks of Ni and Cu overlapped and both were recorded from 680-950 eV. After the linear temperature heating measurement running, the crystal was pre-heated at 961 K for 24 h again to restore the initial condition of the crystal (uniform bulk concentration) and then cooled to 423 K at rate of -0.05 K/s.

The constant temperature measurements were carried out between 770 K and 860 K at 30 K intervals. The ternary Ni-Cu(S) alloy crystal was heated to the desired temperature, and after stabilization of the temperature ternary Ni-Cu(S) alloy crystals was sputtered cleaned for exactly 30 s. The Auger spectrums for the Auger peaks of Ni, Cu, S, C and O were recorded as a function of time. The monitored Auger peak ranges were the same as for linear heating measurement (see previous paragraph). Again, after each constant temperature heating measurement running, the crystal was pre-heated at 961 K for 24 h and then cooled to 423 K at rate of -0.05 K/s.

For the Ni-Cu alloy thin films, the segregation measurements were performed on a PHI 600 SAM. A static primary electron beam of 10 keV and beam current of 2.83 μA with beam size diameter of 12.2 μm was used for the AES measurements. The ion gun used for sputter cleaning was performed with 2 keV Ar^+ ion at the pressure of 5.0 $\times 10^{-3}$ Pa, and the beam was rastered over a 2×2 mm^2 area. The Ni-Cu alloy thin film was mounted on a heater inside the ultra-high vacuum (UHV) chamber with the pressure about 1.0×10^{-9} Torr. And the sample was tilted with the normal of the crystal surface at a 30 °angle with respect to the direction of the incident electron beam. The

others measurement setting parameters for surface segregation are listed in Table 4.3.

Surface segregation measurements with linear program heating were carried out in the temperature range 403-823 K at a constant heating rate of 0.03 K/s. Before each segregation measurement run, the Sample 10 was *in suit* annealed at 698 K for 4 h (or Sample 20 at 698 K for 25 h) to form the uniform bulk concentration Ni-Cu alloy thin films. The annealing temperature and time selected was further discussed with AES depth profile as shown in section 9.3.1. The Ni-Cu alloy thin film was then cooled to 403 K with constant heating rate of -0.5 K/s. After stabilization of the temperature at 403 K, the Ni-Cu thin films was then sputter cleaned for exactly 10 s with a 2 keV argon ions beam. After sputtering, the measured Auger spectrum were immediately recorded as a function of temperature for Ni & Cu _L (40-110 eV), C (240-275 eV), O (480-529 eV) and Ni & Cu_H (680-960 eV).

The APPH data was quantified using the method as the following Section 4.4.5.

Table 4.3: The values of the setting parameters were used for the surface segregation measurement with the PHI 590 and PHI 600.

	Parameters	**PHI 600**	**PHI 590**
Electron gun:	Primary beam voltage	10 keV	5 keV
	Primary beam voltage (elastic peak)	2 keV	2 keV
	Emission current	29 μA	150 μA
	Beam current	2.83 μA	0.71μA
	Beam size (diameter)	12.2 μm	13.4 μm
Ion gun:	Argon beam voltage	2 keV	2 keV
	Beam current	44.1 nA	4.4 nA
	Raster size	2x2 mm^2	2x2 mm^2
	Emission current	25mA	25 mA
	Ar Pressure	5 mPa	2 mPa
Measurement settings	eV/step	1 eV	1 eV
	Time/step	200 ms/ eV	200 ms/ eV
	Photomultiplier voltage (measurements)	1700 eV	2350 eV
	Photomultiplier voltage (elastic peak)	1400 eV	1850 eV

4.4.5 AES quantification

(1) ***Separation of the overlapped Cu/Ni peaks***

From the standard Auger spectra of pure Cu and Ni it is clear that the high energy peaks (see in Fig. 4.13(a)) are overlapped. The Linear Least Square (LLS) method was used to determine each elements (Cu and Ni) contribution to the measured signal [8]. In this method, the measured spectrum [**b**] of **N** channels is represented by a linear combination of the **K** standard spectra:

$$[\mathbf{A}][\mathbf{x}] = [\mathbf{b}] \tag{4.5}$$

where [**A**] is an **N**×**K** matrix with the standard spectra as columns and [**x**] is a vector with length **K** channels containing the fractional concentration. In practice, **N** is much larger than **K** and therefore the system (Eq. 4.5) is overdetermined. If one includes a weight matrix function [**W**], which has as its diagonal elements the squares of the reciprocal standard deviations of the error in each channel and all the others off-diagonal elements as zero, the quantification becomes considerably easier. Such the weight function [**W**] (see in Fig. 4.13(b)) is introduced to Eq. 4.5 and Eq. 4.5 is rewritten as [9]:

$$[\mathbf{W}][\mathbf{A}][\mathbf{x}] = [\mathbf{W}][\mathbf{b}] \tag{4.6}$$

The solution of weight function LLS Eq. 4.6 is given by:

$$[\mathbf{x}] = ([\mathbf{A}]^{T}[\mathbf{W}][\mathbf{A}])^{-1}([\mathbf{A}]^{T}[\mathbf{W}][\mathbf{b}]) \tag{4.7}$$

where the superscripts T and -1 represent the transpose and inverse matrix, respectively. Fig. 4.14(a) shows the depth profile for the Cu 922 eV peak. After separating the overlapped Cu and Ni measured Auger spectrum in depth profiles were shown in Fig. 4.14(a) for the Cu 922 eV peak and Fig. 4.14(b) for Ni 849 eV peak. In Fig. 4.14(a), no overlapped Cu 922 eV peak was remained unchanged before and after separating with weight function LLS Eq. 4.7, meanwhile, the overlapped Ni 849 eV peak was successfully separated (in Fig. 4.14(b)). It is indicated that the weight function LLS method offers the possibility of separation the overlapped Cu and Ni measured Auger spectrum.

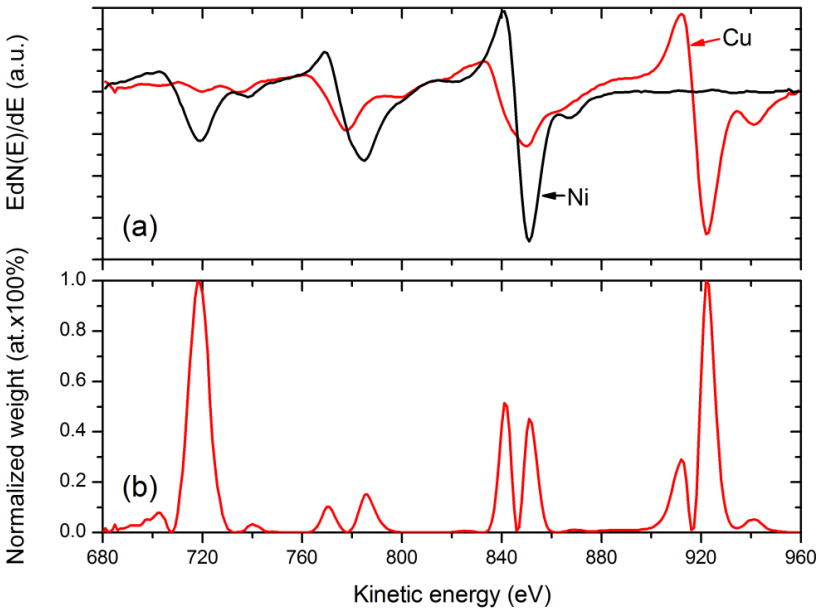

Figure 4.13: The standard high energy Auger spectrum of pure Cu and Ni (a) as well as the weight function (b) used in the LLS method. The weight function is calculated by $[Ed\mathrm{NE(Cu)}/dE - Ed\mathrm{NE(Ni)}/dE]^2$ and normalized in the range of 680-750 eV and 750-960 eV, respectively.

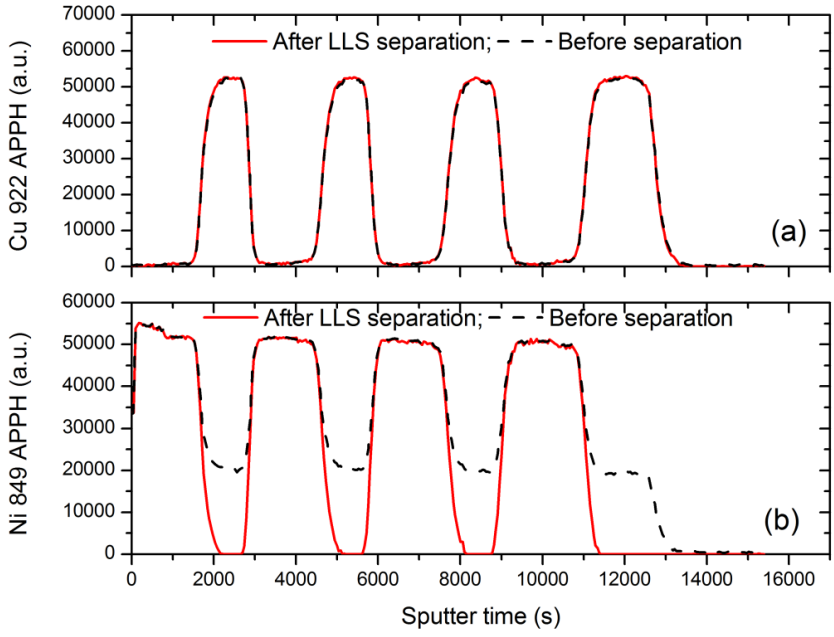

Figure 4.14: The depth profile with sputter depth of Cu (922 eV) in (a) and Ni (849 eV) in (b) before and after separating the overlapped peak by the weight function Linear Least Square method.

(2) ***Quantification of the AES depth profile data***

After separating the overlapped peak, the Auger peak of Cu (922 eV) and Ni (849 eV) with C (275 eV), O (510 eV) and Si (1618 eV) were used to determine the fractional concentration of Cu, Ni, C, O and Si. The fractional (atomic) concentrations of Cu, Ni, C, O and Si were calculated using the relative elemental sensitively factor method [10]

$$X_i = \frac{I_i / I_i^0}{\sum_{j=1}^{n} I_j / I_j^0} \tag{4.8}$$

where I_i is the Auger electron intensity for element i (I_i as the APPH of element i in the differentiated spectrum - differentiation was performed with 9 point in this study) and I_i^0 is the Auger electron intensity for the pure element i (I_i^0 is the relative sensitivity factor for element i at 10 keV from reference [10]). X_i is the measured fractional concentration of element i. (For this study i = Cu, Ni, C, O and Si). The measured depth profile of APPH vs. sputtering time and the fractional concentration vs. sputtering depth profiling for the as-deposited Cu/Ni multilayer are shown in Fig. 4.15(a) and Fig. 4.15(b), respectively (the sputtering as performed with sample rotation).

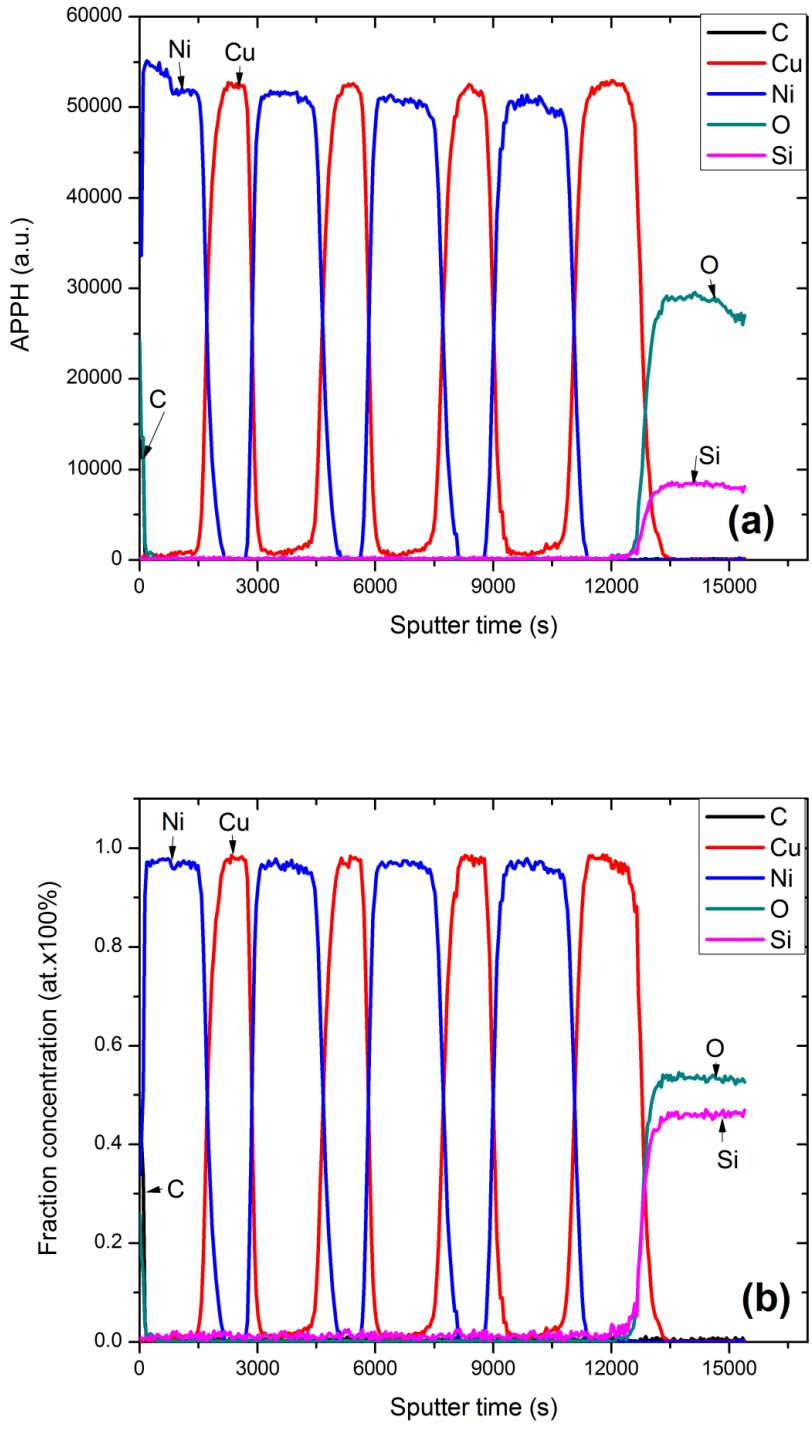

Figure 4.15: AES depth profile for the as-deposited Ni/Cu multilayer thin film (sputtering as performed with sample rotation and 2 keV Ar^{+}ions). (a) APPH vs. sputtering time and (b) the calculated fractional concentration vs. sputtering time.

(3) ***Quantification of the AES monolayer surface segregation data***

The Auger electron current intensity of an elemental *A* in matrix *M* can be written as [11]:

$$I_A = I_P \sigma_A(E_P)\left[1 + r^M(E_A, \alpha)\right] T(E_A) D(E_A) \times \int_0^\infty n_A^M(z) \exp\left[-z / \lambda_M(E_A) \cos(\theta)\right] dz \tag{4.9}$$

Where I_P is the primary electron current, $\sigma_A(E_P)$ is the ionization cross section of atom *A* by electrons with energy E_P, $r^M(E_A, \alpha)$ is the backscattering term that dependents on both the matrix *M* and the binding energies for the core level electrons involved in the transitions leading to an Auger electron with energy E_A, $T(E_A)$ is the transmission efficiency of the spectrometer, $D(E_A)$ is the transmission efficiency of the electron detector, $n_A^M(z)$ is the atomic density (in atoms/m^3) of element *A* at a depth *z* from the surface, $\lambda_M(E_A)$ is the elastic mean free path in the matrix *M* and θ is the angle of emission.

To reach a workable formula in Eq. 4.9 the following assumption are made: (i) the instrument factors $T(E_A)$ and $D(E_A)$ are constant, and (ii) the concentration distribution $N_A(z)$ is constant. As we have discussed in the Chapter 2, the surface segregation modelling and calculation simplifies if we make use of a layer model. This is also true for the quantification of Auger measurements during segregation. We divided the crystal in planes parallel to the surface, each separated by the inter-planar distance *d* and the integral in Eq. 4.9 is then approximated by discreet summation. By take the instrumentation factors to be constant Eq. 4.9 can write as:

$$I_A = const\ \sigma_A(E_P) R_A \sum_0^\infty N_A(nd) \exp\left[-nd / \lambda_{AD} \cos(\theta)\right] \tag{4.10}$$

where $N_A(nd)$ is the atomic density (in atoms/m^3) of element *A* at a depth *nd* from the surface. For pure element A Eq.4.10 can be written as:

$$I_A^\infty = const\ \sigma_A(E_P) R_A^\infty \sum_0^\infty N_A^\infty(nd^\infty) \exp\left[-nd_A^\infty / \lambda_{AD}^\infty \cos(\theta)\right] \tag{4.11}$$

The Auger yield for the element *A* in the alloy (note that the expression is not restricted to binary alloys) is given by [11]

$$I_A = const\ \sigma_A(E_P) R_A N \left[X_A^S + \sum_1^\infty X_A^{bulk} \exp\left(-nd / \lambda_{AD} \cos(\theta)\right) \right] \tag{4.12}$$

where X_A^S is the surface concentration of element *A* and X_A^{bulk} is the bulk concentration of element *A*. Solving Eq. 4.10 for $\sigma_A(E_P)$ and substituting the result into Eq. 4.12:

$$I_A = \frac{I_A^\infty R_A N}{R_A^\infty \sum_0^\infty N_A^\infty (nd^\infty) \exp\left[-nd_A^\infty / \lambda_{AD}^\infty \cos(\theta)\right]} \left[X_A^S + X_A^{bulk} \sum_1^\infty \exp\left(-nd / \lambda_{AD} \cos(\theta)\right) \right] \tag{4.13}$$

A similar expression can be written for other elements. Thus, taking the ratio the Auger intensity of any two components *A* and *B* it follows that:

$$\frac{I_A}{I_B} = \frac{I_A^\infty}{I_B^\infty} \frac{R_A R_B^\infty}{R_B R_A^\infty} \frac{N_B^\infty}{N_A^\infty} \frac{\sum_0^\infty \exp\left[-nd_B^\infty / \lambda_{BD}^\infty \cos(\theta)\right]}{\sum_0^\infty \exp\left[-nd_A^\infty / \lambda_{AD}^\infty \cos(\theta)\right]} \frac{\left[X_A^S + X_A^{bulk} \sum_1^\infty \exp\left(-nd / \lambda_{AD} \cos(\theta)\right) \right]}{\left[X_B^S + X_B^{bulk} \sum_1^\infty \exp\left(-nd / \lambda_{BD} \cos(\theta)\right) \right]} \tag{4.14}$$

Where:

$$\alpha_{AB} = \frac{I_A^\infty}{I_B^\infty} \frac{R_A R_B^\infty}{R_B R_A^\infty} \frac{N_B^\infty}{N_A^\infty} \frac{\sum_0^\infty \exp\left[-nd_B^\infty / \lambda_{BD}^\infty \cos(\theta)\right]}{\sum_0^\infty \exp\left[-nd_A^\infty / \lambda_{AD}^\infty \cos(\theta)\right]} \tag{4.15}$$

$$\beta_A = \sum_1^\infty \exp\left(-nd / \lambda_{AD} \cos(\theta)\right) \quad \text{and} \quad \beta_B = \sum_1^\infty \exp\left(-nd / \lambda_{BD} \cos(\theta)\right) \tag{4.16}$$

Therefore, Eq. 4.12 is re-written as

$$\frac{I_A}{I_B} = \alpha_{AB} \frac{X_A^S + \beta_A X_A^{bulk}}{X_B^S + \beta_B X_B^{bulk}} \tag{4.17}$$

Eq. 4.17 can be expanded to m-1 expressions in for a system consisting of m components. For the binary system, in combination with $X_A^S + X_B^S = 1, and\ X_A^{bulk} + X_B^{bulk} = 1$, the surface concentration of *A*, X_A^S , can be expressed as:

$$X_A^S = \frac{\alpha_{AB} + \alpha_{AB}\beta_B(1 - X_A^{bulk}) - I_A/I_B\,\beta_A X_A^{bulk}}{I_A/I_B + \alpha_{AB}} \tag{4.18}$$

And for the ternary system, in combination with $X_A^S + X_B^S + X_C^S = 1, and\ X_A^{bulk} + X_B^{bulk} + X_C^{bulk} = 1$, the surface concentration of A and C, X_A^S and X_C^S, can be expressed as:

$$X_A^S = \frac{\alpha_{CB}\, I_A/I_B + (\alpha_{CB}\beta_B\, I_A/I_B + \alpha_{AB}\beta_A\, I_C/I_B)X_B^{bulk} - \alpha_{AB}\alpha_{CB}\beta_A}{\alpha_{AB}\alpha_{CB} + \alpha_{AB} I_C/I_B + \alpha_{CB}\, I_A/I_B} \tag{4.19}$$

$$X_C^S = \frac{\alpha_{AB}\, I_C/I_B + (\beta_B - \beta_A)\alpha_{AB} X_B^{bulk}\, I_C/I_B + \alpha_{AB}\beta_A\, I_C/I_B}{\alpha_{AB}\alpha_{CB} + \alpha_{AB} I_C/I_B + \alpha_{CB}\, I_A/I_B} \tag{4.20}$$

Where the parameters of the backscattering coefficients *R* and the inelastic mean free path $\lambda(E_A)$ in Eqs. 4.18, 4.19 and 4.20 are described as following:

1. The backscattering coefficient *R* was calculated from Shimizu [12]:

$$R = 1 + (0.462 - 0.777Z^{0.2})U_o^{-0.32} + (1.15Z^{0.2} - 1.05) \tag{4.21}$$

where *Z* is the mean atomic number of the matrix in the near surface region, $U_o = E_o/E_b$, E_o is the energy of the primary electron beam and E_b is the binding energy of the core level involved in the Auger transition.

2. The inelastic mean free path $\lambda(E_A)$ was calculated from TPP-2 formula [13]:

$$\lambda = E/\{E_P^2\ [\beta \ln(\gamma E) - (C/E) + (D/E^2)]\} \tag{4.22}$$

where

E is the electron energy,

$E_P = 28.8\,(N_V \rho/M)^{0.5}$ is the Free-electron plasmon energy (in eV), N_V is the number of valence electrons per atom, ρ is the density (in g/cm^3) and M is the atomic mass,

$B = -0.10 + 0.944/(E_P^2+E_g^2)^{0.5} + 0.069\rho^{0.1}$ (E_g is the band-gap energy),

$\gamma = 0.191\rho - 0.5, C = 1.97 - 0.91\,N_V \rho/M,$

$D = 53.4 - 20.8\,N_V \rho/M.$

4.5 ToF-SIMS measurements

Time-of-Flight secondary ion mass spectrometry (ToF-SIMS) is a powerful and sensitive surface analytical technique to determine detailed elemental and molecular information from a surface and/or interface of a sample. It is widely used for the semiconductors, polymers, paint, coatings, glass, paper, metals, ceramics, biomaterials, pharmaceuticals and organic tissue. There are four main modes of operation of ToF-SIMS: large area surface analysis, surface imaging and micro area analysis, depth profiling analysis and trace analysis of individual substances. [14] In this study ToF-SIMS was used to perform depth profiles on Ni/Cu multilayer thin films under various bombardment conditions.

4.5.1 ToF-SIMS principle

In ToF-SIMS, a pulsed primary beam of Bi or Au ions is widely used to bombard a sample to produce the emission of secondary ions. All the secondary ions generated from one such pulse are then accelerated by a constant voltage U (~2 keV in this study) over a very short distance (1.5 mm in this sudy), thereby giving all secondary ions virtually the same kinetic energy, E_k, before they enter the field free flight path of length L. Fig. 4.16 illustrate this process. If one neglects the relatively small initial energy of the secondary ions, the kinetic energy of the secondary ions is given by,

$$E_k = z \bullet U = \frac{1}{2} m v^2 \tag{4.23}$$

where z is the charge of a secondary ion, m is its mass and v is its velocity. Ions of different mass will have different velocities and consequently a mass separation will occur. Accordingly, the mass separation is given by the flight time, t, from the sample

to the detector. This is approximately given by,

$$t = \frac{L}{v} = L\sqrt{\frac{m}{2zU}} \tag{4.24}$$

Therefore, particles with different mass-to-charge ratios (*m/q*) can be detected with multi-channel according to the time-of-fight *t*:

$$\frac{m}{z} = \frac{2U^2t}{L^2} \tag{4.25}$$

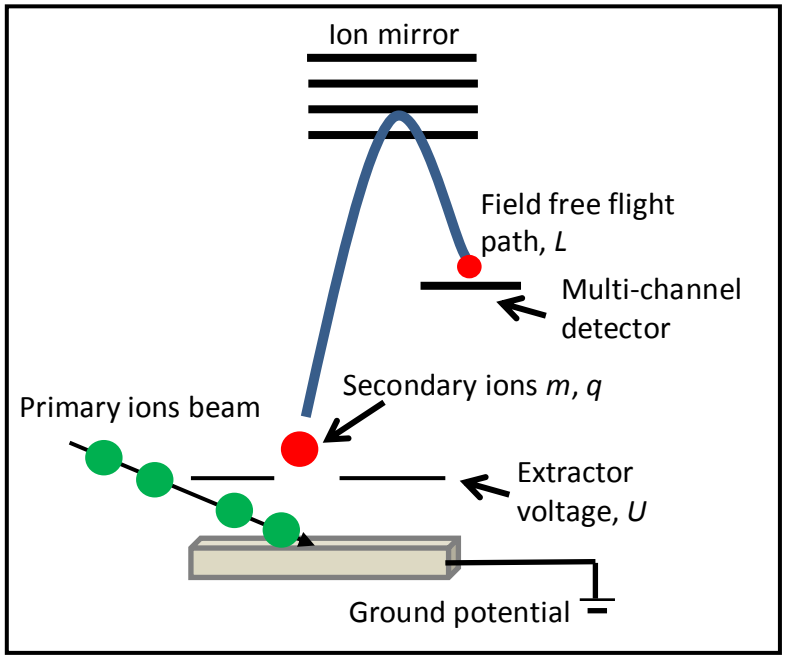

Figure 4.16: The principle of a linear time of flight mass spectrometer (for explanation see text).

4.5.2 ToF-SIMS measurement

ToF-SIMS depth profiling measurements were performed by using an ION-TOF ToF-SIMS V instrument (shown in Fig. 4.17, from the department of physics at the University of the Free State) equipped with a Bismuth liquid metal ion gun (LMIG) and an O_2^+ ions sputter ion gun. Both ions gun sources were aligned at an incidence angle of 45 °with respect to the sample surface. The analysis chamber was maintained at pressure less than 5×10^{-9} torr. A 30 keV Bi^+ analysis beam generated by LMIG was

used to analyse a area of 100×100 μm^2 with a scan resolution of 512×512 pixels in the central of the sputtering crater used for depth profiling. The target current of the analysis beam was maintained as 1.4 pA before and after sputtering. The ion source employed to etch through the sample was O_2^+ ion sputtered at different energies (0.5, 1 and 2 keV) while rastering over an area of 300×300 μm^2. The target current of the O_2^+ ions (used for sputtering) was maintained the same current before and after sputtering. The other experimental parameters used for the ion sputtering with the ToF-SIMS are given in Table 4.4

A low energy electron flood gun was employed for charge neutralization. This ensured accurate analysis of the samples. The positive secondary ion mass spectra were calibrated to the following mass peaks: H^+, CH^+, CH_2^+, Si^+, SiO^+, Ni^+, Cu^+, Ni_2^+ and Cu_2^+. Peaks in the positive ion spectra at *m/z*=44 (SiO^+), 58(Ni^+) and 63(Cu^+), were identified as characteristic peaks of the SiO_2 substrate, Ni sublayer and Cu sublayer, respectively.

Figure 4.17: A photo of the TOF.SIMS 5.

Table 4.4: Summarised sputtering parameters as used in the ToF-SIMS depth profiles with different ion species and energy.

Ion Beam energy(keV)	Ion Beam current(nA)	Scan area (μm^2)	Analysed area(μm^2)	Incidence angle(°)	Sputter rate (nm/min.)
2.0 (O_2^+)	620.5	300×300	100×100	45	60.0
1.0 (O_2^+)	248.8	300×300	100×100	45	15.7
0.5 (O_2^+)	99.8	300×300	100×100	45	3.7
1.0 (Cs^+)	76.8	300×300	100×100	45	19.4
1.0 (Xe^+)	18.8	300×300	100×100	45	4.5

4.5.3 Compared with AES in depth profiles

AES and TOF-SIMS are the primary research techniques used in this study and knowledge concerning their strengths and weaknesses are important in order to obtain the desired information. Some of these characteristics have already been mentioned earlier in this chapter. Below Table 4.5 contains a more detailed comparison of the two techniques.

Table 4.5: The comparison of AES and ToF-SIMS techniques in the depth profiles.

	AES	**ToF-SIMS**
Incident particles:	Electron (0.5-20 keV)	Ions (0.1-30 keV)
Detected particles:	Auger Electron (20-2000 eV)	Second ions (0-500 amu)
Element range:	Z > 3	Z > 1
Detection range:	0.05%	PPT
Depth information:	2 nm	1-2 monolayer
Lateral resolution:	> 5 nm	> 50nm
Chemical information:	limited	Mass spectrum from the surface layer
Quantification:	Semi-quantitative elemental standards required and matrix effects need to be considered.	Difficulty: requires standards. Matrix effects are more complex

The AES and ToF-SIMS depth profiles measurement data of the Ni/Cu multilayer thin films will be discussed in next Chapters (Chapter 5 and Chapter 6). In addition, the interdiffusion of the Ni/Cu multilayer thin films with AES depth profiles will be discussed in next Chapter 7. The surface segregation measurement data for the bulk Ni-Cu alloy systems and for the Ni-Cu alloy thin films will be further discussed in Chapter 8 and Chapter 9, respectably.

References

[1] V.K. Pecharsky, P.Y. Zavalij, Fundamentals of Powder Diffraction and Structural Characterization of Materials, 2nd Edition, Springer, New York 2009.

[2] R.R.L. De Oliveira, D.A.C. Albuquerque, T.G.S. Cruz, F.M. Yamaji, F.L. Leite, Measurement of the Nanoscale Roughness by Atomic Force Microscopy: Basic Principles and Applications, Atomic Force Microscopy-Imaging, Measuring and Manipulating Surfaces at the Atomic Scale (edited by Victor Bellitto), InTech, 2012.

[3] P. Eaton, P. West, Atomic Force Microscopy, Oxford University Press, New York, USA 2010.

[4] D. Briggs, M.P. Seah, Practical surface analysis by Auger and Photoelectron spectroscopy, John Wiley & Sons, New York 1983.

[5] J.F. Watts, J. Wolstenholme, An Introduction to Surface Analysis by XPS and AES, John Wiley & Sons, New York, USA 2002.

[6] J.J. Terblans, Modellering en eksperimentele ondersoek van Sb-oppervlak segregasie in Cu-enkelkristalle, PhD thesis, University of the Free State 2001.

[7] P.E. Barnard, An investigation on surface segregation of S in Fe and a Fe-Cr alloy using computational models and experimental methods, PhD thesis, University of the Free State 2015.

[8] S. Hofmann, J. Steffen, Factor analysis and superposition of Auger electron spectra applied to room temperature oxidation of Ni and NiCr21Fel2, Surf. Interface Anal. **14** (1989) 59-65.

[9] W.D. Roos, G.N. van Wyk, J. du Plessis, Weight function for linear least squares fit of binary CuNi and PtPd alloy Auger spectra, Surf. Interface Anal. **22** (1994) 65-68.

[10] C.L. Hedberg, Handbook of Auger Electron spectroscopy, Third Edition, Physical Electronics Industries, Eden Prairie, MN, USA 1976.

[11] J. Du Plessis, Solid State Phenomena - Part B, Volume 11 (Diffusion and Defect Data), Sci-Tech Publications, Brookfield USA 1990.

[12] R. Shimizu, Quantitative analysis by Auger electron spectroscopy, Jpn. J. Appl. Phys., **22** (1983) 1631-1642.

[13] S. Tanuma, C.J. Powell, D.R. Penn, Calculations of electron inelastic mean free paths, Surf. Interface Anal. **37**(2005) 1-14.

[14] https://www.iontof.com/tof-sims-secondary-ion-mass-spectrometry.html (Accessed 12 December 2016)

Chapter 5
Quantitative evaluation of sputtering induced surface roughness and its influence on AES depth profiling of polycrystalline Ni/Cu multilayer thin films

5.1 Introduction

Auger electron spectroscopy (AES) is a powerful technique for performing composition-depth profiles on thin films in combination with ion beam sputtering. The quality of a measured depth profile can be characterized by the so-called depth resolution Δz, which is defined conventionally as the depth range over which a signal measured intensity change from 16% to 84% (or 84% to 16%) when profiling an ideally sharp interface between two media [1]. Since the ions sputtering is a destructive process, the depth resolution in the measured depth profiles is always influenced by factors such as atomic mixing [2], sputtering induced surface roughness [3,4], information depth, preferential sputtering, diffusion and segregation *etc* [5,6]. Recently, ion sputtering induced roughness has been given considerable attention [7-12], since the surface topography development during the sputter depth profiling plays a key role in degradation of the depth resolution. Additionally, the control of the atomic-scale surface roughness becomes more important in microelectronics, which can strongly impact basic materials properties, such as heat transfer, electron transport,

magnetism, and device performance in a wide range of technologies including spin-based electronics, giant magnetoresistance structures/devices [13-15].

However, the understanding of the surface topography development due to ion beam sputtering is still incomplete, even though the surface roughening problem could be practically minimized in the experimental techniques e.g. by applying sample rotation [16], multidirectional ion beam sputtering [17], glancing incidence angle and low ion energy, and ion species of large mass [18, 19]. However, the distinct contributions of ion sputter erosion (that leads to surface roughness) on the depth resolution (Δz) still remains uncertain [20]. From theoretical models studied, the influence that Ion sputtering has on surface roughness has been qualitatively understood in the framework of the kinetic theory suggested by Bradley and Harper [21] and developed by Barabasi and co-workers [22] and Stepanova [23] and Kim [24]. These models allow accounting for the surface curvature through an increase of the local sputter rate at troughs and a decrease at crests [25]. However, these models are not capable of explaining some experimental results that sputtering induced surface roughness increase with sputtered depth. Therefore, further systematic experiments are required to tackle this very complicated phenomenon.

In this chapter, we investigate the quantitative evaluation of sputtering-induced surface roughness with the MRI model on sputtered depth profiles of polycrystalline Ni/Cu multilayer thin films measured by AES depth–profiling. The AES depth profiles were obtained from both rotating and stationary with single and dual-ion gun sputtering. The sputtering also performed at different ion bombardment energies. The more advanced MRI model used for calculation of the concentration-depth profile accounts for the broadening of the measured depth profiles due to the effects like atomic mixing, surface roughness and the information depth of the Auger electrons. As a result, upon fitting the MRI model to the both rotating and stationary measurements data, the depth dependence of the ion sputtering induced roughness and depth resolution during depth profiling was quantitative evaluated. The fitting roughness values were compared with those measured by Atomic Force Microscopy (AFM).

5.2 Experimental

5.2.1 Sample preparation and characterization

The detailed procedures for preparation of the Ni/Cu multilayer on SiO_2 substrates have been described in Chapter 3. The main procedure can be summarized as follows. The Ni/Cu multi-layered structures composed of four pairs of Ni and Cu sublayers. The samples used in this study were prepared by electron beam physical vapour deposition onto passivated silicon (SiO_2) substrates. During the deposition, the base pressure in the deposition chamber was less than 6×10^{-6} Torr. To avoid metal oxidization, pure Ti was evaporated to clean the residual oxygens in the chamber for 1 minute before deposition of Cu (or Ni). Then, Cu and Ni were alternately deposited onto SiO_2 substrates, the deposition rate of Cu was ~0.7 nm/s and Ni was ~0.4 nm/s, respectively. The thickness of the individual sublayer was controlled using a calibrated Inficom XTC thickness monitor during vapor deposition.

The crystalline structure of the as-deposited Ni/Cu multilayer was investigated using XRD, which uses a Cu anode and monochromatic Ni-filter producing X-rays with a wavelength of $\lambda = 0.15406$ nm. The diffraction angle (2θ) was scanned from 30° to 80° with a step size of 0.01 ° and the X-ray photons were counted for 0.5 s at each step. The XRD spectrum obtains from the multilayer thin film is shown in Fig. 5.1. From the XRD spectrum it is clear that the Cu and Ni sublayers were polycrystalline with a (111), (200) and (220) orientation texture.

The cross-section and surface topography of the as-deposited Ni/Cu multilayer measurements were performed with Shimadzu SPM-9600 Atom Force Microscope (AFM) in contact model. The scan area was 1×1 μm^2 for the cross-section measurement and 3×3 μm^2 for surface topography measurement, respectively. The surface roughness was represented by the root mean square (RMS) value Rq=1.6 nm of the as-deposited sample surface in ambient condition, which shows the Ni/Cu multilayer deposited by e-beam evaporation has a smooth surface for this study.

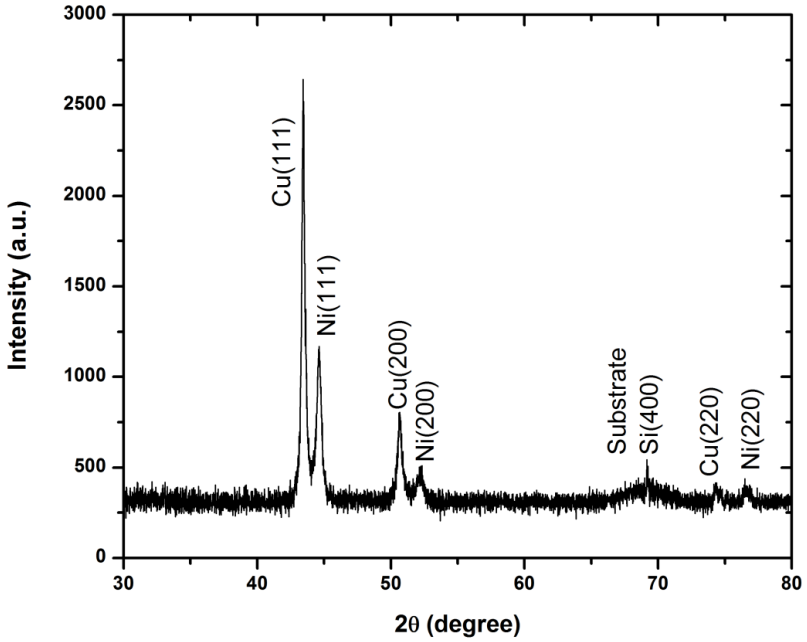

Figure 5.1: XRD pattern of as-deposited Ni/Cu multilayer crystalline structure with 2θ range of 30-80 degree.

5.2.2 AES depth profiling measurement

The detailed procedures for AES depth profiling measurements have been described in Chapter 4. The main points are summarized as follows: AES depth profiling with sample rotation was performed by using a PHI 700 Auger NanoProbe instrument equipped with a Schottky thermal field emission e-gun and a single pass coaxial cylindrical mirror analyser (CMA) operated at a base pressure below 10^{-10} Torr. A static primary electron beam energy of 25 keV and a beam current of 10 nA were used for AES measurement. The diameter of the electron beam measured by Faraday cup was about 20 nm. Ion sputtering was performed with 2 keV Ar^+ ions at an incidence angle of 45 ° with respect to the sample surface normal, and sample Zalar rotation with speed of 4 rpm was used during the ion sputtering.

AES depth profiling without sample rotation (stationary) were performed using a PHI 600 Scanning Auger Microprobe (PHI 600 SAM). The PHI 600 instrument is equipped with a LaB_6 emitter e-gun and a single pass coaxial CMA operated at a base pressure < 10^{-9} Torr. A static primary electron beam energy of 10 keV with a beam

current of 2.6 μA and the beam diameter of 9.2 μm were used for AES measurement. Ion sputtering with single and dual symmetrical ion gun was performed with 2 keV (and 1 keV) Ar^+ ions at an incidence angle of 40° with respect to the sample surface normal. For the dual symmetrical ion guns, the angle between the ion guns was 60°, and the current density and scan area for each ion gun were set to the same values. All other experimental sputtering parameters as used during the AES depth profile with and without rotation are listed in Table 5.1. The measured Auger spectrum in AES depth profiling with and without rotation were recorded as a function of sputtering time for C (240-275 eV), O (480-529 eV), Ni & Cu (680-960 eV) and Si (1580-1649 eV).

5.2.3 Quantitative AES depth profile of Ni/Cu multilayer

The aim of sputter depth profiling is to determine the in-depth distribution of the elemental composition of the thin films. Firstly, the measured intensity of the Auger Peak-to-Peak Heights (APPHs) should be converted to the elemental fractional concentration. Since the whole range of Ni Auger peaks overlapped with the Cu peaks in the high energy peak for standard Auger spectra of pure Cu and Ni. The overlapped Ni 849 eV and Cu 922 eV peak was successfully separated utilising the weight function linear least square (LLS) method. For a detailed discussion of this method see chapter 4. After separating the overlapped peaks, the Auger peak of Cu (922 eV), Ni (849 eV), C (275 eV), O (510 eV) and Si (1618 eV) were used to determine the fractional concentration of Cu, Ni, C, O and Si, respectively. The atomic concentrations of Cu, Ni, C, O and Si, respectively, was calculated using the relative elemental sensitively factor method [26]:

$$X_i = \frac{I_i / I_i^0}{\sum_{j=i}^{n} I_j / I_j^0} \tag{5.1}$$

where I_i is the Auger electron intensity for element i (I_i as the Auger APPHs of element i in the differentiated spectrum – differentiation was performed with 9 point in this study) and I_i^0 is the Auger electron intensity for the pure element i (I_i^0 is the

relative sensitivity factor for element *i* at 10 keV from reference [26]). X_i is the measured fractional concentration of element *i* . (For this study *i* = Cu, Ni, C, O and Si).

Table 5.1: Summarised sputtering parameters as used in the AES depth profiles with and without sample rotation.

	Ion Beam energy, (keV)	Ion Beam current, (nA) *	Scan area, (mm^2)	Analysed area, (e-beam diameter, μm)	Incidence angle, ( )	Cu Sputter rate, (nm/min.)
Rotation	2 (Ar^+)	110.0	1 ×1	0.02	45	2.6
Single gun	2 (Ar^+)	44.1	2 ×2	9.2	40	5.9
Dual gun	2 (Ar^+)	63.0	2 ×2	9.2	40	7.6
Dual gun	1 (Ar^+)	30.8	2 ×2	9.2	40	3.3

* Ion beam current measured for Zalar rotation in PHI 700 without raster scanning, and the others measured in PHI 600 with raster scanning area 2 ×2 mm^2.

The sputter time scale of the AES depth profile data with and without rotation was converted into the sputter depth using a first-order approximation of a corrected time/depth relation for a Cu/Ni binary system. The sputter rates of the pure Cu and pure Ni are $\dot{z}_{Cu}$ and $\dot{z}_{Ni}$, respectively, using a linear approximation the corrected sputtering can be written as [1]:

$$\dot{z} = \dot{z}_{Cu} X_{Cu} + \dot{z}_{Ni} X_{Ni} = \dot{z}_{Cu} \left[\left(\frac{\dot{z}_{Ni}}{\dot{z}_{Cu}} - 1 \right) X_{Cu} + 1 \right] \tag{5.2}$$

where $\dot{z}$ is the total sputtering rate which determined the sputtering time/depth relation. The ratio of sputter rates of the pure Ni and pure Cu, $\dot{z}_{Ni}/\dot{z}_{Cu}$, was determined as 0.79 for 2 keV Ar^+ sputtering with an incident angle of 45 [27]. The film thickness of Ni/Cu multilayer was determined as 489.5 nm by AFM as shown in Fig. 5.2(a) and Fig. 5.2(b). The sputter rate of Cu under the different sputter conditions was calculated and the results are listed in the last column in Table 1. It should be noted that the ion beam current (the third column in Table 1) measured for Zalar rotation in PHI 700 was without raster scanning, and the others measured in PHI 600 were with a raster scanning area of 2 ×2 mm^2. The measured AES APPHs-sputter time and the converted

AES concentration-sputter depth profiling data for the as-deposited Cu/Ni multilayer with sample rotation are shown in Fig. 5.3(a) and Fig. 5.3(b), respectively. As shown in Figs. 5.3, C and O were not detected at the interface of Ni/Cu (or Cu/Ni) in the Ni/Cu multilayer thin films. C and O were only seen on surface layer that were in contact with air. It indicates that the as-deposited Ni/Cu multilayer thin film is a perfect sample for investigating sputtering induced roughness.

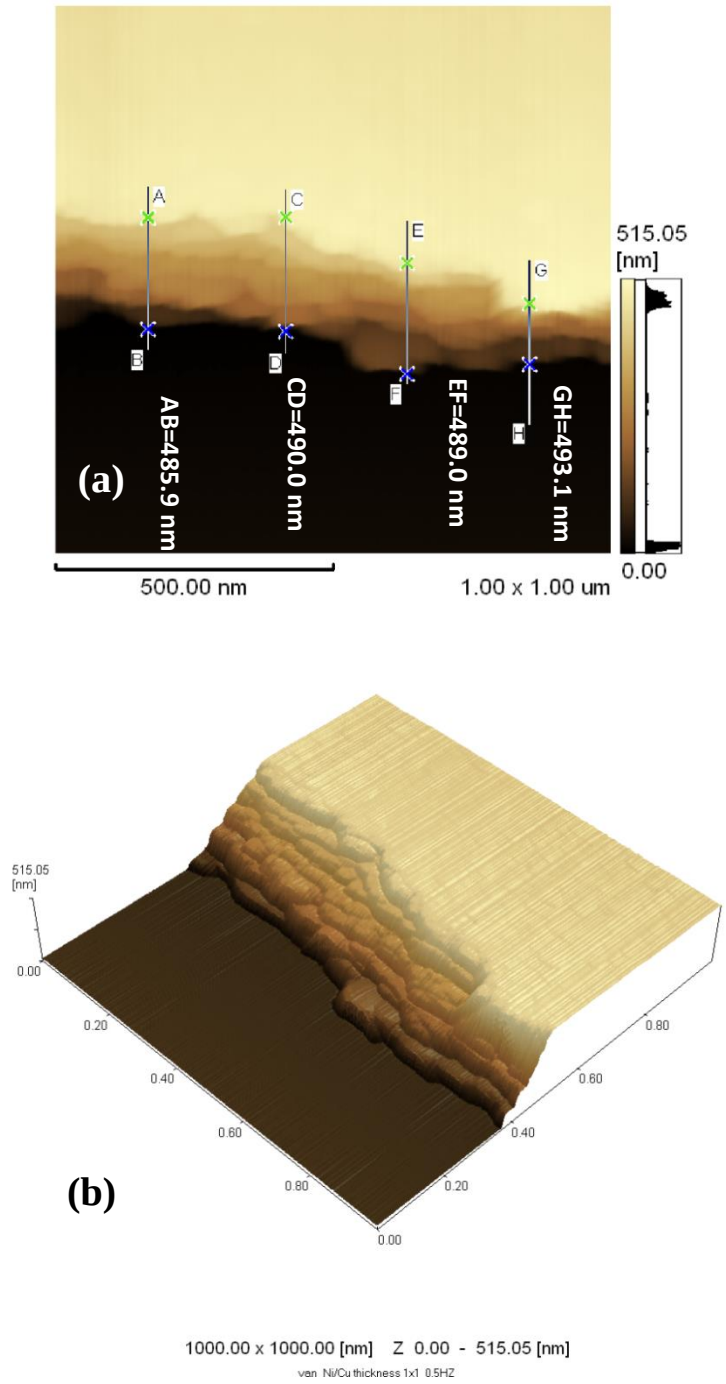

Figure 5.2: AFM images of the cross-section of the as-deposited Ni/Cu multilayer thin films 2D in (a) and 3D in (b), respectively. The average of the thickness values of Ni/Cu multilayer was determined as 489.5 nm.

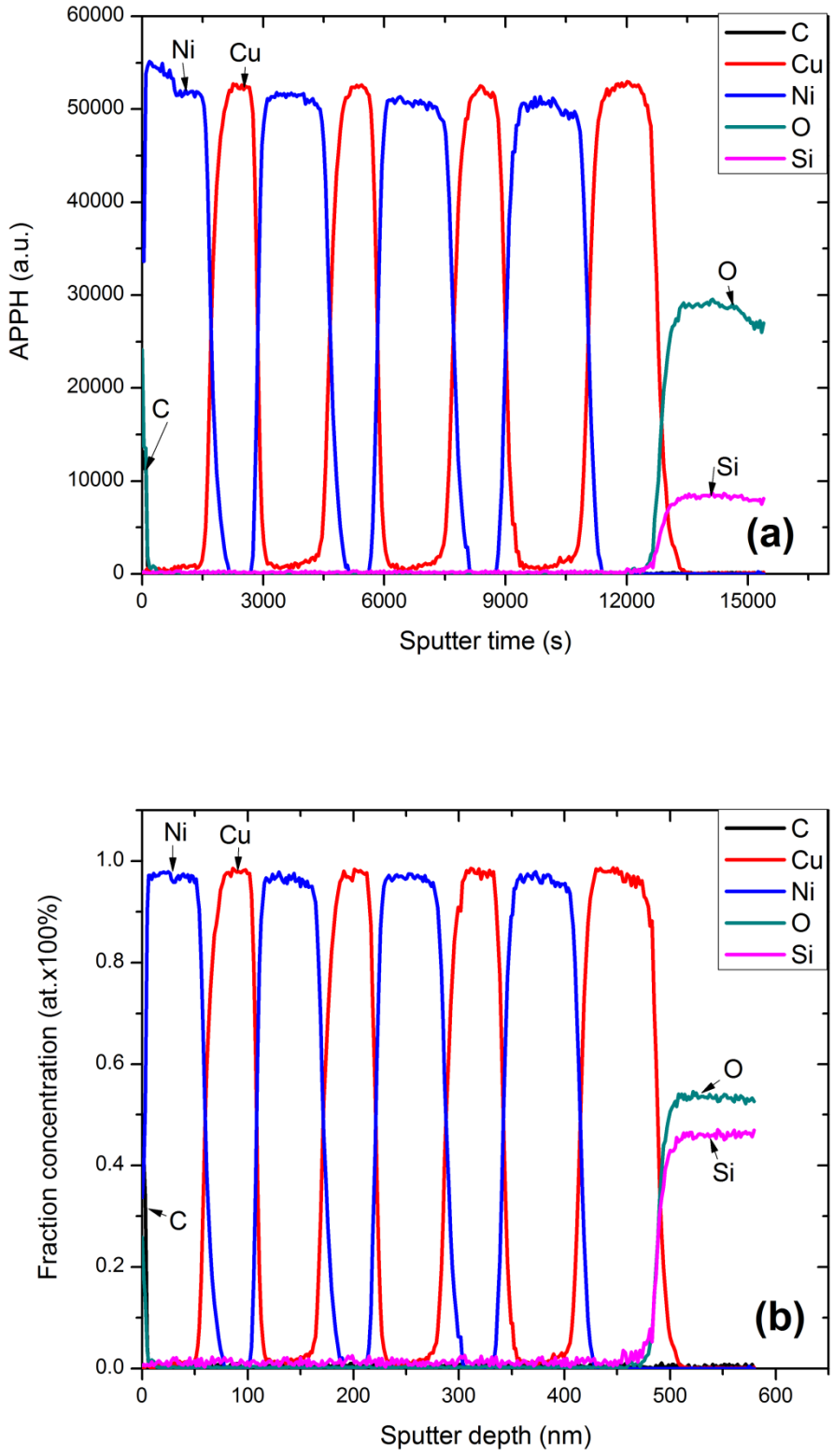

Figure 5.3: AES depth profiling measured of the as-deposited Ni/Cu multilayer thin films data with sample rotation 2 keV Ar^+ for (a) APPHs vs. sputter time and (b) converted to fractional concentration vs. sputter depth calculated with Eqs. 5.1 and 5.2.

5.3 Depth resolution and MRI model

The depth resolution Δz is defined conventionally as the depth range over which the signal change from 16 to 84% (or 84 to 16%) when profiling an ideally sharp interface between two media (see Fig. 5.4) [1]. This definition has a physical meaning for a Gaussian shape of the depth resolution function as shown in Fig. 5.4.

The measured depth profiles differ from the true concentration-depth profiles as a result of various interactions of the ion beam bombardment with the measured sample, e.g. ion implantation, cascade mixing, etc. A so-called depth resolution function (DRF) is used to describe the distortion of the measured depth profiles as compared to the true depth profiles, which causes the depth profiles degradation in the physical mechanism. In sputter depth profiling, the measured and normalized intensity $I(z)/I_o$ can be described as the convolution of the true concentration $X(z')$ at the original depth z' in the sample and a DRF $g(z-z')$ [1]:

$$\frac{I(z)}{I_0} = \int_0^\infty X(z')g(z-z')dz' \tag{5.3}$$

where z' is the running depth parameter for which the composition is defined and z is the sputtered depth. With the measured and normalized intensity $I(z)/I_o$ and a known DRF $g(z-z')$, the true in-depth distribution of composition can be calculated by Eq. 5.3. Therefore, the exact knowledge of the DRF is the key to accurate reconstruction of the original depth distribution of the composition from the measured depth profile. In the MRI model, the DRF $g(z-z')$ takes into account three physically meaningful effects: atomic mixing, escape depth of Auger electrons, surface/interface roughness and is described by [1, 28]:

Mixing length (w): $$g_w(z-z') = \frac{1}{w}\exp\left[-\left(z-z'+w\right)/w\right] \tag{5.4}$$

Roughness (σ): $$g_\sigma(z-z') = \frac{1}{\sqrt{2\pi}\sigma}\exp\left[-(z-z')^2/2\sigma^2\right] \tag{5.5}$$

Information depth (λ): $$g_\lambda(z-z') = \frac{1}{\lambda}\exp\left[-\left(z-z'\right)/\lambda\right] \tag{5.6}$$

where *w* is atomic mixing length, σ is the surface roughness and λ is the information depth parameter. With the above three partial resolution function (Eqs. 5.4, 5.5 and 5.6) depth resolution function g(z-z') can be written as:

$$g(z-z') = g_w(z-z') \otimes g_\sigma(z-z') \otimes g_\lambda(z-z') \tag{5.7}$$

In general, quantitative results of the MRI model are obtained by numerical solution of the convolution integral with combining Eq. 5.3 and Eq. 5.7.

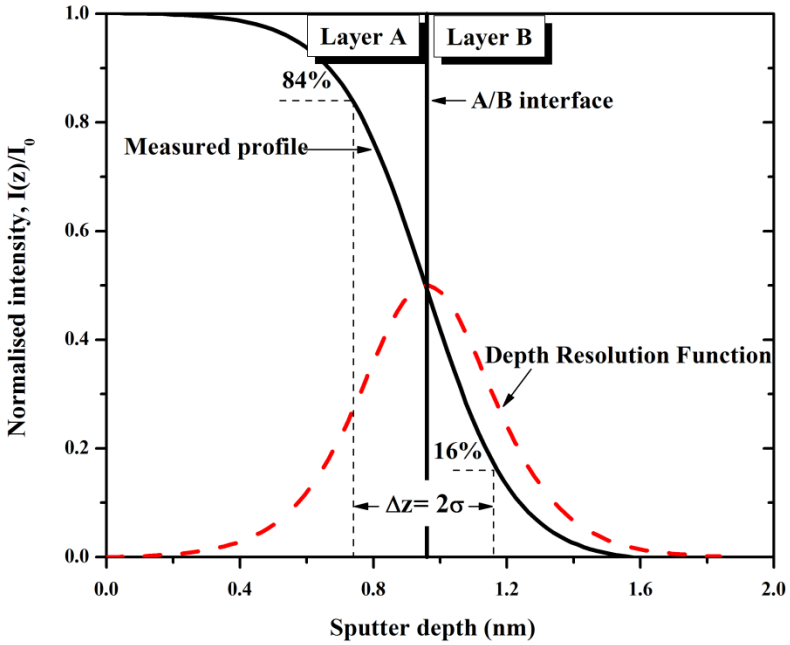

Figure 5.4: Schematic definition of the depth resolution, Δz (84-16%), at a sharp interface in the broadening profile and a Gaussian resolution function (red dashed line).

With respect to the above-discussed refinements of the DRF in terms of symmetric (Gaussian functions) and asymmetric (non-Gaussian functions), it is necessary to clarify the contribution to the depth resolution Δz (16-84%). According to the MRI model three physically meaningful effects contribute to the depth resolution function, the symmetric contribution to the depth resolution function originates from the intrinsic roughness and the surface roughening by ion sputtering, which both are described by a Gaussian smearing function (see Eq. 5.5), characterized by its standard deviation: the surface roughness parameter σ ($\Delta z_\sigma^2 = (2\sigma)^2 = (2\sigma_o)^2 + (2\sigma_s)^2$), where σ_o is the intrinsic roughness, σ_s is the sputter induced roughness. For the asymmetric

broadening functions, the atomic mixing is described by an exponential function (see Eq. 5.4) and this exponential function is characterized by the atomic mixing parameter w ($\Delta z_w = 1.668w$); the information depth of the Auger electrons (for AES) is also described by an exponential function (see Eq. 5.6) and this exponential function is characterized by the information depth parameter λ ($\Delta z_\lambda = 1.668\lambda$). These three parameters (σ, w and λ) are sufficient to characterize the total smearing, Δz (see Ref. [20]). Values for these three parameters may be obtained experimentally and/or calculated theoretically (see the section 5.4.1). Hence, on the basis of the MRI model fitting parameters, the total depth resolution can approximately be rewritten as [20]:

$$\Delta z = \left((2\sigma)^2 + (1.668w)^2 + (1.668\lambda)^2 \right)^{1/2} \tag{5.8}$$

with σ, w and λ in nm.

5.4 Results and discussion

5.4.1 AES depth profiling data reconstruction with MRI model

The Cu and Ni concentration-sputter depth profiling data of the as-deposited polycrystalline Ni/Cu multilayer thin films as measured by AES sputter depth profiling with 2 keV Ar^+ and using sample rotation are shown in Fig. 5.5(a) and Fig. 5.5(b), respectively, as open circles. The solid line in Fig. 5.5(a) represents the results of the fitting obtained with MRI model calculations by minimizing the least mean squares with a standard deviation of 5.6%. In the case of sample rotation the roughness parameter was taken as depth independence, a contribution of ion sputtering induced roughness is negligible [29]. The parameters λ was used as a known constants parameter in the fitting and the other two parameters w and σ_o were determined by MRI fitting the measured data. The Auger electron escape depth λ (effective attenuation length times cos(θ), where θ is the angle of emission of the detected electrons) for Cu (922 eV) and Ni (849 eV) were calculated as 1.1 nm and 1.0 nm, respectively, using the software of the NIST Database82 [30]. The fitted atomic mixing length of 1.6 nm agree very well the ion longitudinal range of 1.6 nm calculated using SRIM code [31] for an interface between the Cu and Ni sublayers

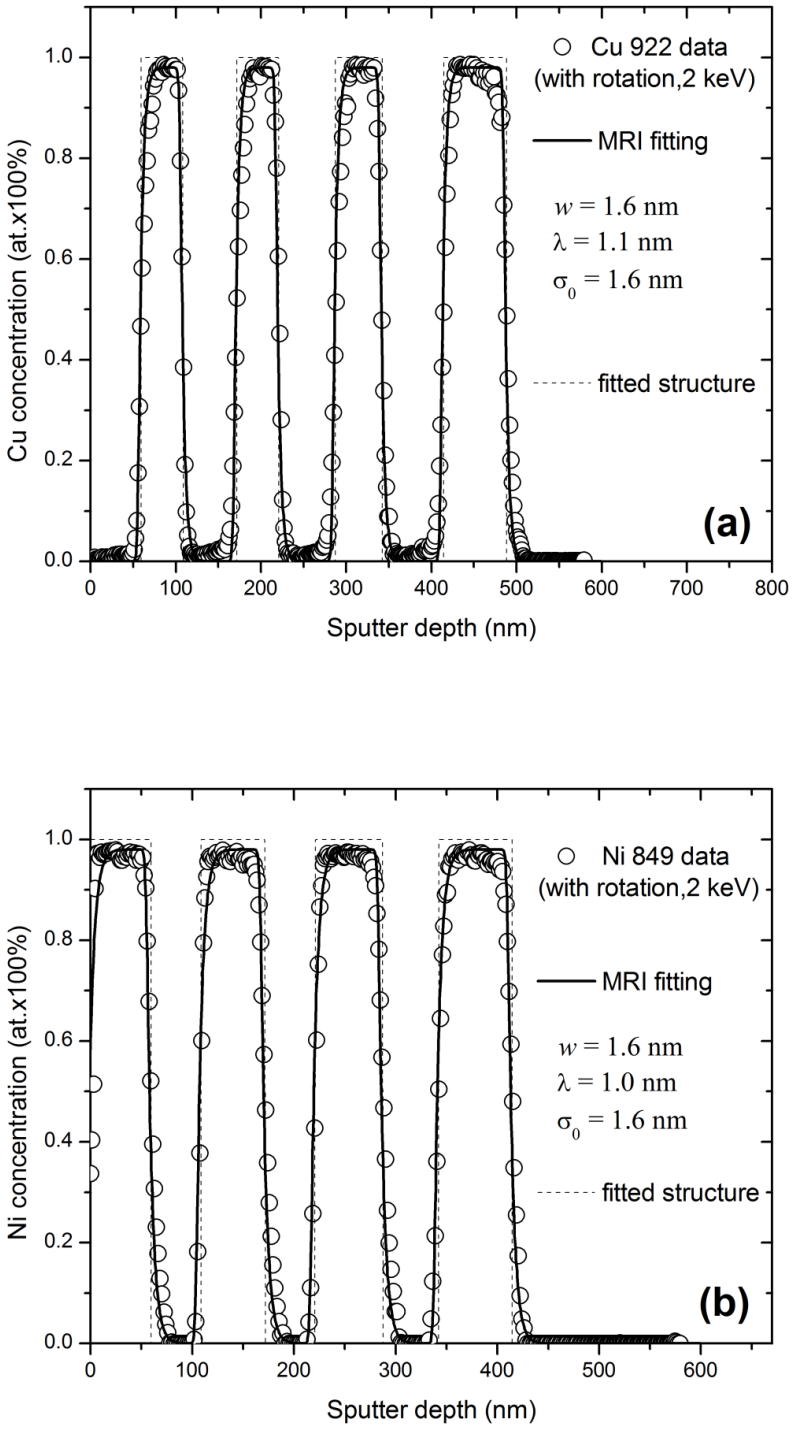

Figure 5.5: (a) The AES measured Cu concentration-depth profiling data (open circle) and (b) the measured Ni concentration-depth depth profiling data (open circle) with sample rotation 2 keV Ar^+ sputtering and the best fit to the measured data by the MRI model (solid line). Values for the atomic mixing parameter (w), the information depth of Auger electrons (λ) and the surface roughness (σ_o) are shown in (a) and (b). Dashed line represents the fitted Cu and Ni layered structure.

with 2 keV Ar^+ ions sputtered at an incident angle of 45° with respect to the normal. The value of the fitted roughness parameter in MRI model was obtained as σ_o = 1.6 nm, which was the same as the measured RMS *Rq* values of 1.6 nm by AFM on the surface of as-deposited Ni/Cu multilayer as shown in Fig. 5.6. It is noted that the Ni concentration-sputter depth profiling data could also be fitted well with the same MRI parameters *w* and σ_o by only changing the Auger electron escape depth λ for Ni (849 eV) to 1.0, as shown in Fig. 5.5(b) as solid line with a standard deviation of 4.6%. The fitted Cu and Ni layered structure as shown as dashed line in Fig. 5.5 can be regarded as the grown layered structure. Therefore, the thickness values of each Ni and Cu sublayer were obtained and are listed in Table 5.2.

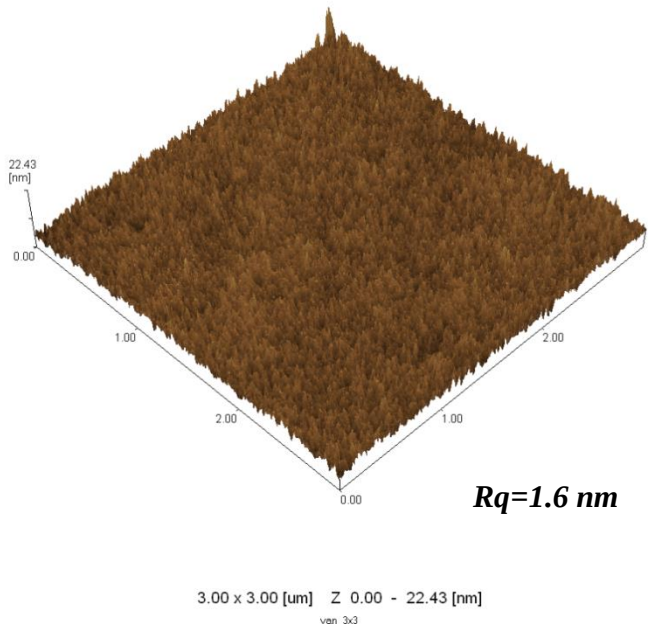

Figure 5.6: AFM images of the surface topography of the as-deposited Ni/Cu multilayer. The corresponding root mean square (RMS) *Rq* roughness value was determined as 1.6 nm.

The Cu concentration-sputter depth profiling data of the Ni/Cu multilayer thin films as measured by AES sputter depth profiling with a single ion gun 2 keV Ar^+ without rotation (stationary) are shown in Fig. 5.7(a), as open circles. A close examination of Fig. 5.7(a) revealed that the measured maximum/minimum value of each sublayer decreased/increased with the sputtered depth. This effect is related to the development of the ion bombardment induced roughness for polycrystalline material upon stationary depth profiling because of the dependence of the ion sputtering yield on the

orientation of the crystal. Indeed, X-ray diffraction measurements, performed in this study, indicated that the Ni and Cu films in Ni/Cu multilayer thin films were polycrystalline structure with a (111), (200) and (220) orientation texture (see Fig. 5.1). A significant effect of ion bombardment induced roughness does not occur if sample rotation is applied during the sputtering, as demonstrated in Figs. 5.5. The measured Cu depth profiling data was fitted with the MRI model (with the least mean squares method) and is shown as a solid line in Fig. 5.7(a). The roughness parameter σ is regards as a composition of initial roughness and the sputtering induced roughness [11, 32]. For simplicity, the sputtering induced roughness is assumed to be proportional to the sputtered depth for polycrystalline material upon stationary AES depth profile according to Seah and Lea [33]. Therefore, the total roughness could be descripted as $\sigma = \sigma_o + C*z$, where σ_o is the initial surface roughness, C is a constant and z is the sputtered depth. The atomic mixing length (w) and the information depth of Auger electrons (λ) were kept the same as for the sample that were rotated (see Fig. 5.5(a)) and only the linear depth dependence of the roughness (σ) was changed in the MRI model. The fitted standard deviation was 3.4% and the fitting parameters values are indicated in Fig. 5.7(a). The depth-dependent ion sputtering induced roughness (σ_s) can be calculated from the roughness values determined for the stationary (σ) and rotating (σ_o) samples with (see section 5.3):

$$\sigma_s = \sqrt{\sigma^2 - {\sigma_o}^2} \tag{5.9}$$

In order to investigate the influence of the dual-ion gun, depth profiling of the Ni/Cu multilayer thin films were performed by using dual ion guns with 2 keV Ar^+ without rotation (stationary).The measured Cu concentration depth profiling data (open circles) was shown in Fig. 5.7(b). Comparing it with the single ion gun data in Fig .5.7(a), it is clear that the last Cu sublayer appear broader with in single ion gun compared to the dual-ion gun. This means that dual-ion gun has a better depth resolution. It is noted that the measured maximum concentration value of the Cu in sublayer decreased with sputter depth see Fig. 5.7(b). The measured depth profiling data could be fitted well with MRI model by using a roughness parameter (σ) that increases linearly with sputter depth z. The fitted standard deviation was 4.4% and the fitted parameters are indicated in Fig. 5.7(b).

In order to investigate the influence of the sputtering ion energy on a depth profile, depth profile of Ni/Cu multilayer was performed using 1 keV Ar^+ dual-ion gun without rotation (stationary). The measured Cu concentration depth profiling data are shown in Fig. 5.7(c) as open circles. Again, in the absence of sample rotation, the measured maximum value of the Cu concentration of each sublayer decreased with sputter depth. Therefore, the measured depth profiling data was fitted (solid line in Fig. 5.7(c)) by the MRI model with assuming a roughness parameter (σ) that increases linearly with sputter depth z. The fitted result had standard deviation of 4.8% and the fitted parameters are indicated in Fig. 5.7(c).

The fitted Ni/Cu layered structures by the AES depth profiling with sample stationary (no rotation) by single ion gun (2 keV Ar^+) and dual symmetrical ion gun (2 and 1 keV Ar^+) sputtering are shown as dashed lines in Figs. 5.7(a), Figs. 5.7(b) and Figs. 5.7(c), respectively, and the corresponding thickness values of each Ni and Cu sublayer are listed in Table 5.2. The total film thickness values of Ni/Cu multilayer thin films calculated from Table 5.2 are 488.0 nm, 488.5 nm, 488.5 nm and 488.5 nm for sample rotation by ion gun 2 keV Ar^+ sputtering, sample stationary by dual ion gun 2 keV Ar^+ sputtering, and sample stationary by dual ion gun 1 keV Ar^+ sputtering, respectively. These values are very close to the values of 489.5 nm measured by AFM cross-section of the as-deposited Ni/Cu multilayer (see Fig. 5.2). The sample rotation one was performed with PHI 700 system and sample stationary (no rotation) performed with PHI 600 system. This may be the reason why the variation of thickness in the different Cu or Ni sublayers exists in the rotation and stationary (no rotation).

Table 5.2: The thickness values of the Ni and Cu sublayers and total multilayer determined by MRI fitting and AFM measurement.

Sublayer	Ni_1st (nm)	Cu_1st (nm)	Ni_2nd (nm)	Cu_2nd (nm)	Ni_3rd (nm)	Cu_3rd (nm)	Ni_4th (nm)	Cu_4th (nm)	Total (nm)
Rotation 2 keV	59.3	49.1	63.2	49.1	66.5	54.9	72.2	73.7	488.0
Single gun 2 keV	59.3	49.1	63.4	48.9	67.5	54.7	72.5	73.1	488.5
Dual gun 2 keV	59.3	49.1	63.4	48.9	67.5	54.7	72.5	73.1	488.5
Dual gun 1 keV	59.3	49.1	63.4	48.9	67.5	54.7	72.5	73.1	488.5
AFM									489.5

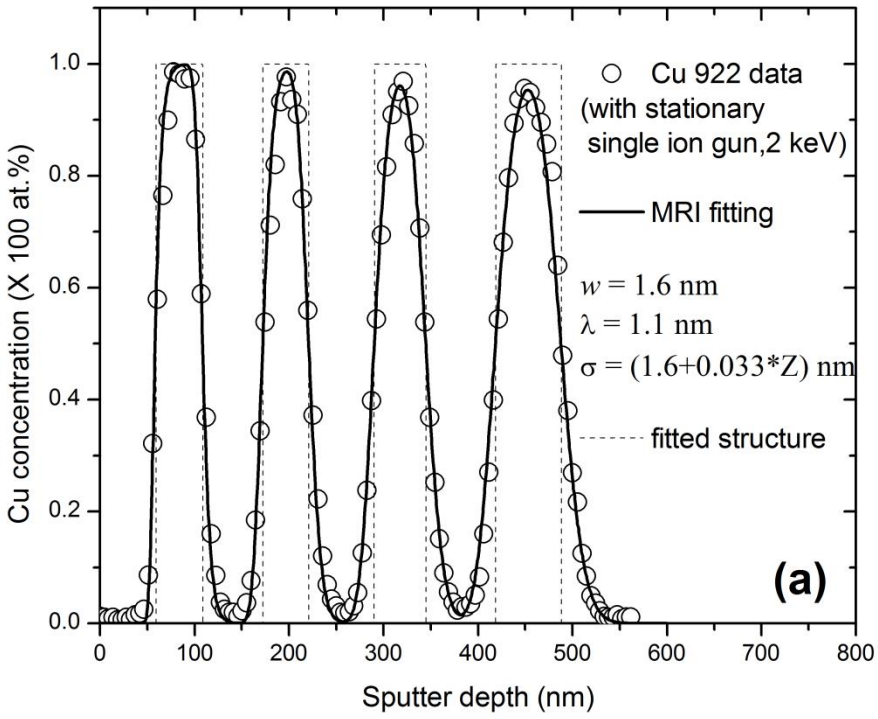

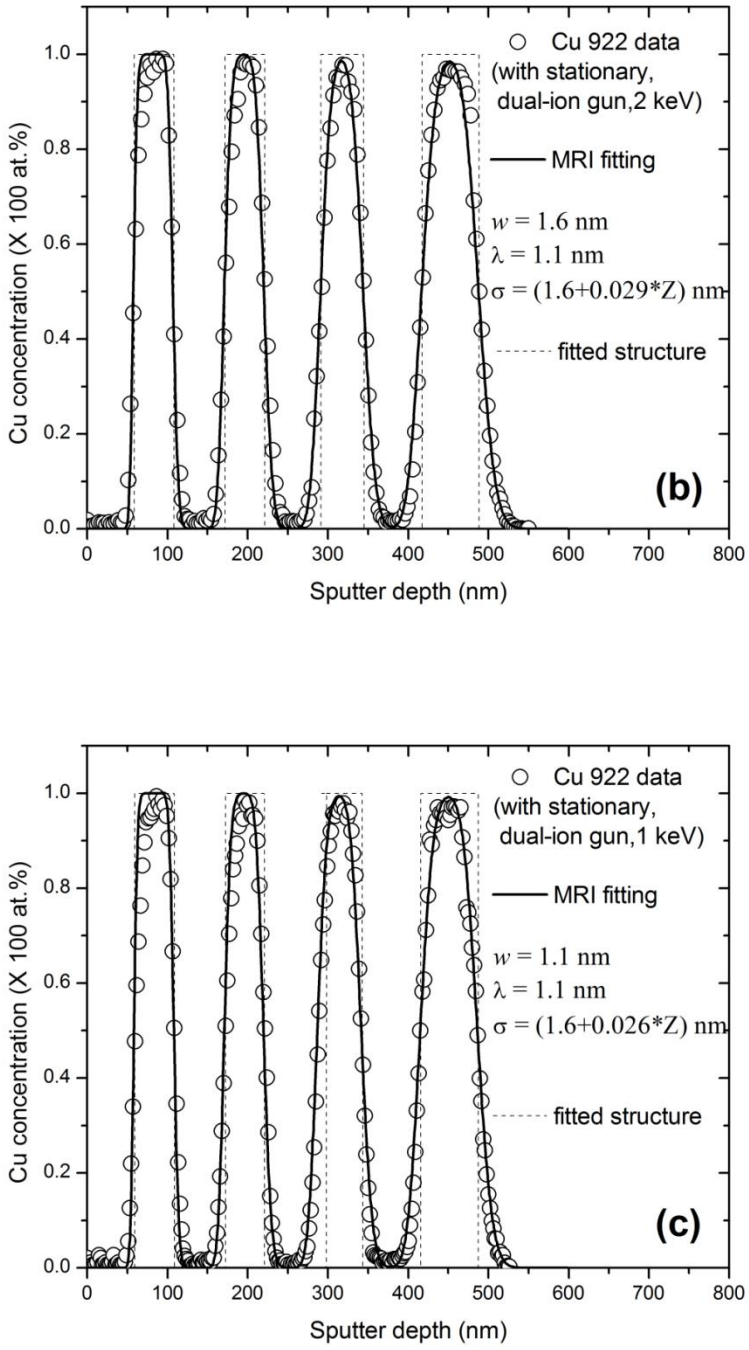

Figure 5.7: AES measured Cu concentration-depth profiling data (open circle) and the best fit to the measured data by the MRI model (solid line) for (a) sample stationary with single ion gun 2 keV Ar^+ sputtering, (b) sample stationary with dual ion gun 2 keV Ar^+ sputtering, and (c) sample stationary with dual ion gun 1 keV Ar^+ sputtering. Values for the atomic mixing parameter (w), the information depth of Auger electrons (λ_{Cu}) and the linear depth dependence of the surface roughness (σ) with the sputter depth z are shown in (a), (b) and (c). Dashed line represents the fitted Cu and Ni layered structure.

Table 5.3: Summarised MRI parameters for the best fit to the AES depth profiles with and without sample rotation.

MRI parameters	Mixing length, *w* (nm)	Auger electron depth information, λ (nm)	Surface roughness, σ (nm)
Rotation 2 keV (Ar^+)	1.6	1.1 (Cu 922 eV) 1.0 (Ni 849 eV)	1.6
Single gun 2 keV (Ar^+)	1.6	1.1 (Cu 922 eV)	1.6+0.033 ×z
Dual gun 2 keV (Ar^+)	1.6	1.1 (Cu 922 eV)	1.6+0.029 ×z
Dual gun 1 keV (Ar^+)	1.1	1.1 (Cu 922 eV)	1.6+0.026 ×z

5.4.2 The depth dependence of sputter-induced roughness and depth resolution

The MRI fitted parameters (Mixing length, *w*, depth information of Auger electron, λ and surface roughness, σ) values for the AES depth profiles with and without sample rotation are summarized in Table 5.3. With the fitted parameters in Table 5.3 the depth resolution Δ*z* can be calculated with Eq. 5.8 for a sample sputtered with a single ion gun (2 keV Ar^+) without rotation (stationary). The calculated depth resolution Δ*z* as a function of the sputter depth is shown in Fig. 5.8 as a solid line. The fitted roughness σ agrees very well with the *Rq* roughness values measured by AFM at *z* = 0 nm (the solid square denoted in Fig. 5.8) and its corresponding 2σ contribution in the depth resolution (see the first term of right side in Eq. 5.8) is presented in Fig. 5.8 as red colour dashed lines. The ion sputtering-induced roughness σ_s has been calculated using Eq. 5.9 as a function of sputter depth and its corresponding $2\sigma_s$ is also presented in Fig. 5.8 as blue colour dash-dot-doted lines. As is shown in Fig. 5.8, when the sputter depth increases, the values of ion sputtering-induced roughness $2\sigma_s$ is closer to the values of depth resolution Δ*z*. This result implies that the ion sputtering-induced roughness contribution was the dominant factor leading to the degradation the depth resolution with sputtered depth. It was also note that the MRI fitting roughness parameter σ_s = 18.0 nm at a depth of 489.5 nm was much larger than the two parameters *w* =1.6 nm and λ=1.1 nm. Similar result that the roughness increase with sputtered depth was observed for the polycrystalline Ni thin films

sputtered with 5 keV Ar^+ with an incidence angle of 45 °[12]. Wöhner et al. [34] have calculated the evolution of the surface roughness of the polycrystalline Al thin films with both depth distribution function and the angular distribution function in combination with using AFM images at different sputtered depths in AES depth profile with Ar^+ sputtering.

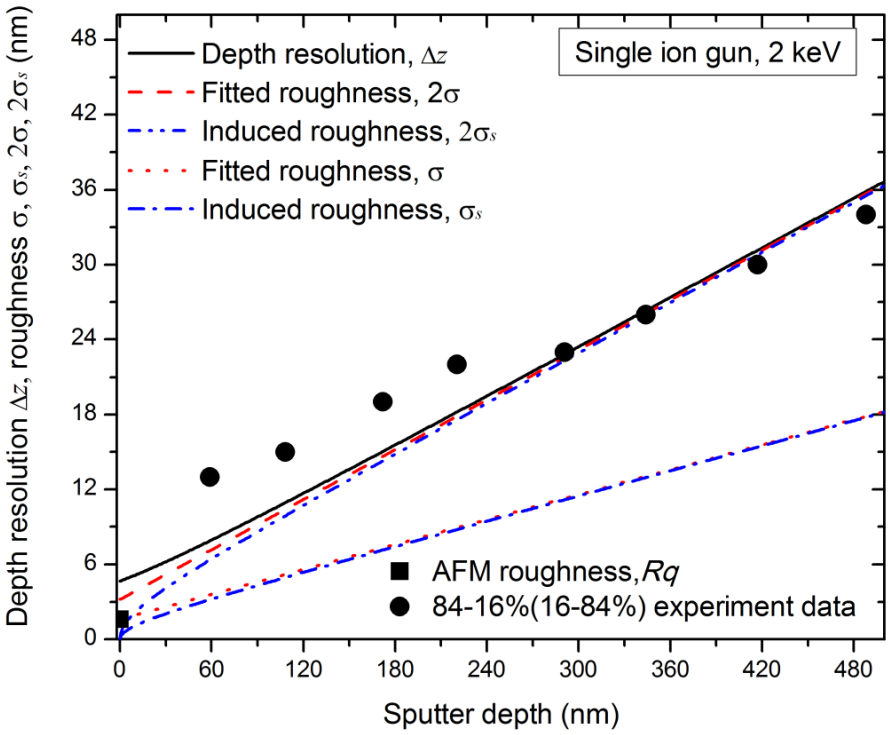

Figure 5.8: The depth resolution Δz and the fitted roughness parameter σ, 2σ and ion sputtering induced roughness σ_s, $2\sigma_s$ as a function of the sputter depth for the as-deposited sample with stationary by single ion gun with 2 keV Ar^+ sputtering. The closed circles and squares represent the values of the depth resolution by 84-16% (16-84%) method and the *Rq* roughness values determined by AFM (see Fig. 5.6), respectively.

In additional, the tendency of depth resolution in MRI calculation is in accordance with the experimental depth resolution extracted directly from the data with the 84-16% (16-84%) method. The experimental depth resolutions are shown as closed circles in Fig. 5.8. This conforms further the capability of the MRI model with the linear roughness in the Ni/Cu polycrystalline multilayer structure. The calculated Δz/2 value of 15.6 nm at the last Ni/Cu interface (corresponding to a depth of 414.3 nm) for the as-deposited sample is less than the thickness of the last sublayer Ni/Cu under present

measurement conditions.

The fitted roughness values (σ) and the calculated ion bombardment induced roughness values (σ_s) as a function with sputter depth are shown in the insert in Fig. 5.9. and Fig. 5.9 respectively, as determined for AES depth profiling performed with 2 keV Ar^+ ions sputtering with sample rotation, without sample rotation (stationary) and also for, single ion beam and with dual ion beam sputtering. The initial surface roughens seen in Fig. 5.9 the insert is 1.6 nm, which is comparable to the *Rq* roughness values (1.6 nm) measured by AFM (see Fig. 5.6). It can be seen in the Fig. 5.9 that the ion sputtering induced roughness for AES depth profiling measured with dual ion beam less than profiling with single ion beam. This can be explained in terms of shadowing and redisposition effects which are diminished wen using dual beam for sputtering. This result is similar to the findings of Hofmann and Zalar [35] that the use of a dual ion beam will improve the depth resolution of AES depth profiling for Ni/Cr multilayer on rough substrates.

The depth resolution (calculated with Eq. 5.9) of AES depth profiling also improve by lowering the sputtering energy, this can be seen in Fig. 5.10 where the 1 keV Ar^+ sputtering has a better depth resolution than the 2 keV Ar^+. This is can be explained in terms of the low atomic mixing length (w = 1.1 nm) when sputtering with 1 keV Ar^+ compared to larger atomic mixing length (w = 1.6 nm) when sputtering 2 keV Ar^+ sputtering. In addition, there is a lower the ion sputter induced surface roughness for the profiling sputtering with 1 keV Ar^+ compared to that profiling with 2 keV Ar^+ (see Fig. 5.9).

In general, AES depth profiling with sample rotation yields the best depth resolution (the lowest Δz values) because its ion sputtering induced roughness is the lowest. Profiling with dual-ion beams has a better depth resolution than sputtering with a single ion beam (see Fig. 5.10). The dual-ion cause less ion bombardment induced roughness. Profiling with less energetic has a better depth resolution (Fig. 5.10) because by decreasing the energy of the bombardment ions will reduce the atomic mixing length *w* (see Table 5.3).

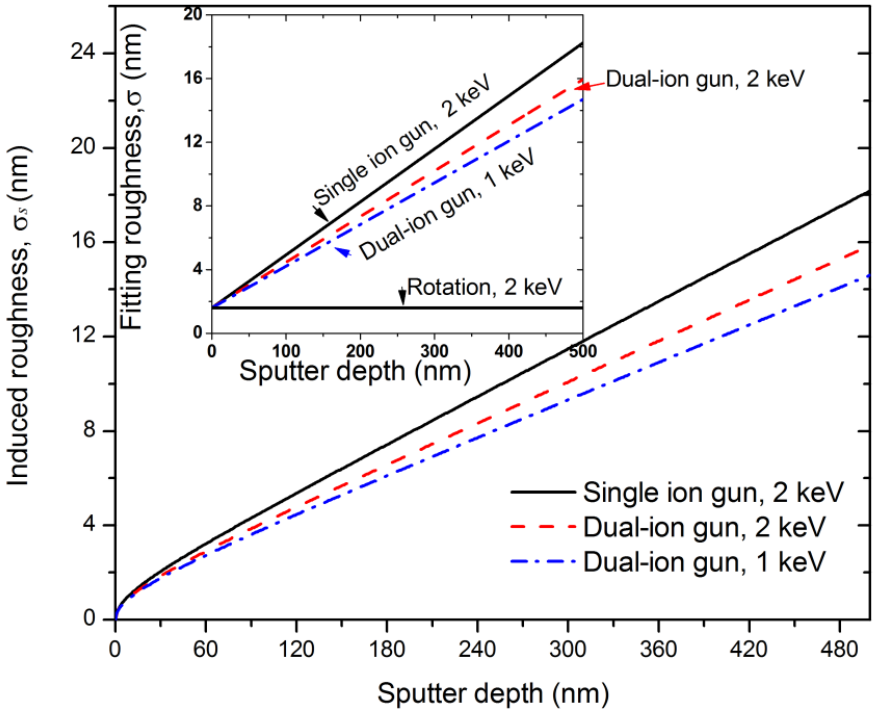

Figure 5.9: The ion sputtering induced roughness parameter σ_s as a function of the sputter depth for sample rotation with 2 keV Ar^+ ions sputtering and for sample stationary with single ion gun 2 keV Ar^+ sputtering and with dual ion gun 2 and 1 keV Ar^+ sputtering. Inset: the fitted roughness parameter σ.

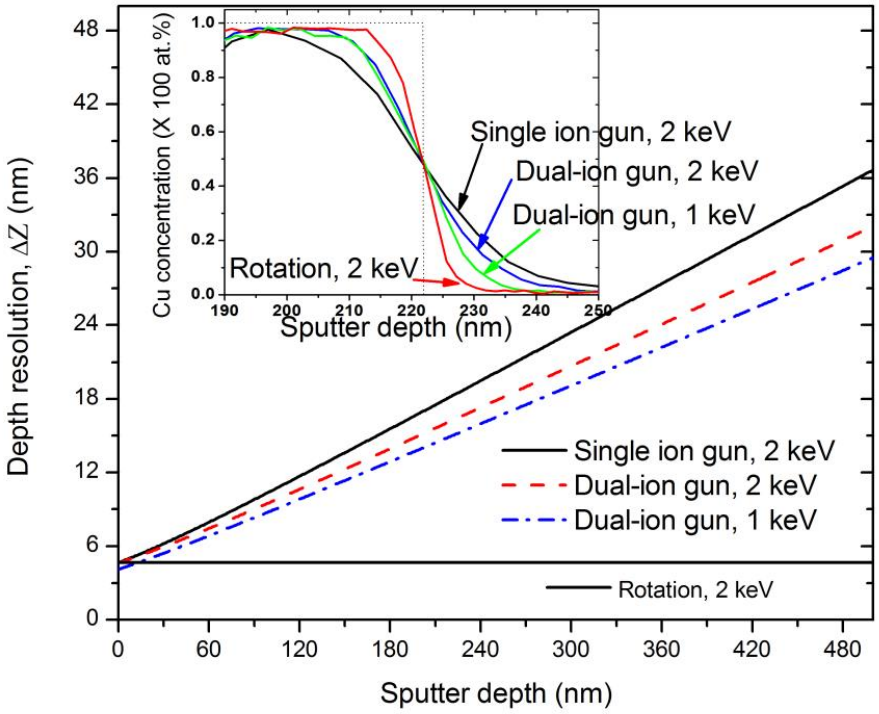

Figure 5.10: The depth resolution Δz a as a function of the sputter depth for sample rotation with 2 keV Ar^+ ions sputtering and for sample stationary with single ion gun 2 keV Ar^+ sputtering and with dual ion gun 2 and 1 keV Ar^+ sputtering. Inset: The enlarged view of the AES measured Cu depth profiling data of the second Cu/Ni interface corresponding to the measurement condition.

5.6 Summary

The as-deposited Ni/Cu polycrystalline multilayer thin films were characterized by AES depth profiling with sample rotation, without sample rotation (stationary), with single ion beam sputtering and dual ion beam sputtering. The measured concentration-depth profiles data were quantitative analysed with the MRI model assuming that the roughness parameter is linearly increasing with the sputtered depth. The roughness values extracted from the depth profiling data fits agreed well with those measured by AFM. It was concluded that the depth resolution is smaller when profiling with dual-ion beam vs. a single-ion beam. It was also found that profiling with a lower ion energy result in a better (smaller) depth resolution. Rotation of the sample during ion sputtering had the best (smallest) depth resolution steps of depth profiling reduces the ion bombardment induced roughness and avoids a depth dependence of the depth resolution.

References

[1] S. Hofmann, Chap. 7: Quantitative Compositional Depth Profiling, in Auger-and X-ray Photoelectron Spectroscopy in Materials Science, Springer Verlag Heidelberg, New York, Dordrecht, London 2013.

[2] J.Y. Wang, Y. Liu, S. Hofmann, J. Kovac, Influence of nonstationary atomic mixing on depth resolution in sputter depth profiling, Surf. Interface Anal. **44** (2012) 569-572.

[3] D.W. Moon, K.J. Kim, Surface topography development on ion beam sputtered surfaces: Role of surface inhomogeneity induced by ion-beam bombardment, J. Vac. Sci. Technol. A **14** (1996) 2744-2756.

[4] A. Barna, M. Menyhard, A. Zalar, P. Panjan, Ion bombardment induced interface broadening in Co/Cu system as a function of layer thickness, Appl. Surf. Sci. **242** (2005) 375-379.

[5] K.J. Kim, D.W. Moon, Significant improvement in depth resolution of Cr/Ni interfaces by secondary ion mass spectrometry profiling under normal O_2^+ ion bombardment, Appl. Phys. Lett. **60** (1992) 1178.

[6] T. Bungo, T. Nagatomi, Y. Takai, Dependence of depth resolution on primary energy of low-energy Ar^+ ions (100-1000 eV) in AES sputter depth profiling of GaAs/AlAs superlattice, Surf. Interface Anal. **38** (2006) 1598-1603.

[7] V. Micheli, N. Laidani, R. Bartali, G. Gottardi, M. Anderle, Interface effects study in hard-soft carbon multilayered films by AES depth profiling, Plasma Process. Polym. **4** (2007) S259-S264.

[8] W. Jian, Y. Liu, X.Y. Wang, S.P. Rao, S. Hofmann, J.Y. Wang, Quantification of AES depth profiling data of polycrystalline Al films with Gaussian and non-Gaussian surface height distributions, Surf. Interface Anal. **45** (2013) 1148-1151.

[9] Y. Liu, W. Jian, J.Y. Wang, S. Hofmann, J. Kovac, Influence of non-Gaussian roughness on sputter depth profiles, Appl. Surf. Sci. **276** (2013) 447-453.

[10] R.E. Galindo, L. Vázquez, Dynamics of GDOES-induced surface roughening in metal interfaces, Anal. Bioanal. Chem. **406** (2014)7483-7495.

[11] X.L. Yan, Y. Liu, H.C. Swart, J.Y. Wang, J.J. Terblans, Investigation of interdiffusion and depth resolution in Cu/Ni multilayer by means of AES depth profiling, Appl. Surf. Sci. **364** (2016) 567-572.

[12] T. Škereň, K. Temst, W. Vandervorst, A. Vantomme, Ion-induced roughening and ripple formation on polycrystalline metallic films, New J. Phys. **15** (2013) 093047.

[13] P.E. Hopkins, J.C. Duda, C.W. Petz, J.A. Floro, Controlling thermal conductance through quantum dot roughening at interfaces, Phys. Rev. B **84** (2011) 035438 .

[14] S.P. Dash, S. Sharma, J.C. Le Breton, J. Peiro, H. Jaffrès, J.M. George, A. Lemaître, R. Jansen, Spin precession and inverted Hanle effect in a semiconductor near a finite-roughness ferromagnetic interface, Phys. Rev. B **84** (2011) 054410 .

[15] I. Bakonyi, L. Péter, Electrodeposited multilayer films with giant magnetoresistance (GMR): progress and problems, Prog. Mater. Sci. **55** (2010) 107-245.

[16] A. Zalar, Improved depth resolution by sample rotation during Auger electron spectroscopy depth profiling, Thin Solid Films **124** (1985) 223-230.

[17] D.E. Sykes, D.D. Hall, R.E. Thurstans, J.M. Walls, Improved sputter-depth profiles using two ion guns, Appl. Surf. Sci. **5** (1980) 103-106.

[18] W. Pamler, K. Wangemann, S. Kampermann, W. Hosler, Depth resolution in Auger depth profile analysis of aluminum metallization in microelectronics: The effect of crystalline texture, Nucl. Instrum. Methods B **51**(1990)34-40.

[19] K. Wittmaak, D.B. Poker, Interface broadening in sputter depth profiling through alternating layers of isotopically purified silicon: I. Experimental results, Nucl. Instrum. Methods B **47** (1990) 224-235.

[20] J.Y. Wang, S. Hofmann, A. Zalar, E.J. Mittemeijer, Quantitative evaluation of sputtering induced surface roughness in depth profiling of polycrystalline multilayers using Auger electron spectroscopy, Thin Solid Films, **444** (2003) 120-124.

[21] R.M. Bradley, J.M.E. Harper, Theory of ripple topography induced by ion bombardment, J. Vac. Sci. Technol. A **6** (1988) 2390-2395.

[22] S. Park, B. Kahng, H. Jeong, A.L. Barabasi, Dynamics of ripple formation in sputter erosion: Nonlinear phenomena, Phys. Rev. Lett. **83** (1999)3486.

[23] M. Stepanova, S.K. Dew, I.P. Soshnikov, Sputtering from ion-beam-roughened Cu surfaces, Phys. Rev. B **66** (2002) 125407.

[24] T.C. Kim, C.M. Ghim, H.J. Kim, D.H. Kim, D.Y. Noh, N.D. Kim, J.W. Chung, J.S. Yang, Y.J. Chang, T.W. Noh, B. Kahng, J.S. Kim, Kinetic roughening of ion-sputtered Pd(001) surface: Beyond the Kuramoto-Sivashinsky model, Phys. Rev. Lett. **92** (2004) 246104.

[25] P. Sigmund, Theory of sputtering I: Sputtering yield of amorphous and polycrystalline targets, Phys. Rev. **184** (1969) 383.

[26] C.L. Hedberg, Handbook of Auger Electron spectroscopy, Third Edition, Physical Electronics Industries, Eden Prairie, MN, USA 1995.

[27] M.P. Seah, C.A. Clifford, F.M. Green, I.S. Gilmore, An accurate semi-empirical equation for sputtering yields I: For argon ions. Surf. Interface Anal. **37** (2005) 444-458.

[28] S. Hofmann, Sputter depth profile analysis of interfaces, Rep. Prog. Phys. **61** (1998) 827-888.

[29] J.Y. Wang, A. Zalar, E.J. Mittemeijer, Depth dependence of the ion bombardment induced roughness and of the interdiffusion coefficient for Si/Al multilayers, Appl. Surf. Sci. **222** (2004)171-179.

[30] C.J. Powell, A. Jablonski, 2011 NIST Electron Effective-Attenuation-Length Database, Version 1.3, Standard Reference Data Program Database 82.

[31] J.F. Ziegler, TRIM Code, IBM Corporation, Yorktown Heights, New York, (http://www.srim.org).

[32] H.L. Kang, J.B. Lao, Z.P. Li, W.Q. Yao, C. Liu, J.Y. Wang, Reconstruction of GaAs/AlAs supper lattice multilayer structure by quantification of AES and SIMS sputter depth profiles, Appl. Surf. Sci. **388** (2016) 584-588.

[33] M.P. Seah, C. Lea, Depth resolution in composition profiles by ion sputtering and surface analysis for single-layer and multilayer structures on real substrates, Thin Solid Films **81** (1981) 257-270.

[34] T. Wöhner, G. Ecke, H. Roessler, S. Hofmann, Sputtering-induced surface roughness of polycrystalline Al films and its influence on AES depth profiles, Surf. Interface Anal. **26** (1998) 1-8.

[35] S. Hofmann, A. Zalar, Depth resolution improvement in AES sputter profiling of Ni/Cr multilayers on rough substrates using two ion beams, Surf. Interface Anal. **10** (1987) 7-12.

Chapter 6
Depth dependence of the ion sputtering induced roughness and depth resolution of Ni/Cu multilayer thin films by ToF-SIMS depth profiling

6.1 Introduction

Time-of-flight secondary ion mass spectrometry (ToF-SIMS) is a powerful and sensitive surface analytical technique to determine detailed elemental and molecular information from a surface and/or interface of the sample, and give a full three-dimensional analysis. It is particularly useful in the depth profile analysis of thin films as analysis of the sputtered matter (secondary ions), which is different from the other types of the distinguished depth profile method of the analysis of the remaining surface, *i.e.* Auger electron spectroscopy (AES) and X-ray photoelectron spectroscopy (XPS) depth profiling. Compared with AES and XPS surface analysis method, the SIMS has some advantages: (i) detect ion of parts per million for most elements and even parts per billion atomic for certain elements; (ii) isotopes can be distinguished; (iii) chemical information can be obtained from relative ion abundances [1]. However, SIMS is also a destructive technique with ion beams sputtering where the surface constituent materials must be removed. For this case, ion beam sputtering induced the surface deformations, such as atomic mixing, radiation-induced diffusion, surface

segregation and surface roughness development, leads to affect the measured depth profiles [2-5]. Nowadays the surface topographic development during sputter depth profiling has been given considerable attention because it plays a key role in degradation of the depth resolution [2-6].

In the previous Chapter (Chapter 5) the MRI model was used to investigate the depth resolution of AES depth profiles and how it is effected by different experiment setups (sample rotation with single ion beam sputtering, no sample rotation with single ion beam sputtering, no sample rotation with dual ion beam sputtering and no sample rotation with single ion beam sputtering at different ion energies). In this chapter, the influence of the different ion source (O_2^+, Cs^+ and Xe^+) and different sputter ion energies will be investigated using ToF-SIMS depth profiling of polycrystalline Ni/Cu multilayer thin films (the same sample as AES as in Chapter 5). The measured depth profiles data were quantitative analysed with the MRI model to account for atomic mixing and surface roughness. The surface topography of the crater bottom after sputtering with different ion energy and at different sputter depth was measured with the AFM. The roughness values obtained from MRI model fitting will be compared with those measured by AFM. Ion sputtering induced roughness and depth resolution during the ToF-SIMS depth profiling of a polycrystalline Ni/Cu multilayer were evaluated according to the MRI model fitting parameters.

6.2 Experimental

6.2.1 ToF-SIMS depth profiling measurement

A detailed description of procedure used for the ToF-SIMS depth profiling measurement of the Ni/Cu multilayer thin films have been described in Chapter 4. The main points are summarized as follows: ToF-SIMS depth profiling measurements were performed by a ToF-SIMS V instrument (Munster, Germany) equipped with a Bismuth liquid metal ion gun and gas ion (O_2^+, Cs^+ or Xe^+) sputter gun. Both ion gun sources are at an angle of 45 ° with respect to the substrate surface. A 30 keV Bi^+ analysis beam generated by the liquid metal ion gun (LMIG) was used for analyse of a central area in the sputtering crater. The size of the analyse area was 100 ×100 μm^2 and analyse lateral resolution was 512 ×512 pixels. The target current of the analysis beam was maintained

as 1.4 pA before and after sputter. The ion source employed to etch through the sample was O_2^+ (with 0.5, 1.0 and 2.0 keV ion beam energy), Cs^+ (with 1.0 keV ion beam energy) and Xe^+ (with 1.0 keV ion beam energy). The raster-ring area was 300×300 μm^2, which is larger than the analyse area. The sputtering parameters as used in the ToF-SIMS depth profiling measurements are summarised in Table 6.1. To ensure accurate mass measurements of positive secondary ions the mass spectra were calibrated to the masses of H^+, CH^+, CH_2^+, Si^+, SiO^+, Cu^+, Ni^+, Cu_2^+, Ni_2^+, $CuCs^+$, $NiCs^+$, $CuCs_2^+$ and $NiCs_2^+$. The measured ToF-SIMS depth profile for Ni^+ (sputtering with O_2^+ and Xe^+) and $NiCs^+$ (sputtering with Cs^+) was used for the quantitative evaluation with the MRI model.

Table 6.1: Summarised sputtering parameters as used in the ToF-SIMS depth profiles with different ion species and energy.

Ion Beam energy, (keV)	Ion Beam current, (nA)	Scan area, (μm^2)	Analysed area, (μm^2)	Incidence angle, (ϑ)	Sputter rate, (nm/min.)
2.0 (O_2^+)	620.5	300×300	100×100	45	60.0
1.0 (O_2^+)	248.8	300×300	100×100	45	15.7
0.5 (O_2^+)	99.8	300×300	100×100	45	3.7
1.0 (Cs^+)	76.8	300×300	100×100	45	19.4
1.0 (Xe^+)	18.8	300×300	100×100	45	4.5

6.2.2 Crater roughness measurements

The roughness of the bottom of the sputter craters produced in Ni/Cu multilayer films was determined with Atom Force Microscope (AFM). Craters measuring 300×300 μm^2 were produced in Ni/Cu multilayer films by O_2^+ ion sputtering at the different energies (0.5, 1.0 and 2.0 keV) and stopped at the 3rd Ni surface and the SiO_2 surface. The center area of the crater bottom and original surfaces of the as-deposited Ni/Cu multilayer films were analysed with using a Shimadzu SPM-9600 AFM in contact model. All the AFM images of surface topography measurement were collected using the same AFM tip with scan area of 3×3 μm^2. The surface roughness is represented by the root mean square (RMS) value R_q of the as-deposited sample surface and after

sputtering in the air ambient condition.

6.2.3 Conversion of the SIMS intensity-sputter time profile into a normalized intensity-sputter depth profile

In order to apply the MRI model, the measured SIMS intensity- sputter time profiles were converted into normalised intensity- sputter depth profiles. The measured SIMS intensities was first corrected for instrument drift and then normalised. Instrument drift may occur during the long measuring times. The measured intensities can be corrected by dividing it with the total ions counted (for a particular mass spectrum):

$$I_i' = \frac{I_i}{\sum_{j=1}^{n} I_j} \tag{6.1}$$

where I_i is the measured the intensity, $\sum_{j=1}^{n} I_j$ is the total measured intensity which include all the second ions, I_i' is the corrected measured intensity of species i (For this study i = Ni^+ (sputtering with O_2^+ and Xe^+ ion) and $NiCs^+$ (sputtering with Cs^+ ion)). The corrected intensities of the Ni^+ and $NiCs^+$ were then normalized to the maximum corrected intensity in the profile recorded for the as-deposited Ni/Cu multilayer thin films. The sputter time of the ToF-SIMS measured depth profile was converted into the sputter depth by assuming a constant sputter rate of Cu and Ni. The film thickness of Ni/Cu multilayer was determined as 489.5 nm by AFM measurement as shown in Fig. 5.2 in Chapter 5. The average sputter rate for the different measuring conditions was calculated and is shown in Table 6.1 (the last column). For example, the intensity of $CuCs^+$ ($NiCs^+$, Si^+) in ToF-SIMS measured depth profile, sputtered with 1.0 keV Cs^+ ions (see in Fig. 6.1(a)) was also normalized to the maximum of the intensity of the as-deposited Ni/Cu multilayer thin film and the sputter time was also converted into the sputter depth by assuming a constant average sputter rate (Fig. 6.1(b)). A three-dimensional (3D) secondary ion images were reconstructed from the ToF-SIMS measured depth profiling data for the 1.0 keV Cs^+ sputtering (see in Fig. 6.1). The 3D reconstruction images of the 4 Ni layers and 4 Cu layers on the SiO_2

substrate are shown in Fig. 6.2. From the 3D images it is clear that the Cu and Ni are homogeneously distributed latterly in the Cu and Ni layers, respectively.

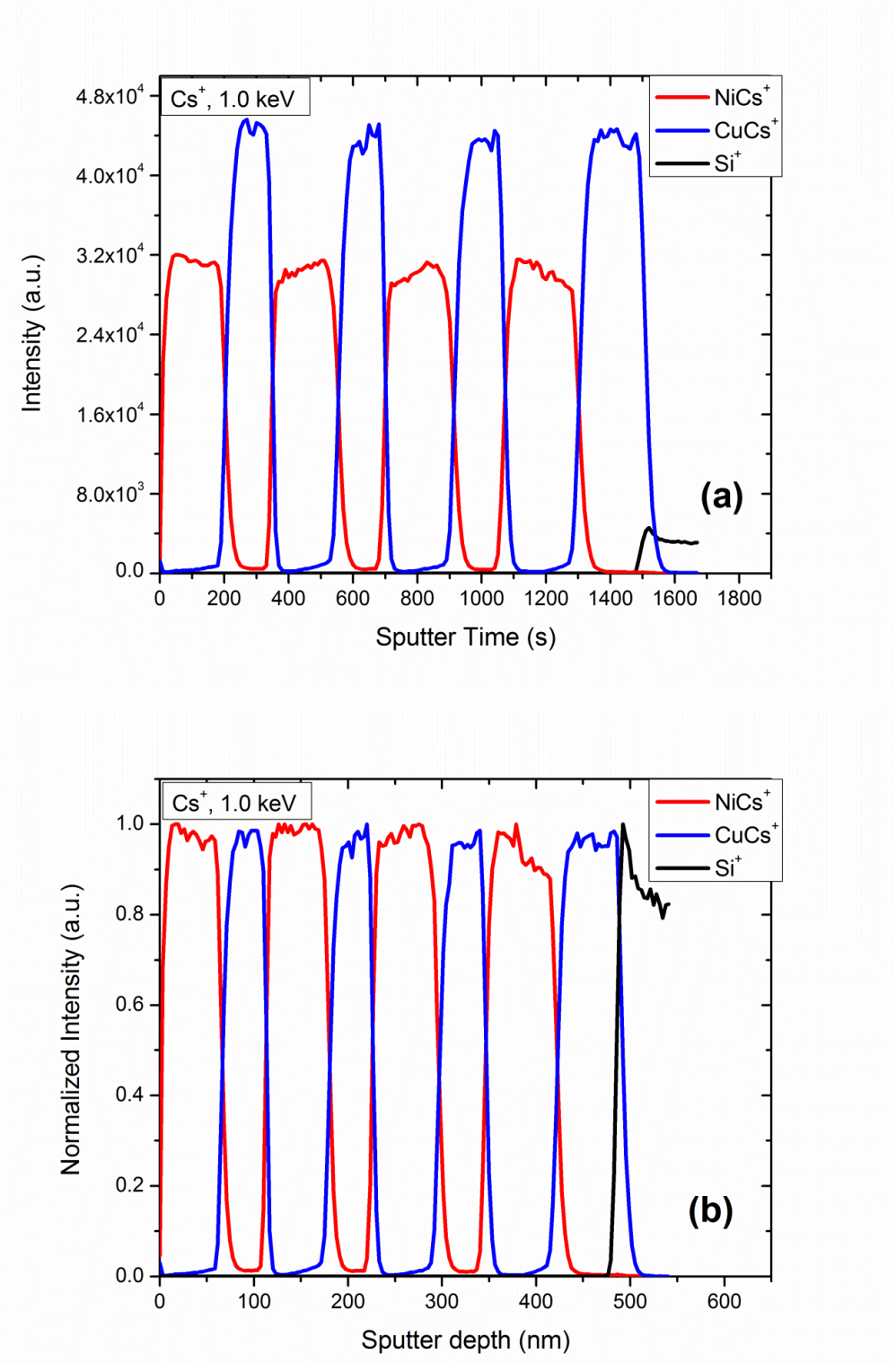

Figure 6.1: The ToF-SIMS depth profiling measured data of the as-deposited Ni/Cu multilayer thin films with 1.0 keV Cs^+ for (a) intensity vs. sputter time and (b) normalized intensity vs. sputter depth.

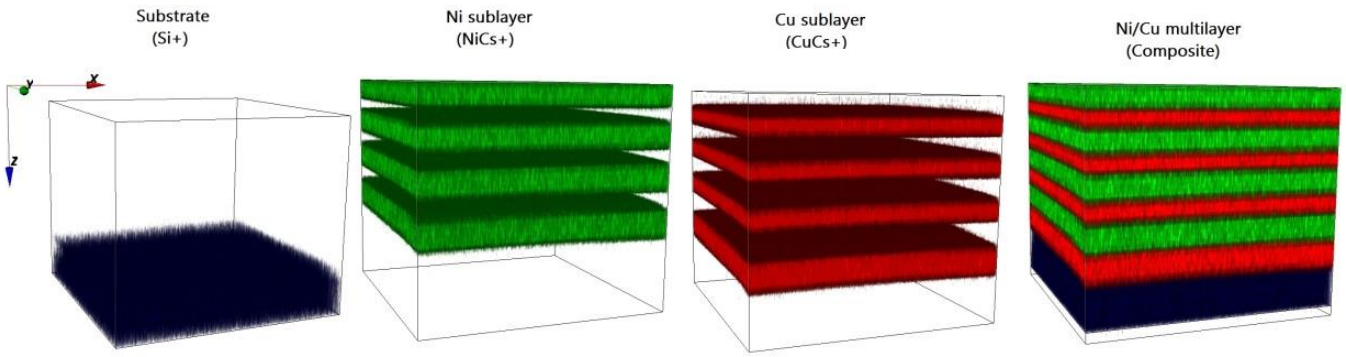

Figure 6.2: Reconstructed 3D image (300×300 μm^2) from a ToF-SIMS depth profile of the as-deposited Ni/Cu multilayer thin film. A 1.0 keV Cs^+ ion beam was used for bombardment and depth profiling data shown in Fig. 6.1.

6.3 Results and discussion

6.3.1 SIMS depth profiles under different energies O_2^+ ions sputtering

Fig. 6.3(a) shows the ToF-SIMS measured intensity depth profiling data of Ni^+, Cu^+ and SiO^+ positive ions obtained for the as-deposited Cu/Ni multilayer thin film with O_2^+ ion sputtering at the 1.0 keV without sample rotation. From the Fig. 6.3(a) it is clear that the maximum value of the Cu^+ intensity of the last (deepest) Cu sublayer is much higher than that of the other Cu sublayers. This is caused by the matrix effect caused by the deepest Cu sublayer near SiO_2 substrate layer (see AES depth profile data as shown in Fig. 5.3 in Chapter 5). This matrix effect in SIMS means a strong dependence of secondary ion emission on composition, in particular, the oxygen it can significantly influence the ionization yield of secondary metal ions sample [7]. In additional, the maximum of Ni^+ intensity in the first Ni sublayer shown in Fig. 6.3(a) is significantly lower than that of the other sublayers. This can be discussed as follows. By sputtering with the O_2^+ ions, the elements (including Ni, Cu and contamination) on the surface react with oxygen and form oxide compounds, such as carbon oxide, sodium oxide, nickel oxide, copper oxide and silicon oxide and so on. The nickel and copper formed small nickel oxide and copper oxide islands during the O_2^+ ions sputtering by the reaction of nickel and copper with oxygen. This have been observed with XPS for the Ni/Cr multilayer thin film under the O_2^+ ion sputtering by Moon and

Kim in Ref.[4]. However, a constant ion yield during O_2^+ ions sputtering will only occur after the contamination elements from the initial surface have been sputtered away and a stationary state has been reached. As a result that the Ni^+ intensity value for the first sublayer can be lower than that for the other sublayers. This result also can be found in Figs. 6.3(c) and 6.3(d) with O_2^+ ions sputtering but not in Fig. 6.1(a) with Cs^+ ions sputtering.

In order to examine the ion energy effect on a ToF-SIMS depth profile, depth profiles of Ni/Cu multilayer thin films were created using 2.0 keV, 1.0 keV and 0.5 keV O_2^+ ions in a ToF-SIMS. The normalized Ni^+ intensity- depth profiles data for 2.0 keV, 1.0 keV and 0.5 keV O_2^+ sputtering are plotted as open circles in Fig. 6.3(b), Fig. 6.3(c) and Fig. 6.3(d), respectively. By comparison is it is clear that for a particular depth profile there is a broadening of the Cu\Ni interfaces with depth. It is also clear the broadening is more severe for higher sputtering energies. To quantify the influence of the different sputter energies on a ToF-SIMS depth profile, the Ni^+ intensity of the depth profile were reconstructed with the MRI model. The MRI model was developed by Hofmann [8] and is one of the few models (the maximum entropy reconstruction based on the response function by Dowsett *et al* [9] and semi-empirical models considered atomic mixing and preferential sputtering by King *et al* [10]) describing the quality reconstruction of SIMS depth profiles. These models are all based on a so-called depth resolution function, which is used to describe the distortion of the measured depth profiles as compared to the true depth profiles. In the MRI model, the depth resolution function $g(z\text{-}z')$ can be taken into account three physically meaningful effects: (i) atomic mixing, (ii) surface/interface roughness and (iii) information depth. The three effects in the MRI model are described by [8, 11, 12]:

Mixing length (w): $$g_w(z-z') = \frac{1}{w}\exp\left[-\left(z-z'+w\right)/w\right] \tag{6.2}$$

Roughness (σ): $$g_\sigma(z-z') = \frac{1}{\sqrt{2\pi}\sigma}\exp\left[-(z-z')^2/2\sigma^2\right] \tag{6.3}$$

Information depth (λ): $$g_\lambda(z-z') = \frac{1}{\lambda}\exp\left[-\left(z-z'\right)/\lambda\right] \tag{6.4}$$

where z is the sputtered depth and z' is the running depth parameter, w is atomic mixing length, σ is the surface roughness and λ is the information depth parameter. With the above three partial resolution function (Eqs. 6.2, 6.3 and 6.4) depth resolution function $g(z-z')$ can be written as:

$$g(z-z') = g_w(z-z') \otimes g_\sigma(z-z') \otimes g_\lambda(z-z') \tag{6.5}$$

In sputter depth profiling, the measured and normalized intensity $I(z)/I_o$ can be described as the convolution of the true concentration $X(z')$ at the original depth z' in the sample and a depth resolution function $g(z-z')$ (Eq. 6.5) [12]:

$$\frac{I(z)}{I^0} = \int_0^\infty X(z')g(z-z')dz' \tag{6.6}$$

If the original in depth distribution of composition is known, like here, these three parameters in MRI model can be obtained by optimization of profile fitting with numerical solution of the convolution integral with combining Eq. 6.5 and Eq. 6.6.

A close examination of Fig. 6.3(b), Fig. 6.3(c) and Fig. 6.3(d), it was found that the measured maximum/minimum value of the 2^{nd}-4^{th} Ni sublayer decreased/increased with the sputtered depth. This effect is related to the development of the ion sputtering induced roughness (σ_s) for polycrystalline material upon stationary depth profiling due to the dependence of ion sputtering yield on the orientation of the crystal. In fact, the Ni/Cu multilayer thin films studied in this chapter were polycrystalline structure with a (111), (200) and (220) orientation texture (shown by XRD data in Fig. 5.1 in Chapter 5). Consequently, the roughness parameter σ is regarded as a composition of initial roughness and the sputtering induced roughness [13, 14]. For simplicity, the sputtering induced roughness was assumed to be proportional to the sputtered depth for polycrystalline material upon stationary depth profiling according to Seah and Lea [15]. Therefore, the total roughness could be written as

$$\sigma = \sigma_0 + Cz, \tag{6.7}$$

where σ_o is the initial surface roughness, C is a constant and z is the sputtered depth.

The information depth parameter (λ) in MRI model fitting can be set to zero for SIMS due to the SIMS analysis of the sputtered matter (secondary ions) [14]. The atomic mixing length (w) and the linear depth dependence of the roughness (σ) was used to fit the SIMS measured depth profile data with the MRI model. The solid line in Fig. 6.3(b-d) represents the best fit to the measured data by the MRI model. The fitting values for the atomic mixing parameter (w), the information depth (λ) and the surface roughness (σ) are indicated in Fig. 6.3(b-d) and is also listed in Table 6.2. The fitted standard deviation was about 5% as is shown in the last column of Table 6.2.

Based on the above discussion, the depth-dependent ion sputtering induced roughness (σ_s) can be calculated from the fitting roughness (σ) for a stationary sample sputtering (no rotation) with an initial surface roughness (σ_o) [16]:

$$\sigma_s = \sqrt{\sigma^2 - {\sigma_o}^2} \tag{6.8}$$

The calculation results of the sputtering induced surface roughness σ_s are discussed further in the next section.

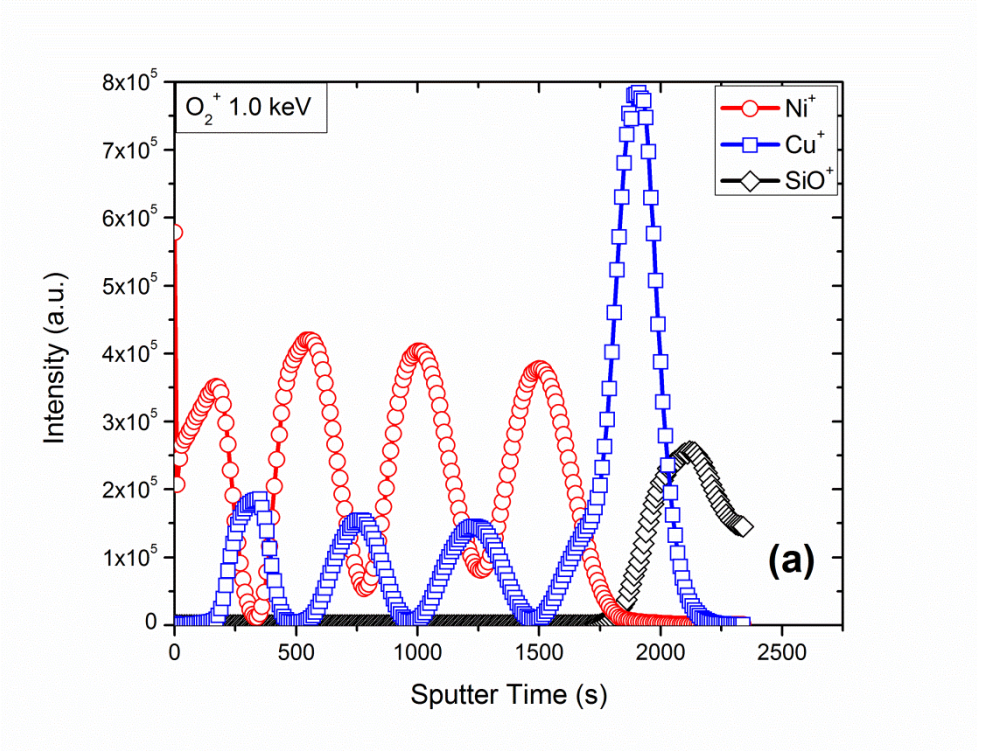
O_2^+ 1.0 keV
Ni^+
Cu^+
SiO^+
(a)
Intensity (a.u.)
Sputter Time (s)
8x10^5
7x10^5
6x10^5
5x10^5
4x10^5
3x10^5
2x10^5
1x10^5
0
0
500
1000
1500
2000
2500

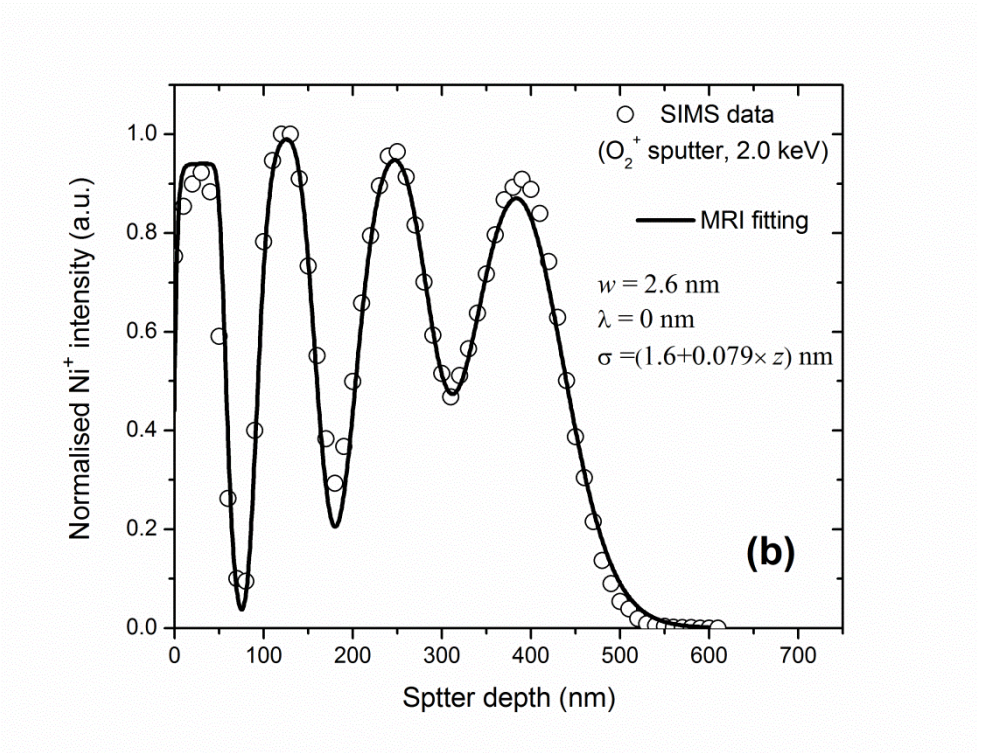
SIMS data
(O_2^+ sputter, 2.0 keV)
MRI fitting
w = 2.6 nm
λ = 0 nm
σ =(1.6+0.079× z) nm
(b)
Normalised Ni^+ intensity (a.u.)
Sptter depth (nm)
1.0
0.8
0.6
0.4
0.2
0.0
0
100
200
300
400
500
600
700

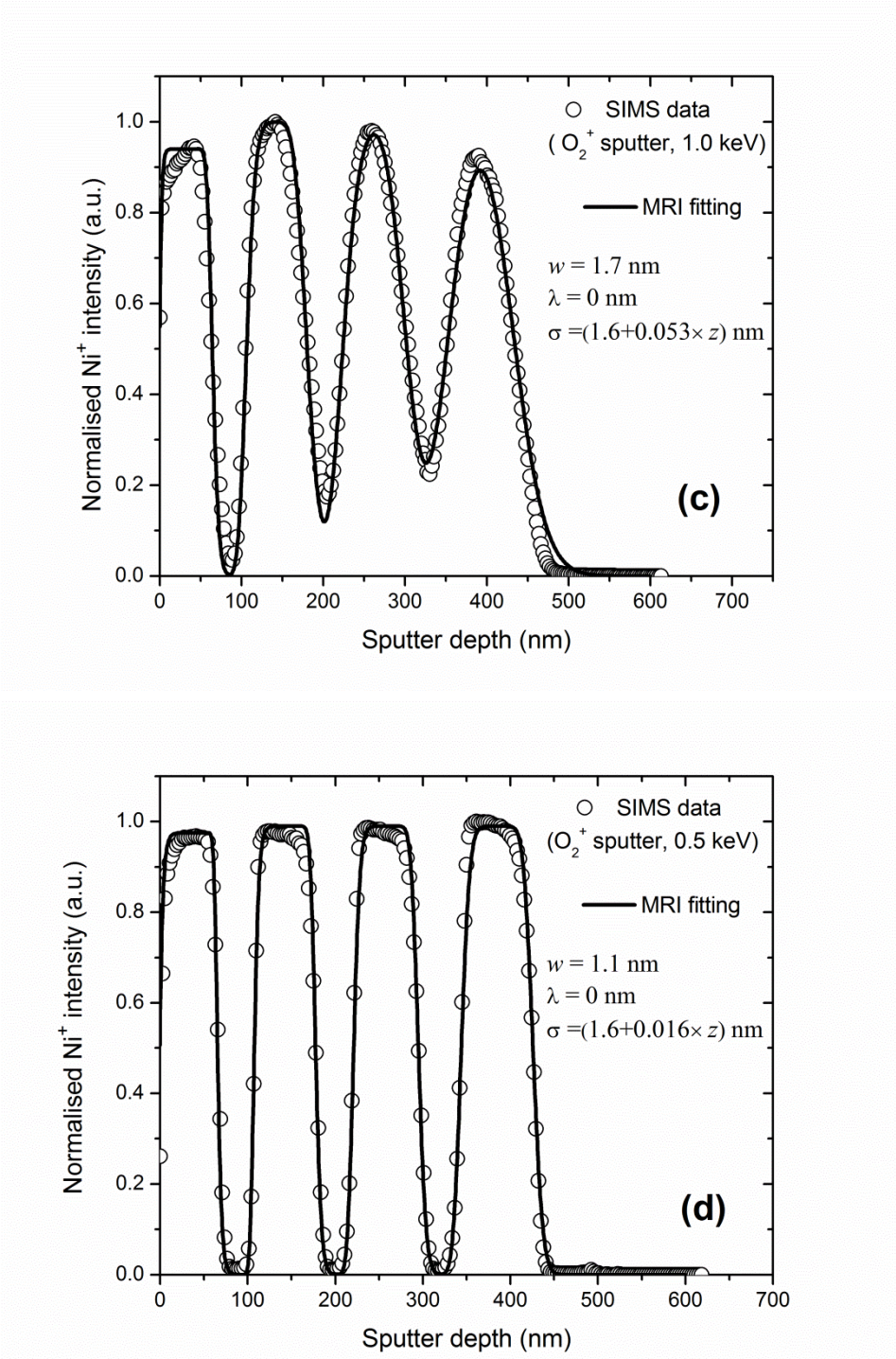

Figure 6.3: (a) The measured intensity-sputter time data of as-deposited Cu/Ni multilayer thin films obtained by ToF-SIMS depth profiling with 1.0 keV O_2^+. The normalized Ni^+ intensity-sputter depth profiling data (open circle) obtained by ToF-SIMS depth profiling with 2.0 keV O_2^+ in (b), 1.0 keV O_2^+ in (c) and 0.5 keV O_2^+ in (d). The solid line in Fig. 6.3(b), (c) and (d) represent the best fit to the measured data by the MRI model and the fitted values for the atomic mixing parameter (*w*), the information depth (λ) and the surface roughness (σ) are indicated in Fig. 6.3(b), (c) and (d).

Table 6.2: Summarized MRI parameters for the best fit to the ToF-SIMS depth profiling data obtained with O_2^+ ion sputtering at different ions energies (2.0, 1.0 and 0.5 keV).

MRI parameters	Mixing length, *w* (nm)	information depth, λ (nm)	Surface roughness, σ (nm)	Standard deviation (at.%)
2.0 (O_2^+)	2.6	0	1.6+0.079 ×z	4.1
1.0 (O_2^+)	1.7	0	1.6+0.053 ×z	4.2
0.5 (O_2^+)	1.1	0	1.6+0.016 ×z	5.0
AES Rotation	1.6	1.0 (Ni 849 eV)	1.6	5.4

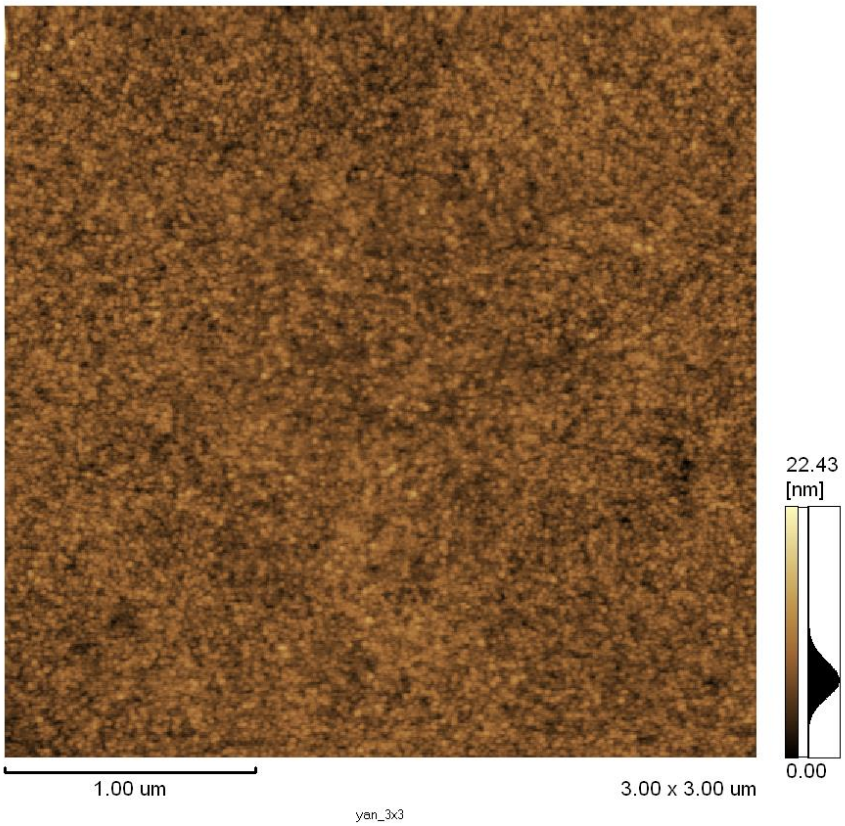

Figure 6.4: AFM images of the surface topography of the as-deposited Ni/Cu multilayer thin films. The corresponding RMS R_q roughness value was determined as 1.6 nm.

It is well-known that the depth resolution in SIMS depth profile is invariably limited by effects such as surface roughening and atomic mixing. [2-5] In order to understand the influence of the surface roughness development with the different energies O_2^+ ions bombardment for Ni/Cu multilayer, the roughness of the bottom of the sputter craters produced in Ni/Cu multilayer was measured with AFM. Craters measuring 300×300 μm^2 were produced in Ni/Cu multilayer by O_2^+ ion bombardment at the different energies (2.0, 1.0 and 0.5 keV) and stopped at the 3rd Ni surface and the SiO_2 surface. The images shown in Fig. 6.5 are AFM topographical images ($3\times3\mu m^2$) recorded inside the sputtered crater of the as-deposited Ni/Cu multilayer thin films were sputtered by O_2^+ ions with energy of 0.5, 1.0 and 2.0 keV. The images on the left are recorded at a sputtering depth of 222 nm (the surface of 3rd Ni sublayer) and the one on the right are 490 nm (SiO_2 surface) corresponding to the depth profiles in Fig. 6.3. On comparing no microstructures at the surface of the as-deposited sample before sputtering (shown in Fig. 6.4.), it was found that small particles type topographies begin to be formed at the sputtering depth of 222 nm (the surface of 3rd Ni sublayer) with 0.5 keV O_2^+ ion sputtering in Fig. 6.5(a). The sizes of the particles increase with further sputtering depth of 490 nm (SiO_2 surface) as shown in Fig. 6.5(b). In additional, the sizes of the particles increase with higher energies sputtering as shown in Fig. 6.5(c) and Fig. 6.5(e). It should be noted that the shape of the terraces is clearer at the deeper depth with higher energy O_2^+ ion sputtering and the sizes also increase with sputter depth in Fig. 6.5(d) and Fig. 6.5(f). The roughness RMS values R_q are also shown in Fig. 6.5 and it clear that the roughness increase with sputtered depth and it also increasing with sputtering energy. The AFM results are in agreement with the measured SIMS depth profiling data in Fig. 6.3, indicating that the roughening of the surface broadens the SIMS Ni^+ layer at deeper depth and high bombardment energy. This clearly shows that surface roughening is a direct cause for the degradation in the SIMS depth profiles. The degradation in the SIMS depth profile may also be affected by the atomic mixing apart from the change in topography. Similar result that the roughness increase with sputtered depth was observed with AFM and SIMS depth profiles for a Si/SiGe heterostructure multilayer thin film [2]. Fares *et al*. [6] have studied the evolution of the surface roughness as a function of sputter depth of the boron δ-doped Si thin films with using AFM and SIMS depth profiles sputtered with 0.5 and 1.0 keV O_2^+ at an incidence angle of 44 °(54 °).

In order to understand the influence of the atomic mixing at the different primary energies O_2^+ ions bombardment for Ni/Cu multilayer, SRIM simulations [17] were carried out with the different energies of (0.5, 1.0 and 2.0 keV) O_2^+ ion beam irradiation of three layers (3 nm Ni / 3 nm Cu / 3 nm Ni) at an incident angle of 45° with respect to the surface normal. The simulation results show that the number of vacancies per ion created by O_2^+ ions increases with 12.8, 26.0 and 51.1 when primary energy increase with 0.5, 1.0 and 2.0 keV, respectively. These numbers are related to both the sputter yields from the surface as well as to the transmission and atomic mixing at the interfaces. The calculated sputter yield of Ni for O_2^+ increases with 2.2, 3.4 and 4.6 at/ion. These results correspond with the average sputtering rates of 3.7, 15.7 and 60.0 nm/min. for sputtering energies of 0.5, 1.0 and 2.0 keV, respectively (see in the last column in Table 6.1). The simulation results shows the amount number of the Ni atomic layer mixing in Cu layer target increase with the sputter energy from 0.5 keV to 2.0 keV with O_2^+ ions bombardment. And the values of mixing length with ion longitudinal range are 1.0, 1.6 and 2.5 nm at the interface between the Ni and Cu sublayers with 0.5, 1.0 and 2.0 keV O_2^+ ions, respectively. And these results are much closed with the atomic mixing length parameters determined by MRI fitting as shown in Table 6.3.

Table 6.3: Summarized the atomic mixing length parameters determined by MRI fitting and SRIM simulation at different ion primary energy 0.5, 1.0 and 2.0 keV.

Ion primary energy (keV)	0.5 (O_2^+)	1.0 (O_2^+)	2.0 (O_2^+)
MRI fitting (nm)	1.1	1.7	2.6
SRIM simulation (nm)	1.0	1.6	2.5

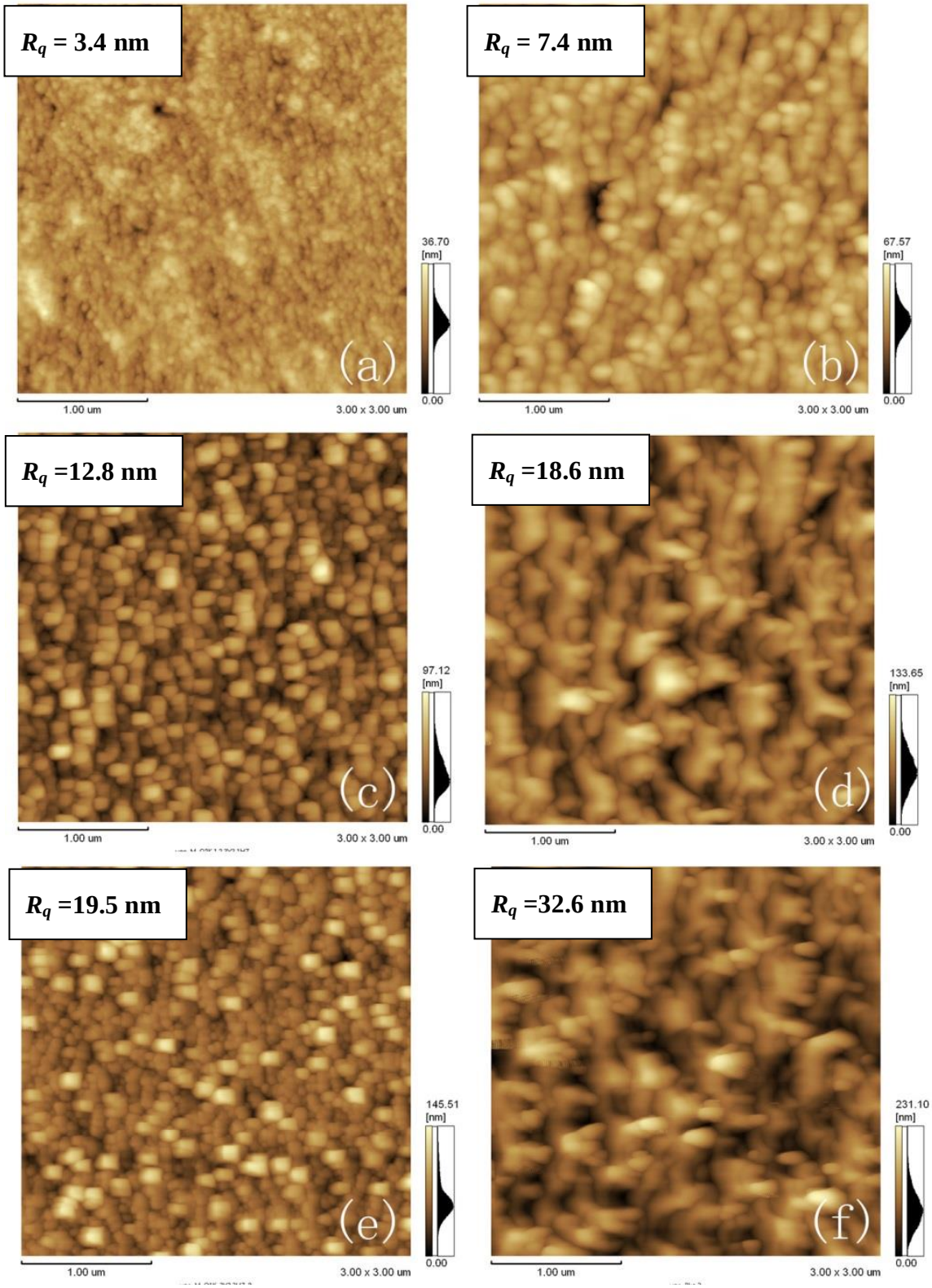

Figure 6.5: AFM images of the surface topography of the centre of the sputtered crater of the as-deposited Ni/Cu multilayer thin films with O_2^+ ions sputter at different energy and at different sputter depth: (a) 222 nm (3rd Ni surface) with 0.5 keV O_2^+, (b) 490 nm (SiO_2 surface) with 0.5 keV O_2^+,(c) 222 nm (3rd Ni surface) with 1.0 keV O_2^+, (d) 490 nm (SiO_2 surface) with 1.0 keV O_2^+,(e) 222 nm (3rd Ni surface) with 2.0 keV O_2^+, and (f) 490 nm (SiO_2 surface) with 2.0 keV O_2^+.

With the fitted MRI model parameters in Table 6.2, the fitted roughness parameter σ as a function of the sputter depth are presented in Fig. 6.6 for ToF-SIMS depth profile sputtered with O_2^+ ions at different energies 0.5, 1.0 and 2.0 keV and compared to AES depth profile with sample rotation sputtered with 2.0 keV Ar^+ ions. The roughness RMS values *Rq* measured with AFM in the sputtered crater at 222 nm (the surface of 3rd Ni layer) and 490 nm (the surface of SiO_2 layer) are also plotted in the Fig. 6.6 as solid circles. Fig. 6.6 shows the same initial surface roughens with the value of 1.6 nm, which is closed to the *Rq* roughness values measured by AFM in Fig. 6.4. Compared with the values and trends obtained for the MRI roughness parameter σ and that obtained from the AFM roughness parameter *Rq*, the MRI roughness parameter is systematically larger than the AFM measured values. This deviation may be explained by: Firstly, the finite size and shape of the tip that effect limits the roughness values measured by AFM. [2] Secondly, the MRI fitted roughness parameter is not only related to surface roughness but it relates to a combination of roughness and mixing.

The ion sputtering induced roughness parameter (σ_s) has been calculated with Eq. 6.8 as a function of the sputtering depth for ToF-SIMS depth profiling with O_2^+ ions sputtering at different energies (0.5, 1.0 and 2.0 keV) and is plotted in Fig. 6.7. From Fig. 6.7 is clear the ion sputtering induced roughness caused by sputtering is the lowest for 0.5 keV O_2^+ ions sputtering and the highest for 2.0 keV O_2^+ ion sputtering. It is similar to the result that Rar et al [18] have observed that the roughness increased with an increase in ion energy. It should also be note that the MRI fitting roughness parameter σ_s =41.0 nm at the depth of z =490 nm was much larger than the other two parameters (*w*=2.6 nm and λ=0 nm) for ToF-SIMS depth profile with 2.0 keV O_2^+ ion sputtering. This implies that the ion sputtering-induced roughness is the dominant factor that contributes to degradation the depth resolution with sputtered depth.

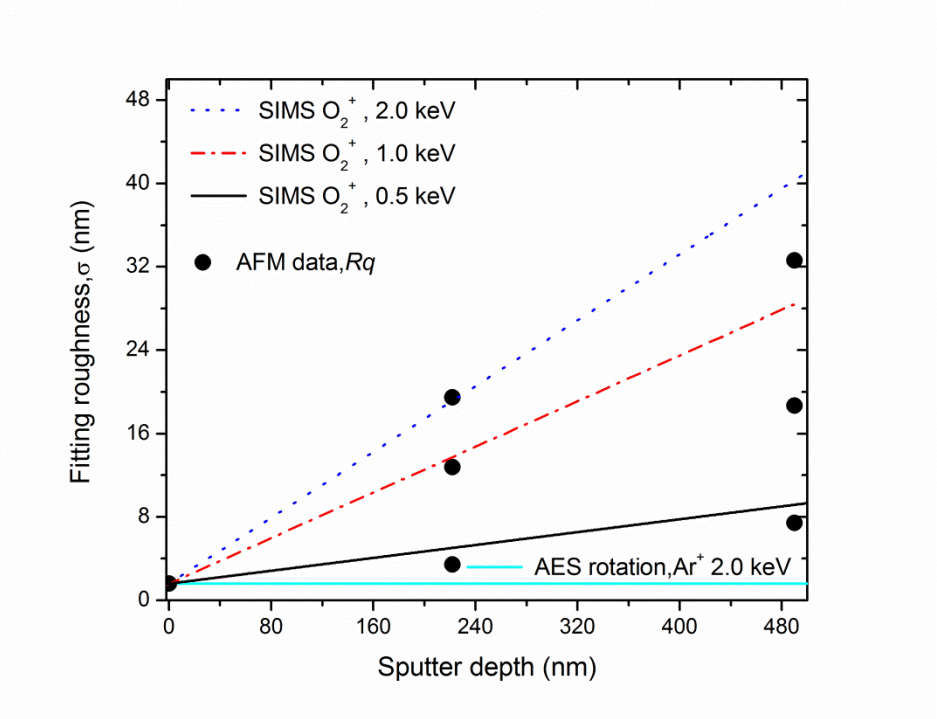

Figure 6.6: The fitted roughness parameter σ as a function of the sputter depth for ToF-SIMS depth profile with O_2^+ ion sputtering at different energies 0.5, 1.0 and 2.0 keV in combination with AES depth profile with sample rotation and 2.0 keV Ar^+ ion sputtering. And the roughness RMS values *Rq* measured by AFM after sputter crater of the sputtered depth position of 222 nm (3rd Ni surface) and the 490 nm (SiO_2 surface) with 0.5, 1.0 and 2.0 keV O_2^+.

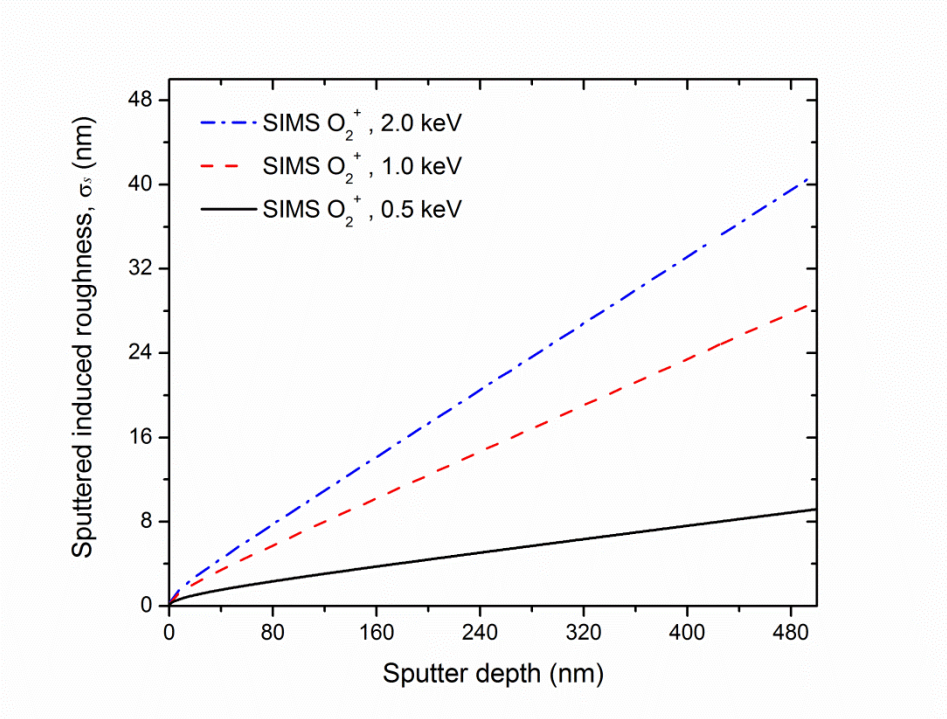

Figure 6.7: The ions sputtering induced roughness parameter σ_s as a function of the sputter depth for ToF-SIMS depth profile with O_2^+ ion sputtering at different energies 0.5, 1.0 and 2.0 keV.

The quality of a SIMS depth profiling experiment is characterized by the so-called depth resolution Δz, which is defined conventionally as the depth range over which a signal intensity (elemental concentration) change from 16% to 84% (or 84% to 16%) upon crossing the interface between two layers[11,12]. In the MRI model three physically meaningful effects are considered to contribute to the depth resolution function, (i) a symmetric contribution to the depth resolution function originates from the intrinsic roughness, (ii) the ion sputter induced surface roughening; which both are described by a Gaussian smearing function (Eq. 6.4 that is characterized by a standard deviation- the surface roughness parameter σ ($(\Delta z_\sigma)^2 = (2\sigma)^2 = (2\sigma_i)^2 + (2\sigma_s)^2$ where σ_i is the intrinsic roughness, σ_s is the sputter induced roughness) and (iii) the asymmetric broadening due to atomic mixing which is described by an exponential function (Eq. 6.3 that is characterized by the atomic mixing parameter w (Δz_w = 1.668w)),. The information depth for SIMS measurements can be set to zero therefore the total depth resolution used in the MRI model can be rewritten as [19]:

$$\Delta z = \left((2\sigma)^2 + (1.668w)^2 \right)^{1/2} \tag{6.9}$$

Using the MRI model and the fitted parameters listed in Table 6.2 the depth resolution Δz was calculated (as function of sputter depth) with Eq. 6.9, for SIMS depth profile with O_2^+ ion sputtering at different ion energies (0.5,1.0 and 2.0 keV) see Fig. 6.8. SIMS depth profiling with the lowest sputtering energy had the best depth resolution and the highest sputtering energy had the worst depth resolution (Fig. 6.8). This can be explained by the mixing length (w) and ion bombardment induced roughness which is the smallest for the lowest sputtering energy.

Comparing the depth resolution (Δz values) of the SIMS depth profile with 0.5 keV O_2^+ ion sputtering to AES depth profiling with sample rotation and 2.0 keV Ar^+ ion sputtering it is clear that SIMS depth profiling has a better depth resolution that the AES depth profiling when the sputtered depth is lower than 37.4 nm. This can be explained by (i) the smaller atomic mixing length (w) of 1.1 nm for the 0.5 keV O_2^+ ions sputtering compared to the 1.6 nm mixing length for the 2.0 keV Ar^+ ions sputtering and (ii) the information depth (λ) which is 0 nm in SIMS and 1.1 nm for the Cu 922 eV peak in AES. When the sputtered depth is more than 37.4 nm, the depth

resolution (Δz) for AES depth profiling is smaller than that of the SIMS depth profiling. The reason for this is the ion sputtering induced roughness in the SIMS depth profile (without sample rotation) increase with sputtered depth where, for the AES depth profiling (with rotation) the ion sputtering induced roughness is effectively restrained form increasing with the sputtered depth.

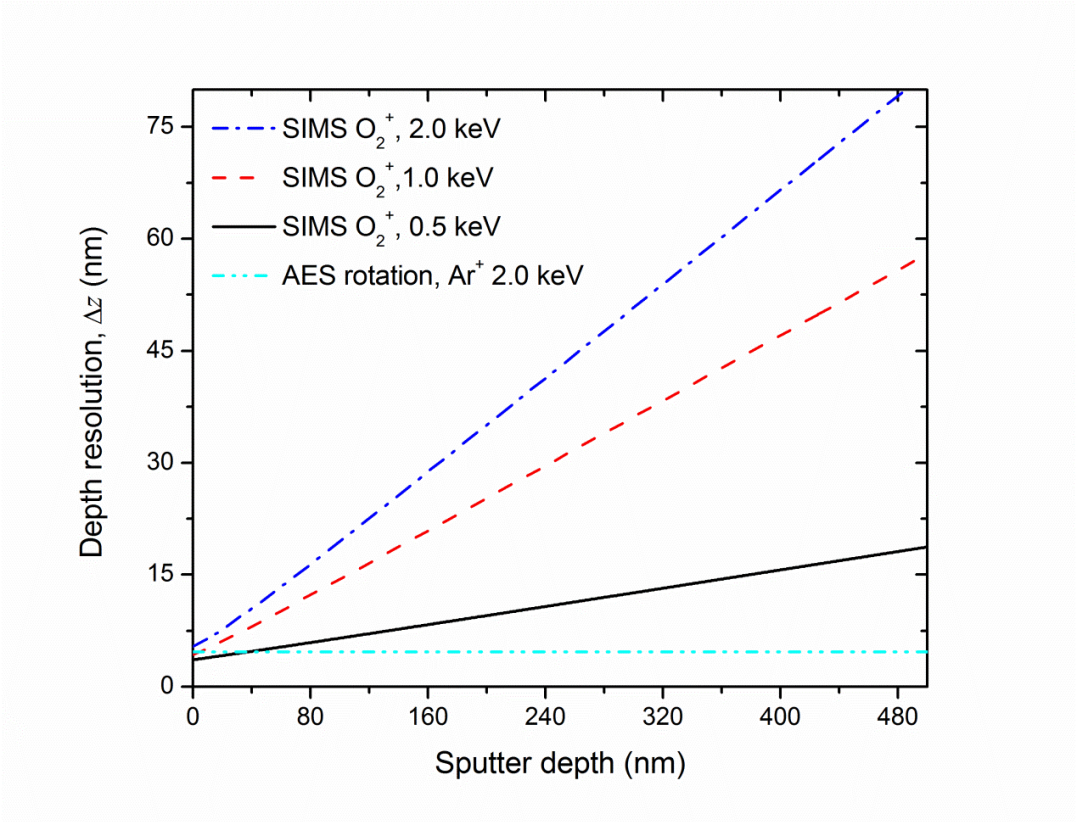

Figure 6.8: The depth resolution Δz as a function of the sputter depth for ToF-SIMS depth profile with O_2^+ ion sputtering at different energy (0.5, 1.0 and 2.0 keV) in combination with AES depth profile with sample rotation at 2.0 keV Ar^+ ion sputtering.

6.3.2 SIMS depth profiles with Cs^+ and Xe^+ ions sputtering at 1.0 keV

In this section, the influence that different ion species (used for depth profiling) have on the quality of a depth profile will be discussed. For this study the Ni/Cu multilayer were profiled in the ToF-SIMS with O_2^+, Cs^+ and Xe^+ ions, all with a sputtering energy of 1.0 keV. In Fig. 6.9(a) and (b) the normalized intensity (open circles) depth profiles for 1.0 keV Cs^+ and 1.0 keV Xe^+ sputtering are plotted, respectively. In order to understand the effect of the different ion species on a depth profile, the measured (normalized)

depth profiles were reconstructed (fitted) with the MRI model. These MRI fits (for a stationary sample) are also shown in Fig. 6.9 as a solid line. Since the sample was stationary during sputtering it was assuming that the roughness parameter (σ) increase linearly with sputter depth *z*. The fitted MRI parameters, the atomic mixing parameter (*w*), the information depth (λ) and the surface roughness (σ), are also summarized in Table 6.4. The fitted MRI parameters for the AES depth profile with sample rotation and sputtered with 2.0 keV Ar^+ ion are also listed in Table 6.4 for comparison.

The fitted roughness parameter σ as a function of the sputter depth are presented in Fig. 6.10 for ToF-SIMS depth profiling with O_2^+, Cs^+ and Xe^+ ions (all sputtering was at 1.0 keV). For comparison the roughness parameter σ as a function of the sputter depth for AES depth profiling with sample rotation and sputtering with 2.0 keV Ar^+ ion is also shown in Fig. 6.10. In Fig. 6.10 can be seen that all the depth profiles have the same initial surface roughness value of 1.6 nm, which is similar to the R_q roughness values measured by AFM in Fig. 6.4. The ion sputtering induced roughness parameter σ_s has been calculated with Eq. 6.8 as a function of the sputter depth for ToF-SIMS depth profiling with O_2^+, Cs^+ and Xe^+ ions (all sputtering at the same energy 1.0 keV) and plotted in Fig. 6.11. In general, the ion sputtering induced roughness (σ_s) increase as the sputter depth increase. From Fig 6.11 it is seen that the sputtering induced roughness σ_s for 1.0 keV Cs^+ ion sputtering is the lowest and that the 1.0 keV O_2^+ ion sputtering has the highest roughness values. This may be because that the atomic mixing length w = 1.1 nm for 1 keV Cs^+ compared with atomic mixing length value of w = 1.6 nm in the 1 keV O_2^+ ions sputtering, which is related to the SRIM simulation results. Moreover, the small nickel oxide islands (or copper oxide) will be formed during the O_2^+ ions sputtering by the reaction of nickel (or copper) with oxygen [4]. This will enhance the sputtering induced roughness with the O_2^+ ion sputtering.

Based on the MRI model fitted parameters listed in Table 6.4, the depth resolution Δz was calculated (by Eq. 6.9) for ToF-SIMS depth profiling with O_2^+, Cs^+ and Xe^+ ion sputtering at 1.0 keV. The calculated resolution Δz is shown in Fig. 6.12 as a function of the sputtered depth, also shown is the resolution Δz for the AES depth profiling with sample rotation and sputtered with 2.0 keV Ar^+ ion. The depth profiling with 1.0 keV Cs^+ ion sputtering had the best depth resolution followed by 1.0 keV Xe^+ ion sputtering and then 1.0 keV O_2^+ with the worst depth resolution (see Fig. 6.9). This is explained in terms of atomic mixing length w and the ion bombardment induced roughness σ_s. Comparing the SIMS depth profile (1.0 keV Cs^+ ion sputtering) to AES depth profiling with sample rotation and sputtered with 2.0 keV Ar^+ ion, it is clear that the depth resolution (Δz values) for the SIMS depth profile is initially better than the AES depth profiling. This is explained by the lower atomic mixing length w=1.1 compared to w=1.6 nm for AES; and also the information, that is zero for SIMS compared to the 1.1 nm for AES.

Table 6.4: Summarized MRI parameters for the best fit on the ToF-SIMS depth profiling data obtained with O_2^+, Cs^+ and Xe^+ ions sputtering at the same energy (1.0 keV).

MRI parameters	Mixing length, w (nm)	information depth, λ (nm)	Surface roughness, σ (nm)	Standard deviation (%)
1.0 (O_2^+)	1.7	0	$1.6+0.053\times z$	4.1
1.0 (Cs^+)	1.1	0	$1.6+0.004\times z$	6.2
1.0 (Xe^+)	1.2	0	$1.6+0.013\times z$	6.8
AES Rotation	1.6	1.1 (Cu 922 eV)	1.6	5.4

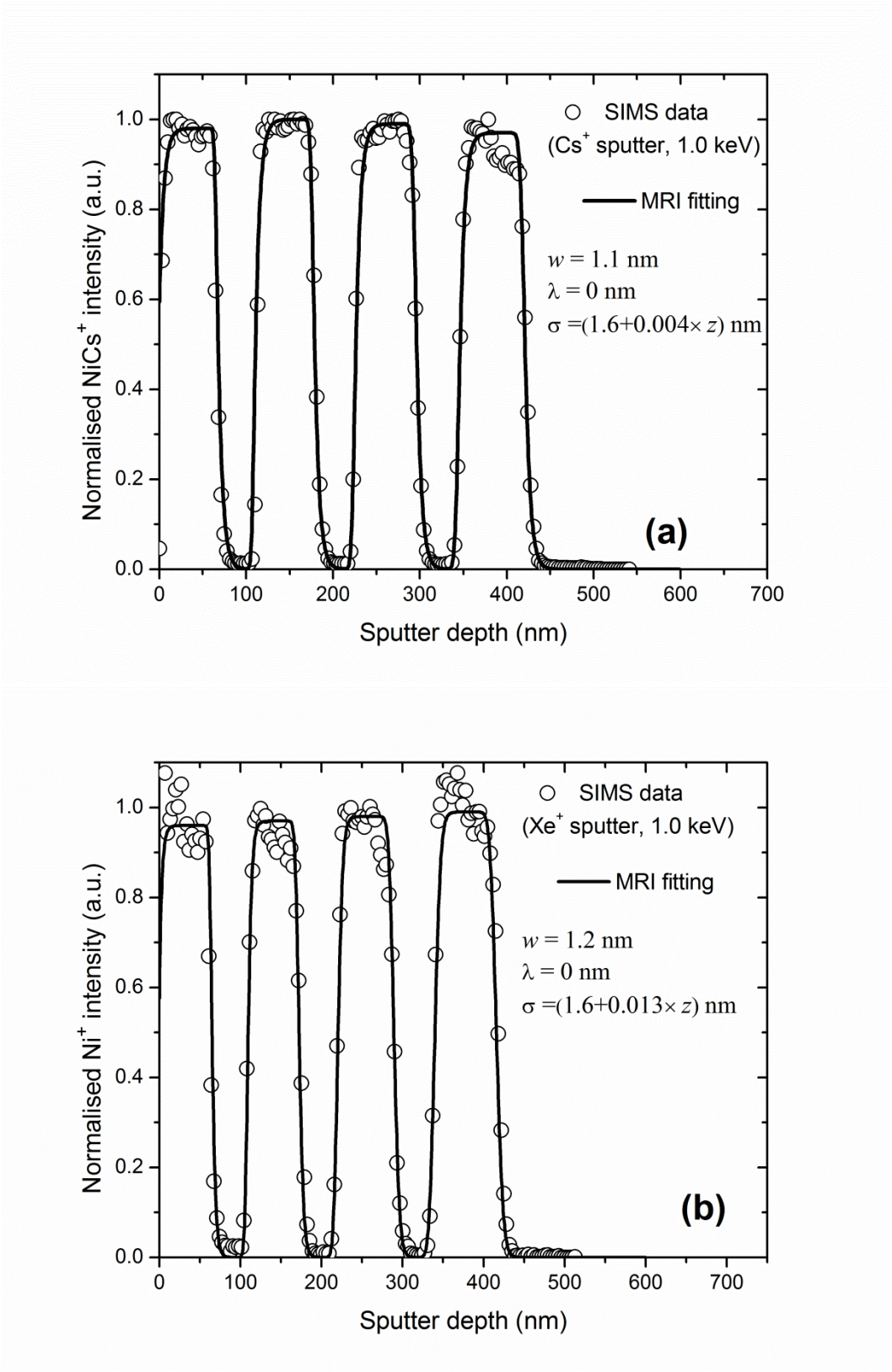

Figure 6.9: ToF-SIMS measured $NiCs^+$ (or Ni^+) normalized intensity vs. depth profiling data (open circles) of as-deposited sample and the best fit to the measured data by the MRI model for (a) 1.0 keV Cs^+ ion sputtering and (b) 1.0 keV Xe^+ ions sputtering. The fitted values for the atomic mixing parameter (w), the information depth (λ) and the surface roughness (σ) are indicated in Fig. 6.9(a) and (b).

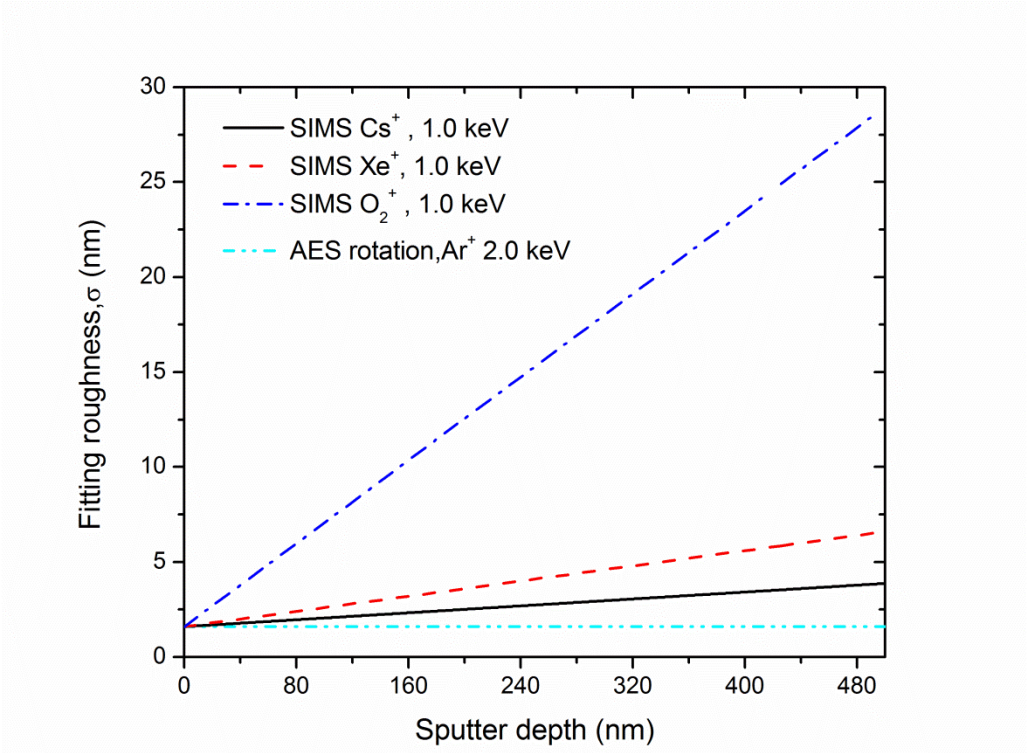

Figure 6.10: The fitted roughness parameter σ as a function of the sputter depth for ToF-SIMS depth profile with O_2^+, Cs^+ and Xe^+ ions sputtering at the same energy of 1.0 keV in combination with AES depth profile with sample rotation with 2.0 keV Ar^+ ion sputtering.

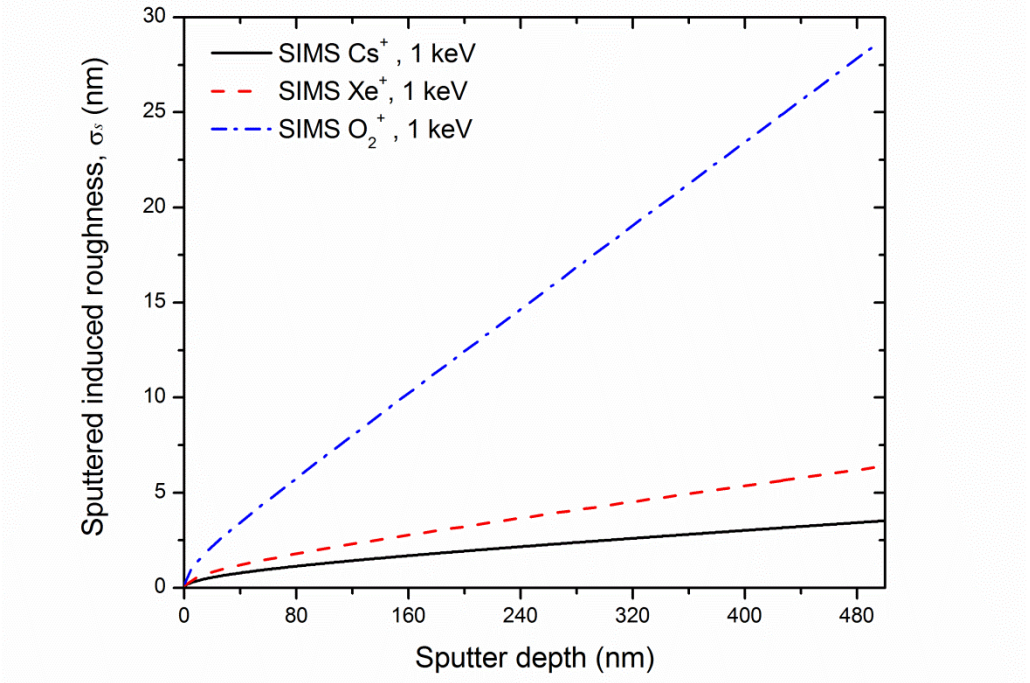

Figure 6.11: The ion sputtering induced roughness parameter σ_s as a function of the sputter depth for ToF-SIMS depth profile with O_2^+, Cs^+ and Xe^+ ions sputtering at the same energy of 1.0 keV.

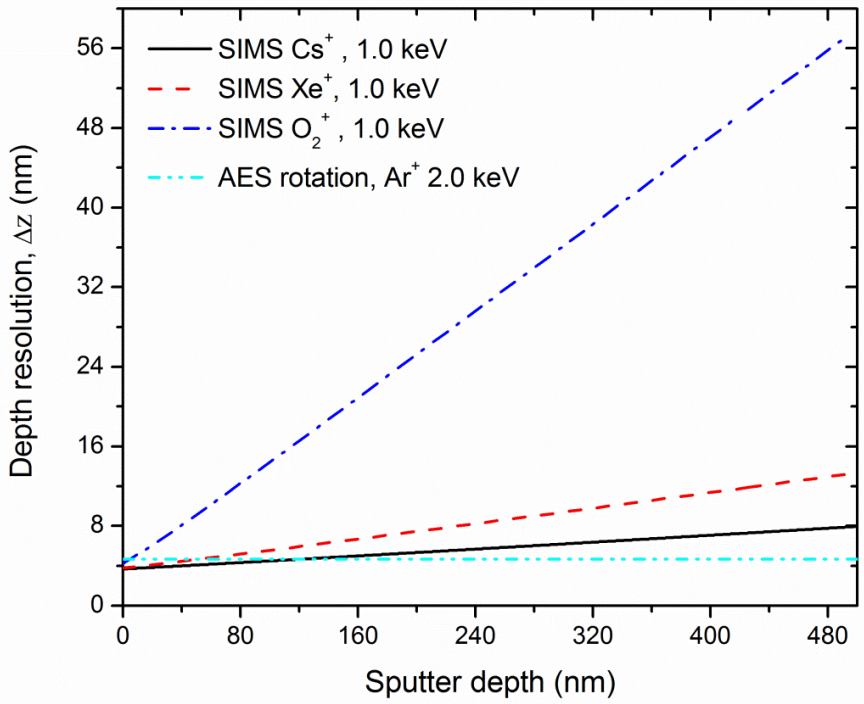

Figure 6.12: The depth resolution Δz as a function of the sputter depth for ToF-SIMS depth profile with O_2^+, Cs^+ and Xe^+ ions sputtering at the same energy of 1.0 keV in combination with AES depth profile with sample rotation with 2.0 keV Ar^+ ion sputtering.

6.4 Summary

The as-deposited Ni/Cu polycrystalline multilayer thin films were characterized by ToF-SIMS depth profiling with different ion species (O_2^+, Cs^+ and Xe^+) and with different sputtering energies. The measured depth profiles data were quantitatively analysed by the MRI model, assuming that the roughness parameter is linearly increasing with the sputtered depth for a stationary sample. The MRI fitted roughness parameters obtained for the ToF-SIMS depth profiling compared well with the root-mean-square roughness obtained from the AFM topography scans of crater bottom. Ion sputtering induced roughness and depth resolution during ToF-SIMS depth profiling of a polycrystalline Ni/Cu multilayer were evaluated. The results indicated that the depth resolution is noticeably better for depth profiling with lower primary ion energies, which can be credited to the lowest ion sputter induced roughness and the smallest atomic mixing length. Depth profiling with Cs^+ ion sputtering had the best depth resolution compared to Xe^+ and O_2^+ ion sputtering. The

initial depth resolution of ToF-SIMS depth profile with 1.0 keV Cs^+ ion sputtering is also better that AES depth profiling with sample rotation and 2.0 keV Ar^+ ion sputtering.

References

[1] R.G. Wilson, F.A. Stevie, C.W. Magee, Secondary Ion mass Spectrometry: A Practical Handbook for Depth Profiling and Bulk Impurity Analysis, Wiley-Interscience, New York 1989.

[2] G.S. Lau, E.S. Tok, R. Liu, A.T.S. Wee, J. Zhang, Roughening behavior in Si/SiGe heterostructures under O_2^+ bombardment, Nucl. Instr. Meth. Phys. B **215** (2004) 76-82.

[3] B. Fares, B. Gautier, J.C. Dupuy, G. Prudon, P. Holliger, Deconvolution of very low primary energy SIMS depth profiles, Appl. Surf. Sci. **252** (2006) 6478-6481.

[4] D.W. Moon, K.J. Kim, Surface topography development on ion-beam-sputtered surfaces: Role of surface inhomogeneity induced by ion-beam bombardment, J. Vac. Sci. Technol. A **14** (1996) 2744-2756.

[5] K.J. Kim, D.W. Moon, Significant improvement in depth resolution of Cr/Ni interfaces by secondary ion mass spectrometry profiling under normal O_2^+ ion bombardment, Appl. Phys. Lett. **60** (1992) 1178.

[6] B. Fares, B. Gautier, Ph. Holliger, N. Baboux, G. Prudon, J.C. Dupuy, Surface roughening and erosion rate change at low energy SIMS depth profiling of silicon during oblique O_2^+ bombardment, Appl. Surf. Sci. **253** (2006) 2662-2670.

[7] Y. Kudriavtsev, S. Gallardo, O. Koudriavtseva, A. Escobosa, V.M. SanchezR, M. Avendaño, R. Asomoza, M. Lopez-Lopez, SIMS depth profiling of semiconductor interfaces: experimental study of depth resolution function, Surf. Interface Anal. **43** (2011)1277-1281.

[8] S. Hofmann, Atomic mixing, surface roughness and information depth in high-resolution AES depth profiling of a GaAs/AlAs superlattice structure, Surf. Interface Anal. **21** (1994) 673-678.

[9] P.N. Allen, M.G. Dowsett, R. Collins. SIMS profile quantification by maximum entropy deconvolution, Surf. Interface Anal. **20** (1993) 696-702.

[10] B.V. King, I.S.T. Tsong, A model for atomic mixing and preferential sputtering effects in SIMS depth profiling, J. Vac. Sci. Technol. A **2** (1984)1443-1447.

[11] S. Hofmann, Sputter depth profile analysis of interfaces, Rep. Prog. Phys. **61**(1998) 827-888.

[12] S. Hofmann, Chap. 7: Quantitative Compositional Depth Profiling, in Auger-and X-ray Photoelectron Spectroscopy in Materials Science, Springer Verlag Heidelberg, New York, Dordrecht, London 2013.

[13] X.L. Yan, Y. Liu, H.C. Swart, J.Y. Wang, J.J. Terblans, Investigation of interdiffusion and depth resolution in Cu/Ni multilayers by means of AES depth profiling, Appl. Surf. Sci. **364** (2016) 567-572.

[14] H.L. Kang, J.B. Lao, Z.P. Li, W.Q. Yao, C. Liu, J.Y. Wang, Reconstruction of GaAs/AlAs supper lattice multilayer structure by quantification of AES and SIMS sputter depth profiles, Appl. Surf. Sci. **388** (2016) 584-588.

[15] M.P. Seah, C. Lea, Depth resolution in composition profiles by ion sputtering and surface analysis for single-layer and multilayer structures on real substrates, Thin Solid Films **81** (1981) 257-270.

[16] J.Y. Wang, S. Hofmann, A. Zalar, E.J. Mittemeijer, Quantitative evaluation of sputtering induced surface roughness in depth profiling of polycrystalline ultilayers using Auger electron spectroscopy, Thin Solid Films **444** (2003) 120-124.

[17] J.F. Ziegler, TRIM Code, IBM Corporation, Yorktown Heights, New York, (http://www.srim.org)

[18] A Rar, S. Hofmann, K. Yoshihara, K. Kajiwara, Optimization of depth resolution parameters in AES sputter profiling of GaAs/AlAs multilayer structures, Appl. Surf. Sci. **144-145** (1999) 310-314.

[19] J.Y. Wang, U. Starke, E.J. Mittemeijer, Evaluation of the depth resolutions of Auger electron spectroscopic, X-ray photoelectron spectroscopic and time-of-flight secondary ion mass spectrometric sputter depth profiling techniques, Thin Solid Films **517**(2009) 3402-3407.

Chapter 7
Interdiffusion in the Ni/Cu multilayer thin films

7.1 Introduction

Ni/Cu multilayer has been extensively studied for their magnetic, mechanical, optical properties and surface segregation [1-5]. These physical properties depend critically on interfaces and require a good control on the evolution of composition under heat treatment. Understanding of how interdiffusion proceeds in these nano-multilayers should therefore improve these practical aspects, which differ from those of bulk materials and single-layer thin films [6]. For example, Ni and Cu atoms interdiffused in the monolayer regime within the first atomic layers when Ni was deposited on a Cu(001) single crystal at room temperature, where the Ni diffused beneath the first copper layer[7, 8]. In addition, the diffusion in polycrystalline thin films is much faster than that in bulk materials due to the high density of defects such as dislocations, vacancies, and grain boundaries, which act as a short-cut for diffusion. Therefore, the diffusion in polycrystalline thin films cannot be described by extrapolating diffusion parameter obtained for bulk materials at higher temperatures.

The Auger electron spectroscopy (AES) depth profiling technique is one of the most commonly used methods for the study interdiffusion in multilayers due to its high surface sensitivity. In the past decades, several methods have been proposed to extract

the interdiffusion coefficient from AES depth profiles. For example: the plateau-rise method [9], the center-gradient method [10], and the interface-width method [11] for a bilayer sample and a Fourier series method for a multilayer sample [12]. In these four methods, only parts of the measured depth profile are used for extracting the interdiffusion coefficient. Recently, based on the Mixing-Roughness-Information depth (MRI) model [13], a new method for fitting the entire measured AES depth profile has been proposed [14] and is widely used to extract the interdiffusion coefficient in layered structures [15-18]. The MRI model considers three physical effects, atomic mixing, the escape depth of Auger electrons and surface roughness, which distort a measured depth profile and reconstruct the true depth profile. For case where the diffusion-induced concentration profile can be described as a Gaussian function of an initial concentration profile, it is possible to extract the values of interdiffusion coefficient from the roughness parameters obtained by fitting the measured depth profile with the MRI model.

This chapter is to demonstrate how to determine the interdiffusion coefficients in Ni/Cu multilayer structures by fitting the AES depth profiles by using the MRI model and assuming a linear roughness with sputter depth. The fitting roughness values are compared with those measured by AFM. And the depth-dependent interdiffusion coefficients of the annealed samples and depth resolution upon depth profiling of the as-deposited sample are quantitatively evaluated accordingly.

7.2 Experimental

7.2.1 Sample preparation and heat treatment

The detailed procedures for preparation of the Ni/Cu multilayer on SiO_2 substrates have been described in Chapter 3. The main procedure can be summarized as follows. The Ni/Cu multilayer structures composed of four pairs of Cu and Ni sublayers were prepared by electron beam physical vapour deposition onto passivated (SiO_2) silicon (100) substrates at a base pressure of $<7\times10^{-6}$ Torr. The deposition rates were ~0.4 nm/s for nickel and ~0.7 nm/s for copper, respectively. The thickness of each sublayer was monitored by an Inficom XTC thin film monitor and the thickness of each sublayer is shown in the sketch Fig. 7.1. The samples were then annealed at 325 ℃,

350 ℃ and 375 ℃ for 30 min, respectively, in a high vacuum tube furnace at the base pressure of $< 5 \times 10^{-6}$ Torr. After annealing, the sample was left to cool down to room temperature in the furnace at the same pressure.

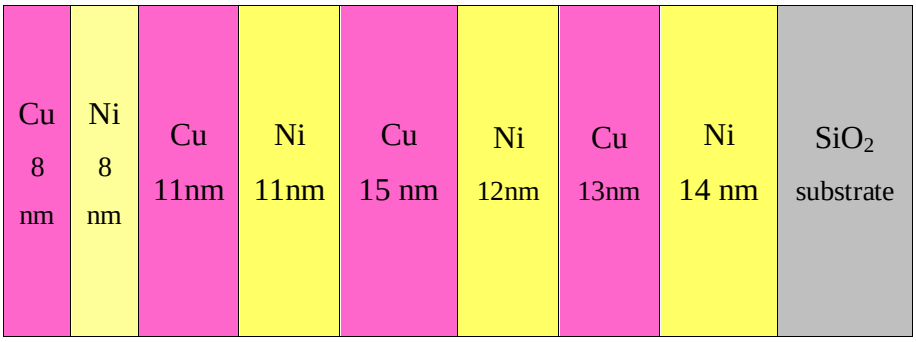

Figure 7.1: The sketch of the Ni/Cu multilayer structures composed of four pairs of Cu and Ni sublayers.

7.2.2 Sample characterization and AES depth profile measurement

Atomic force microscopy (AFM) images and surface roughness measurements were obtained from a Shimadzu SPM-9600. The topographies measured by AFM are shown in Fig. 7.2(a) for the surface of the as-deposited sample and in Fig. 7.2(b) for the crater centre for sample sputtered at a depth of 100 nm (substrate SiO_2 surface), respectively. The corresponding root mean square (RMS) roughness values were determined as 0.91 nm and 5.54 nm, respectively. Hence, the roughness value increased with the sputtered depth upon depth profiling.

The AES depth profiles of the as-deposited and annealed samples were measured using a PHI 600 Scanning Auger Microscope at a base pressure $< 10^{-9}$ Torr. A static primary electron beam of 10 keV and beam current of 200 nA with beam size diameter of 9.2 μm was used. Ion sputtering was performed with 2 keV Ar^+ ions at an incidence angle of 40° with respect to the sample surface normal, the beam current density was 0.127 A/m^2 with a raster area of 2×2 mm^2. The Auger peak-to-peak heights (APPH) were recorded as a function of sputtering time for Ni(718 eV), Cu(922 eV), C(275 eV), O(510 eV) and Si(96 eV). The average sputter rate of the Ni/Cu multilayer was 3 nm/min. determined by the as-deposited reference Ni/Cu bilayer thin films. The thicknesses value of Cu and Ni layers on the reference, shown

in Fig. 7.3 and Fig. 7.4, were ~28 nm and ~52 nm and the sputtering time were 550 s and 1050 s, respectively.

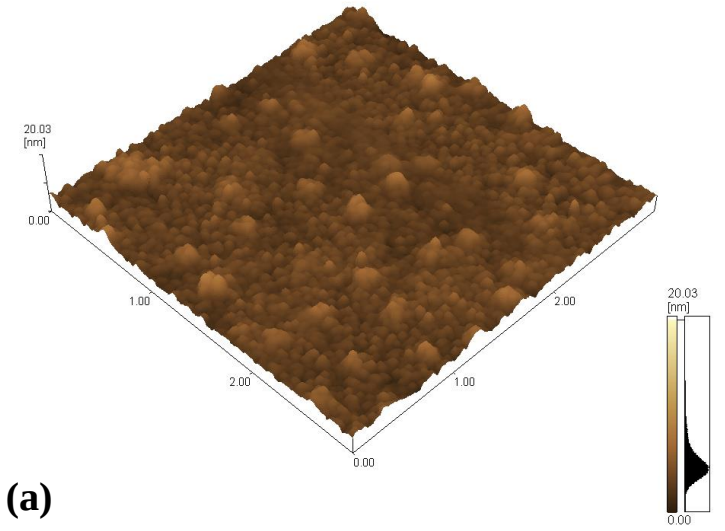

(a)

3.00 x 3.00 [um] Z 0.00 - 20.03 [nm]

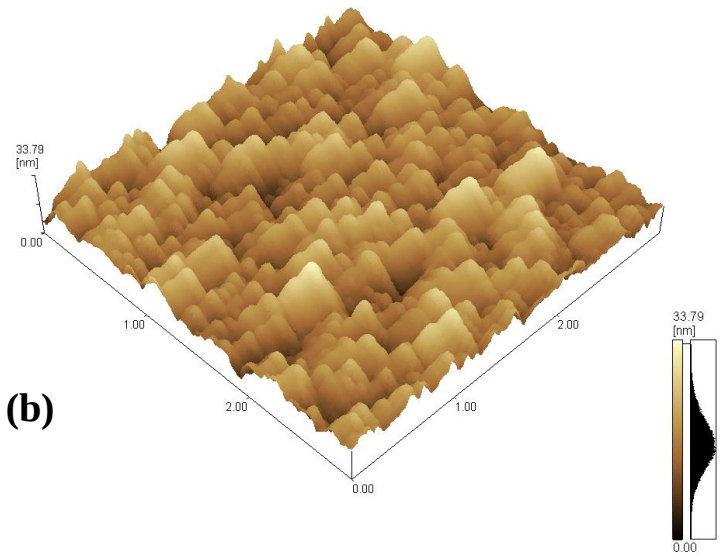

(b)

3.00 x 3.00 [um] Z 0.00 - 33.79 [nm]

Figure 7.2: AFM images of (a) the surface of the as-deposited sample and (b) the crater center for sample sputtered at the depth of 100 nm (substrate SiO_2 surface). The corresponding root mean square (RMS) roughness values were determined as 0.91 and 5.54 nm, respectively.

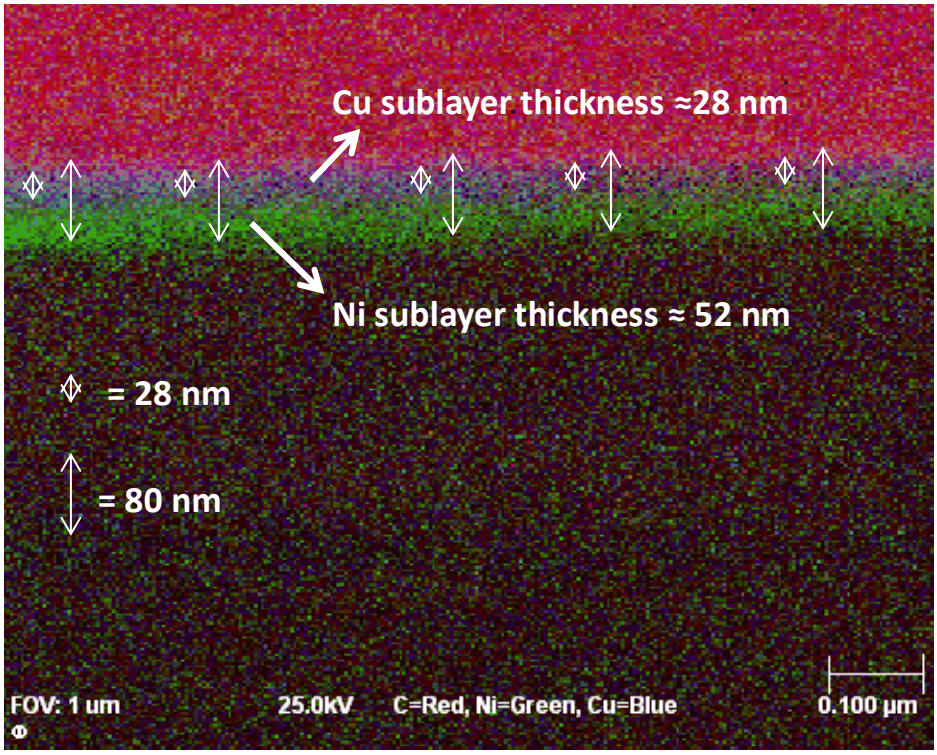

Figure 7.3: The Auger map image of the cross-section of reference Ni/Cu bilayer thin film.

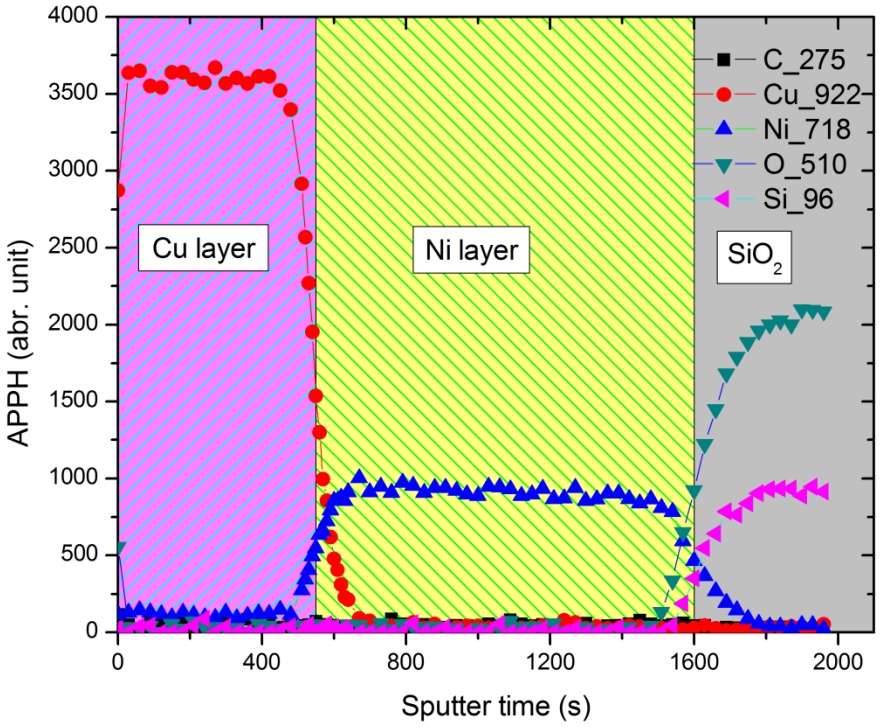

Figure 7.4: The measured AES depth profile data of reference Ni/Cu bilayer thin film.

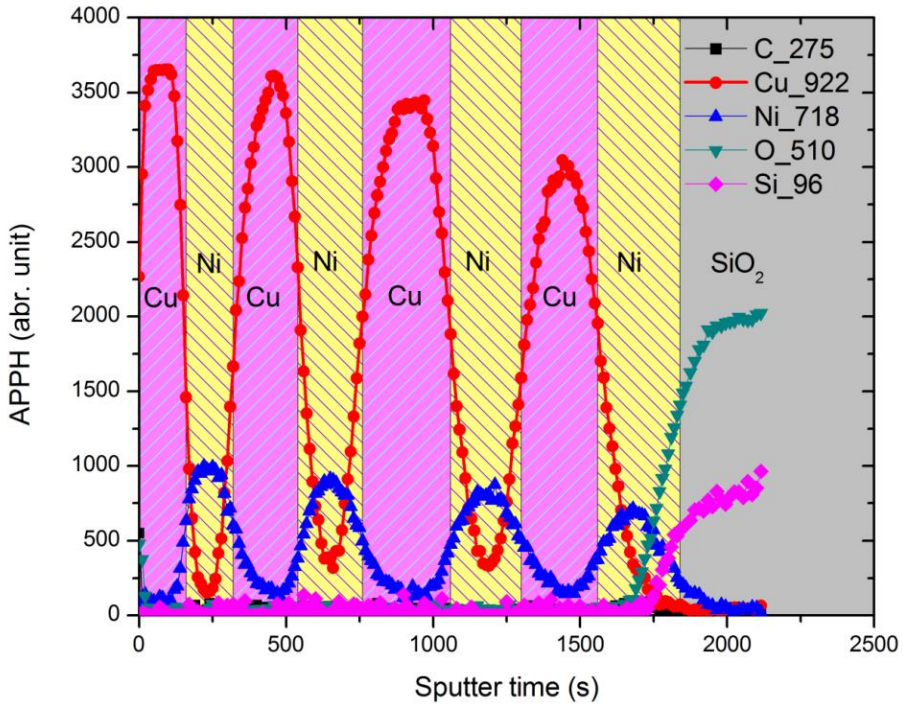

Figure 7.5: The measured AES depth profile data of as-deposited Ni/Cu multilayer thin film.

7.2.3 Conversion of the intensity-sputter time profile into a normalized APPH depth profile

According to the standard Auger spectra of pure Cu and Ni [19], the range of Ni peaks overlapped with the Cu Auger peaks except for the Cu 922 eV peak. The measured APPH with sputter time of the as-deposited Ni/Cu multilayer thin films is shown in Fig. 7.5. The Cu APPH was then normalized to the maximum of the Cu 922 eV APPH in the as-deposited sample. The time scale was converted into the depth scale using the obtained average sputtering rate of 3 nm/min (see section 7.2.2). The measured and normalised depth profiles are shown in Fig. 7.6 for the as-deposited and annealed samples.

7.3 The MRI model

The Mixing-Roughness-Information depth (MRI) model is a theoretical description of the depth resolution function (DRF) taking into account atom mixing, sputter-induced surface roughness and information depth. The model developed by Hofmann was first given in reference [13]. Since then, numerous extensions were developed to enable its applicability for preferential sputtering [14], non-stationary mixing, information depth as well as for non-Gaussian roughness [15,16], and the analytical depth resolution function for thin delta layer [17]. Often the distortion of the measured depth profile as compared to the true concentration-depth profile is described by a so-called depth resolution function, which represents the broadening of the measured concentration depth profile upon depth profiling. In the sputter depth profiling, the measured normalised intensity $I(z)/I^0$ as a function of the sputter depth z is given by[13,20]:

$$\frac{I(z)}{I^0} = \int_0^\infty X(z')g(z-z')dz' \tag{7.1}$$

where z' is the running depth parameter, $X(z')$ is the mole fraction of the respective element at the original depth z' in the sample and $g(z-z')$ is a depth resolution function. The depth resolution function $g(z-z')$ in the MRI model takes into account three physically meaningful effects: atomic mixing, escape depth of Auger electrons, surface/interface roughness and is described by [13, 20]:

Mixing length (w): $$g_w(z) = \frac{1}{w}\exp\left[-\left(z-z'+w\right)/w\right] \tag{7.2}$$

Roughness (σ): $$g_\sigma(z) = \frac{1}{\sqrt{2\pi}\sigma}\exp\left[-(z-z')^2/2\sigma^2\right] \tag{7.3}$$

Information depth (λ): $$g_\lambda(z) = \frac{1}{\lambda}\exp\left[-\left(z-z'\right)/\lambda\right] \tag{7.4}$$

where w is atomic mixing length, σ is the surface roughness and λ is the information depth parameter. With the above three partial resolution function (Eqs. 7.2, 7.3 and 7.4) depth resolution function g*(z-z')* can be written as:

$$g(z) = g_w(z) \otimes g_\sigma(z) \otimes g_\lambda(z) \tag{7.5}$$

In general, quantitative results of the MRI model are obtained by numerical solution of the convolution integral with combining Eq. 7.1 and Eq. 7.5.

In an initial stage of diffusion, the diffusion-induced concentration profile can be described by a Gaussian function ~exp*[-z²/4Dt],* where *z* represents the diffusion depth. Therefore, the square of the diffusion length can be expressed in terms of the interface roughness as [14]:

$$2Dt = \sigma_T^2 - \sigma_o^2 \tag{7.6}$$

where *t* is the annealing time, σ_o and σ_T are the values of the roughness parameter before and after annealing at temperature *T*, respectively. Using Eq. 7.6, the interdiffusion coefficient *D* can be determined from the fitted interface roughness parameter by the MRI model.

7.4 Results and discussion

7.4.1 Depth dependence of the Interdiffusion parameters

The measured Cu depth profiling data of the as-deposited Ni/Cu multilayer are shown in Fig. 7.6(a) as open circles. A close examination of Fig. 7.6(a) revealed that the measured maximum/minimum value of each sublayer decreased/increased with the sputtered depth. This effect is related to the development of the ion bombardment induced roughness for polycrystalline material upon stationary depth profiling because of the dependence of ion sputtering yield on the orientation of the crystal. The measured Cu depth profile data for the as-deposited sample was fitted with the MRI model taking three MRI parameters into account. The solid line in Fig. 7.6(a) presents the fit. The roughness parameter σ is regards as a composition of the initial roughness and sputtering induced roughness [16]. For simplicity, the sputtering induced roughness was assumed to be proportional to the sputtered depth for polycrystalline material upon stationary AES depth profiling according to Seah [21].

Therefore, the total roughness could be descripted as $\sigma_o = \sigma_{oo} + C*z$, where σ_{oo} is the initial surface roughness, C is a constant and z is the sputtered depth. The atomic mixing length w was estimated as 1.0 nm by the TRIM code [22] and the Auger electron escape depth λ (effective attenuation length times Cos(θ), where θ is the angle of emission of the detected electrons) for Cu (922 eV) was calculated as 0.8 nm [23]. The fitted roughness parameter was obtained as σ_o = (0.9+0.049*z) nm, which agreed very well with the measured RMS *Rq* values of 0.91 nm and 5.54 nm. The measured RMS values was obtained by means of AFM at a depth of z = 0 nm and z =100 nm as indicated in Fig. 7.2.

The as-deposited Cu layered structure is also shown as a dashed line in Fig. 7.6(a). For the annealed samples, the measured Cu depth profile data and the best fit to the measured data are shown in Figs. 7.6(b-d). The fitting parameters w and λ were kept the same as for the as-deposited sample and only the roughness parameter was changed in the MRI model fitting. The determined linear depth dependence of the roughness parameter σ, at the three different temperatures of 325 ℃, 350 ℃ and 375 ℃, were indicated in Figs. 7.6(b-d), respectively.

Using the roughness parameter values presented in Figs. 7.6(a-d), the calculated values of the interdiffusion coefficient according to Eq. 7.7 at the two locations, namely at the first and the last Cu/Ni interface, as indicated in Fig.7.6(a), are presented in Fig. 7.7 as open and filled circles, respectively. The corresponding values of the interdiffusion parameters, the pre-exponential factor D_o and the activation energy Q, as obtained from the a linear fit on the data in Arrhenius plot, $D = D_o \exp(-Q/RT)$, are indicated in Fig. 7.7. In Fig. 7.7 the measured interdiffusion parameters are also compared with the literature values listed in Table 7.1. The interdiffusion in the Ni/Cu multilayer at the first Cu/Ni interface was determined as $D_o = 6.2 \times 10^{-13}$ m^2/s and Q = 101.4 kJ/mol, and at the last (deepest) Cu/Ni interface as $D_o = 6.3 \times 10^{-14}$ m^2/s and Q = 79.0 kJ/mol. The dash-dotted line shown in Fig. 7.7 was also obtained from measured AES depth profile data for Ni/Cu multilayer (m) films deposited on glass substrates [24]. The dashed line shown in Fig. 7.7 was obtained for a Cu(~100 nm)/Ni(~500 nm) bilayer (b) films sample [25].

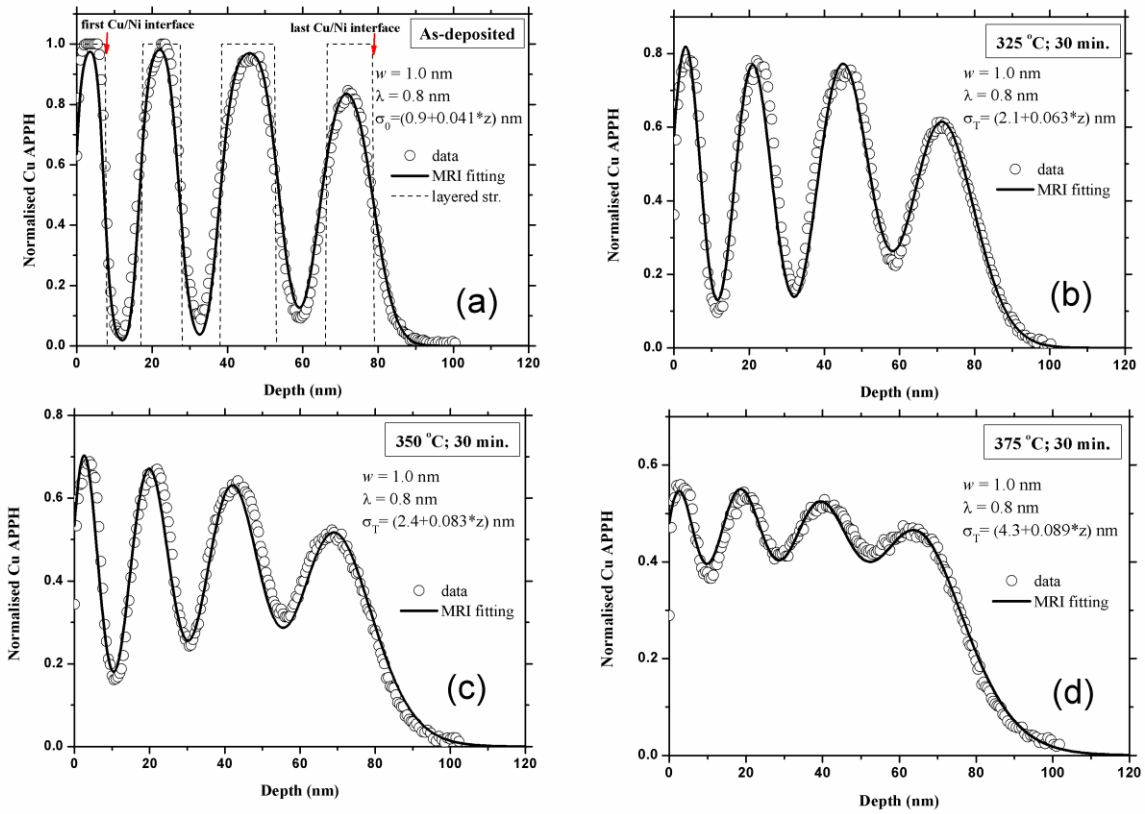

Figure 7.6: The normalized Cu depth profiling data and the best fit to the measured data by the MRI model for (a) the as-deposited sample, and the annealed samples for 30 min at (b) 325 ℃ (c) 350 ℃ and (d) 375 ℃. The dashed line drawn in Fig. 7.5a represents the as-deposited Cu sublayer structure.

The low activation energy Q values of 101.4 kJ/mol (79.0 kJ/mol) obtained in this study in comparison with an Q value of 228.7 kJ/mol from a single crystalline copper [26], suggests that grain boundary and high defect density play a dominant role in the diffusion process of the investigated multilayer thin films. The obtained diffusion parameters, measured at the low temperature range of 325 -375 ℃, agree reasonably well with the ones listed in Table 7.1 for the polycrystalline bi-/multilayer films samples [24, 25, 26, 28], which support the grain boundary diffusion mechanism at low temperatures for polycrystalline Ni/Cu.

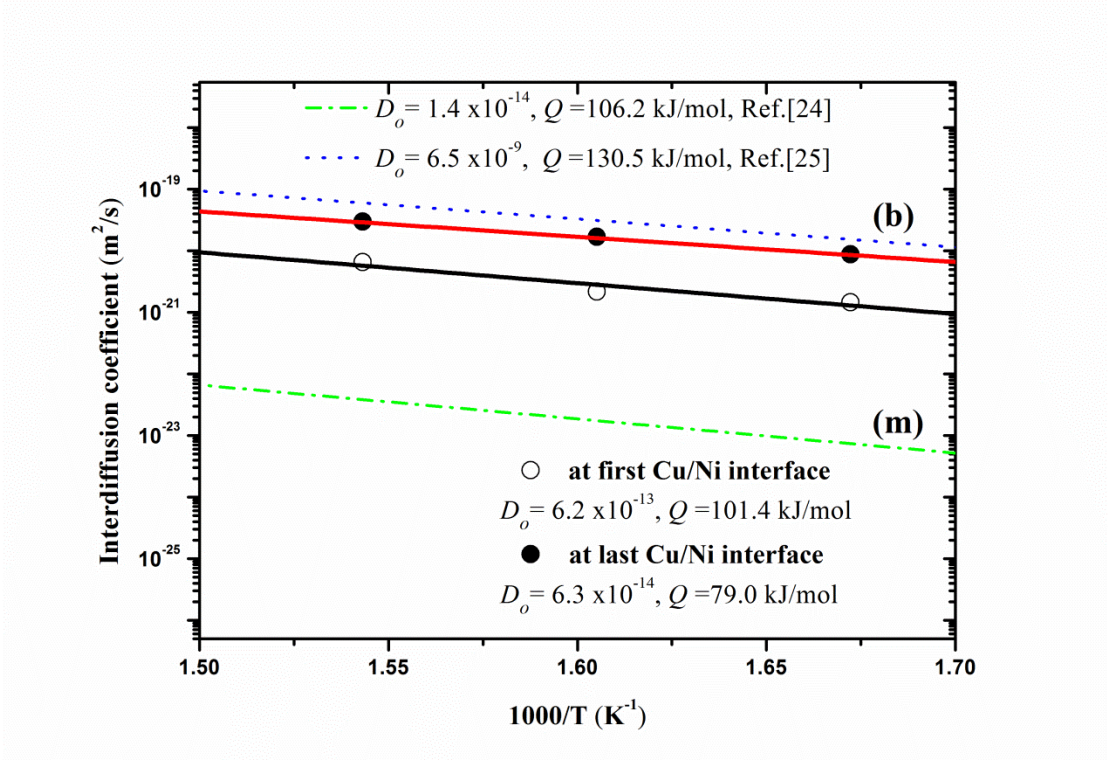

Figure 7.7: Arrhenius plots for the interdiffusion coefficients calculated from the fitted roughness parameters (see Fig. 7.6) by applying Eq. 7.6. The open and filled circles represent the values of the interdiffusion coefficient at the locations of the first and last Cu/Ni interfaces, respectively. The corresponding interdiffusion parameters (pre-exponential factor D_o and activation energy Q) are indicated n bilayer (b) and multilayer (m) thin films.

Table 7.1: Diffusion parameters obtained in this study and from literature.

Source	Pre-exponential factor, D_o (m^2/s)	Activation energy, Q (kJ/mol)	Temperature range, (K)	Method/Remarks
This study (first interface)	**6.2×10^{-13}**	**101.4**	**598-648**	**Multilayer thin films, AES depth profile**
This study (last interface)	**6.3×10^{-14}**	**79.0**		
Ref.[24]	1.4×10^{-14}	106.2	523-673	Multilayer thin films, AES depth profile
Ref.[25]	6.5×10^{-9}	130.5	523-723	Bilayer thin films, AES depth profile
Ref.[26]	6.0×10^{-12}	94.1	473-773	Bilayer thin films, AES depth profile
Ref.[27]	6.9×10^{-7}	90.4	476-1156	Polycrystalline, Tracer
Ref.[28]	2.0×10^{-5}	228.7	723-823	Bilayer, Moire spacing

A close examination of Fig. 7.7 revealed that the interdiffusion in the Ni/Cu multilayer is faster across the last Cu/Ni interface (near the substrate) than across the first Cu/Ni interface (near the surface) with a difference in activation energy value of 22.4 kJ/mol. In order to quantitatively evaluate the depth-dependent interdiffusion coefficient, Fig. 7.8 shows the interdiffusion coefficient as a function of sputtered depth for the same annealing time of 30 min at the three different investigated annealing temperatures, based on Eq. 7.6 with a linear depth dependence adopted for σ_T (see Fig. 7.6). The open circle, square, triangle and filled circle represent the values of the interdiffusion coefficient at the locations of the first, second, third and last Cu/Ni interfaces, respectively. It was found that the interdiffusion coefficient increased with the sputtered depth at the three different annealed temperatures. This result is related to the reduction of the activation energy with sputtered depth for interdiffusion at the first, second, third and last Cu/Ni interfaces as 101.4 kJ/mol, 87.7 kJ/mol, 81.9 kJ/mol and 79.0 kJ/mol, respectively, shown in Fig. 7.9. This reduction of the activation energy with sputtered depth was also observed in Cu/Ag, Au/Ag, Pd/Au and Pd/Cu multilayer structure with AES measured by Bukaluk [29, 30]. In addition, enhanced grain boundary diffusion could be involved in the multilayer closer to the substrate; this however needs to be investigated further.

Using the extracted interdiffusion coefficient value, the interdiffusion length $(2Dt)^{1/2}$ across the first Cu/Ni interface for the sample annealed at 325 ℃ for relatively short annealing time 30 min was calculated as approximately 2 nm. This result indicates that the MRI model offers the possibility of detecting quantitatively the local diffusion constants with a resolution of a few nanometres for quantification of nanoscale thin film structures.

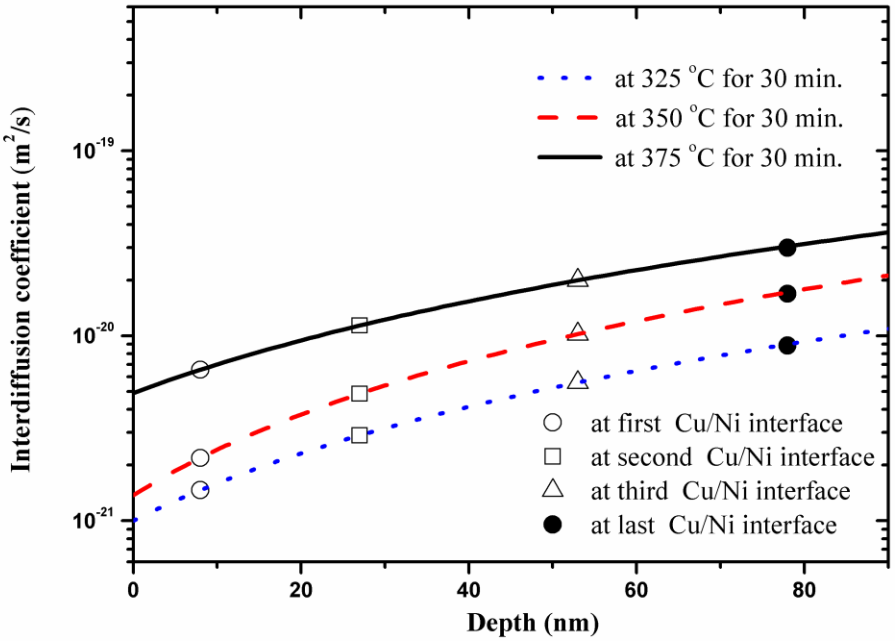

Figure 7.8: The interdiffusion coefficient as a function of the sputter depth for the annealed sample for 30 min at 325 ℃, 350 ℃ and 375 ℃, respectively. The open circles, squares, triangles and filled circles represent the values of the interdiffusion coefficient at the locations of the first, second, third and last Cu/Ni interfaces, respectively.

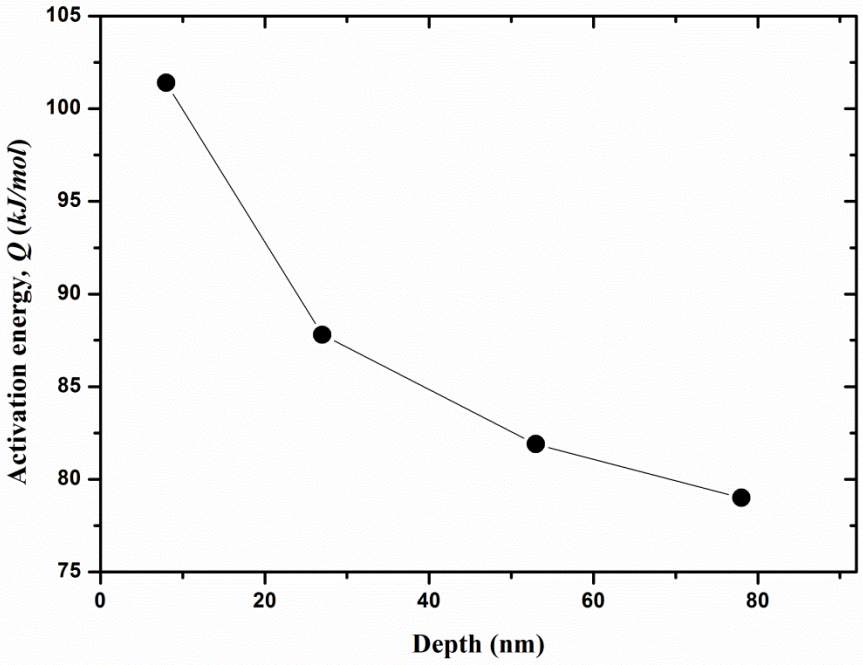

Figure 7.9: The activation energy *Q* with sputtered depth for interdiffusion at the first, second, third and last Cu/Ni interfaces, respectively.

7.4.2 The depth-dependence of depth resolution

The quality of a AES depth profiling experiment can be characterized by the so-called depth resolution Δz, which is defined conventionally as the distance (depth) in which measured intensity of the signal change from 16-84% (or 84-16%) upon crossing an interface [20]. However, if saturation levels of 100% and 0% for the signal analyzed no longer occur, for example, in case of sputter depth profiling of a thin multilayered film, the determination of Δz defined above is no longer possible.

With respect to the above-discussed refinements of the DRF in terms of symmetric (Gaussian functions) and asymmetric (non-Gaussian functions), it is necessary to clarify the contribution to the depth resolution Δz (16-84%). According to the MRI model considered three physically meaningful effects contribution to the depth resolution function, a symmetric contribution to the depth resolution function originates from the intrinsic roughness and the surface roughening by ion sputtering, which both are described by a Gaussian smearing function (see Eq. 7.3), characterized by its standard deviation: the surface roughness parameter σ ($\Delta z_\sigma^2 = (2\sigma)^2 = (2\sigma_i)^2 + (2\sigma_s)^2$, where σ_i is the intrinsic roughness, σ_s is the sputter induced roughness.). For the asymmetric broadening functions, the atomic mixing is described by an exponential function (see Eq. 7.2) and this exponential function is characterized by the atomic mixing parameter w ($\Delta z_w = 1.668w$); the information depth of the Auger electrons (for AES) is also described by an exponential function (see Eq. 7.4) and this exponential function is characterized by the information depth parameter ($\Delta z = 1.668\lambda$). Thus, three parameters (σ, w and λ) suffice to characterize the total smearing, Δz (see Ref. [13]). Values for these three parameters may be obtained experimentally and/or calculated theoretically (see the section 7.4). Hence, on the basis of the MRI model fitting parameters, the total depth resolution can approximately be rewritten as [31]

$$\Delta z = \left((2\sigma)^2 + (1.668w)^2 + (1.668\lambda)^2 \right)^{1/2} \tag{7.7}$$

with σ, w and λ in nm.

Using the aforementioned fitted parameters in MRI model, the depth resolution Δz, as given by Eq. 7.7, for the as-deposited sample have been calculated as a function of the sputter depth in Fig. 7.10 as solid line. The fitted roughness σ for the as-deposited sample agrees very well with the *Rq* roughness values measured by AFM at the depth of z = 0 nm and z =100 nm as filled squares denoted in Fig. 7.10 and its corresponding twice value 2σ contribution in depth resolution, see the first term of right side in Eq. 7.7 is presented in Fig. 7.10 as dashed lines.

As is shown in Fig. 7.10, when the sputter depth increases, the values of depth resolution Δz approach the values of roughness 2σ. This result implies that the roughness was the dominant factor for the degradation of the depth resolution at the deeper sputtering depth. We should also note that the MRI fitting roughness parameter σ =5.0 nm at the depth *z* =100 nm was larger than the other two parameters (*w* =1.0 nm and λ=0.8 nm).

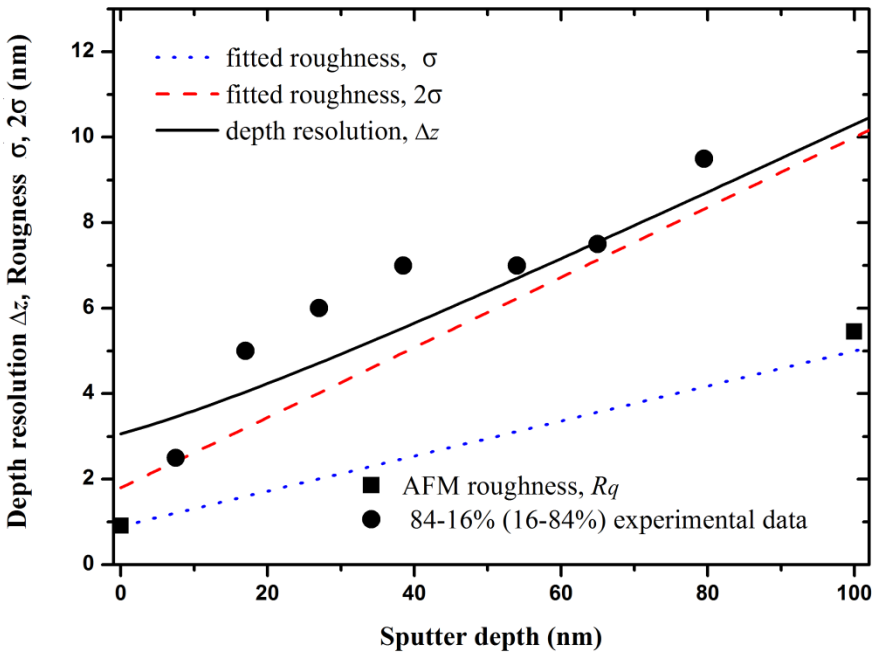

Figure 7.10: The depth resolution Δz (solid line) and the fitted roughness parameter σ and its double value 2σ (dotted and dashed lines, respectively) as a function of the sputter depth for the as-deposited sample. The filled circles and squares represent the values of the depth resolution by 84-16% (16-84%) method and the *Rq* roughness values determined by AFM (see Fig. 7.2), respectively.

In additional, the tendency of depth resolution in MRI calculation is in accordance with the one in experimental data by 84-16% (16-84%) method shown as filled circles in Fig. 7.10. This conforms further the capability of the MRI model with the linear roughness in the Ni/Cu polycrystalline multilayer structure. The calculated $\Delta z/2$ value of 4.1 nm at the last (deepest) Cu/Ni interface (corresponding to a depth of 78 nm) for the as-deposited sample is less than the thickness of the last sublayer Cu/Ni under present measurement conditions.

7.6 Summary

The MRI model with a roughness parameter that is linearly increasing with the sputtered depth was used for extracting the interdiffusion coefficients in Ni/Cu multilayer from measured AES depth profiles. The roughness values extracted from the depth profiling data fits agreed well with those measured by AFM. The interdiffusion in the Ni/Cu multilayer at the first Cu/Ni interface was determined as $D_o = 6.2 \times 10^{-13}$ m^2/s and Q = 101.4 kJ/mol, and at the last (deepest) Cu/Ni interface as $D_o = 6.3 \times 10^{-14}$ m^2/s and Q = 79.0 kJ/mol. The depth-dependent interdiffusion coefficients of the annealed samples were quantitatively evaluated with relating to the reduction of the activation energy at deeper depth during sputtering. Extents of interdiffusion characterized by diffusion length as small as a nanometre could be measured. The depth-dependent depth resolution upon depth profiling of the as-deposited polycrystalline Ni/Cu multilayer were quantitatively evaluated accordingly. The surface roughness induced by the ion bombardment was the dominant factor degradation of the depth resolution upon sputtering during AES depth profiling of polycrystalline Ni/Cu multilayer thin film.

References

[1] B.J. Thaler, J.B. Ketterson, J.E. Hilliard, Enhanced magnetization density of a compositionally modulated CuNi thin film, Phys. Rev. Lett. **41**(1978)336.

[2] M.C. Benoudia, F. Gao, J.M. Roussel, S. Labat, M. Gailhanou, O. Thomas, D.L. Beke, Z. Erdelyi, G. Langer, A. Csik, M. KisVarga, Thermoelasticity and interdiffusion in CuNi multilayers, Phys. Rev. B. **85** (2012) 235404.

[3] H. Barshilia, K. Rajam, Characterization of Cu/Ni multilayer coatings by nanoindentation and atomic force microscopy, Surf. Coat. Technol. **155** (2002) 195-202.

[4] X.L. Yan, J.Y. Wang, Size effects on surface segregation in Ni-Cu alloy thin films, Thin Solid Films **529** (2013) 483-487.

[5] X.Y. Zhu, X.J. Liu, R.L. Zong, F. Zeng, F. Pan, Microstructure and mechanical properties of nanoscale Cu/Ni multilayers, Mater. Sci. Eng. A **527**(2010) 1243-1248.

[6] J. Jeon, J.H. Hong, Y.P. Lee, Study of interdiffusion in Pd/Cu multilayered films by Auger depth profiling, J. Appl. Phys. **75** (1994) 7825-7828.

[7] T.C.Q. Noakes, P. Bailey, G. van der Laan, Site exchange in ultrathin layers of Ni on Cu (100) studied with element-specific layer-by-layer resolution, Phys. Rev. B. **67** (2003) 153401.

[8] C.M. Teodorescu, Low temperature two-dimensional behaviour of spin and orbital moments in Ni monolayers grown on Cu(001), Surf. Sci. **601** (2007) 4292-4296.

[9] A. Bukaluk, Analysis of diffusion mechanisms in thin polycrystalline Au-Ag films using auger electron spectroscopy, Surf. Interface Anal. **5** (1983)20-27

[10] P.M. Hall, J.M. Morabito, A formalism for extracting diffusion coefficients from concentration profiles, Surf. Sci. **54** (1976) 79-90.

[11] H.C. Swart, A.J. Jonker, C.H. Claassens, R. Chen, L.A. Venter, P. Ramoshebe, E. Wurth, J.J. Terblans, W.D. Roos. Extracting inter-diffusion parameters of TiC from AES depth profiles, Appl. Surf. Sci. **205** (2003) 231-239.

[12] W. Pamler, Application of Auger electron depth profile analysis to thin film interdiffusion studies, Appl. Phys. A **42** (1987) 219-226.

[13] S. Hofmann, Atomic mixing, surface roughness and information depth in high-resolution AES depth profiling of a GaAs/AlAs superlattice structure, Surf. Interface Anal. **21** (1994) 673-678.

[14] V. Kesler, S. Hofmann, Interdiffusion at Ge/Si interfaces studied with AES depth profiling, J. Surf. Anal. **9** (2002) 428-431.

[15] J.Y. Wang, E.J. Mittemeijer, A new method for the determination of the diffusion-induced concentration profile and the interdiffusion coefficient for thin film systems by Auger electron spectroscopic sputter depth profiling, J. Mater. Res. **19** (2004) 3389-3397.

[16] J.Y. Wang, A. Zalar, E.J. Mittemeijer, Depth dependence of the ion bombardment induced roughness and of the interdiffusion coefficient for Si/Al multilayers, Appl. Surf. Sci. **222** (2004)171-179.

[17] M. Cekada, M. Panjan, D. Cimpric, J. Kovac, P. Panjan, J. Dolinsek, A. Zalar, Analysis of the diffusion processes in Al/Cr, Al/Fe and Cr/Fe multilayers using the MRI model, Vacuum **84** (2010) 147-151.

[18] M.A. Noah, D. Flötotto, Z.M. Wang, E.J. Mittemeijer, Single and multiple profile fitting of AES and XPS intensity-depth profiles for analysis of interdiffusion in thin films, Surf. Interface Anal. **46** (2014) 1057-1063.

[19] C.L. Hedberg, Handbook of Auger Electron spectroscopy, *Third Edition,* Physical Electronics Industries, Eden Prairie, MN, USA 1976.

[20] S. Hofmann, Sputter depth profile analysis of interfaces, Rep. Prog. Phys. **61**(1998) 827-888.

[21] M.P. Seah, C. Lea, Depth resolution in composition profiles by ion sputtering and surface analysis for single-layer and multilayer structures on real substrates, Thin Solid Films **81** (1981) 257-270.

[22] J.F. Ziegler, TRIM Code, IBM Corporation, Yorktown Heights, New York, (http:// www.srim.org)

[23] NIST Electron EAL, 2001 *NIST Database* 82.

[24] R. Venos, W. Pamler, H. Hoffmann, Grain boundary diffusion in Ni-Cu multilayer films, Thin Solid Films **162** (1988)155-160.

[25] H.D. Joubert, J.J. Terblans, H.C. Swart, Extracting interdiffusion parameters from Ni/Cu thin films by means of profile reconstruction with the MRI model Surf. Interface Anal. **42** (2010)1281-1283.

[26] A.M. Abdul-Lettif, Investigation of interdiffusion in copper–nickel bilayer thin films, Phys. B **388** (2007) 107-111.

[27] S. Divinski, J. Ribbe, G. Schmitz, C. Herzig, Grain boundary diffusion and segregation of Ni in Cu, Acta Mater. **55** (2007) 3337-3346.

[28] T. Van Dijk, E.J. Mittemeijer, The effect of interdiffusion on moiré patterns of thin bimetallic films, Thin Solid Films **41** (1977) 173-178.

[29] A. Bukaluk, Auger electron spectroscopy investigations of the effect of degradation of depth resolution and its influence on the interdiffusion data in thin film Au/Ag, Cu/Ag, Pd/Au and Pd/Cu multilayer structures, Appl. Surf. Sci. **175-176** (2001) 790-796.

[30] A. Bukaluk, Influence of depth resolution on interdiffusion measurements in polycrystalline Cu/Pd multilayers, Surf. Interface Anal. **30** (2000) 597-602.

[31] J.Y. Wang, U. Starke, E.J. Mittemeijer, Evaluation of the depth resolutions of Auger electron spectroscopic, X-ray photoelectron spectroscopic and time-of-flight secondary ion mass spectrometric sputter depth profiling techniques, Thin Solid Films **517** (2009) 3402-3407.

Chapter 8

Surface segregation in a ternary Ni-Cu (S) alloys system

8.1 Introduction

Surface segregation is a well-known interface segregation phenomenon which has many academic and practical interests. Interface segregation (*i.e.* surface or grain boundary) is regarded as the redistribution of solute atoms between the interface and the bulk of a material resulting in a solute interface concentration, which is generally higher than the solute bulk concentration [1]. Interface segregation is not a new phenomenon, it was treated formally by Gibbs a century ago [2]. Today, interface segregation investigations have been applied in many aspects, for example, surface segregation influences adsorption and catalytic properties of the material [3-4]; grain boundary segregation is directly responsible for the processes of inter-crystalline corrosion, hydrogen and liquid metal embrittlement, and high and low-temperature fracture [5-10]. Especially, S impurity segregation is a common phenomenon in many metals and alloys. Grain boundary segregation of S can cause embrittlement of a metal or alloy due to the S-induced changes in the electronic structure that can lead to the weakening of atomic bonds between grain boundaries [8-10]. Surface segregation of S have been investigated in Ni-S, [11] Cu(In, S),[12] Fe-S, [13] Cu(Bi, S)[14], Cu(Sn, S) [15] and Ni-Cu(S)[16,17].

The Ni-Cu alloy system has been extensity investigated because of its application in catalysis and metallurgy [18]. It has a simple phase diagram and it forms a solid solution across the entire range of compositions. Therefore, surface segregation in Ni-Cu alloy system has been a subject of many investigations over more than thirty years [19-26]. Numerous models (methods) have been (or can be) used for simulating segregation in Ni-Cu alloy system, for example: Monte Carlo [19], electronic-structure based methods [20] and the Langmuir-Mclean model [21]. All the above models predict that Cu atoms will segregate to the surface (for the entire compositions range) of a Ni-Cu alloy. This prediction has been verified experimentally by X-ray photoelectron spectroscopy (XPS) [22], atom probe field ion microscopy (AP-FIM) [23], ion-scattering-spectroscopy (ISS) [24], low-energy ion scattering (LEIS) [25] and Auger electron spectroscopy (AES) [26].

A successful thermodynamic description of equilibrium segregation in ternary alloys was formulated by Guttmann [27] who included the interaction between the segregating atoms and the bulk atoms as described in a regular solution model. The kinetics of segregation is mainly controlled by diffusion of segregating species in the bulk. McLean [28] gave the first simple approach to solve this problem. The Modified Darken model proposed by du Plessis and van Wyk [1] based on the Darken approach, which is a unified model giving the full description of surface segregation from kinetics to equilibrium in combination with the regular solution approximation and sub-regular solution approximation. This model has been successfully used in the equilibrium and kinetic surface segregation and linear heating measurements in the binary and ternary system [12-14, 29-31]. In this chapter, the surface segregations of Cu and S from a ternary Ni-Cu(S) alloy system will be measured using AES with both the linear temperature programmed heating and constant temperature heating method in Ni-18.7at.%Cu(S) alloys. The segregation measured data was used to extracted for the segregation parameters, namely, segregation energy, interaction energy and diffusion coefficient (pre-exponential and activation energy) with a theoretical segregation model (modified Darken model). The result in this study will be further compared with experimental data values obtained from others literature.

8.2 Experimental

Ni-Cu alloy crystals used in this study were order from Mat-Cn Company (China) with six different Cu concentrations (0, 18.7, 38.1, 58.1, 78.7 and 100 at.%, purity 99.99+ at.%). The Ni-18.7at.%Cu alloy crystal used for the segregation study contained 0.0007at.% S as an impurity. Prior to analysis, the Ni-18.7at.%Cu alloy crystal was mechanically polished to a surface roughness of $\leq$ 0.05 μm using a diamond suspension. The Ni-18.7at.%Cu alloy crystal was then mounted on a resistance heater with a built-in chromel-alumel thermocouple (Type K) directly at the back of crystal. The back side temperature was calibrated in terms of the *true surface* temperature using a second thermocouple that was pressed into the surface of a dummy copper sample. Once the calibration was completed the Ni-18.7at.%Cu alloy crystal was placed in front of the Auger analyser.

The surface segregation measurement of the Ni-18.7at.%Cu(S) ternary alloy crystal was performed with a PHI 590 Scanning Auger Microscope (SAM) at a base pressure of 2×10^{-9} Torr. The experimental detail is given in Chapter 4 but some important parameters are given here again. A static primary electron beam of 5 keV and beam current of 0.7 μA with beam size diameter of 13.4 μm was used for the AES measurements, the modulation energy was 2.0 eV, the scan rate was 5.0 eV/s and the time constant was set at 0.1 s. The ion gun sputter (for cleaning) was performed with 2 keV Ar^+ ion, the argon pressure was 2.0×10^{-3} Pa and the ion beam was rastered over a 2×2 mm^2 area, which is much larger than the Auger primary electron beam diameter (13.4 μm) to avoid the influence from the lateral surface diffusion of impurities. The ion beams and the electron beams were aligned to the same position in the centre of the analysis area using a Faraday cup. The crystal was tilted with the normal of the crystal surface at a 30 ° angle with respect to the direction of the incident electron beam.

Surface segregations were measured with both linear and constant temperature heating methods. Before these segregation measurements, the ternary Ni-Cu(S) alloy crystal was first sputter cleaned at room temperature, then the temperature was increased to 727 K and sputter cleaned and then cold to room temperature, the

cleaning procedure was repeated few times to clean the surface by removing the impurity (*i.e.* C, O, and N) on the surface. The alloy crystal was then annealed at 961 K for 24 h to restore the initial condition of the crystal (uniform bulk concentration) and cooled to 423 K at rate of -0.05 K/s. Fig. 8.1 shows Auger spectrums of the surface before and after the 24 h annealing. After the reconditioning heat treatment the segregation measurements were performed by either linear or constant temperature heating.

For linear temperature heating measurements, the ternary Cu-Ni(S) alloys was pre-heated at the initial temperature of 423 K for 1 h and sputter cleaned for exactly 30 s. Then the linear temperature heating was immediately carried out in the temperature range 423-1121 K at a constant heating rate of 0.02 K/s. Auger spectrums were recorded as a function of temperature for the Auger peaks of Ni, Cu, S, C and O. The low energy peaks of Ni and Cu are overlapped and they were recorded as one region that ranging from 40-130 eV, the S peak was recorded from 131-239 eV, the C peak was recorded from 240-275 eV, the O peak was recorded from 480-529 eV and then the high energy peaks of Ni and Cu overlapped and both were recorded from 680-950 eV. After the linear temperature heating measurement running, the crystal was pre-heated at 961 K for 24 h again to restore the initial condition of the crystal (uniform bulk concentration) and then cooled to 423 K at rate of -0.05 K/s.

The constant temperature measurements were carried out between 770 K and 860 K at 30 K intervals. The ternary Cu-Ni(S) alloy crystal was heated to the desired temperature, and after stabilization of the temperature ternary Cu-Ni(S) alloy crystals was sputtered cleaned for exactly 30 s. The Auger spectrums for the Auger peaks of Ni, Cu, S, C and O were recorded as a function of time. The monitored Auger peak ranges were the same as for linear heating measurement (see previous paragraph). Again, after each constant temperature heating measurement running, the crystal was pre-heated at 961 K for 24 h and then cooled to 423 K at rate of -0.05 K/s.

The surface segregation measurement data was quantified using the method discussed in Chapter 4. Some important points are discussed again here. In the quantification, the sensitivity factors of Cu, Ni and S were determined from the pure elemental standards under the identical measurement conditions, the backscattering factor were

calculated from Shimizu [32], the inelastic mean free path were calculated with the TPP-2M formula [33] and the segregated layer thickness *d* values was obtained from X-ray diffraction (XRD) (see the section 8.3.1). It was assumed that segregation of the Cu and S is restricted to a monolayer on the surface and that the concentration of Cu and S beneath the surface layer is equal to the bulk concentration.

The crystalline structure of the $Ni_{1-x}Cu_x$ alloys (x = 0, 0.187, 0.381, 0.581, 0.787 and 1) were characterized by XRD, which used a Cu anode and monochromatic X-rays (Ni-filter) with a wavelength of λ = 0.15406 nm. The diffraction angle (2θ) was scanned from 42 °to 78 °with a step size of 0.01 °and the X-ray photons counted for 0.5 s at each step.

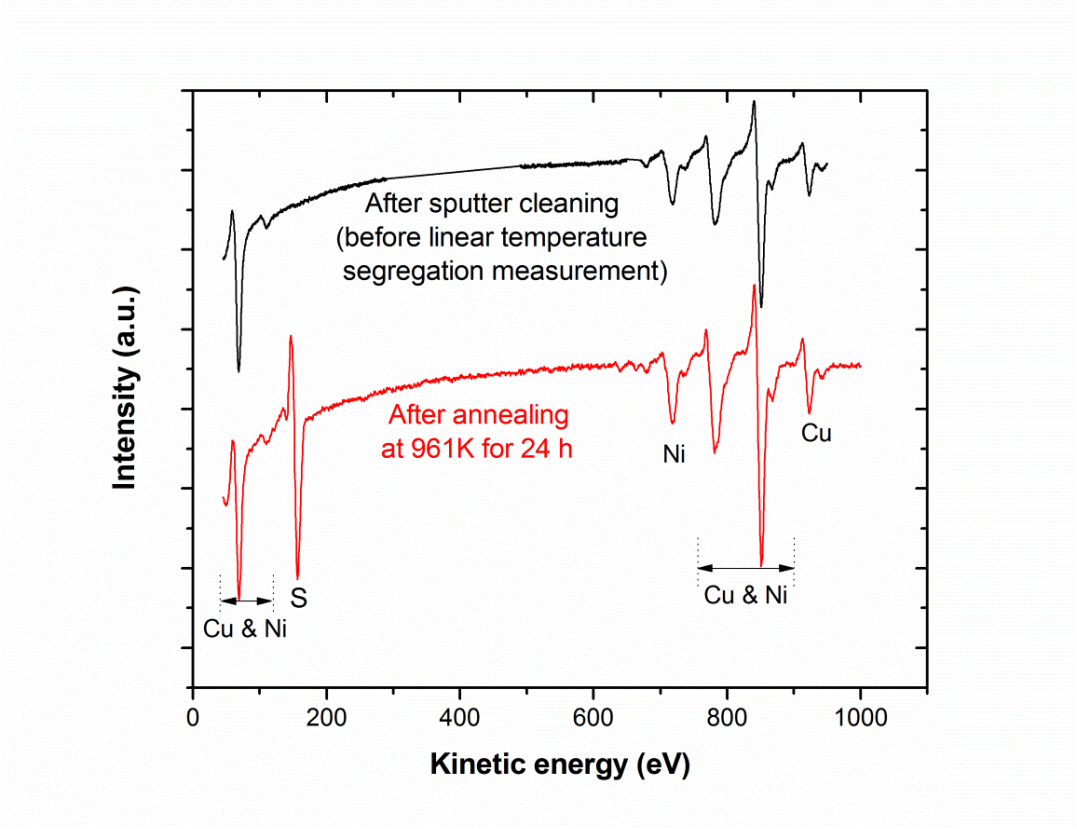

Figure 8.1: Auger spectrum of a Ni-Cu(S) ternary alloy annealing at 961 K for 24 h and after sputter cleaning with Ar^+ ion (before the segregation measurement).

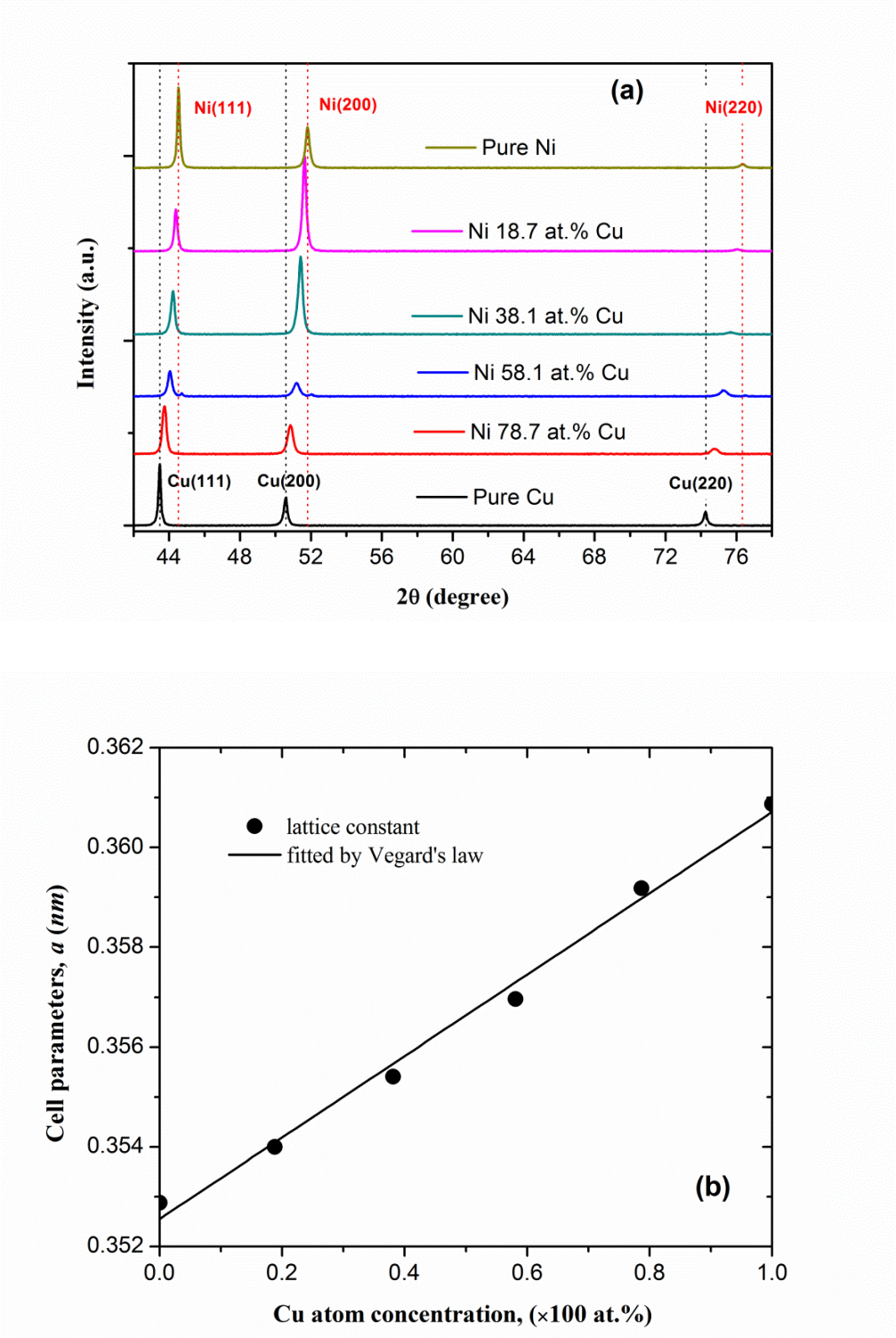

Figure 8.2: (a) XRD patterns of $Ni_{1-x}Cu_x$ alloys crystalline structure with 2θ range of 42-78 degree. The dashed lines with black and red colour are the pure copper and pure nickel reflection peaks position, respectively. (b) The values of cell parameter *a* with variation Cu atomic fractional concentration in the $Ni_{1-x}Cu_x$ alloy. The solid line is a best fit of the cell parameters using the Vegard's law.

8.3 Results and discussion

8.3.1 XRD data

Fig. 8.2(a) shows that the XRD patterns of the $Ni_{1-x}Cu_x$ alloys (x= 0, 0.187, 0.381, 0.581, 0.787 and 1) consist of broad diffraction peaks, covering the (111), (200) and (220) reflections peak, which match those of the face-centred cubic (fcc) polycrystalline Ni-Cu alloys phase. On close inspection of Fig. 8.2(a) it was found that there is a progressive shift in the Ni-Cu peak positions towards larger 2θ angles with a decreasing Cu concentration.

The cell parameter (a) are related to Miller indexes (hkl) of each reflection plane and inter-planar distance (d_{hkl}). The $Ni_{1-x}Cu_x$ alloy is cubic structures and the lattice parameter (a) can be calculated with:

$$a = 2d_{hkl}\sqrt{h^2 + k^2 + l^2} \tag{8.1}$$

where inter-planar distance (d_{hkl}) can be obtained from Bragg's law:

$$n\lambda = 2d_{hkl}\sin\theta_{hkl} \tag{8.2}$$

where n is an integer that indicates the order of the reflection, θ_{hkl} is the Bragg angle and d_{hkl} is the different space in polycrystalline materials.

The cell parameters are also calculated with Eqs. 8.1 and 8.2 for the reflection plane (111) as shown in Fig. 8.2(b) as solid black circles. The cell parameter dependence with alloy composition obey Vegard's law the solid line shown in Fig. 8.2(b), which is an indication that the Ni-Cu alloy forms a solid solution for the entire range of composition.

In additional, the average values of d for the polycrystalline $Ni_{0.813}Cu_{0.187}$ alloys with (111), (200) and (220) reflections peak (see in Fig. 8. 2(a)) was obtained as 0.194 *nm* from Eq. 8.2, which is used as the thickness for segregated layer for the

Ni-18.7at.%Cu(S) ternary alloy.

8.3.2 Surface segregation measurement with linear temperature

Fig. 8.3 shows the surface segregation of Cu and S as a function of the temperature with a linear heating rate of 0.02 K/s for the Ni-18.7at.%Cu(S) ternary alloys. Similar experimental results with the linear heating method have also been found for Cu(In, S) [12] and Cu(Sn, Sb) ternary alloys [31].

Four different regions can be distinguished in the Fig. 8.3. In region A (Fig. 8.3) the surface concentration of Cu and S are almost flat at these low temperatures and the bulk diffusion rate of Cu and S are very low in this region. In region B, the Cu surface concentration increases with increasing temperature and reached a maximum surface concentration of 41.4 at.%. This region is regarded as the Cu kinetic region and is used to extract the Cu diffusion coefficient with Fick's model. It should be pointed out that the maximum surface concentration of Cu is determined by its segregation energy and the interaction energy between the Cu, S and Ni according to the surface segregation theory (*i.e.* modified Darken model). In region C, the S surface concentration start to increase with increasing the temperature and the Cu surface concentration simultaneously decreases with increasing temperature. As the S segregate to the surface it replaced the Cu atom from the surface. This phenomenon is a result of the S segregation energy that is more negative than that for Cu. This region is regarded as the S kinetic region and used to extract the S diffusion coefficient with Fick's model. In region D, the S surface concentration reached a maximum values of 17.1 at.% and the Cu surface concentration stabilise close to the bulk concentration after being displaced by S. This stable region is regarded as the equilibrium region and is used to extract the segregation parameters (segregation energy ΔG and interaction energy Ω) using the Guttmann model. The data suggest that there is a large difference between the segregation energies for Cu and S according to the Guttmann model. Swart et al. [29] have demonstrated that a repulsive interaction between two segregating species (Cu and S in this study) resulting in a higher equilibrium concentration of S and a lower equilibrium concentration of Cu. Therefore, the interaction between the Cu and S atoms should be repulsive.

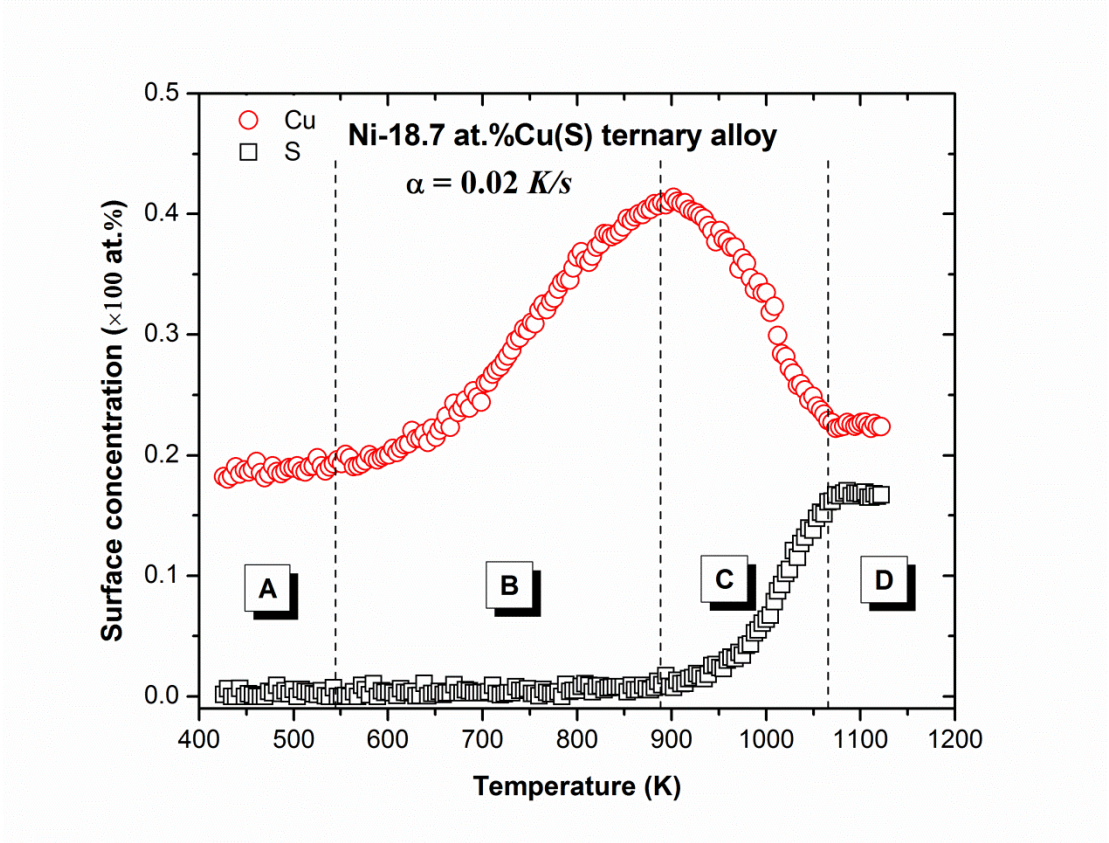

Figure 8.3: Surface segregation of Cu and S as a function of the temperature with a linear heating rate of 0.02 K/s for the Ni-18.7at.%Cu(S) ternary alloys. Four different regions can be distinguished and marked as A, B, C and D region.

Fick's model fittings:

The modified semi-infinity Fick's model was described in detail in Chapter 2 (section 2.3.1), and only the final result is presented here (by Eq. 8.3). Eq. 8.3 is used to fit the segregation data.

$$\frac{1}{2}\beta^2 = \frac{2D_o}{\pi\alpha d^2}\int_{T_0}^{T_E}\exp(-Q/RT)dT \qquad (8.3)$$

where β is surface enrichment factor ($\beta=(C^S - C^B)/C^B$ with the C^S the surface concentration of Cu and S, C^B the bulk concentration of Cu), α is the heating rate (0.02 K/s for this work), d is the thickness of the segregated layer taken as 0.194 nm

(see section 8.3.1), D_o is the pre-exponential factor, Q is the activation energy and R is the universal gas constant with a value of 8.314 kJ/mol.

The modified Fick semi-infinite model (Eq. 8.3) was employed to fit the kinetic regions in the experimental data of Cu and S (regions B and C in Fig. 8.3). The diffusion coefficients, pre-exponential factor D_o and the activation energy Q, were extracted from the best fit of Eq. 8.3 for both Cu and S as shown in Fig. 8.4. The diffusion of Cu in the Ni-18.7at.%Cu(S) ternary alloys was determined as D_o = 5.8×10^{-14} m^2/s and Q = 138.5 kJ/mol, and the S in the Ni-18.7at.%Cu(S) ternary alloys containing S concentration 0.0007 at.% as D_o = 8.5×10^{-3} m^2/s and Q = 222.0 kJ/mol.

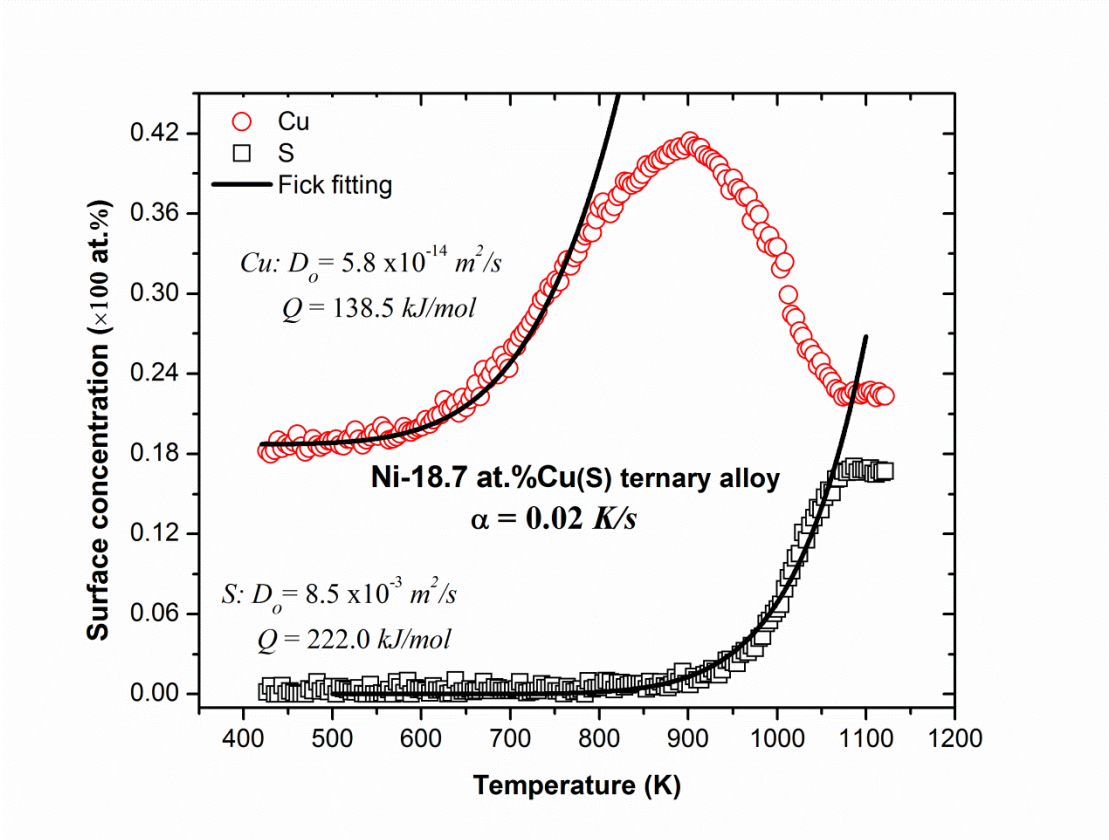

Figure 8.4: Surface segregation of Cu and S as a function of the temperature with a linear heating rate of 0.02 K/s for the ternary Ni-18.7at.%Cu(S) alloys. The solid lines are the best fits of the modified semi-infinity Fick's model (Eq. 8.3) which yields the diffusion parameters (pre-exponential factor D_o and activation energy Q) for both Cu and S in the ternary Ni-Cu(S) alloys.

Guttmann model fitting:

The Guttmann model was described in detail in Chapter 2 (section 2.2.3), and only the main equations are presented here (Eqs. 8.4-8.7) for clarity.

$$C_{Cu}^{S} = \frac{C_{Cu}^{B}\exp(\Delta G_{Cu}^{'}/RT)}{1-C_{Cu}^{B}+C_{Cu}^{B}\exp(\Delta G_{Cu}/RT)-C_{S}^{B}+C_{S}^{B}\exp(\Delta G_{S}/RT)} \quad (8.4)$$

$$C_{S}^{S} = \frac{C_{S}^{B}\exp(\Delta G_{S}^{'}/RT)}{1-C_{S}^{B}+C_{S}^{B}\exp(\Delta G_{S}/RT)-C_{Cu}^{B}+C_{Cu}^{B}\exp(\Delta G_{Cu}/RT)} \quad (8.5)$$

with

$$\Delta G_{Cu}^{'} = \Delta G_{Cu} + 2\Omega_{CuNi}(C_{Cu}^{s}-C_{Cu}^{B}) + \Omega'(C_{S}^{B}-C_{S}^{S}) \quad (8.6)$$

$$\Delta G_{S}^{'} = \Delta G_{S} + 2\Omega_{SNi}(C_{S}^{s}-C_{S}^{B}) + \Omega'(C_{Cu}^{B}-C_{Cu}^{S}) \quad (8.7)$$

where $\Omega' = \Omega_{CuS} - \Omega_{CuNi} - \Omega_{SNi}$, C_{Cu}^{s} and C_{S}^{s} are the surface concentrations of Cu and S, respectively, C_{Cu}^{B} and C_{S}^{B} are the bulk concentrations of Cu and S, respectively, Ω_{CuS} is the interaction energy of Cu and S, Ω_{CuNi} is the interaction energy of Cu and Ni and Ω_{SNi} is the interaction energy of S and Ni. ΔG_{Cu} and ΔG_{S} are the surface segregation energy of Cu and S, respectively.

The Guttmann model (Eqs. 8.4 and 8.5) was employed to fit the Cu and S equilibrium regions of the experimental data (region D in Fig. 8.3) and from the best fits, the segregation energies ΔG and the interaction energies Ω were extracted for both Cu and S. The best fits on the equilibrium data are shown in Fig. 8.5. The parameters determent by fitting the data with the Guttmann equations (Fig. 8.5) are ΔG_{Cu} = -37.1 kJ/mol, ΔG_{S} = -135.0 kJ/mol and $\Omega_{Cu\text{-}Ni}$=8.0 kJ/mol, $\Omega_{S\text{-}Ni}$=28.1 kJ/mol and $\Omega_{Cu\text{-}S}$=-10.3 kJ/mol.

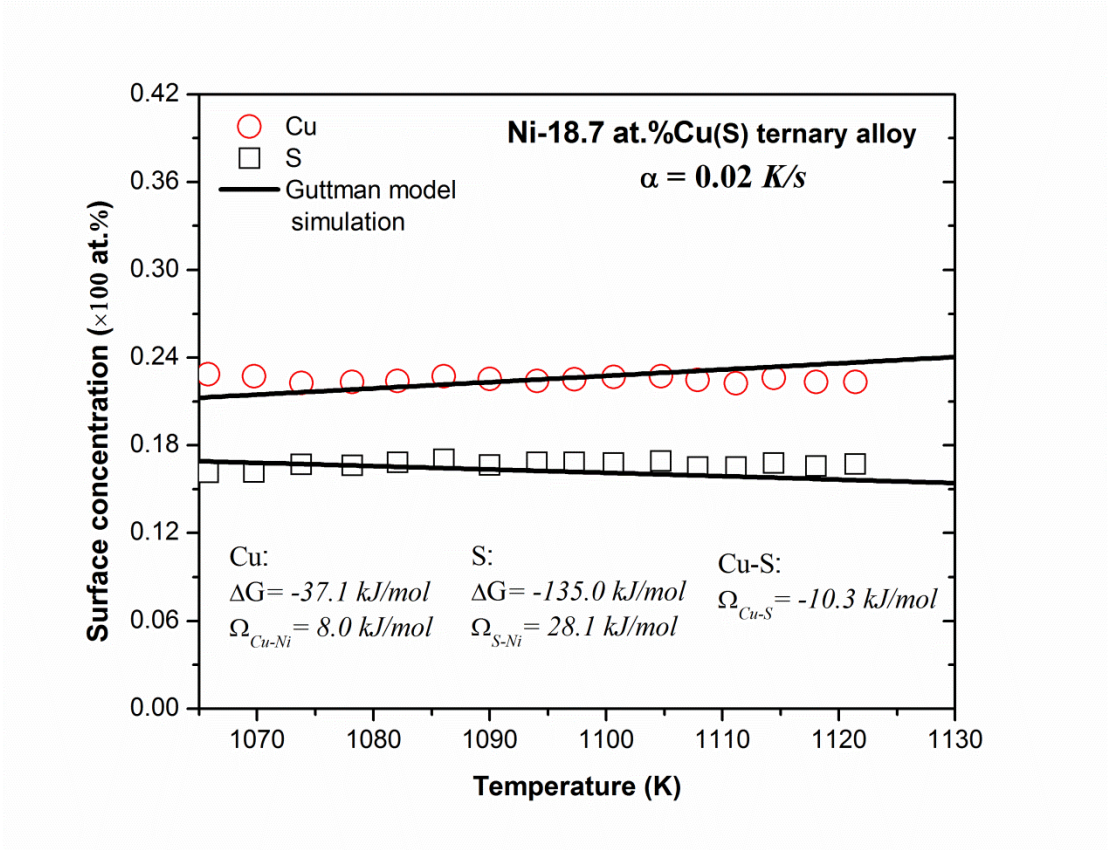

Figure 8.5: Surface segregation of Cu and S as a function of the temperature with a linear heating rate of 0.02 K/s for the Ni-18.7at.%Cu(S) ternary alloys. The solid lines are the best fits of the Guttmann model (Eqs. 8.4 and 8.5) which yields the segregation parameters, segregation energy ΔG and interaction energy Ω, for both Cu and S in the Ni-Cu(S) ternary alloys.

The modified Darken model simulation:

The modified Darken model was described in detail in Chapter 2 (section 2.3) and only the final result is presented here (Eq. 8.8). The modified Darken model is a unified model giving a full description of surface segregation from kinetics to equilibrium. Therefore, the segregation parameters, segregation energy ΔG, interaction energy Ω and diffusion coefficient (pre-exponential D_o and activation energy Q), can be obtained with modified Darken model. It is a complete description (simulation) for segregation.

$$
\begin{aligned}
&\frac{\partial C_i^S}{\partial t} = \frac{D_i C_i^{B_1}}{RTd^2}\Delta\mu_i^{B_1,S} \\
&\frac{\partial C_i^{B_1}}{\partial t} = \frac{D_i C_i^{B_2}}{RTd^2}\Delta\mu_i^{B_2,B_1} - \frac{D_i C_i^{B_1}}{RTd^2}\Delta\mu_i^{B_1,S} \\
&\vdots \\
&\frac{\partial C_i^{(j)}}{\partial t} = \frac{D_i C_i^{(j+1)}}{RTd^2}\Delta\mu_i^{(j+1,j)} - \frac{D_i C_i^{(j)}}{RTd^2}\Delta\mu_i^{(j,j-1)} \\
&\vdots \\
&\frac{\partial C_i^{(N)}}{\partial t} = -\frac{D_i C_i^{B_N}}{RTd^2}\Delta\mu_i^{B_N,B_{N-1}}
\end{aligned}
\tag{8.8}
$$

where species i is Cu and S, j=1, 2,…, N+1. C_i^S is the surface concentration of Cu (or S), and C_i^{B1} is the first bulk concentration of Cu (or S), D is the diffusion coefficient of Cu (or S), d is the thickness of the segregated layer and the temperature $T=T_o+\alpha t$, T_o is the initial heating temperature of segregation measurement as 423 K in this study, t is the heating time and α is the constant heating rate of 0.02 K/s.

Using the values of the parameters D_o, Q, ΔG and Ω extracted from the best fits of the Fick and Guttmann models as the initial fitting parameters in the modified Darken model, the profiles that best simulate the measured segregation data were calculated for the heating rates of 0.02 K/s as shown in Fig. 8.6. The parameters of the modified Darken model calculations fitted to the segregation profiles data in Fig. 8.6 are listed in Table 8.1.

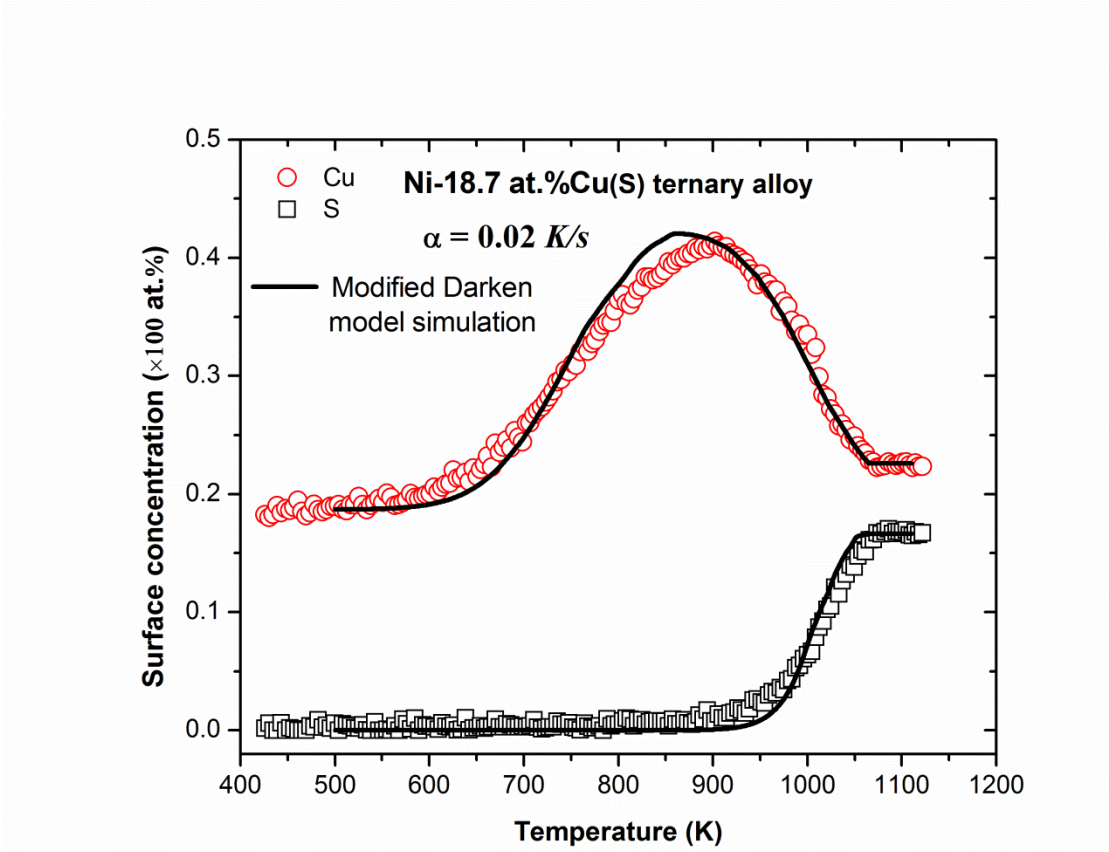

Figure 8.6: Surface segregation of Cu and S as a function of the temperature with a linear heating rate of 0.02 K/s for the Ni-18.7at.%Cu(S) ternary alloys. The solid lines are the simulation of the modified Darken model (Eq. 8.8) with surface segregation parameters of the Ni-Cu(S) ternary alloys listed in Table 8.1.

Table 8.1: surface segregation parameters used in the modified Darken model (Eq. 8.8) simulation (shown in Fig. 8.6) and compared with others group from literatures.

Segregation parameter	Segregation species		Ref.[18]	Ref.[34]
	Cu	S		
Activation energy, Q (kJ/mol)	145.2	224.0		
Pre-exponential factor, D_o (m^2/s)	8.6×10^{-14}	9.2×10^{-3}		
Segregation energy, ΔG_{Cu} (kJ/mol)	-36.1		-29.8	
Segregation energy, ΔG_S (kJ/mol)		-136.0		-135.0
Interaction energy, Ω_{CuNi} (kJ/mol)	7.6		14.4	
Interaction energy, Ω_{SNi} (kJ/mol)		28.1		
Interaction energy, Ω_{CuS} (kJ/mol)	-10.3			

As listed in Table 8.1, it is clearly that the activation energy of Cu (Q = 145.2 kJ/mol) is much lower than that of S (Q = 224.0 kJ/mol). As a result, the Cu segregates first (before S) at lower temperatures in the Ni-18.7at.%Cu(S) ternary alloy. The maximum surface concentration of Cu of 41.4 at.% is determined by the surface segregation energy for Cu (ΔG_{Cu} = -36.1 kJ/mol), the attractive interaction between the Ni and Cu atoms (Ω_{NiCu} = 7.6 kJ/mol) and the repulsive interaction between the Cu and S atoms (Ω_{CuS}= -10.3 kJ/mol). The value of the surface segregation energy for Cu on Ni (ΔG_{Cu} = -36.1 kJ/mol) agrees with the experimental results reported for atom probe-field ion microscopy (see also Table 8.1) [18]. They observed a depletion of Cu in the near-surface atomic planes for a Ni-4.6 at.%Cu sample. The attractive interaction between the Cu and Ni atoms set a preference for unlike first-neighbour bonds formation between the Cu and Ni atoms and that proposes that a Cu atom prefers to be surrounded by Ni atoms in the Cu-Ni system. It is known from the Cu-Ni binary phase diagram that Cu-Ni alloys can be form a solid solution for the entire range of composition [18]. The value of attractive interaction between the Cu and Ni atoms Ni (Ω_{NiCu} = 7.6 kJ/mol) agrees with the experimental results using atom probe-field ion microscopy (Ω_{NiCu} = 14.4 kJ/mol) (see Table 8.1) [18]. Strong repulsion energy between the Cu and S atoms shows less or no tendency of Cu-S atomic bonds formation. At the segregation equilibrium (region D in Fig. 8.3), a high surface enrichment of S is determined by its lower surface segregation energy (more negative) (ΔG_S = -136.0 kJ/mol), the attractive interaction between the S and Ni atoms (Ω_{NiS}= 28.1 kJ/mol) and the repulsive interaction between the S and Cu atoms (Ω_{CuS}= -10.3 kJ/mol). A much more negative surface segregation energy for S is the reason why S stay on the surface. There is a large difference in the segregation energies for Cu (ΔG_{Cu} = -36.1 kJ/mol) and S (ΔG_S = -136.0 kJ/mol) and that explains the displacement of Cu in the surface layer by S (the segregation of S is more energetically favourable than that of Cu). Similar to the attractive interaction between the Cu and Ni atoms and a strong attractive interaction between the Cu and S atoms set a preference for unlike first-neighbour bonds formation between the Cu and S atoms. The value of the surface segregation energy for S segregating from Ni (ΔG_S = -136.0 kJ/mol) agree with the experimental results obtained by AES (see also Table 8.1) [18]. They observed a depletion of S from the near-surface atomic planes for a Ni (S =200 ppm at.%) sample.

8.3.3 Surface segregation measurement with constant temperature

Fig. 8.7(a-d) shows the surface concentration of Cu and S that was measured as a function of the annealing time for the Ni-18.7at.%Cu(S) ternary alloys annealed at the constant temperature 770 K, 800 K, 830 K and 860, respectively. From these profiles in Fig. 8.7, it is clear that initially both Cu and S segregated to the surface and it is also clear that the segregation rate of Cu is higher than that of S. The higher segregation rate of Cu is due to high bulk concentration of Cu (18.7 at.%), which is much higher than that of S (0.0007 at.%), and the lower activation energy of Cu (Q = 145.2 kJ/mol), which is lower than that of S (Q = 224.0 kJ/mol). The Cu segregated to surface until it reached a maximum concentration of about 33.0 at.% (see in Fig. 8.7), and at this point Cu started to desegregate with slower rate. It can be seen clearly in Fig. 8.7(c) and Fig. 8.7(d) that at the higher temperatures the S segregation is increasing and S atoms are replacing Cu atoms on the surface, which can be explained by surface segregation energy for S in Ni (-136.0 kJ/mol) it is much more negative than the segregation energy for Cu in Ni (-36.1 kJ/mol) (see Table 8.1).

It is assumed that the influence of the atom interaction between Cu, Ni and S is very small at the initial phase of segregation when the segregated concentration is very low. These behaviours have also been demonstrated by Swart *et al.*[29]. Therefore, the semi-infinite solution of Fick's equation can be used to describe the *bulk-to-surface* segregation rates of Cu and S in the ternary Ni-Cu(S) system in Fig. 8.7. To get a more accurate interpretation of the segregation profiles data, the modified semi-infinite solution of Fick's equation (Eq. 8.9) used to fit the constant temperatures data. Note that Eq. 8.9 also compensate for the segregation that occur during the sputtering [35].

$$C^S = C_0^S + C^B\left[1+\frac{2}{d}\left(\frac{D(t+t_0)}{\pi}\right)^{1/2}\right] - C^B\left[\frac{2}{d}\left(\frac{Dt_0}{\pi}\right)^{1/2}\right] \qquad (8.9)$$

where C^S and C^B are the surface concentration and bulk concentration, D is the diffusion coefficient, d is the thickness of a segregated layer, t_0 is the sputtering time (in this study t_0 =30 s), C_0^S is the concentration of the atoms that segregated to the surface but that had not sputtered, as a fitting parameters in the fits. Parameters C_0^S

and D are used as the fitting parameters for the best fit to the experimental surface segregation data.

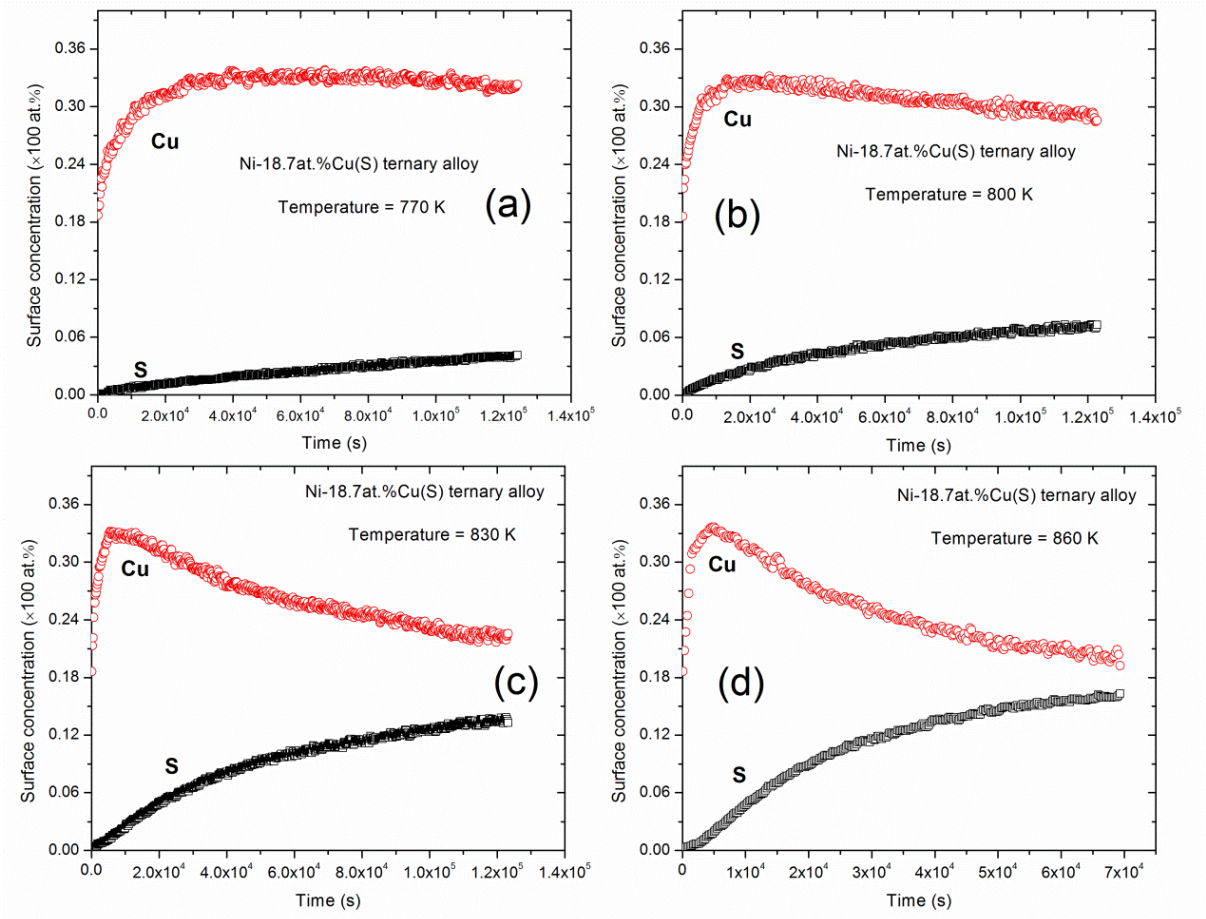

Figure 8.7: Surface segregation of Cu and S in the Ni-18.7at.%Cu(S) ternary alloys at the constant temperature of (a) 770 K, (b) 800 K, (c) 830 K and (d) 860 K.

The solid lines in the Fig. 8.8 are the best fits on the surface segregation data utilizing the modified semi-infinity Fick's model (Eq. 8.9). The diffusion coefficients (D) for Cu in the Ni-Cu(S) alloy that were obtained from the fitting (shown in Fig. 8.8) are listed in Table 8.2. The corresponding values of the diffusion parameters, the pre-exponential factor D_o and the activation energy Q, as obtained from a linear fit on the data in the Arrhenius plot, $D = D_o \exp(-Q/RT)$, are indicated in Fig. 8.9. In Fig. 8.9 the measured diffusion parameters are also compared with the literature values listed in Table 8.3. The diffusion parameters of Cu in the Ni-Cu(S) ternary alloy was determined as D_o = 5.8×10^{-14} m^2/s and Q = 160.1 kJ/mol which are in good comparison with those bulk

diffusion parameters from literature as shown in Fig. 8.9. It should be pointed out that the dash-dotted blue colour line was measured with tracer method for Ni-15at.%Cu polycrystalline alloy at a higher temperature range 1379 K to 1618 K [37]. The dash-dot-dotted pink colour line was for a Cu in a Ni polycrystalline alloy also measured at a higher temperature range 1080 K to 1613 K [38]. In additional, the diffusion parameters of Cu in the Ni-Cu(S) ternary alloy determent with the linear temperature heating method was $D_o = 8.6 \times 10^{-14}$ m^2/s and $Q = 145.2$ kJ/mol and is also shown in Fig. 8.9. The activation energy Q values of 160 kJ/mol obtained in this study is much higher than that value of 79.0 kJ/mol, which obtained interdiffusion parameters for polycrystalline Cu/Ni multilayer thin films (that was measured with AES depth profiling). The very low activation energy as determent for interdiffusion of the Cu/Ni multilayer thin films (that occurred in the temperature range of 598 - 648 K) is associated with the grain boundary diffusion mechanism [36].

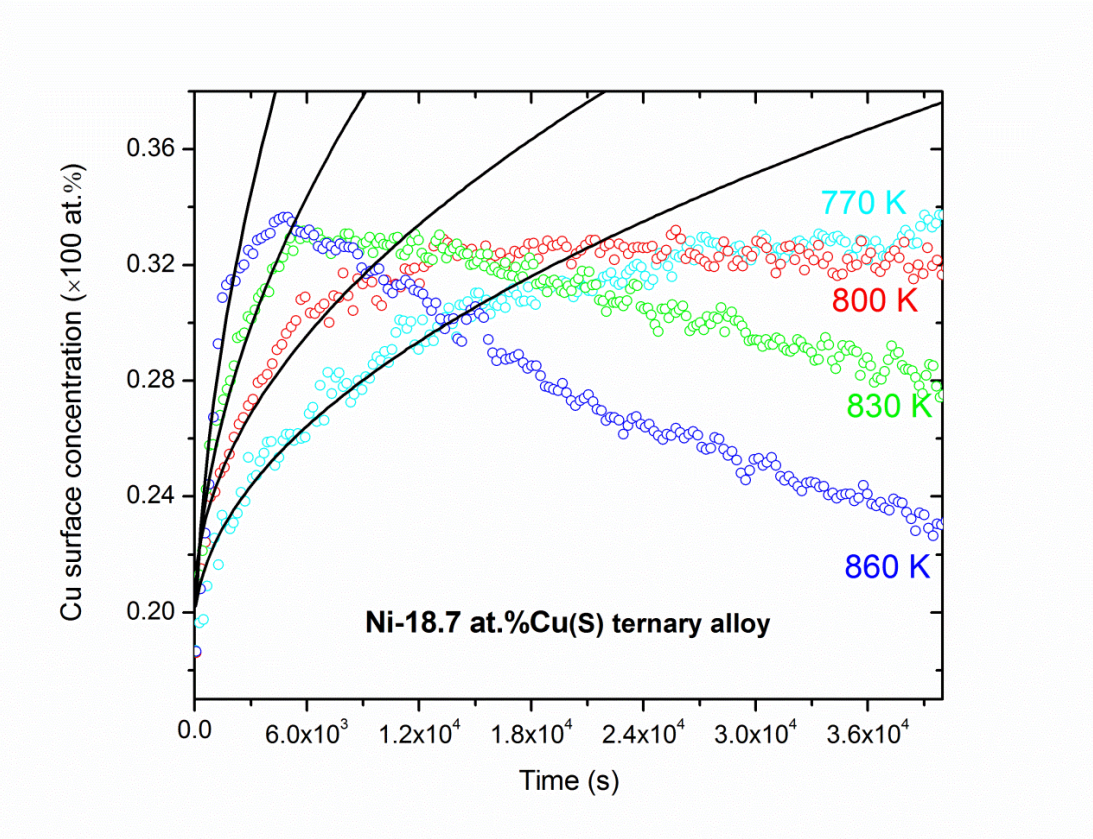

Figure 8.8: Cu surface segregation in the Ni-18.7at.%Cu(S) ternary alloys at the constant temperature of (a) 770 K, (b) 800 K, (c) 830 K and (d) 860 K. The solid lines are the best fits of the modified semi-infinity Fick's model (Eq. 8.9) which yields the diffusion coefficients (D) for Cu in the Ni-Cu(S) ternary alloys.

Table 8.2: The diffusion coefficients for Cu diffusion in Ni-18.7at.%Cu(S) calculated from the segregation profiles in Fig. 8.8, obtained for various temperatures.

Temperature, (K)	Diffusion coefficients, D (m^2/s)
770	9.95×10^{-25}
800	1.68×10^{-24}
830	4.72×10^{-24}
860	1.20×10^{-23}

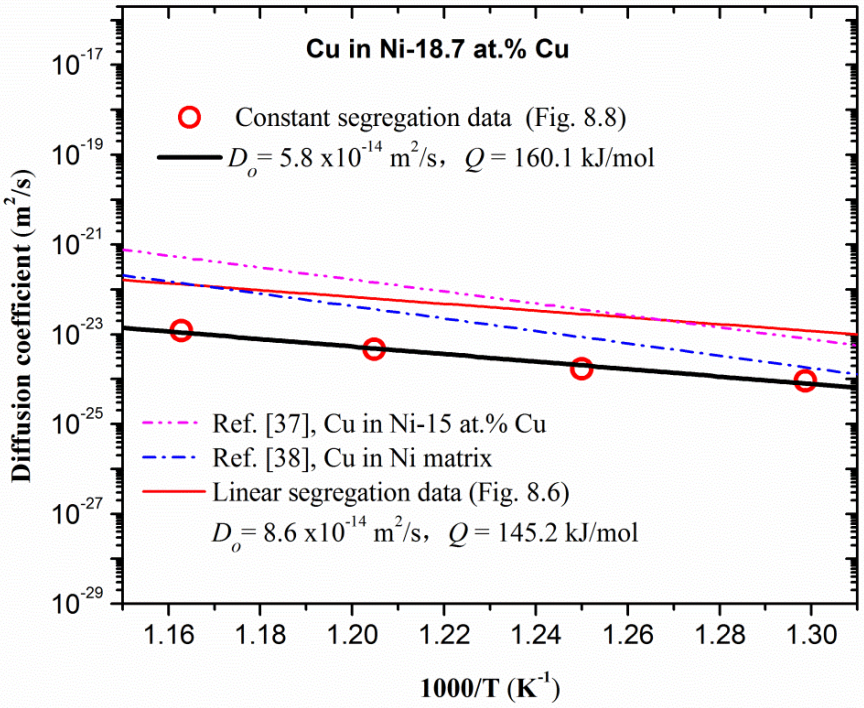

Figure 8.9: Arrhenius plots for the Cu diffusion in Ni-18.7at.%Cu(S) and the corresponding Cu or Ni bulk diffusion in Ni crystal listed in Table 8.3. The open circles represent the values of diffusion coefficients extracted from the Fig. 8.8.

Table 8.3: Diffusion parameters obtained for Cu diffusion in Ni-Cu calculated from Fig. 8.10 and from literatures.

Source	Pre-exponential factor, D_o (m^2/s)	Activation energy, Q (kJ/mol)	Temperature range, (K)	Method/Remarks
This study (Constant)	**5.8 ×10^{-14}**	**160.1**	**770-860**	**Polycrystalline, AES surface segregation**
This study (Linear)	**8.6 ×10^{-14}**	**145.2**	**560-896**	
Interdiffusion Ref.[36]	6.3 ×10^{-14}	79.0	598-648	Multilayer films, AES depth profile
Cu in Cu-Ni Ref.[37]	1.5 ×10^{-6}	264.0	1379-1618	Polycrystalline Cu-Ni alloy, Trace
Cu in Ni Ref.[38]	6.1 ×10^{-6}	255.0	1080-1613	Polycrystalline, Atomic absorption analysis

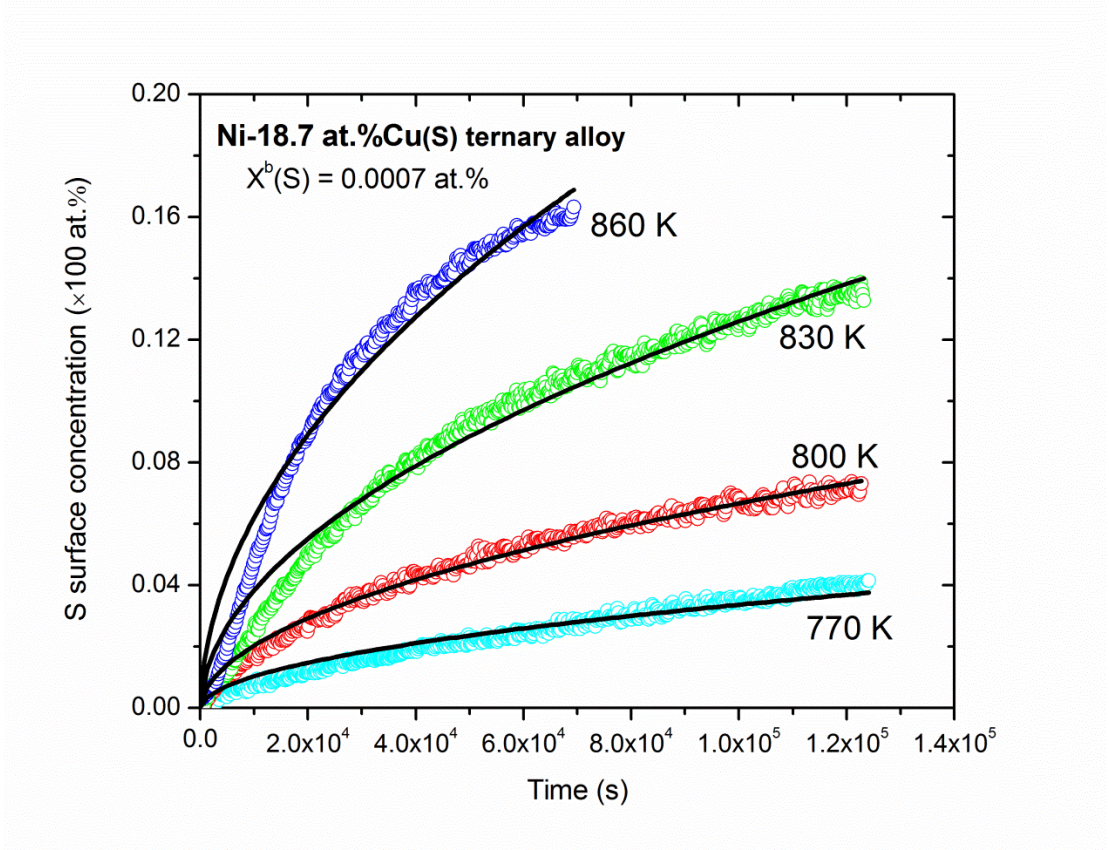

Figure 8.10: S surface segregation in the Ni-18.7at.%Cu(S) ternary alloys at the constant temperature of (a) 770 K, (b) 800 K, (c) 830 K and (d) 860 K. The solid lines are the best fits of the modified semi-infinity Fick's model (Eq. 8.9) which yields the diffusion coefficients (D) for S in the Ni-Cu(S) ternary alloys. The bulk concentration of S in Ni-Cu alloys was 0.0007 at.%.

Table 8.4: The diffusion coefficients for S diffusion in Ni-Cu calculated from the segregation profiles in Fig. 8.8, obtained for various temperatures.

Temperature, (K)	Diffusion coefficients, D (m^2/s)
770	9.73×10^{-18}
800	3.83×10^{-17}
830	1.38×10^{-16}
860	3.57×10^{-16}

For the S surface segregation in the Ni-18.7at.%Cu(S) ternary alloy, the whole measured time is used as the kinetic regions to fit due to the S surface concentration sequentially increasing with the annealing time. The best fits the experimental data results are shown in Fig. 8.10 as the solid lines. The diffusion coefficients (D) for the S in the Ni-18.7at.%Cu(S) ternary alloy obtained from the fitting (in Fig. 8.10) are listed in Table 8.4. The corresponding values of the diffusion parameters (the pre-exponential factor D_o and the activation energy Q) as obtained from a linear fit on the data in Arrhenius plot, $D = D_o\exp(-Q/RT)$, are indicated in Fig. 8.11. In Fig. 8.11 the measured diffusion parameters are also compared with the literature values listed in Table 8.5. The diffusion parameters of S in the Ni-18.7at.%Cu(S) ternary alloy was determined as $D_o = 1.2\times10^{-2}$ m^2/s and Q = 222.1 kJ/mol which are in good agreement with those obtained bulk diffusion from literatures as shown in Fig. 8.11. The dash-dot-dotted pink colour line was measured with tracer method for Cu matrix single crystalline at a higher temperature range 1073 K to 1273 K [40]. The dashed green colour line was for a Ni matrix single crystalline also measured at a higher temperature range 1078 K to 1495 K [39]. In additional, the diffusion parameters of S in the Ni-Cu(S) ternary alloys with linear temperature heating method obtained as $D_o = 9.2\times10^{-3}$ m^2/s and Q = 224.0 kJ/mol and is also shown in Fig. 8.9. Most of the previous results listed in Table 8.5 indicate that the activation energy Q values are between 206 and 224 kJ/mol for the S in the Cu or Ni matrix. The present data of the activation energy Q values obtained in this study is in this range and are in good agreement.

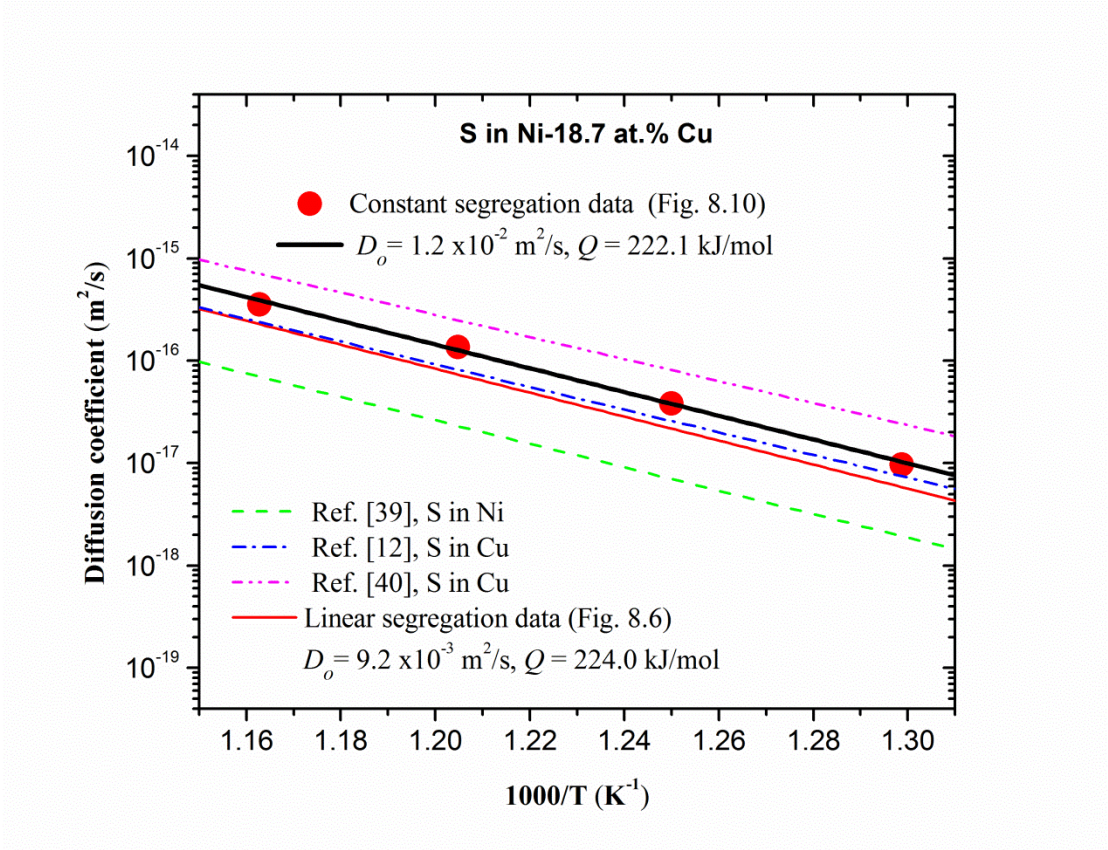

Figure 8.11: Arrhenius plots for the S diffusion in Ni-18.7at.%Cu(S) and the corresponding S bulk diffusion in Cu (or Ni) crystal listed in Table 8.5. The filled circles represent the values of diffusion coefficients extracted from the Fig. 8.10.

Table 8.5: Diffusion parameters obtained for S diffusion in Ni-Cu calculated from Fig. 8.11 and from literatures.

Source	Pre-exponential factor, D_o (m^2/s)	Activation energy, Q (kJ/mol)	Temperature range, (K)	Method/Remarks
This study (constant)	**1.2×10^{-2}**	**222.1**	**770-860**	**Polycrystalline, AES surface segregation**
This study (Linear)	**9.2×10^{-3}**	**224.0**	**896-1065**	
S in Cu Ref.[12]	8.9×10^{-3}	212.8	800-980	Cu-In(S) , AES surface segregation
S in Cu Ref.[15]	8.1×10^{-3}	216.0	949-1059	Cu(S), AES surface segregation
S in Ni Ref.[39]	1.4×10^{-3}	219.0	1379-1618	Single crystalline, Trace
S in Cu Ref.[40]	2.3×10^{-3}	206.6	1080-1613	Single crystalline, Trace

8.4 Summary

In this chapter, the surface segregations of Cu and S from a ternary Ni-Cu(S) alloy system was measured using AES with both linear temperatures programmed heating and constant temperature heating methods. A linear temperature programmed heating method was employed to *in-situ* heat the sample with the temperature range 423 K to 1121 K at a constant rate of 0.002 K/s. It was found that the Cu initially segregated to the surface at temperature 560 K and reached the maximum surface coverage values of 41.4at.% at temperature 896 K. Once the Cu reached the maximum surface coverage, it started to desegregate until Cu was replaced by S. At this point S segregation reach the maximum surface coverage values of 17.1at.%. The segregation data measured with the linear temperature programmed heating method were re-evaluated by the modified Darken model based on these obtained segregation parameters fitted with both Fick's model and Guttmann models. The parameters of the modified Darken model calculations fitted to the segregation data are $D_{o\text{Cu in Ni}}$ = 8.6×10^{-14} m^2/s and $Q_{\text{Cu in Ni}}$ = 145.2 kJ/mol, $D_{o\text{S in Ni}}$ = 9.2×10^{-2} m^2/s and $Q_{\text{S in Ni}}$ = 224.0 kJ/mol, ΔG_{Cu}= -36.0 kJ/mol, ΔGs= -136.0 kJ/mol and $\Omega_{Cu\text{-}Ni}$= 7.6 kJ/mol, $\Omega_{S\text{-}Ni}$= 28.1 kJ/mol and $\Omega_{Cu\text{-}S}$= -10.3 kJ/mol.

The constant temperatures were carried out in the temperature range 770 K to 860 K at a 30 K interval. The results show that the initially both Cu and S segregated to the surface and the first segregation rate of Cu is higher than that of S. Once the Cu reached the maximum surface coverage, it started to desegregate until Cu was replaced by S. The segregation measured profile data with a constant temperature heating method were fitted by the modified Fick's model extracted the bulk diffusion coefficient as $D_{o\text{Cu in Ni}}$ = 5.8×10^{-14} m^2/s and $Q_{\text{Cu in Ni}}$ = 160.1 kJ/mol, $D_{o\text{S in Ni}}$ = 1.2×10^{-2} m^2/s and $Q_{\text{S in Ni}}$ = 222.1 kJ/mol. The segregation parameters obtained in this study were compared well with experimental data values obtained from others in literature.

References

[1] J. Du Plessis, Solid State Phenomena-Part B, surface segregation, Sci-Tech Publications, Brookfield USA, 1990.

[2] J.W. Gibbs, The scientific papers of J.W. Gibbs, Dover, New York, 1961.

[3] V. Stamenković, T.J. Schmidt, P.N. Ross, N.M. Marković, Surface segregation effects in electro catalysis: kinetics of oxygen reduction reaction on polycrystalline Pt_3Ni alloy surfaces, J. Electroanal. Chem. **554** (2003) 191-199.

[4] H.B. Liao, F. Adrian, Z.J. Xu, Surface segregation in bimetallic nanoparticles: a critical issue in electro catalyst engineering, Small **11** (2015) 3221-3246.

[5] L.S. Chang, E. Rabkin, B.B. Straumal, B. Baretzky, W. Gust, Thermodynamic aspects of the grain boundary segregation in Cu (Bi) alloys, Acta Mater. **47**(1999) 4041-4046.

[6] J. Kang, G.C. Glatzmaier, S.H. Wei, Origin of the Bismuth-induced decohesion of nickel and copper grain boundaries, Phys. Rev. Lett. **111** (2013) 055502.

[7] M.R. Chellali, L. Zheng, R. Schlesiger, B. Bakhti, A. Hamou, J. Janovec, G. Schmitz, Grain boundary segregation in binary nickel-bismuth alloy, Acta Mater. **103** (2016) 754-760.

[8] M. Allart, F. Christien, R. Le Gall, Ultra-fast sulphur grain boundary segregation during hot deformation of nickel, Acta Mater. **61** (2013) 7938-7946.

[9] E. Pellicer, A. Varea, K.M. Sivaraman, S. Pane, S. Surinach, M.D. Baro, J. Nogues, B.J. Nelson, J. Sort, Grain boundary segregation and interdiffusion effects in nickel-copper alloys: an effective means to improve the thermal stability of nanocrystalline nickel, ACS Appl. Mater. Interfaces **3** (2011) 2265-2274.

[10] M. Yamaguchi, S. Motoyuki, K. Hideo, Grain boundary decohesion by impurity segregation in a nickel-sulfur system, Science **307** (2005) 393-397.

[11] A.P. Dementjev, O.P. Ivanova. Sulfur segregation and chemical interaction on Ti, Co, Ni, Cu, Pd surfaces in the temperature range 300 to 1300 K studied by AES and UPS, Vacuum **45** (1994) 901-905.

[12] M.J. Madito, H.C. Swart, J.J. Terblans, Surface segregation measurements of In and S impurities from a dilute Cu (In, S) ternary alloy, Surf. Interface Anal. **45** (2013) 1020-1025.

[13] P.E. Barnard, J.J. Terblans, H.C. Swart, Surface orientation dependence of the activation energy of S diffusion in bcc Fe, Appl. Surf. Sci. **356** (2015) 213-220.

[14] J.J. Terblans, H.C. Swart, The segregation of Bi and S from a Cu (Bi, S) ternary system, e-J. Surf. Sci. Nanotech. **7** (2009) 480-485.

[15] E.C. Viljoen, J. Du Plessis, Auger/LEED linear heating study of Sn and S bulk - to-surface diffusion in a Cu (111)(Sn, S) single crystal, Surf. Interface Anal. **23** (1995) 110-114.

[16] S. Ichimura, M. Shikata, R. Shimizu, Observation of surface segregation of sulphur in Cu-Ni alloys at elevated temperature with scanning Auger electron microscope, Surf. Sci. **108** (1981) L393-L398.

[17] M.L. Shek, Sulphur segregation-induced changes in the near-surface composition of a NiCu (100) single crystal surface, Surf. Sci. **149** (1985) L39-L45.

[18] T. Sakurai, T. Hashizume, A. Kobayashi, A. Sakai, S. Hyodo, Y. Kuk, H.W. Pickering, Surface segregation of Ni-Cu binary alloys studied by an atom-probe, Phys. Rev. B **34** (1986) 8379.

[19] S. Ouannasser, L.T. Wille, H. Dreysse, Cluster expansions at alloy surfaces: Formalism and application to segregation in Ni-Cu, Phys. Rev. B **55** (1997) 14245.

[20] A.V. Ruban, I.A. Abrikosov, D.Ya. Kats, D. Gorelikov, K.W. Jacobsen, H.L. Skriver, Self-consistent electronic structure and segregation profiles of the Cu-Ni (001) random-alloy surface, Phys. Rev. B **49** (1994) 11383.

[21] X.L. Yan, J.Y. Wang, Size effects on surface segregation in Ni-Cu alloy thin films, Thin Solid Films **529** (2013) 483-487.

[22] W.F. Egelhoff Jr, Thermochemical Values for Cu-Ni Surface and Interface Segregation Deduced from Core-Level Binding-Energy Shifts, Phys. Rev. Lett. **50** (1983) 587.

[23] T.Sakurai, T. Hashizume, A. Jimbo, A. Sakai, S. Hyodo, New result in surface segregation of Ni-Cu binary alloys, Phys. Rev. Lett. **55** (1985) 514.

[24] Y.S. Ng, T.T. Tsong, S.B. McLane, Jr., Absolute composition depth profile of a NiCu alloy in a surface segregation study, Phys. Rev. Lett. **42** (1979) 588.

[25] H.H. Brongersma, M.J. Sparnaay, T.M. Buck, Surface segregation in Cu-Ni and Cu-Pt alloys: a comparison of low-energy ion-scattering results with theory, Surf. Sci.**71** (1978) 657-678.

[26] K. Watanabe, M. Hashiba, T. Yamashina, A quantitative analysis of surface segregation and in-depth profile of copper-nickel alloys, Surf. Sci. **61** (1976) 483-490.

[27] M. Guttmann, Equilibrium segregation in a ternary solution: A model for temper

embrittlement, Surf. Sci. **53** (1975) 213-227.

[28] D. McLean, Grain boundaries in Metals, Oxford University Press, Oxford, 1957.

[29] H.C. Swart, W.D. Roos, J.J. Terblans, Surface segregating kinetics in a ternary system, Surf. Interface Anal. **36** (2004) 285-289.

[30] J.J. Terblans, W.J. Erasmus, E.C. Viljoen, J. Du Plessis, Orientation dependence of the surface segregation kinetics in single crystals, Surf. Interface Anal.**28** (1999) 70-72.

[31] J.K.O. Asante, W.D. Roos, J.J. Terblans, Sequential segregation of Sn and Sb in a Cu (111) single crystal, Surf. Interface Anal. **35** (2003) 441-444.

[32] R. Shimizu, Quantitative analysis by Auger electron spectroscopy, Jpn. J. Appl. Phys., **22** (1983) 1631-1642.

[33] S. Tanuma, C.J. Powell and D.R. Penn, Calculations of electron inelastic mean free paths, Surf. Interface Anal. **37** (2005) 1-14.

[34] T. Miyahara, K. Stolt, D.A. Reed, H.K. Birnbaum, Sulfur segregation on nickel, Scripta Mater. **19** (1985) 117-121.

[35] J. du Plessis, P.E. Viljoen, G.N. van Wyk, The effect of high temperature sputtering on the $t^{1/2}$ dependence of segregation kinetics in an Al alloy, Surf. Sci. **244** (1991) 277-284.

[36] X.L. Yan, Y. Liu, H.C. Swart, J.Y. Wang, J.J. Terblans, Investigation of interdiffusion and depth resolution in Cu/Ni multilayers by means of AES depth profiling, Appl. Surf. Sci. **364** (2016) 567-572.

[37] K. Monma, H. Suto, H. Oikawa, Diffusion of Ni^{63} and Cu^{64} in nickel-copper alloys, J. Japan Inst. Metals **28** (1964) 192-194.

[38] O. Taguchi, Y. Iilima, K. Hirano, Application of atomic absorption analysis to impurity diffusion of copper in nickel in a wide range of temperature, J. Japan Inst. Metals **48** (1984) 20-24.

[39] B. Vladimirov, V.N. Kaigorodov, S.M. Klotsman, I.S. Trakhtenberg, Diffusion of antimony in nickel, Fiz. Met. Metalloved **39** (1975) 319.

[40] F. Moya, G.E. Moya-Gontier, F. Cabane-Brouty, Sulphur diffusion in copper: departure from the Arrhenius plot, Phys. status solidi (b) **35** (1969) 893-901.

[41] K. Watanabe, M. Hashiba, T. Yamashina, A quantitative analysis of surface segregation and in-depth profile of copper-nickel alloys, Surf. Sci. **61**(1976) 483-490.

Chapter 9
Surface segregation in Ni-Cu alloy thin films

9.1 Introduction

Nanoscale metallic alloy systems (thin films and particles) have become increasingly important in a wide range of technologically important applications. For example, nanoscale particles are used in catalysis because of their high reactivity and reaction specificity. The catalytic properties of a material are largely determined by the composition and structure of its surface which in turn depend on the composition [1]. Although there has been a great deal of experimental and theoretical work devoted to understanding the thermodynamics of bulk systems [2, 3], there have been relatively few studies of the thermodynamics of nanoscale systems [4-12]. In nanoscale systems, unlike in bulk materials, the surface properties also depend on the size of the system and can vary significantly from those of surfaces bounding a semi-infinite bulk.

In the previous chapter (Chapter 8), the surface segregation in a Ni-Cu alloy bulk system was studied using AES in combination with a linear temperature programmed heating and constant temperature method. The measured surface segregation profiles for the Ni-Cu alloy bulk system were recorded and fitted with the modified Darken model. However, for a thin film system, the number of segregated atoms on the surface is a significant fraction of the total number of atoms in the system so that the bulk concentration of the system is modified significantly during segregation. The

lack of a reservoir of the segregating atoms in thin films may cause significant differences in surface segregation behavior compared with that of bulk materials.

In this chapter, two various thicknesses of Ni-Cu alloy thin films (Sample 10 and Sample 20) were prepared by electron beam physical vapour deposition. Surface segregation in the Ni-Cu alloy thin films was studied by using AES. A linear temperature programmed heating method was employed for *in-situ* heat of a sample. The heating temperature range was 403 K to 823 K with a constant heating rate of 0.03 K/s. To understand the size effects on surface segregations in thin films system, the modified Darken model under a constrained condition applied for thin film system are also simulated for both the kinetic and equilibrium in a Ni-Cu alloy thin films system.

9.2 Experimental

9.2.1 Sample preparation and annealing

The detailed procedure for the preparation of the Ni/Cu/Ni thin films on SiO_2 substrates was described in Chapter 3. The main procedure can be summarized as follows. The Ni/Cu/Ni sandwich layered structures (in this chapter) were prepared by electron beam physical vapour deposition onto passivated silicon (SiO_2) substrates. The SiO_2 was prepared by wet oxidation of Si(100) annealed at 1000 ℃ for 1h in a Lindberg tube furnace. The Si(100) wafers were exposed to oxygen gas that flowed through boiling water and then into the tube that was at 1000 ℃.

During the deposition, the base pressure in the deposition chamber was less than 6×10^{-6} Torr. To avoid metal oxidization, pure Ti was evaporated (to clean the residual oxygens in the chamber) for 1 minute before deposition of Ni (or Cu). Then, Ni and Cu were alternately deposited onto SiO_2 substrates, the deposition rate of Ni was ~0.4 nm/s and Cu was ~0.7 nm/s, respectively. The thickness of the individual sublayer was controlled using a calibrated Inficom XTC thickness monitor during vapor deposition. Two kinds of the Ni/Cu/Ni thin films (marked Sample 10 and Sample 20) were prepared and each sublayer thickness is listed in Table 9.1.

The Ni/Cu/Ni sandwich thin films were cut into small piece (1×1 cm^2) and then annealed in a high vacuum tube furnace at the base pressure about 5×10^{-6} Torr. The annealing chamber is a custom built system with a carousel holder, allowing one to multiple samples sequentially without breaking the vacuum. The samples were placed on a ceramic boat and a magnetically coupled arm pushed the ceramic boat into and out of the furnace. The simulation results in Chapter 3 were used to select the annealing temperatures and times for both Sample 10 and Sample 20. The selected annealing temperatures and times and listed in Table 9.2. After each annealing run, the sample was spontaneously cooled down to the room temperature in the furnace and the same pressure.

Table 9.1: Each sublayer thickness for the Sample 10 and Sample 20. (Unit in nm)

Sublayer	Sample 10	Sample 20
The first layer (Ni)	10.4	23.7
The second layer (Cu)	3.6	5.8
The third layer (Ni)	12.0	22.5
Total	26.0	52.0

Table 9.2: Annealing temperatures and times for the Sample 10 and Sample 20.

No.	1	2	3
Sample 10	648 K, 1 h	698 K, 1 h	698 K, 4 h
Sample 20	648 K , 1 h	698 K, 1 h	698 K, 25 h

9.2.2 AES depth profiling measurement

The detailed procedures for AES depth profiling measurements have been described in Chapter 4. The main points are summarized as follows. The AES depth profiles of the as-deposited and annealed Ni/Cu/Ni thin films were measured using a PHI 600 Scanning Auger Microprobe (SAM) at a base pressure $< 10^{-9}$ Torr. A static primary electron beam of 10 keV and current of 200 nA with beam size (diameter) of 7.2 μm

was used. Ion sputtering was performed with 2 keV Ar^+ ions at an incidence angle of 40° with respect to the sample surface normal, the beam current density was 0.074 A/m^2 with a raster area 2×2 mm^2. The Auger peak-to-peak heights (APPH) were recorded as a function of sputtering time for C(275 eV), O(510 eV), Ni(718 eV), Cu(922 eV) and Si(1618 eV).

9.2.3 AES Surface segregation measurement

The surface segregation measurement for the Ni-Cu alloys thin films were performed by Auger electron Microprobe with a PHI 600 SAM at a base pressure of 1×10^{-9} Torr. The experimental detail is given in Chapter 4, some the important points are given here again. A static primary electron beam of 10 keV and beam current of 2.83 μA with beam size (diameter) of 12.2 μm was used for the AES measurements. The ion gun used for sputter cleaning was performed with 2 keV Ar^+ ions with an argon pressure of 5.0×10^{-3} Pa, the beam was rastered over a 2×2 mm^2 area, which is much larger than the primary electron beam diameter (12.2 μm). The crystal was tilted with the normal of the crystal surface at a 30 ° angle with respect to the direction of the incident electron beam.

Surface segregation measurements with linear program heating were carried out in the temperature range 403-823 K at a constant heating rate of 0.03 K/s. Before the segregation measurements Sample 10 was *in-suit* annealed at 698 K for 4 h and Sample 20 at 698 K for 25 h to form a Ni-Cu alloy thin film with a uniform concentration. The Ni-Cu alloy thin film was then cooled to 403 K with constant heating rate of -0.5 K/s. After stabilization of the temperature at 403 K, the Ni-Cu thin films was then sputter cleaned for exactly 10 s with a 2 keV argon ions beam. After sputtering, the measured Auger spectrums were immediately recorded as a function of temperature for Ni&Cu_L (40-110 eV), C (240-275 eV), O (480-529 eV) and Ni&Cu_H (680-960 eV). The APPH data was quantified using the method as following the Chapter 8.

9.3 Results and discussion

9.3.1 AES depth profile data for Ni-Cu thin films

The AES intensity and sputter time was converted into elemental composition and sputtered depth. The atomic concentrations of Cu, Ni, C, O and Si, respectively, were calculated using the relative elemental sensitively factor method [13]

$$X_i = \frac{I_i / I_i^0}{\sum_{j=i}^{n} I_j / I_j^0} \tag{9.1}$$

where I_i is the measured APPH (intensity) for element i and the I_i^0 is the APPH (intensity) for the pure element i. X_i is the measured fractional concentration of element i (For this study i = Cu, Ni, C, O and Si). The sputter time scale of the AES depth profile data for the as-deposited and annealed Ni/Cu/Ni sandwich thin films were converted into the sputter depth by assuming a constant sputter rate for the Cu/Ni binary system. The more detail for the sputter rate of Cu and Ni see the previous Chapter 5 and 7. The AES measured APPHs-sputter time and the converted concentration-sputter depth profiling data for the as-deposited Ni/Cu/Ni sandwich thin film (Sample 20) are shown in Fig. 9.1(a) and Fig. 9.1(b), respectively.

Fig. 9.2 shows AES depth profiles of Sample 10 for the as-deposited and annealed thin films. The Ni-Cu thin films alloy was completely formed when annealing at 698 K for 4h as shown in Fig. 9.2(d), this was also supported by the simulation done with Fick's equation in Chapter 3. From the annealed depth profiles of Sample 10, shown in Fig. 9.2(b-d), it is clear that the Cu segregated to the surface.

Fig. 9.3 shows AES depth profiles of Sample 20 for the as-deposited and annealed thin films. The Ni-Cu thin films alloy was completely formed by annealing at 698 K for 25h as is shown in Fig. 9.3(d). Again, it is clear that the Cu segregated to the surface of the annealed samples as is shown in Fig. 9.3(b-d).

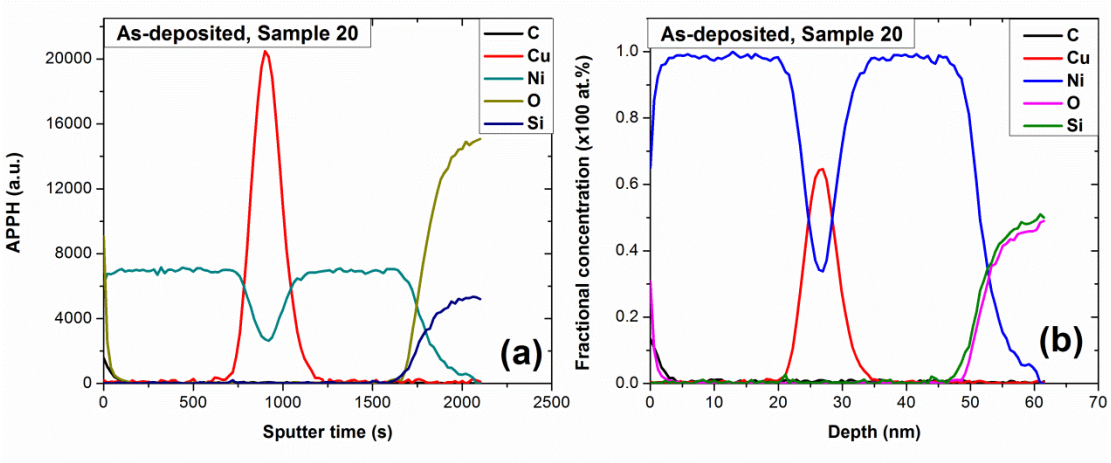

Figure 9.1: AES depth profiling measured of the as-deposited Sample 20 for (a) APPHs vs. sputter time and (b) fractional concentration vs. sputter depth.

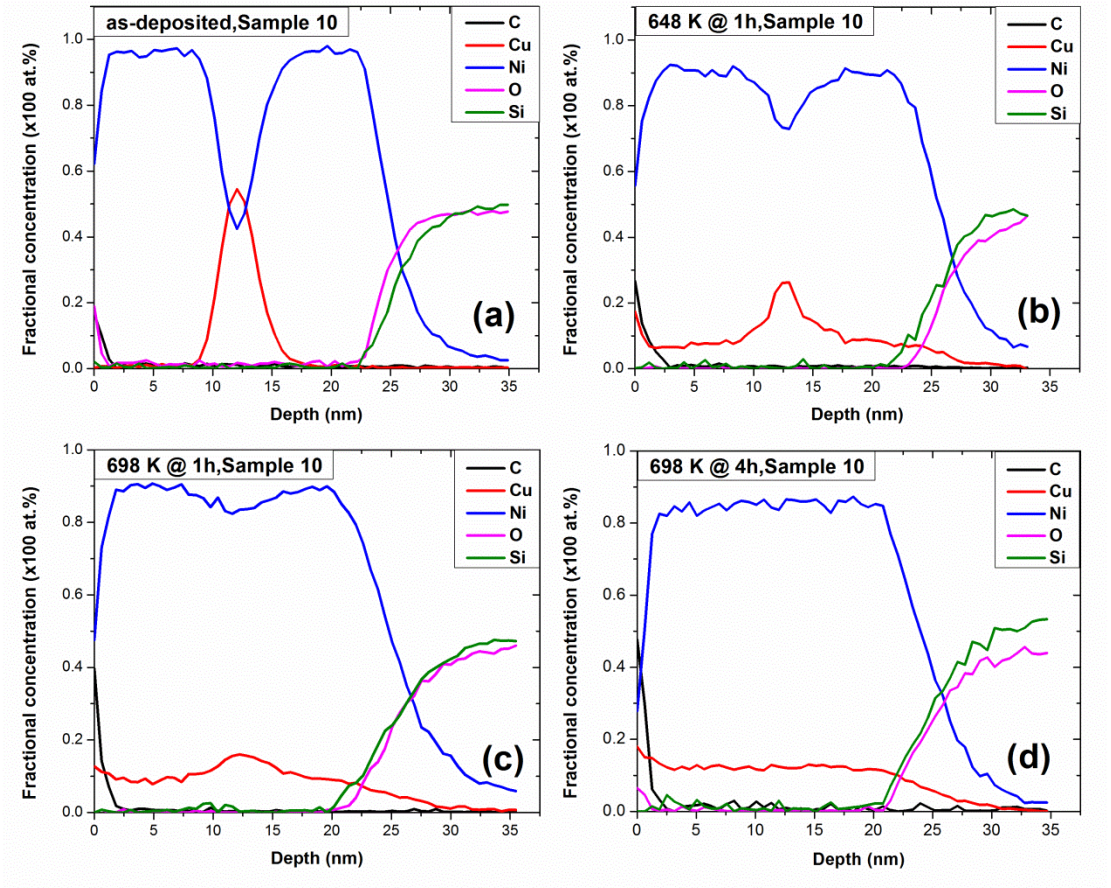

Figure 9.2: AES depth profiles for the Sample 10 (a) as-deposited, (b) annealing at 648 K @1 h, (c) annealing at 698 K @1 h and (d) annealing at 698 K @4 h.

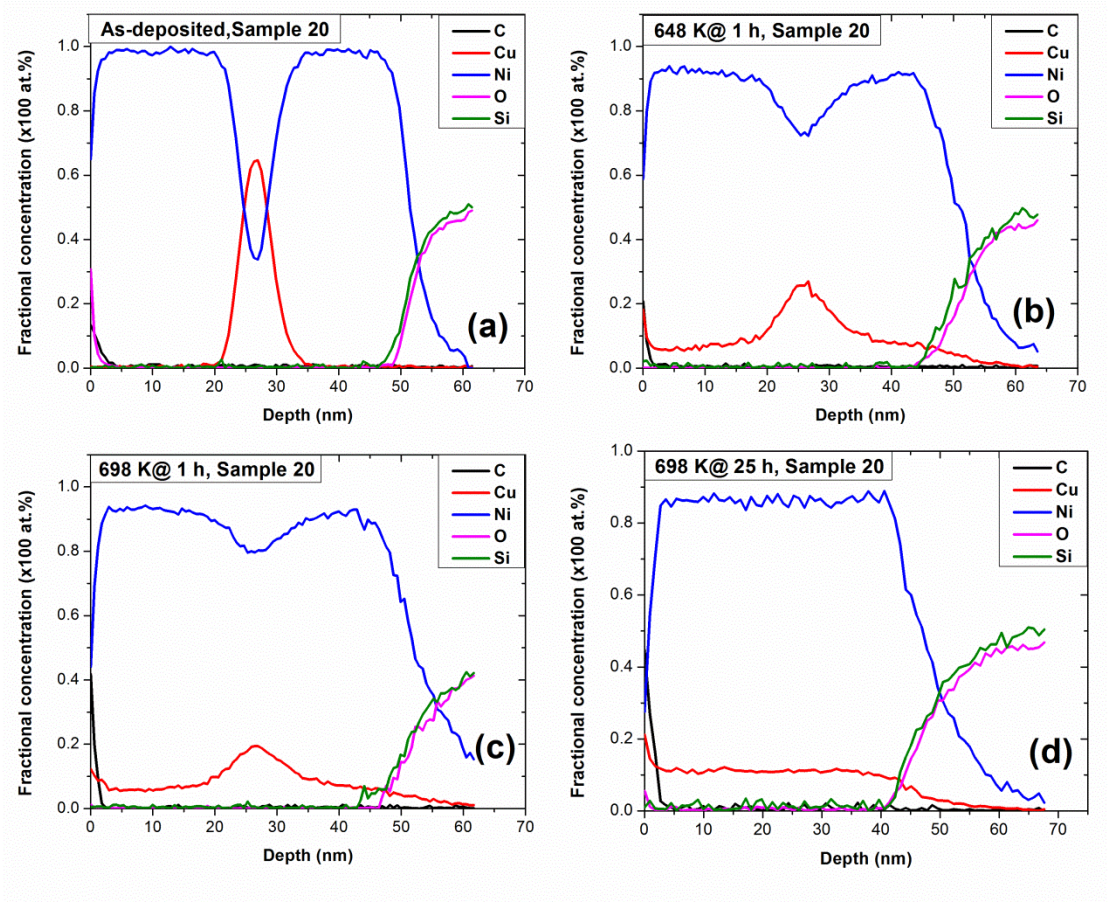

Figure 9.3: AES depth profiles for the Sample 20 (a) as-deposited, (b) annealing at 648 K @1 h, (c) annealing at 698 K @1 h and (d) annealing at 698 K @25 h.

9.3.2 Surface segregation data for Ni-Cu thin films

Fig. 9.4 shows the full Auger spectrum before and after the surface segregation measurement for the Ni-Cu alloy thin film (Sample 10). It was found that the C and O impurity were detected on the surface before and after segregation measurement running and both were monitored during the segregation measurement. Fortunately, no S impurity was detected in the Ni-Cu alloy thin films.

Fig. 9.5 shows the surface concentration of Cu, C and O as a function of the temperature with a linear heating rate of 0.03 K/s for the Ni-Cu alloy thin films with both Sample 10 and Sample 20. For the thinner film (Sample 10, 26 nm), as is shown in Fig. 9.5(a), the C segregation occur at a lower temperature range (403-545 K) the segregation of C is slow and it reach a maximum surface concentration of 8.0 at.%. The surface concentration of Cu is almost constant at these low temperatures because the bulk diffusion rate of Cu is very low in this temperature region. In the higher

temperature region (545-730 K), the Cu surface concentration increases and reached a maximum surface concentration of 26.0 at.%. The C surface concentration decrease as the Cu segregate to the surface and it replaced the C atom from the surface. This temperature region is regarded as the Cu kinetic region and is used to extract the Cu diffusion coefficient with Fick's model. It should be pointed out that the maximum surface concentration of Cu is determined by its segregation energy and the interaction energy between the Cu, C and Ni according to the surface segregation theory (*i.e.* modified Darken model). In the equilibrium region (730-823K), the Cu surface concentration reached a maximum values of 26.0 at.% and the C surface concentration stabilise close to 5.5 at.%.

For a thicker Sample 20 (52 nm) as shown in Fig. 9.5(b), the Cu start to segregation at 570 K, which is high than thinner layer (Sample 10). This indicates that the thicker layer (Sample 20) has higher activation energy. It should be pointed out the oxygen signal remains the constant level (5-6 at.%) during the surface segregation measurement for the both films (Sample 10 and Sample 20).

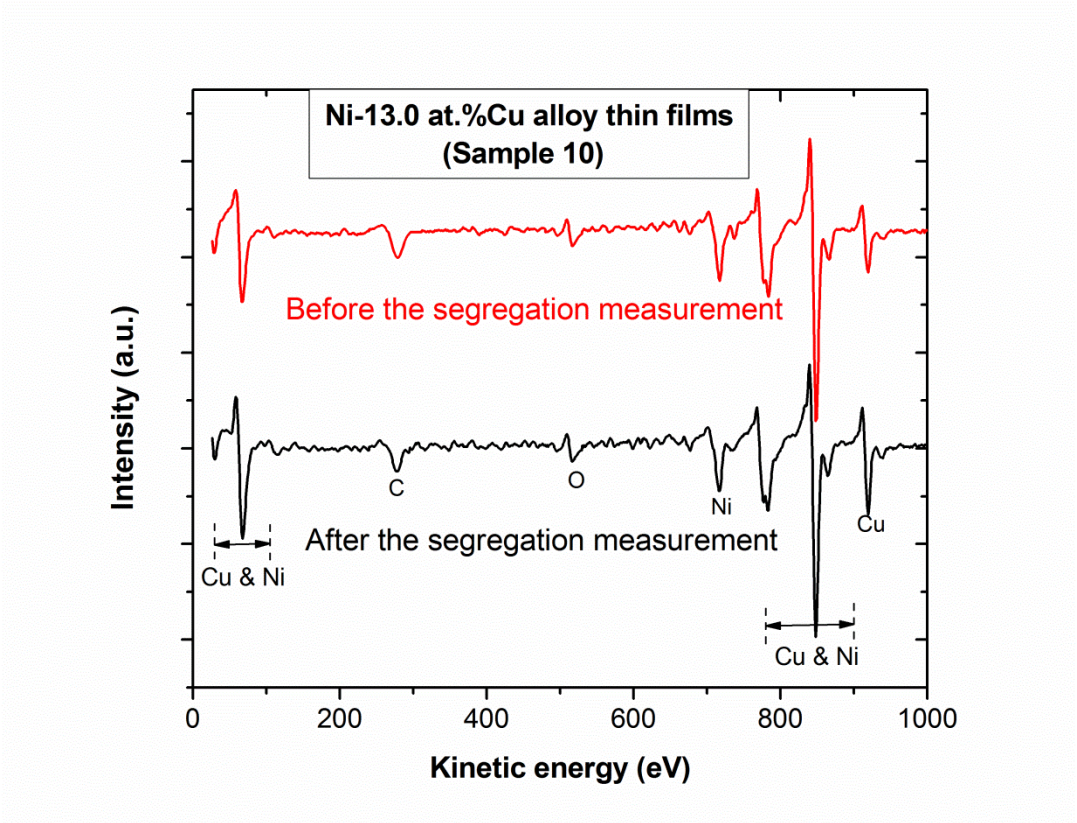

Figure 9.4: Auger spectrum of a Sample 10 Ni-Cu alloy thin film before and after the segregation measurement.

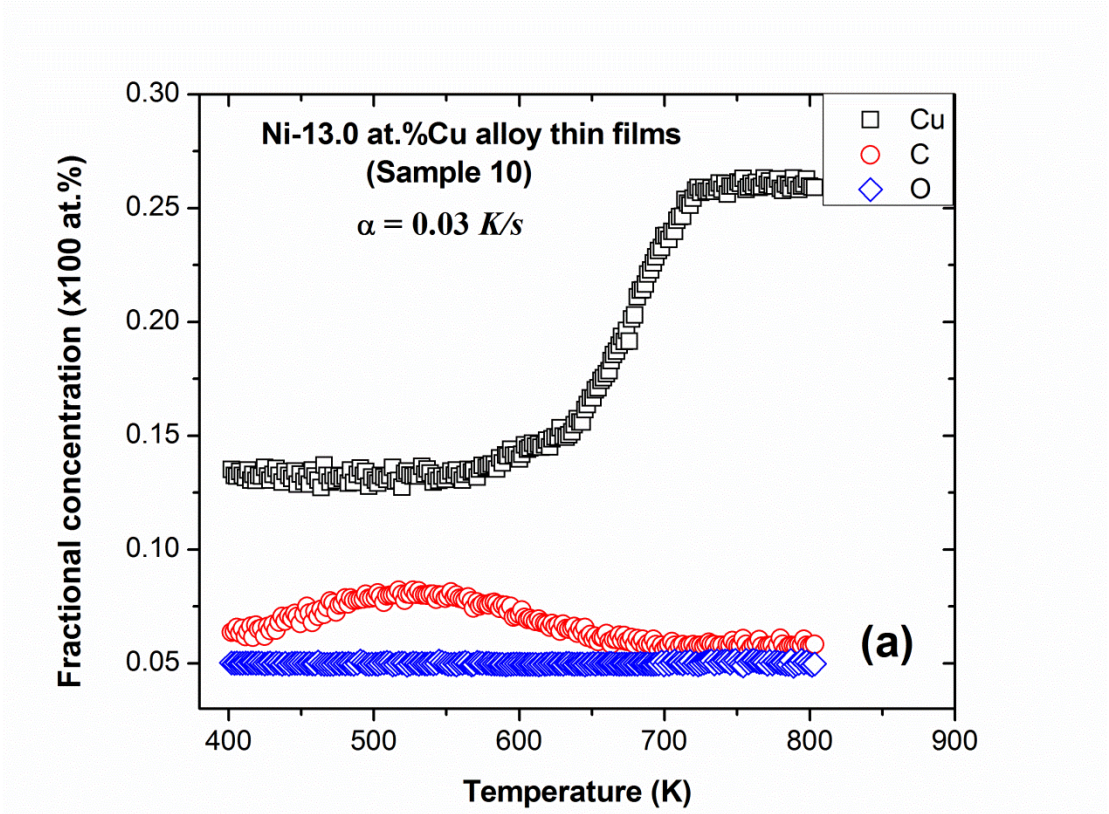

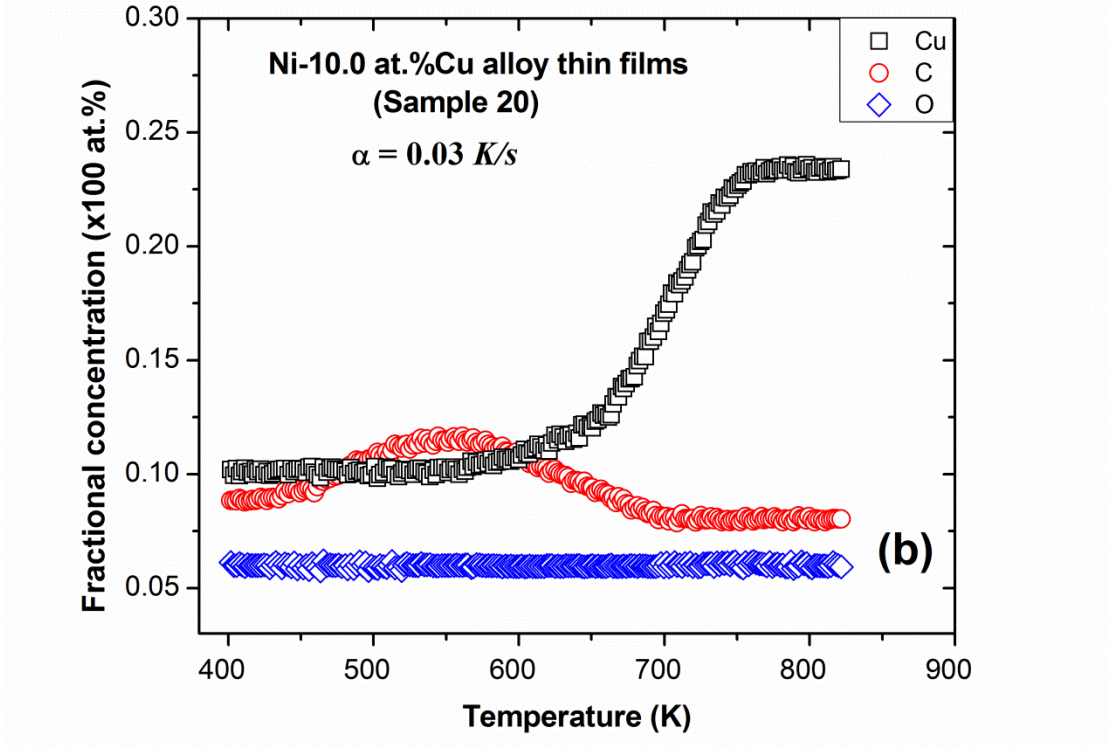

Figure 9.5: Surface segregation of Cu, C and O as a function of the temperature with a linear heating method at a rate of 0.03 K/s for the Ni-Cu alloy thin films (a) Sample 10 and (b) Sample 20.

The modified semi-infinity Fick's model was described in detail in Chapter 2 (section 2.3.1), and only the final result is presented here Eq. 9.2. Eq. 9.2 was used to fit the segregation data.

$$\frac{1}{2}\beta^2 = \frac{2D_o}{\pi\alpha d^2}\int_{T_0}^{T_E} \exp(-Q/RT)dT \qquad (9.2)$$

where β is surface enrichment factor ($\beta = (C^S - C^B)/C^B$ with the C^S and C^B are the surface and bulk concentration of Cu), α is the heating rate (0.03 K/s for this work), d is the thickness of the segregated layer taken as 0.194 nm (see in Chapter 8), D_o is the pre-exponential factor, Q is the activation energy and R is the universal gas constant with a value of 8.314 kJ/mol.

The modified Fick semi-infinite model (Eq. 9.2) was employed to fit the kinetic regions in the segregation data of Cu. The diffusion coefficients, pre-exponential factor D_o and the activation energy Q, were extracted from the best fit of Eq. 9.2 for Cu segregating from the Ni-Cu alloy thin films (for both Sample 10 and Sample 20) as is shown in Fig. 9.6. The diffusion of Cu in the Ni-Cu alloys thin films was determined as $D_o = 2.8\times10^{-13}$ m^2/s and Q = 135.3 kJ/mol for the Sample 10 and $D_o = 2.9\times10^{-13}$ m^2/s and Q = 140.5 kJ/mol for the Sample 20.

Fig. 9.7 summarizes the present results of the diffusion parameters for the Ni-Cu alloys thin films, previous results (Chapter 7 and Chapter 8) and others literature values. The diffusion coefficients are plotted as a function with temperature (1/T) for the Cu in Ni-Cu alloy.These diffusion parameters are also listed in Table 9.3. As shown in Fig. 9.7, the *bulk-to-surface* diffusion coefficient in this study shows a good comparison with those obtained diffusion from literature. The activation energy Q values obtained in this study are 135.3 kJ/mol for Sample 10 (thickness 26 nm) and 140.5 kJ/mol for Sample 20 (thickness 52 nm). These values are higher than that value of 101.3 kJ/mol, is the interdiffusion parameter for polycrystalline Cu/Ni multilayer thin films (that was measured with AES depth profiling). The very low activation energy as determent for interdiffusion of the Cu/Ni multilayer thin films (that occurred in the temperature range of 598- 648 K) and is associated with the grain boundary diffusion mechanism (see the previous Chapter 7). These values are lower than that

value (160.1 kJ/mol) which was obtained *bulk-to-surface* diffusion for a polycrystalline Ni-18.7at.%Cu bulk material. The highs activation energy was determined with *bulk-to-surface* segregation measurement in the temperature range of 770-830 K for a polycrystalline Ni-18.7at.%Cu bulk material (see the previous Chapter 8). It should be pointed out that the activation energy *Q* values of 264.0 kJ/mol was the bulk diffusion parameter for Cu in Ni-15at.%Cu polycrystalline alloys and measured with tracer method at the higher temperature range 1379 K to 1618 K [14].

In addition, by comparing the activation energy *Q* values of the Sample 10 and Sample 20 in Table 9.3, it is clear that the activation energy *Q* values of 140.5 kJ/mol for thicker sample is higher than that the 135.3 kJ/mol for the thinner sample. This is related to the structure of the Cu-Ni alloys thin films at the different thickness (Sample 10 with 26 nm and Sample 20 with 52 nm). As shown in Fig 9.6, the surface enrichment factor β in the equilibrium are calculated as 2.4 for the thicker sample and 2.0 for the thinner sample, which indicates that the thickness of thin film effects the surface segregation. Similar experiment result that the film thickness effects the surface segregation was observed by Nyeki *et al.* [7] in studying the segregation of Ge in amorphous $Si_{1-x}Ge_x$ thin films alloys using AES. Swaminarayan e*t al.* [8] have also studied the influence of film thickness on segregation utilising the Langmuir-Mclean approximation (no interaction parameters) for the Cu-Ni binary system. Brown and Mishin [9] have also studied the surface stresses and surface segregation in (110)NiAl free-standing thin films with different thicknesses with Molecular statics and Monte Carlo simulations in conjunction with an embedded-atom potential. To understand the size effects on surface segregations in thin films system, the modified Darken model are employed to simulate for both the kinetic and equilibrium in a Ni-Cu alloy with constrained condition. And the result will be discussed in next section 9.3.3.

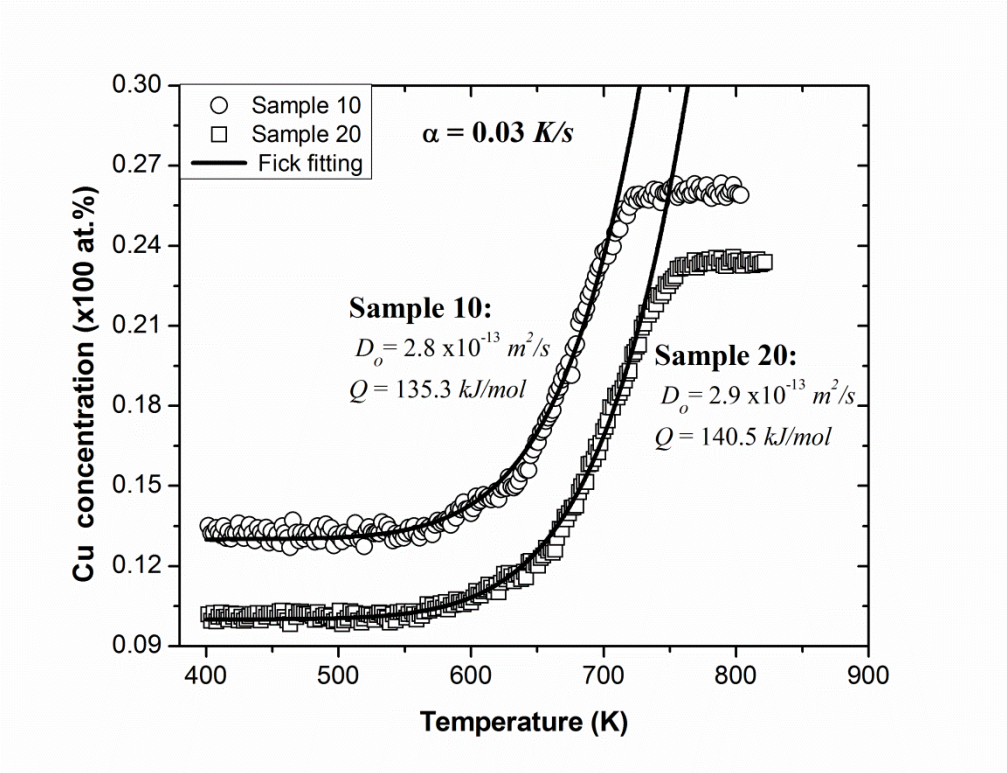

Figure 9.6: Surface segregation of Cu as a function of the temperature with a linear heating rate of 0.03 K/s for the Ni-Cu alloys thin films (Sample 10 and Sample 20). The solid lines are the best fits of the modified semi-infinity Fick's model (Eq. 9.2) which yields the diffusion parameters (pre-exponential factor D_o and activation energy Q).

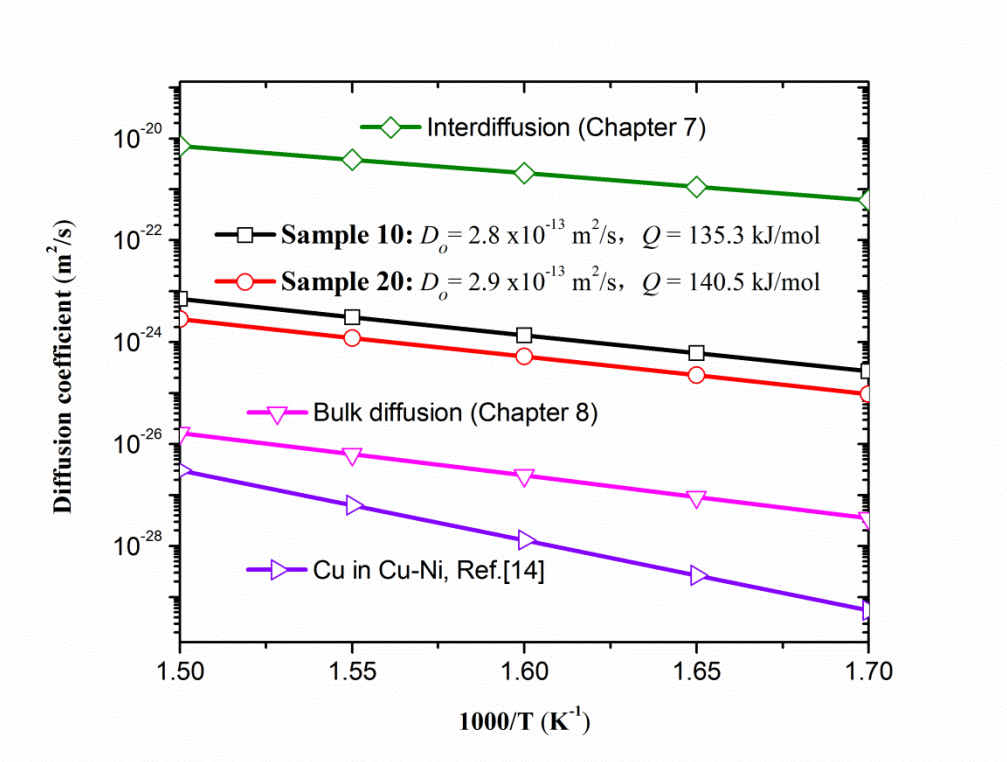

Figure 9.7: Arrhenius plots for the Cu diffusion in Ni-Cu alloys system and the corresponding Cu diffusion in Ni-Cu alloy.

Table 9.3: Diffusion parameters obtained for Cu diffusion in Ni-Cu and from literatures.

Source	Pre-exponential factor, D_o (m^2/s)	Activation energy, Q (kJ/mol)	Temperature range, (K)	Method/Remarks
This study (Sample 10)	**2.8×10^{-13}**	**135.3**	**545-730**	**Thin films alloys, AES surface segregation**
This study (Sample 20)	**2.9×10^{-13}**	**140.5**	**570-750**	
Interdiffusion (Chapter 7)	6.2×10^{-13}	101.3	598-648	Multilayer thin films, AES depth profile
Bulk segregation (Chapter 8)	5.8×10^{-14}	160.1	770-860	Polycrystalline, AES surface segregation
Cu in Cu-Ni Ref.[14]	1.5×10^{-6}	264.0	1379-1618	Polycrystalline Cu-Ni alloy, Trace

9.3.3 Surface segregation simulation for Ni-Cu thin films

The modified Darken model was described in detail in Chapter 2 (section 2.3) and only the final result is presented here (Eq. 9.3). The modified Darken model is a unified model giving a full description of surface segregation from kinetics to equilibrium. It is a complete description (simulation) for segregation.

$$
\begin{aligned}
&\frac{\partial C_i^S}{\partial t} = \frac{D_i C_i^{B_1}}{RTd^2}\Delta\mu_i^{B_1,S} \\
&\frac{\partial C_i^{B_1}}{\partial t} = \frac{D_i C_i^{B_2}}{RTd^2}\Delta\mu_i^{B_2,B_1} - \frac{D_i C_i^{B_1}}{RTd^2}\Delta\mu_i^{B_1,S} \\
&\vdots \\
&\frac{\partial C_i^{(j)}}{\partial t} = \frac{D_i C_i^{(j+1)}}{RTd^2}\Delta\mu_i^{(j+1,j)} - \frac{D_i C_i^{(j)}}{RTd^2}\Delta\mu_i^{(j,j-1)} \\
&\vdots \\
&\frac{\partial C_i^{(N)}}{\partial t} = -\frac{D_i C_i^{B_N}}{RTd^2}\Delta\mu_i^{B_N,B_{N-1}}
\end{aligned}
\qquad (9.3)
$$

where species i is Cu, j=1, 2,…, N+1. C_i^S is the surface concentration of Cu, and C_i^{B1} is the first bulk concentration of Cu, D is the diffusion coefficient of Cu, d is the thickness of the segregated layer. $\Delta\mu^{(j+1,j)}$ is the difference of chemical potential between two adjacent layers, i.e. $\Delta\mu^{(j+1,j)} = \mu_1^{(j+1)} - \mu_1^{(j)} - \mu_2^{(j+1)} + \mu_2^{(j)}$.

If an equilibrium state is reached, all the rate equations equal to zero and the equilibrium surface concentration X^S and the bulk concentration in each bulk layer X^{Bi} follow:

$$\frac{X^S}{1-X^S} = \frac{X^B}{1-X^B}\exp\left[\frac{\Delta G + 2\Omega(X^S - X^B)}{RT}\right] \tag{9.4}$$

where ΔG is called segregation energy and is defined as $\Delta G = \mu_1^{0B} - \mu_1^{0S} - \mu_2^{0B_1} + \mu_2^{0S}$ $\mu_{<i>}^{0B}$ and $\mu_{<i>}^{0S}$ are the standard chemical potentials of pure element *i* for the bulk material and surface region material, respectively. In general, the segregation energy ΔG is independent on the bulk/surface concentration and the temperature.

For a thin film system, because of a limited number of segregating atoms, the final equilibrium bulk concentration value X^B is modified from the initial bulk concentration value X^0 as [8]:

$$X^B = \frac{X^0 - X^S K}{1-K} \tag{9.5}$$

where *K* is the ratio of the number of segregated atoms in the surface layer (N^S) to the total number of segregated atoms in the system (N^{total}), i.e. $K = N^S / N^{total}$. The value of *K* is inversely proportional to the film thickness, i.e. $K=2/l$, where *l* is the film thickness in the unit of ML, $K=1$ represents a two-layer thin film system and $K=0$ represents a bulk system. Eq. 9.5 is a constrained condition for the surface segregation in thin films.

To understand the size effects on surface segregations in thin films system, the modified Darken model (Eq. 9.3 and 9.4) under a constrained condition (Eq. 9.5) is employed to simulate for both the kinetic and equilibrium in a Ni-Cu alloy thin films system. The surface segregation parameters obtained from Chapter 8 and the diffusion parameters obtained from this chapter were used to simulate for the Ni-1.0at.%Cu alloy in this study. The segregation energy is 36.1 kJ/mol, interaction energy is 7.6 kJ/mol, and diffusion parameters $D_o = 2.9\times10^{-13}$ m^2/s and Q = 140.5 kJ/mol.

Fig. 9.8 shows the simulated Cu equilibrium surface concentration as a function of temperature for a bulk system and three thin films (52, 26, 10-nm) with positive interaction and without interaction for a Ni-1.0at.%Cu alloy. The simulations shows that (a) the Cu equilibrium surface concentration with a zero interaction parameter is lower than that with a positive interaction parameter (Ω= 7.6 kJ/mol), and the equilibrium surface concentration decrease with a decrease in film thickness; (b) as the film thickness decrease the effect of the positive interaction is less pronounced. These results imply that (a) the positive interaction parameter enhance the Cu surface segregation; (b) the size effect on Cu equilibrium surface segregation is more pronounced in the Ni-1.0at.%Cu alloy system.

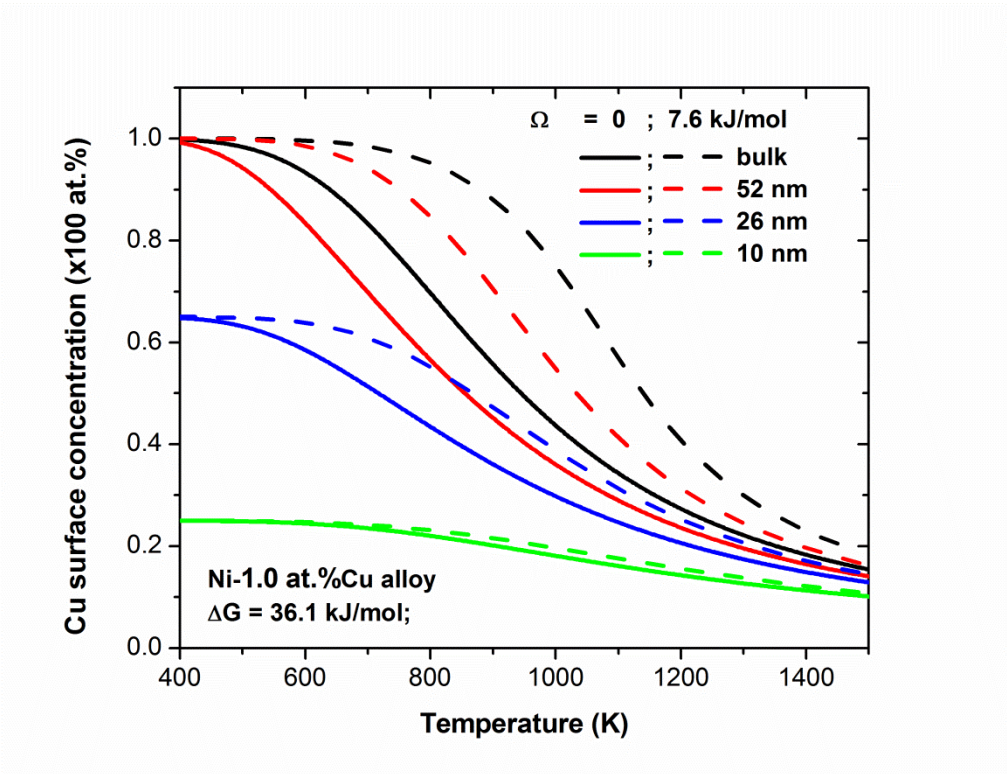

Figure 9.8: Cu equilibrium surface concentration as a function of temperature in bulk and three thin films (52, 26, 10-nm) with positive interaction and without interaction for Ni-1.0at.%Cu alloy.

To examine the influence of film thickness on equilibrium surface segregation, the Cu equilibrium surface concentration was plotted as a function of film thickness at different temperatures (from 500 to 900 K) for the Ni-1.0 at.%Cu alloy (see Fig. 9.9). The value marked by a vertical line in Fig. 9.9 is called the thickness limit, which represents the film thickness where the equilibrium surface concentration of the thin

film system is 10 % less than equilibrium surface concentration of the corresponding bulk system [11, 12]. As is shown in Fig. 9.9, when the film thickness is less than a certain value (4 nm), the Cu surface concentration is close to a constant value and this Cu concentration is independent of temperature. In additional, the thickness limit value as a function of temperature is plotted in Fig. 9.10 and the maximum values of 99.1 nm appear at 900 K for the Ni-1.0at.%Cu alloy. This result implies that there is a specific temperature at which the size effect (on the Cu equilibrium surface segregation) is more pronounced.

Furthermore, Fig. 9.11 shows the thickness limit value as a function of initial bulk concentration for difference segregation energy at a constant temperature of 700 K. The red arrow marked in Fig. 9.11 is the direction of the increasing segregation energy. The thickness limit increased with a decrease in initial bulk concentration. The thickness limit also increased with a decrease in segregation energy.

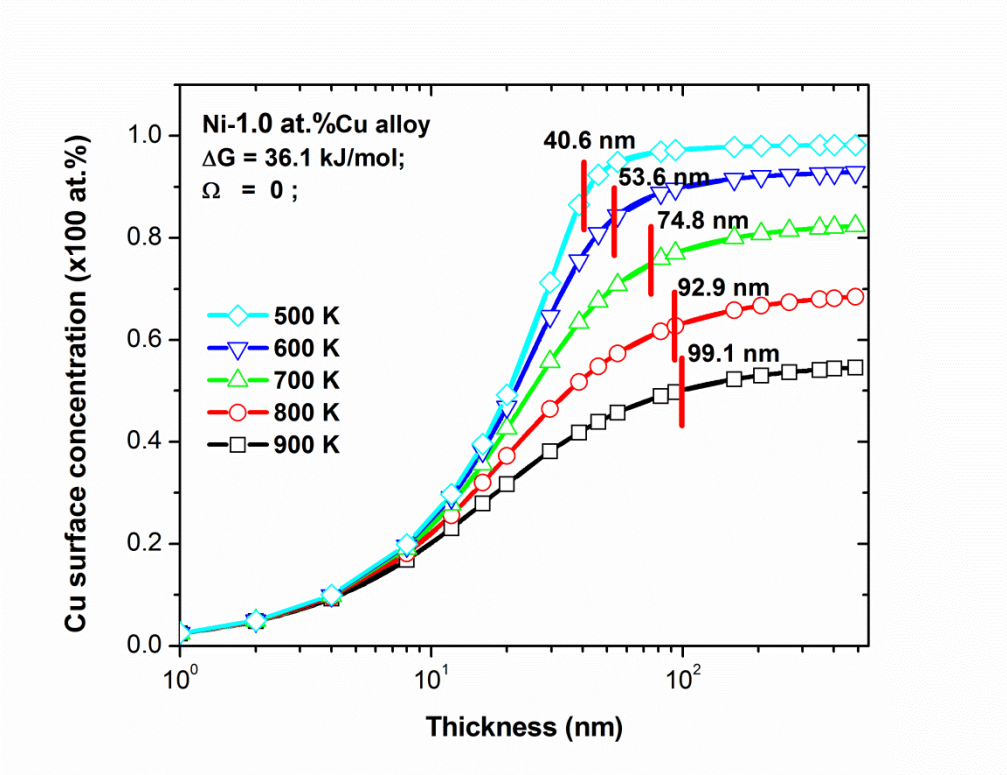

Figure 9.9: Cu equilibrium surface concentration as a function of film thickness with various temperatures for Ni1.0at.%Cu alloy. The marked thickness value is called thickness limit (see text in Section 9.3.3).

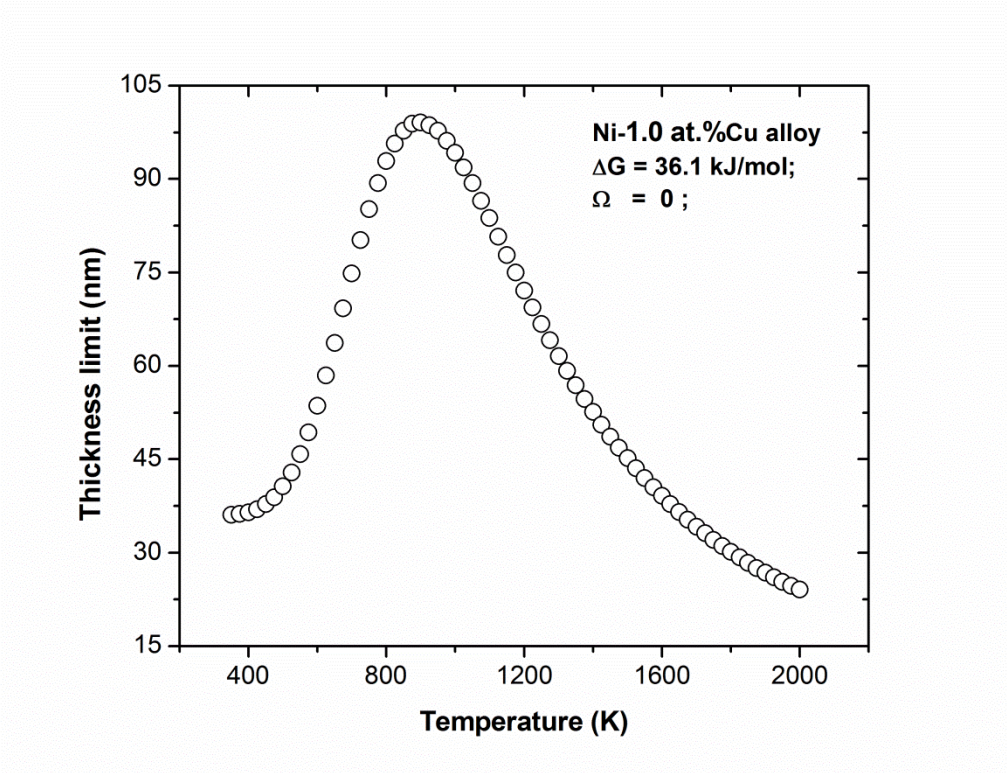

Figure 9.10: Thickness limit value as a function of temperature for Ni1.0at.%Cu alloy.

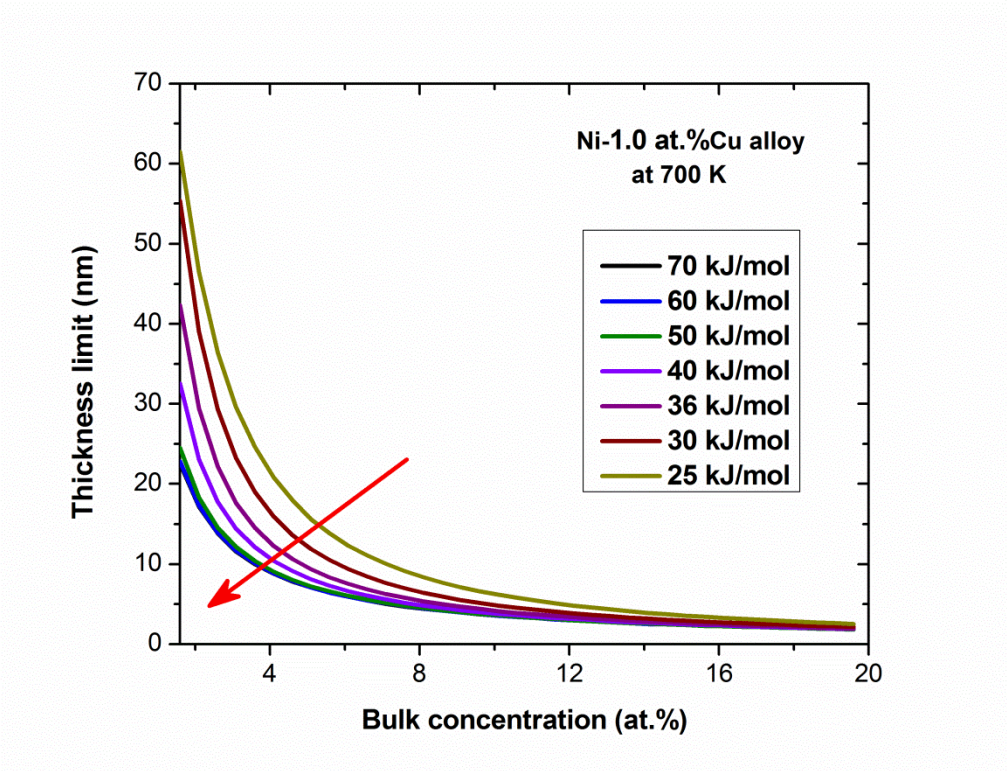

Figure 9.11: Thickness limit value as a function of initial bulk concentration at 700 K with various segregation energy values. The red arrow is the direction of the increasing segregation energy.

To study the influence that film thickness has on the segregation kinetics, the surface concentration was calculated as a function of time for a film at 700 K for four different thicknesses by solving the rate equations (Eq. 9.3) with the constrained condition (Eq. 9.5). The result is plotted in Fig. 9.12. The close-dotted points displayed in Fig. 9.12 represent the corresponding equilibrium surface concentration values, which are calculated independently by introducing Eq. 9.5 into Eq. 9.4. The simulation result as shown in Fig. 9.12 indicates that the time required for reaching an equilibrium state decreases when film thickness decreases. The agreement between the equilibrium and the kinetic simulation results for the final equilibrium stage as indicated in Fig. 9.12 implies that the modified Darken model combined with the constrained condition (Eq. 9.5) can be used to describe both equilibrium and kinetic surface segregations in thin films.

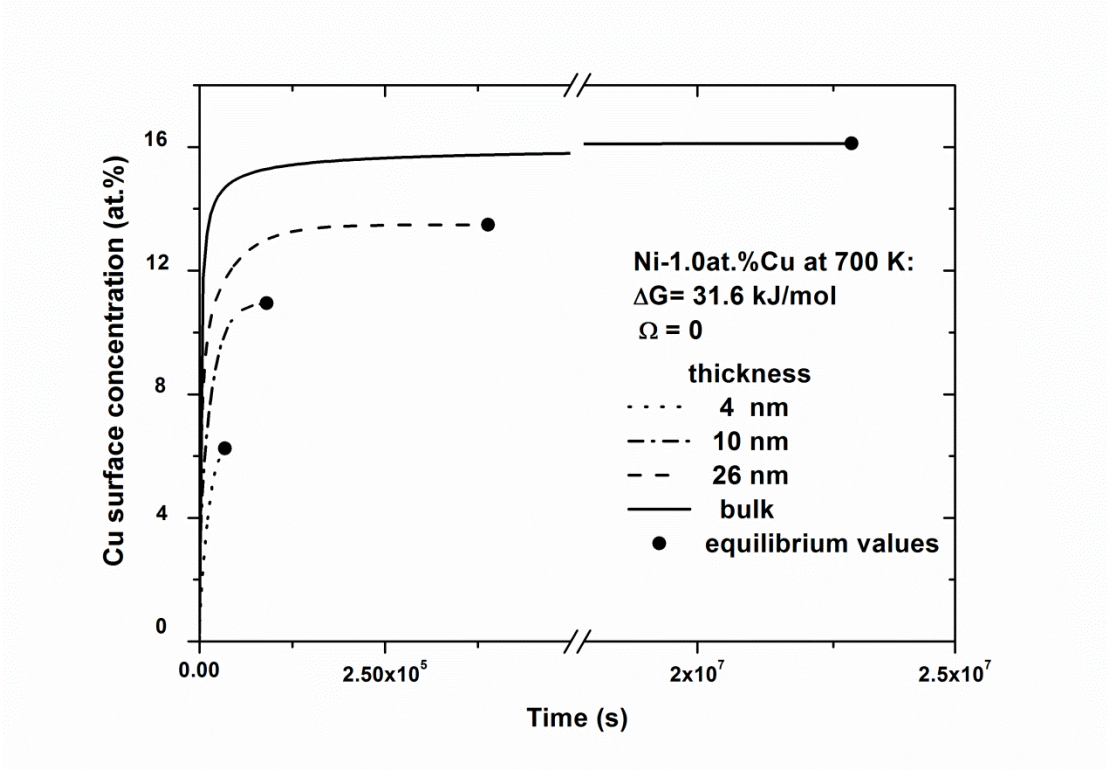

Figure 9.12: Cu surface concentration as a function of time at 700 K with various film thickness values for Ni-1.0at.%Cu alloy. The close-dotted points represent the corresponding equilibrium surface concentration values calculated independently from Eq. 9.4.

9.4 Summary

In this chapter, the surface segregations of Cu from a Ni-Cu alloy thin films system was measured using AES with the linear temperatures programmed heating method and the samples where heated at constant rate of 0.03 K/s from 403 K to 823 K. The segregation measured profile data were fitted with the modified Fick's model extracted the *bulk-to-surface* diffusion coefficient for Cu in Ni-Cu alloy thin films as $D_o = 2.8 \times 10^{-13}$ m^2/s and $Q = 135.3$ kJ/mol for thinner sample (26 nm), for the thicker sample (52 nm) $D_o = 2.9 \times 10^{-13}$ m^2/s and $Q = 140.5$ kJ/mol. These diffusion parameters compared well with experimental data values obtained from others in literature. It was found that the surface enrichment factor β in the equilibrium for thicker sample (52 nm) is higher than that for the thinner sample (26 nm).

To understand the size effects on surface segregations in thin films system, the modified Darken model are employed to simulate for both the kinetics and equilibrium for a Ni-Cu alloy under a constrained condition. From the simulation it was concluded that (a) the Cu equilibrium surface concentration with a zero interaction parameter is lower than that with a positive interaction parameter (Ω= 7.6 kJ/mol); (b) The equilibrium surface concentration decrease with a decrease in film thickness; (c) As the film thickness decrease the effect of the positive interaction is less pronounced; (d) There is a specific temperature at which the size effect on equilibrium surface segregation is more pronounced; and (e) As the film thickness decrease, the time required for reaching the equilibrium state decreases.

References

[1] R. Ferrando, J. Jellinek, R.L. Johnston, Nanoalloys: from theory to applications of alloy clusters and nanoparticles, Chemical reviews **108** (2008) 845-910.

[2] S. Swaminarayan, R. Najafabadi, D.J. Srolovitz, Polycrystalline surface properties from spherical crystallites: Ag, Au, Cu and Pt, Surf. Sci. **306** (1994) 367-380.

[3] F.R. de Boer, R. Boom, W.C.M. Mattens, A.R. Miedema, A.K. Niessen, Cohesion in metals: Transition metals alloys, North Holland, Amsterdam, 1988.

[4] C. Cserháti, I.A. Szabó, D.L. Beke, Size effects in surface segregation, J. Appl. Phys. 83 (1997) 3021-3027.

[5] A.M. Llois, C.R. Mirasso, Segregation in thin films of binary alloys A_xB_{1-x}, Phys. Rev. B **41**(1990) 8112.

[6] M. Schmid, W. Hofer, P. Varga, P. Stoltze, K.W. Jacobsen, J.K. Norskov, Surface stress, surface elasticity, and the size effect in surface segregation, Phys. Rev. B **51** (1995) 10937.

[7] J. Nyeki, C. Girardeaux, G. Erdelyi, A. Rolland, J. Bernardini, Equilibrium surface segregation enthalpy of Ge in concentrated amorphous SiGe alloys. Appl. Surf. Sci. **212** (2003) 244-248.

[8] S. Swaminarayan, D.J. Srolovitz, surface segregation in thin films, Acta Mater. **44 (**1996) 2067-2072.

[9] J.A. Brown, Y. Mishin, Effect of surface stress on Ni segregation in (110) NiAl thin films, Phys. Rev. B **69** (2004) 195407.

[10] S. Swaminarayan, R. Najafabadi, D.J. Srolovitz, Finite size effects on the thermodynamics of Cu-Ni alloys :{100} and {110} thin films, Acta Mater. **45 (**1997) 1715-1724.

[11] X.L. Yan, J.Y. Wang, Size effects on surface segregation in Ni-Cu alloy thin films, Thin Solid Films **529** (2013) 483-487

[12] X.L. Yan, M. Lin, J.Y Wang, Equilibrium and kinetic surface segregations in Cu-Sn thin films. Appl. Phys. A **113**(2013) 423-430

[13] C.L. Hedberg, Handbook of Auger Electron spectroscopy, Third Edition, Physical Electronics Industries, Eden Prairie, MN, USA,1995.

[14] O. Taguchi, Y. Iilima, K. Hirano, Application of atomic absorption analysis to impurity diffusion of copper in nickel in a wide range of temperature, J. Japan Inst. Metals **48** (1984) 20-24.

Chapter 10
Conclusions

In this study, the surface segregation in a Ni-Cu alloy was investigated by both modeling the segregation process theoretically and measuring it experimentally. The experimental measurements were performed on a bulk crystal as well as on thin films. In addition to the segregation measurements, the Ni/Cu multilayer thin films were used to study the interdiffusion of Cu and Ni with AES depth profiling. A quantitative evaluation of sputtering-induced surface roughness and depth resolutions was also performed utilizing the MRI model to fit depth profiles measured with AES and SIMS.

In a first set of experiments, the Ni/Cu polycrystalline multilayer thin films were characterized by AES depth profiling with sample rotation, without sample rotation (stationary), with single ion beam sputtering and dual ion beam sputtering. The measured concentration-depth profiles data were quantitative analyzed with the MRI model. The depth-dependence of the depth resolutions during depth profiling were quantitatively evaluated with the MRI model. It was observed that the depth resolution is smaller when profiling with dual-ion beam vs. a single-ion beam. It was also found that profiling with a lower ion energy result in a better (smaller) depth resolution. Rotation of the sample during ion sputtering had the best (smallest) depth resolution.

In a second set of experiments, the influence of the different ion source (O_2^+, Cs^+ and Xe^+) and different sputter ion energies were investigated using SIMS depth profiling of polycrystalline Ni/Cu multilayer thin films. The measured depth profiles data were quantitative analyzed with the MRI model to account for atomic mixing and surface roughness. The surface topography of the crater bottom after sputtering with different

ion energy and at different sputter depth was measured with the AFM. The MRI fitted roughness parameters obtained for the SIMS depth profiling compared well with the root-mean-square roughness obtained from the AFM topography scans of crater bottom. Depth profiling with Cs^+ ion sputtering had the best depth resolution compared to Xe^+ and O_2^+ ion sputtering.

Ion sputtering induced roughness and depth resolution were determent for SIMS depth profiling performed with different ion energies on a polycrystalline Ni/Cu multilayer. The results indicated that the depth resolution is noticeably better for depth profiling with a lower primary ion energy, which can be credited to a lower ion sputter induced roughness and a smaller atomic mixing length.

In a third set of experiments, the MRI model was used for extracting the interdiffusion coefficients in Ni/Cu multilayer thin films from depth profiles measured with AES. The interdiffusion parameter for Cu/Ni multilayer thin films was characterized for the first interface D_o =6.2×10^{-13} m^2/s and Q =101.4 kJ/mol, and the last Cu/Ni interface D_o=6.3×10^{-14} m^2/s and Q =79.0 kJ/mol.

In a fourth set of experiments, the surface segregations of Cu and S from a ternary Ni-Cu(S) alloy system was measured using AES with both linear temperatures programmed heating and constant temperature heating methods. The segregation data measured with the linear temperature programmed heating method were fitted with the modified Darken model. The diffusion and segregation parameters obtained with the modified Darken model fitted to the linear annealing segregation data are $D_{o\text{Cu in Ni}}$ = 8.6×10^{-14} m^2/s and $Q_{\text{Cu in Ni}}$ = 145.2 kJ/mol, $D_{o\text{S in Ni}}$ = 9.2×10^{-2} m^2/s and $Q_{\text{S in Ni}}$ = 224.0 kJ/mol, ΔG_{Cu}= -36.0 kJ/mol, ΔGs= -136.0 kJ/mol and $\Omega_{Cu\text{-}Ni}$=7.6 kJ/mol, $\Omega_{S\text{-}Ni}$=28.1 kJ/mol and $\Omega_{Cu\text{-}S}$= -10.3 kJ/mol.

The diffusion and segregation parameters determent from the constant temperature heating method were obtained by fitting the segregation profiles with the modified Fick's model. The bulk diffusion coefficient was $D_{o\text{Cu in Ni}}$= 5.8×10^{-14} m^2/s and $Q_{\text{Cu in Ni}}$ = 160.1 kJ/mol, $D_{o\text{S in Ni}}$ = 1.2×10^{-2} m^2/s and $Q_{\text{S in Ni}}$ = 222.1 kJ/mol. The

segregation parameters obtained in this study were compared well with experimental data values obtained from others in literature.

In a last set of experiments, the surface segregation of Cu from Ni-Cu alloy thin films was measured using AES with the linear temperature programmed heating methods. The segregation measured profile data were fitted with the modified Fick's model to extract the *bulk-to-surface* diffusion coefficient for Cu in a Ni-Cu thin film alloy. For the 26 nm thin film the diffusion parameters were $D_o = 2.8 \times 10^{-13}$ m^2/s and $Q = 135.3$ kJ/mol. In the case of the thicker thin film (52 nm) diffusion parameters were $D_o = 2.9 \times 10^{-13}$ m^2/s and $Q = 140.5$ kJ/mol. These diffusion parameters compared well with data found in literature. The equilibrium surface enrichment factor for the thicker thin film is higher than that of the thinner thin film.

To understand the size effects on surface segregations in thin films system, the modified Darken model was employed to simulate the segregation in a Ni-Cu thin film alloy utilising constrained conditions. The simulations shows that (a) the Cu equilibrium surface concentration with a zero interaction parameter is lower than that with a positive interaction parameter (Ω= 7.6 kJ/mol); (b) The equilibrium surface concentration decrease with a decrease in film thickness; (c) As the film thickness decrease the effect of the positive interaction is less pronounced; (d) There is a specific temperature at which the size effect on equilibrium surface segregation is more pronounced; and (e) As the film thickness decrease, the time required for reaching the equilibrium state decreases.

Appendix: Publications and conferences

Publications:

1. **X.L. Yan**, Y. Liu, H.C. Swart, J.Y. Wang, J.J. Terblans, Investigation of interdiffusion and depth resolution in Cu/Ni multilayer by means of AES depth profiling, ***Applied Surface Science,* 364** (2016) 567-572.

2. **X.L. Yan,** E. Coetsee, J.Y. Wang, H.C. Swart, J.J. Terblans, Evaluation of sputtering-induced surface roughness and its influence on AES depth profiling of polycrystalline Ni/Cu multilayers thin films, ***Applied Surface Science,* 411** (2017) 73-81.

3. **X.L. Yan,** M.M. Duvenhage, J.Y. Wang, H.C. Swart, J.J. Terblans, Evaluation of sputtering-induced surface roughness development of Ni/Cu multilayers thin films by ToF-SIMS depth profiling with O_2^+ ion bombardment at the different energies, ***Applied Surface Science***, under reviewed.

4. **X.L. Yan**, Y. Liu, H.C. Swart, J.Y. Wang, J.J. Terblans, A quantification evaluation of the depth resolution of AES depth profiling data of Cu/Ni multilayer thin films using the MRI model, **Proceedings of the 2015 The Proceedings of the 60th Annual Conference of the South African Institute of Physics (SAIP2015)**, (2016) 141-146.

5. **X.L. Yan**, Y. Liu, H.C. Swart, J.Y. Wang, J.J. Terblans, Study of the interdiffusion in Ni/Cu multilayer thin films by Auger electron spectroscopy depth profiling, **Proceedings of the 2015 The Proceedings of the 60th Annual Conference of the South African Institute of Physics (SAIP2015)**, (2016) 147-152.

6. H. A. Abrass, C.C. Theron, E.G. Njoroge, N.G. van der Berg, A.J. Botha, **X.L. Yan**, J.J. Terblans, Cobalt silicide formation on a Si(100) substrate in the presence of an interfacial ($Fe_{90}Zr_{10}$) interlayer, ***Nuclear Instruments and Methods in Physics Research B,* 359** (2015) 85-88.

7. **X.L. Yan,** J.Y. Wang, H.C. Swart, J.J. Terblans, AES study of Cu and S surface segregation in a ternary Ni-Cu(S) alloy in combination with a linear heating method, (submitted to ***Journal of Material Science***).

8. **X.L. Yan,** J.Y. Wang, H.C. Swart, J.J. Terblans, Bulk-to-surface segregation measurements of Cu and S in a Ni-Cu(S) ternary system with Auger electron spectroscopy, (submitted to ***Journal of Alloys and compounds***).

9. **X.L. Yan,** J.Y. Wang, H.C. Swart, J.J. Terblans, Surface segregation measurements of Cu from a NiCu alloy thin film (to be submitted).

Conferences:

1. **X.L. Yan**, Y. Liu, H.C. Swart, J.Y. Wang, J.J. Terblans, Investigation of interdiffusion and depth resolution in Cu/Ni multilayer by means of AES depth profiling, 1st International Conference on Applied Surface Science (ICASS), 27-30 July 2015, Shang Hai, China, **Oral Presentation**

2. **X.L. Yan**, Y. Liu, H.C. Swart, J.Y. Wang, J.J. Terblans, A quantification evaluation of the depth resolution of AES depth profiling data of Cu/Ni multilayer thin films using the MRI model, 2015 South Africa Institute of Physics annual conference, 28 June - 3 July 2015, Port Elizabeth, South Africa, **Poster Presentation (The best poster award of 2015 SAIP)**

3. **X.L. Yan**, Y. Liu, H.C. Swart, J.Y. Wang, J.J. Terblans, Study of the interdiffusion in Ni/Cu multilayer thin films by Auger electron spectroscopy depth profiling, 2015 South Africa Institute of Physics annual conference, 28 June- 3 July 2015, Port Elizabeth, South Africa, **Oral Presentation**

4. **X.L. Yan**, J.Y. Wang, H.C. Swart, J.J. Terblans, Evaluation of sputtering-induced surface roughness of polycrystalline Ni/Cu multilayers thin films with AES and ToF-SIMS depth profiling, 2016 South Africa Institute of Physics annual conference, 4-8 July 2016, Cape Town, South Africa, **Oral Presentation**

5. **X.L. Yan**, J.Y. Wang, H.C. Swart, J.J. Terblans, Surface segregation of Cu and S in Ni-Cu(S) ternary alloy, 10^{th} International Conference on Diffusion in Materials (DIMAT), 7-12 May 2017, Haifa, Israel, **Oral Presentation**

Awards:

1. **XinLiang YAN**, Goodfellow Award, South Africa Institute of Physics, 2016

2. **XinLiang YAN**, Best poster Award, South Africa Institute of Physics, 2015

Goodfellow Cambridge Limited

+44 (0)1480 424800

http://www.goodfellow.com/pwco.asp

Request Information

Categories: Materials

Goodfellow Award Presented at South African Institute of Physics (SAIP) Annual Conference

Mr. Xin-Liang Yan, a doctoral student at the University of the Free State, is this year's winner of the Goodfellow Award for Best Publication by a PhD Student in the field of condensed matter and materials.

8 September 2016

Huntingdon, UK … 7 September 2016 … Mr. Xin-Liang Yan, a doctoral student at the University of the Free State, is this year's winner of the Goodfellow Award for Best Publication by a PhD Student in the field of condensed matter and materials. Mr. Yan's paper, "Investigation of interdiffusion and depth resolution in Cu/Ni multilayers by means of AES depth profiling", was published in Applied Surface Science, volume 364, pages 567-572 of 2016.

The Goodfellow Award, the top honour bestowed by the Division for Physics of Condensed Matter and Materials at the South African Institute of Physics (SAIP) conference each year, is funded by the Goodfellow Group of Companies, international suppliers of high-quality metals, polymers, ceramics and other materials to universities and other research facilities. According to Goodfellow Managing Director Stephen Aldersley, the Goodfellow Award – first given at the SAIP conference in 2000 – is a tangible example of the company's commitment to recognizing talented young scientists. "We at Goodfellow are pleased to highlight the innovative research of these outstanding young professionals", says Aldersley. "They are truly an inspiration to us all".

For more information about Goodfellow, go to www.goodfellow.com. For more information about the South African Institute of Physics, go to www.saip.org.za.

Prof. Japie Engelbrecht, Chairman of SAIP's Division for Physics of Condensed Matter and Materials, presents the 2016 Goodfellow PhD Publication Award to Mr. Xin-Liang Yan.

Related Information

www.goodfellow.com (Weblink) Visit site

What's new

Goodfellow Award Presented at South African Institute of Physics (SAIP) Annual Conference
News | 8 Sep 2016

Mr. Xin-Liang Yan, a doctoral student at the University of the Free State, is this year's winner of the Goodfellow Award for Best Publication by a PhD Student in the field of condensed matter and materials.

High-quality CVD Graphene Films for Innovative Applications
Products | 19 May 2016

Huntingdon (UK) … 17 May 2016… Through state-of-the-art chemical vapour deposition (CVD) methods, Goodfellow is able to offer a new line of exceptionally high quality graphene film for use as transparent conductors and in other innovative applications.

High Thermal Conductivity Silicon Nitride - Ideal as Insulating Substrate for High-Power Electronic Devices
Products | 14 Mar 2016

Goodfellow has expanded its range of advanced ceramics with the addition of high thermal conductivity silicon nitride.

Wide Range of Rare Earth Metal Foils Available from Goodfellow
Products | 26 Aug 2015

A wide range of rare earth metal foils is available from Goodfellow, a leading supplier of high-purity metals and materials for research and industry.

Specialist Polymer Films Available From Goodfellow
Products | 24 Aug 2015

Goodfellow, a leading supplier of polymers, metals and other materials for research and industry, offers a wide selection of polymer films, including specialist products suitable for demanding applications.

- Our News
- Our Products

Search all our content

Related Articles

- **High-quality CVD Graphene Films for Innovative Applications**
  19 May 2016